DEVELOPMENT AND EVALUATION OF A COMPOSITE PHOTOCATALYST FOR WATER TREATMENT PROCESSES

by

Adrián A. Vega

B.Sc., University of Costa Rica, 2005

A THESIS SUBMITTED IN PARTIAL FULFILMENT OF
THE REQUIREMENTS FOR THE DEGREE OF

MASTER OF APPLIED SCIENCE

in

THE FACULTY OF GRADUATE STUDIES
(Chemical and Biological Engineering)

THE UNIVERSITY OF BRITISH COLUMBIA
(Vancouver)

August 2009

Abstract

Titanium dioxide (TiO_2) has been extensively studied for photocatalytic oxidation of organic pollutants, in water and gas effluents, into smaller and harmless substances such as CO_2 and H_2O. However, there are still a number of drawbacks that hinder its large scale applications, for example expensive downstream filtration of the photocatalyst powder, mass transfer limitations, loss of activity, attrition, among others.

Fluidized bed photoreactor (FBPR) with its advantages for potential commercial applications, suffers from the problem of attrition and elutriation of particles. This research focused on addressing this challenge and worked on the development of a template-free composite photocatalyst to be used in a FBPR. It involved the production of TiO_2 nanoparticles, using sol-gel process, and mixing them with TiO_2 pre-calcined powder (Degussa P-25), used as filler material bonded together with the gel-derived TiO_2. This solution was then mixed with a polymeric structure to produce the spheres. A complete characterization of the TiO_2 spheres was performed to determine their morphology (XRD – X Ray Diffraction, SEM – Scanning electron microscopy), physicochemical properties (BET surface area, pore volume and pore diameter) and thermal behaviour (TGA – Thermo gravimetric analysis).

The major achievement of this work was to modify the formulation and synthesis procedure of the composite TiO_2 spheres, producing a photocatalyst with good attrition resistance and high photoactivity. The improvements were made by working on the preparation conditions (modifying the hydrolysis and condensation rates during sol-gel preparation, aging time, spheres formation, drying process, and calcination conditions) and evaluating their impacts on the attrition resistance (amount of TiO_2 particles released to the solution during the normal operation of the FBPR). Photocatalyst activity was measured based on its efficacy at decomposing organic compounds such as formic acid (FA) and 2,4-Dichlorophenoacetic acid (2,4-D), as well as natural organic matter (NOM).

The attrition resistance of the TiO_2 spheres was improved by 70%, corresponding to a reduction in the amount of TiO_2 particles released from the catalyst from 22 mg L^{-1} to 7 mg L^{-1}. This was achieved via the following modifications in the formulation and synthesis procedure:

- Accelerating the rate of hydrolysis and condensation reactions that occur during the formation of the sol-gel matrix, by increasing the amount of water from 0.040 g H_2O per mL^{-1} of Ti precursor to 0.053 g H_2O per mL^{-1} Ti precursor and reducing the amount of catalyst (HCl) from 0.20 mL HCl per mL^{-1} Ti precursor to 0.13 mL HCl per mL^{-1} Ti precursor.
- Increasing pH of the solution, where the spheres are formed, from 11.75 to 12.
- Accelerating the drying process from 15 days at 23°C to 20 h at 80°C.
- Increasing the calcination time from 1 h to 3 h.

In terms of the photocatalytic activity, the composite TiO_2 spheres demonstrated high activity to degrade either FA or 2,4-D. The degradation of both model pollutants followed first order kinetics with rates constants of 0.317 min^{-1} (with fluence rate of 5.32 mW cm^{-2}) and 0.736 min^{-1} (with a fluence rate of 4.16 mW cm^{-2}) for FA and 2,4-D, respectively. A comparison with Degussa P-25 was made showing that the activity of the TiO_2 spheres is higher than that of the commercial TiO_2 powder for both model organic compounds. For NOM degradation, water from Trepanier Creek in Central British Columbia (initial TOC of approximately 5 mg L^{-1}) was treated. There was about 50% reduction of NOM after 1 h, but this was primarily due to the adsorption of NOM on the spheres.

Table of Contents

List of Tables

List of Figures

Nomenclature

a – External surface to volume ratio of the catalyst particles

a_{cat} – Activity of the catalyst

d – Interplanar spacing between crystals

d_{sph} – diameter of the composite TiO_2 spheres

d* – Dimensionless particle diameter

e – Expansion index

e^- – Electrons

f – Total number of tested TiO_2 spheres formulations

g – Gravity force

h^+ – Holes

hν – Energy

i – Integer exponent in power law rate expression

m – Individual observations

m_{sph} – Mass of composite TiO_2 spheres

n – Integer representing order of diffraction

$n_{ph,\ tot}$ – Total number of photons

$n_{ph,\ trans}$ – Number of photons entering into the reactor volume

n_t – number of observations

k'' – Surface second order rate constant

k_C – Fractional site coverage by hydroxyl radicals

k_{CT} – Charge transfer rate

k_{LH} – Apparent Langmuir-Hinshelwood rate constant

k_{MT} – Mass transfer coefficient

k_{obs} – Observed reaction rate constant

k_r – Rate constant for the FA degradation

k'_r – Rate constant for the FA degradation in m s^{-1}

k_R – Electron/ hole recombination rate

$k_{2,4\text{-}D}$ – 2,4-D photodegradation rate constant

pKa – Acid dissociation constant

q_λ - Spectral radiation flux

r – Rate

r_K – Kelvin radius of the pore of the catalyst

r_p – Real pore radius of the catalyst

r_{sph} – Radius of the composite TiO_2 spheres

s_T^2 – Between-formulations mean square

s_R^2 – Within-formulations mean square

t – Thickness of the adsorbed layer in the catalyst

t_l – Time of irradiation

t_v – T distribution

v – Volume of gas adsorbed (m^3)

v_e – Terminal velocity of isolated single particles

v_m – Molar volume of liquid N2 (34.7 cm^3 mol^{-1})

v_t – Terminal velocity of the composite TiO_2 spheres

$\hat{y}$ – Grand average of all the data

$\hat{y}t$ – Average of three experimental values (reaction rate constants)

y_{tm} – m*th* observation in the t*th* formulation

z – Oxidation state

A – Electron acceptor / Titania polymorphic phase (Anatase)

A_N – Nucleophilic addition

Ar – Archimedes number

AOP – Advance oxidation processes

B_{exp} – Expansion of the bed

BET – Brunauer-Emmet-Teller method to measure surface area

BDDT – Brunauer, Demming, Deming and Teller classification for isotherms generated suring surface area determination

BJH – Barrett, Joyce and Halenda method for pore size distribution determination

BSE – Backscattered electrons

C – Molar concentration of the iodide solution

C_{ads} – Amount of 2,4-D adsorbed in the catalyst

C_{Amm} – Ammonia concentration in water (10% v/v)

C_{elem} – Covariance element

C_{eq} – Concentration of 2,4-D in equilibrium

C_{FA} – Concentration of FA in solution

C_{HCl} – Concentration of HCl during the sol-gel preparation

C_{H2O} – Concentration of water during the sol-gel preparation

C_{time} – Time that takes the heat treatment of the composite TiO_2 spheres

$C_{2,4\text{-}D}$ – Concentration of 2,4-D

$C_{2,4\text{-}D0}$ – Initial concentration of 2,4-D

CB – Conduction band

Ch_{conc} – Concentration of Chitosan (15 g L^{-1})

CI – Confidence interval (95%)

COD – Chemical oxygen demand

CSG – Composite sol-gel

D – Electron donor

D_{cool} – Drying process where the composite TiO_2 spheres were dried at 80°C for 20 h, then cool down to room temperature and then the heat treatment was applied

D_{cont} – Continuous drying and heat treatment process (drying process at 80°C for 20 h and immediately after that, the temperature was risen to 600°C for 1 h)

$D_{FA\text{-}W}$ – Diffusive coefficient for FA in water

D_g – Monosaccharide residue (D-glucosamine)

DBP – Desinfection by-products

DSC – Differential scanning calorimetry

E_{est} – Standard error of the estimation

F – F value for statistical analysis for v_T/v_R degrees of freedom

F_{exp} – F value for statistical analysis obtained from experimental results

FA – Formic acid

FBPR – Fluidized bed photoreactor

Ga – Galileo number

H_{II} – Fluence rate using Iodide-Iodate Actinometry

H_{PF} – Fluence rate using Potassium Ferrioxalate Actinometry

H2 – Characteristic hysteresis loop

H3 – Characteristic hysteresis loop

H_{Bed} – Height of the bed

$H_{Bed,O}$ – Height of the static bed

HPLC – High performance liquid chromatography

I – Photon or irradiation flux

I_i – Intermediate product

IEP – Isoelectric point

K – 2,4-D adsorption constant

K_{ads} – Apparent adsorption equilibrium constant

K^{app}_{ads} – Apparent adsorption constant

K_i – Equilibrium adsorption constant for the intermediate i

K_L – Langmuir adsorption constant

K_{O2} – Apparent rate constant for oxygen

K_{O2a} – Equilibrium adsorption constant for oxygen

$K_{2,4\text{-}D}$ – Equilibrium adsorption constant for 2,4-D

L-H – Langmuir Hinshelwood adsortion/kinetic model

LpH – Chitosan solution at pH = 4.01

LP-25 – Low amount of P25 in the sol-gel (0.30 g mL^{-1} TTIP)

M – Network forming element during the sol-gel process

M_v – Density number

M_x - Mean

MA – Mineral acids

MC – Monte Carlo method

MF – Modified formulation to produce the composite TiO_2 spheres

MpH – Chitosan solution at pH = 4.58

MP-25 – High amount of P25 in the sol-gel (0.50 g mL^{-1} TTIP)

N – Maximum coordination number

N_A – Monosaccharide residue (N-acetyl-D-glucosamine)

N_t – Total number of observations

NOM – Natural organic matter

OF – Original formulation

P – Pollutant or Pressure in the system

P_{ads} – Pollutant adsorbed on the catalyst

$P_{lamp,\lambda}$ – Power of the lamp at 254nm

P_{liq} – Pollutant dissolved in a liquid phase

P_{O2} – Oxygen pressure in the system

PPCP – Pharmaceutical and personal care products

Q – Volumetric flow rate

R – Titania polymorphic phase (Rutile)

$R_{reactor}$ – Radius of the quartz tube

ROH – Alcohol

RT – Room temperature

Sc – Schmidt number

S_E – Standard error

S_{Error} – Standard error

S_N – Nucleophilic substitution mechanism

S_{param} – Standard error of the parameter

S_R – Within-formulation sum of squares

S_T – Sum of squares

Sh – Sherwood number

SD – Standard deviation

SE – Secondary Electrons

SEM – Scanning electron microscopy

T - Temperature

TEOS – Tetraethyl orthosilicate

TGA – Thermo gravimetric analysis

THM – Trihalomethanes

TOC – Total organic carbon

TTIP – Titanium IV isopropoxide

U – Fluidization velocity

UV – Ultraviolet light

UV/H_2O_2 – Advance oxidation process utilizing ultraviolet and hydrogen peroxide

UV/O_3 - Advance oxidation process utilizing ultraviolet and ozone

$UV/O_3/H_2O_2$ - Advance oxidation process utilizing ultraviolet, ozone and hydrogen peroxide

VB – Valence band

V – Solution volume

V_{dil} – volume of dilution for the samples taken during the potassium ferrioxalate actinometry

V_{irrad} – Irradiated volume during the potassium ferrioxalate actinometry

V_{samp} – Volume of the samples taken during potassium ferrioxalate actinometry

W – Watts

WHO – World health organization

X – Individual observation

XRD – X-ray diffraction

α – Proportional constant to calculate the reaction rate constant based on the photon flux

β – Exponential constant to calculate the reaction rate constant based on the photon flux

ε - Voidage of the bed or molar extinction coefficient (1.11 x 104 L $gmol^{-1}$ cm^{-1})

σ – Variance

ε_C – Molar extinction coefficient used for the calculations of the irradiation flux using potassium ferrioxalate actinometry

ε_{450} – Molar absorption coefficient of triodide at 450 nm.

γ – Surface tension of N_2 at its boiling point (8.85 ergs cm^2 at 77K)

λ - Wavelength

ξ – Relative efficiency

ρ_{H2O} – Density of water

ρ_{sph} – Density of water

μ_{H2O} – Viscosity of the water

ϕ – Quantum yield

ϕ_s - Sphericity

θ - Bragg angle

ΔA_{450} – Change in the absorbance at 450 nm

ΔG – Change of Gibbs free energy

θ_p – Equilibrium coverage of the pollutant over the surface of the catalyst

θ_{OH} – Fractional site coverage by hydroxyl radicals

$\theta_{2,4\text{-}D}$ – Fractional site coverage by 2,3-D

v_R – Degree of freedom within formulations

v_T – Degree of freedom between formulations

Acknowledgements

My sincere gratitude is due toward my supervisor, Dr. Madjid Mohseni, who provided me with this incredible opportunity to come to UBC and be part of his research group. His support, generosity and constant guidance gave me the chance to overcome many of the challenges that I faced during this process.

I would like also to acknowledge Dr. Mehrdad Keshmiri for his help, trust and support during this process. I am also grateful to Dr. Naoko Ellis and Dr. Dusko Posarac for reviewing my thesis and being part of my research committee. I am very thankful for their valuable advice and comments.

During the last five months of my masters, I received an incredible help from Maxime Thevenin during his exchange program at UBC. He gave an enormous contribution helping me in the conduction and data collection of many experiments. Thanks a lot for your work, your desire to learn, for your diligent work and friendship.

I am especially grateful to Gustavo Imoberdorf, Siva Sarathy, Esteban Durán, Sandra Robaire for their help, advise, constant support and friendship during this process. Certainly, every discussion and brainstorming generated valuable ideas that helped me to achieve my goals during my masters.

I want also to thanks to Dr. Kevin Smith and Dr. Fariborz Taguipour from Chemical Engineering Department for letting me used their laboratories and equipments. I would like also to thank Dr. Tom Troczynski from Materials Department for providing access to the Ceramic Laboratories and Dr. Matti Raudsepp, from the Department of Earth and Ocean Sciences, for teaching and helping me with many important tools and techniques use in materials characterization.

My thanks are also extended to my friends Jana Schmidtova, Jidon Janau, Masakazu Sakaguchi, Anne-Marie Kietzig, Bojan Petkovic, Ryan Anderson, Mohammad Alquaad and so many other graduate students for their friendship and support. I want to thank them all for sharing their expertise on specific topics and for providing their time and minds to solve issues.

Special thanks also to the faculty and staff of the Department of Chemical and Biological Engineering for their support and for the friendly environment that I found here. I would like to acknowledge also the generous funding contributed by BI Pure Water (Canada) Inc. and NSERC.

Lastly, I would like to express my deepest appreciation and respect to my family, especially my parents and my wife for giving me hope, courage and an amazing support throughout this process.

Dedication

First of all, I would like to dedicate this work to God, for His amazing grace, everlasting love and guidance through my academic and personal life.

Secondly, I would like to devote all this work to my family, especially to my wife and parents, for their constant support and advice. They have been always there in my most difficult times of struggles and sorrows.

Additionally, I would like to mention my godfather Luis Emilio (*R.I.P*) who always supported me during my engineering career and encouraged me to continue with my graduate studies abroad. Unfortunately, he is not longer with us to enjoy this moment, but I am sure he would be proud of this new accomplishment.

I also want to dedicate this work to my godson David. He was born almost at the same time I was finishing my work at UBC and, as every new born, he has become in a source of inspiration for everyone.

The victory of success is half won when one gains the habit of setting goals and achieving them. Even the most tedious chore will become endurable as you parade through each day convinced that every task, no matter how menial or boring, brings you closer to fulfilling your dreams.

Og Mandino

Chapter One

Introduction

1.1 Background

Contaminated water, along with its consequent effects on the safety of drinking water resources, has been a major concern in recent decades. In particular, there have been increasing concerns over the contamination of drinking water supplies with trace levels of organic (solvents) and inorganic (metallic compounds) contaminants, as well as bioactive materials like pharmaceuticals and agricultural products. Beyond the impact of population growth, the contamination of water has been rising as a result of industrial development and agricultural activities. For example, pesticides from agricultural field run-offs and other groundwater contaminants are now frequently found in water resources. Also, pharmaceuticals and personal care products (PPCPs) have been identified in outflows from sewage treatment plants and surface waters worldwide (Boyd *et al.*, 2003).

Conventional treatment technologies, such as filtration, chlorination, ozonation and boiling have been applied for many years to remove or inactive pathogens and reduce the levels of contaminants in drinking water. However, it is known that the advantages of these processes are limited to certain levels and forms of microbial/chemical contaminants. In addition, these methods require a lot of chemicals, fuels and electricity (Belapurkar *et al.*, 2006). Further, some of these traditional methods (e.g., chlorination) may be responsible for more drinking water issues, such as generation of disinfection by-products (DBP's) like trihalomethanes (THMs). Additionally, some of the pathogenic viruses and bacteria (*Campylobacter, Yersina, Mycobacteria or Legionella*) and protozoa (*Cryptosporidium* or *Giardia lamblia cysts*) are known to be resistant to chlorine disinfection (Kabir, 2006). Therefore, alternative treatment methods to overcome these and other limitations have been increasingly studied in recent years.

Besides the abovementioned issues, recent environmental regulations have led to the development of novel and more effective treatment technologies that are capable of removing the pollutants rather than transferring them from one phase to another (such as the case for activated carbon adsorption). One such technology that has received significant attention over the past two decades is photochemical oxidation, which is also related to advance oxidation processes (AOPs). These methods are based on the irradiation of the contaminated water with ultraviolet light (UV) under different conditions, such as H_2O_2/UV, Fenton's reagent, O_3/UV, O_3/H_2O_2/UV and photocatalysis (Parson, 2004; Kabir, 2006; Catalkaya and Kargi, 2008).

Photocatalysis is a process where a semiconductor catalyst is activated by UV irradiation promoting electrons from the valence band (VB) to the conduction band (CB) and leaving holes in the VB. These electron-hole pairs migrate to the surface of the photocatalyst where they initiate redox reactions with absorbed molecules. Thus, organic pollutants are degraded to smaller non-toxic species, such as carbon dioxide (CO_2) and water (H_2O) (Turchi and Ollis, 1990; Herrmann, 1999).

Photocatalytic oxidation has gained high levels of attention worldwide, not only because of the attractive multi-science aspects of the field, but also the associated challenging parameters when it comes to the practical large scale applications such as the improvement of the photon utilization, reduction of the overall cost of the process, among others. Nonetheless, there are many advantages associated with these processes (Mills *et al.*, 1993; Kabir, 2006):

1. almost all organic pollutants can be mineralized.
2. the process is generally considered as a green technology because many of the degradation products are environmentally harmless.
3. the most commonly used photocatalysts are cheap, non-toxic, stable, biologically and chemically inert, and insoluble under most conditions and reusable.
4. in most cases a low energy UV source is needed for catalyst activation.

The selection and synthesis of proper semiconductor material are key to having an efficient photocatalytic process. Among many different semiconductor photocatalysts, there is a general consensus that Titanium Dioxide (TiO_2) is more superior because it is cheap, easy to produce, has high chemical stability, and its photogenerated holes are highly oxidizing. The redox potential for titania's photogenerated holes is +2.53V versus the standard hydrogen electrode in pH 7 solution and the redox potential for its conduction band electrons is -0.52V, which is negative enough to reduce dyoxygen to superoxygen or to hydrogen peroxide (Fujishima *et al.*, 2000; Hashimoto *et al.*, 2005; Fujishima and Zhang, 2006; Thiruvenkatachari *et al.*, 2008). TiO_2 exists in three main crystallographic forms of anatase, rutile and brookite. The anatase type has been selectively used for photocatalytic applications because it offers many advantages over the other two forms, e.g., higher surface area and surface density of active sites (Herrmann, 1999; Ambrus *et al.*, 2008; Wetchakun and Phanichphant, 2008).

Sol-gel (solution – gelation) process is one of the methods that has been increasingly used to produce many heterogeneous photocatalysts, including nanosize TiO_2 particles with high photocatalytic activities (Campanati *et al.*, 2003; Su *et al.*, 2004). This technique involves the formation of homogeneous solution of raw materials and the subsequent gelation of the solution to form a porous oxide. Therefore, it can be defined as a sequence of chemical synthesis methods, mainly inorganic polymeralization reactions that need to be carefully controlled (Wen and Wilkes, 1996). In general, the process starts when a metal or semimetal alkoxide precursor, $M(OR)_n$, where M represents a network-forming element such as Si, Al, Ti, etc. and R is typically an alkyl group (C_xH_{2x+1}), is dissolved in alcohol to give a homogenous solution. Then, after the addition of water, hydrolysis and condensation occur simultaneously producing a gel (Hench and West, 1990; Wen and Wilkes, 1996). The process is followed by aging and then drying which are necessary to extract the solvents and reaction liquids trapped inside the gel. Finally, heat treatment and sintering are required to densify the gel. Among the many advantages of the sol-gel process, the low temperature requirement is one of the most important

ones. This allows solids with large specific surface areas and high porosity in the meso and macropore ranges (Livage, 1998).

The produced photocatalyst can be applied for the treatment of contaminated water in different photocatalytic reactors, e.g., slurry reactors, supported catalytic reactors, among others. In slurry reactors, the catalyst is dispersed in an aqueous medium as suspension, with a problem associated with the penetration of the UV irradiation due to the strong absorption by photocatalyst and organic pollutants. In addition, the separation and recycling of the photocatalyst from treated liquid are required. Supported photocatalytic reactors are the ones that have the catalysts immobilized on an inert support. In these reactors, the overall rate of degradation could be affected due to mass transfer limitation and low surface area as well as catalyst attrition (Werther and Reppenhagen, 1999; Kabir, 2006).

Fluidized bed photocatalytic reactors (FBPR) are among the promising alternatives mainly because they present many advantages such as efficient contact between the catalyst and the pollutants, low mass transfer resistance, and high TiO_2 surface exposure to UV radiation (Pozzo *et al.*, 1999, 2000; Bouchy and Zahraa, 2003). However, attrition of particles and elutriation in FBPR are a problem and could induce a decay in the catalyst activity and an increase in the cost of the overall process due to downstream filtration (Werther and Reppenhagen, 1999; Nelson *et al.*, 2007).

1.2 General objective and scope of the present work

Commercial TiO_2 powder (Degussa P-25) is often selected as a reference photocatalyst. It shows high photocatalytic activity mainly because it has a comparatively high surface area and substantial amount of anatase. Nonetheless, complications such as the need for filtration and further separation of the suspended particles after the treatment make the large scale application of P-25 TiO_2 photocatalyst difficult and economically unfeasible.

The main objective of the present study was to develop and standardize a novel composite photocatalyst to be used in a FBPR. The approach focused on a

novel processing method to produce TiO_2 nanoparticles, using sol-gel process, and mixing them with TiO_2 pre-calcined powder (Degussa P-25). TiO_2 powder was used as filler bonded together with the gel-derived TiO_2. The resulting Composite Sol-Gel (CSG) titania was then mixed with a polymeric structure to produce the spheres. The evaluation-standardization aspects of the work included better production process conditions, such as reactant quantities, temperature conditions, among others.

The photo-efficiency of the composite photocatalyst was evaluated in terms of its ability to decompose formic acid (FA) from a water solution. FA was selected as a model pollutant because it is oxidised directly to CO_2 without the formation of any stable intermediate products, and has been used extensively in other photocatalytic studies (McMurray *et al.*, 2004). In addition, 2,4-D (2,4 Dichlorophenoxyacetic acid), a well known micro-pollutant, was selected to test the catalyst with a more complex molecule. Finally, preliminary tests with natural organic matter (NOM) were also conducted.

1.3 Structure of this thesis

The present thesis is organized into seven chapters. In *Chapter Two*, an extensive review of literature on relevant issues is presented. *Chapter Three* describes the scope and the objectives of this investigation. *Chapter Four* presents in detail the experimental methodology that has been followed to reach the goals of this project. *Chapter Five* explains the preliminary experimental results obtained with the CSG TiO_2 spheres before any modification was made. Photocatalyst activity, attrition resistance determination, and photocatalyst characterization are some of the aspects included in this chapter.

Chapter Six discusses in detail the catalyst preparation and modification and how those changes in the catalyst synthesis affected the attrition resistance and the photoactivity of the catalyst. *Chapter Seven,* presents data on Formic Acid (FA) degradation (under different conditions) and a study of the 2,4-D degradation using this CSG catalyst in a fluidized bed photoreactor. In addition, preliminary results of the NOM degradation are also included along with an analysis of the fluence rate within the photoreactor.

Finally, *Chapter Eight* highlights the main conclusions obtained after this investigation and present some recommendations for future work.

Chapter Two

Literature Review

2.1 Background

Water is a natural resource that has direct impact on human health. It is considered vital to humanity regardless of time (Kamble *et al.*, 2006). According to the World Health Organization (WHO), 70% of the Earth's surface is water, but only 2.5% to 3% is considered fresh water. Also, less than 1% is accessible as surface water located in biomass, rivers, lakes, soil moisture and as water vapour distributed in the atmosphere (Kabir, 2006; Kamble *et al.*, 2006; WHO, 2006).

One of the major environmental problems nowadays is water pollution. Many locations with high quality water supplies have been developed intensively, producing a significant industrialization and extensive urbanization resulting in a progressive deterioration of water quality (Matthews, 1992). Particularly, the industrialized world has many industries that require large amounts of water for processing. In fact, it is predicted that water demand by industry, including energy and agriculture sectors, will grow rapidly to keep up with growing population. Nonetheless, the real problem is that the water discharged from these industries is contaminated with toxic organic compounds (Balapurkar *et al.*, 2006; Kamble *et al.*, 2006). In addition, the use of pesticides and herbicides in the agriculture sector causes scarcity of clean drinking water due to the toxicity of these compounds (Krysa *et al.*, 1999; Kabir, 2006).

A balance between continuous improvement and sustainability should be reached in order to minimize water pollution and preserve this vital resource. In addition, developments and improvements of wastewater treatment technologies should be achieved (Kabir, 2006). Conventional treatment technologies, such as filtration and chlorination, have been applied for many years to remove or inactive pathogens and reduce the levels of contaminants in drinking water. However, alternative treatment methods have been increasingly studied in recent years to

overcome some of the drawbacks of these technologies (e.g., generation of disinfection by-products). One group of such technologies are referred to as advance oxidation processes (AOPs), which are based on the irradiation of the contaminated water with ultraviolet light (UV).

AOPs have gained high level of attention in recent years because they offer an interesting approach to remove contaminants from water. In particular, heterogeneous photocatalysis has been the subject of intensive studies by researchers around the world, because of the appeal of the technology in which low energy UV is coupled with a semiconductor inducing mineralization of pollutants into harmless compounds without producing any other waste streams (Ray, 1998). In addition, photocatalysis does not require the use of strong oxidizing chemicals of potentially hazardous nature, e.g., H_2O_2, O_3 (Mills *et al.*, 1993)

2.2 Photocatalysis and environmental remediation

The first mention of photocatalysis was by Plotnikov in the 1930's in his book entitled *Allgemeine Photochemie* (Tremblay, 2001). The word "photocatalysis" is composed of two parts; the prefix "photo" meaning light and the suffix "catalysis" referring to the process in which a substance participates in modifying the rate of transformation of reactants without being altered in the end (Kabir, 2006).

From a thermodynamic point of view, the term "photocatalysis" can be fully applied only to reactions occurring with a reduction in the free energy ($\Delta G < 0$) where the rate of these reactions is increased thanks to a particular reaction pathway involving photocreated species. This pathway then leads to different reaction product selectivity than those for the thermal reactions. In the case of thermodynamic unfavourable reactions ($\Delta G > 0$), the energy of UV irradiation is converted into chemical energy and thus, the term "photosynthesis" is applied (Teichner, 2008). These kinds of reactions can be qualified as photocatalytic only when one catalyst (homogenous or heterogeneous) is clearly highlighted and the energy of irradiation compensates for the potential barrier, which is usually called the activation energy (Ollis *et al.*, 1991).

There has been an increased interest among the scientific community to the development and improvement in photocatalytic processes, especially heterogenous photocatalysis. Much of the interest in photocatalysis is due to the many advantages it has over traditional water and air treatment technologies, particularly the fact that organic pollutants can be degraded to carbon dioxide, water and mineral acids (Ollis *et al.*, 1991). Additionally, other advantages of this technology are: mild reaction conditions and modest reaction times, less chemical input requirement, minimal secondary waste generation, and the capacity for using renewable solar energy (Kabra *et a*l., 2004)

In the last three decades, photocatalysis has been studied more and more for environmental remediation. For example, some of the major applications of photocatalysis recently reported include the removal of colour and the destruction of dye; reduction of COD (chemical oxygen demand); mineralization of hazardous organics; destruction of hazardous inorganic compounds; treatment of heavy metals; degradation of harmful fungicides, herbicides and pesticides; decontamination of soil; destruction of cancer cells and viruses; purification and disinfection of water; among other (Bhatkhande *et al.*, 2001; Kabra *et al.*, 2004; Syoufian *et al.*, 2007; Gaya and Abdullah, 2008; Higgins *et al.*, 2009).

2.3 Heterogeneous photocatalysis

Heterogeneous photocatalysis was first introduced and developed in 1970 to describe the partial oxidation of alkanes and olefinic hydrocarbons at ambient temperature and under UV irradiation (Teichner, 2008). The "heterogeneous" adjective specifies the nature of the reaction medium which is not homogeneous but comprises at least two phases: the solid (catalyst) and the fluid reagent that could be in gas phase, pure organic liquid phases or aqueous solutions (Herrmann, 1999; Teichner, 2008). This is a process in which illumination of an oxide semiconductor (heterogeneous catalyst), usually Titanium Dioxide (TiO_2), produces photoexcited electrons (e^-) and holes (h^+). Then, these electrons and holes can migrate to the oxide surface and participate in half-cell reactions that are part of a closed catalytic cycle (Ollis *et al.*, 1991).

A heterogeneous catalyst is frequently defined as a solid or mixture of solids which accelerate chemical reactions without themselves undergoing changes. However, this definition is limited in scope considering that the properties of catalysts can change significantly with service lives and with certain applications (Campanati *et al.*, 2003). As a composite material, a heterogeneous photocatalyst can be characterized by: i) the relative amount of different components (active species, physical and/or chemical promoters and supports); ii) shape; iii) size; iv) pore volume and distribution; and v) surface area (Campanati *et al.*, 2003). All those characteristics would define operational characteristics of the catalyst, such as photocatalytic activity and mechanical strength of the catalyst.

2.3.1 Electronic excitation process in semiconductor materials

The initiation of the electronic excitation process is defined upon irradiation of a semiconductor. By definition, a semiconductor has a band structure which is usually characterized by a series of energetically closed spaced energy levels (valence band) and spatially diffused levels at higher energy (conduction band). The magnitude of the energy gap between the electronically populated valence band and the vacant conduction band, which is called the Band Gap, governs the extent of thermal population of the conduction band and its intrinsic state (Fox and Dulay, 1993; Linsebigler *et al.*, 1995). This band gap also defines the wavelength sensitivity of the semiconductor to irradiation.

In general, photocatalytic process is described by Equation 2.1, when the semiconductor is irradiated with ultraviolet (UV):

$$hv + semiconductor \rightarrow h^+ + e^- \qquad (2.1)$$

When a semiconductor catalyst of the chalcogenide type (oxides –TiO_2, ZnO, ZrO_2, CeO_2, etc. - or sulfides - CdS, ZnS, etc.) is illuminated by light with a photon energy (hv) equal to or larger than the band gap energy, it excites the electrons in the valence band to the conduction band, resulting in the formation of a positive hole (h^+) in the valence band and an electron (e^-) in the conduction band. These will have

sufficient life-time, in the nanosecond regimen, to undergo charge transfer to adsorbed species on the semiconductor surface (Linsebigler *et al.*, 1995; Herrmann, 1999; Bhatkhande *et al.*, 2001; Kabra *et al.*, 2004; Thiruvenkatachari *et al.*, 2008). Alternatively, these photogenerated electrons and holes can recombine with the subsequent release of phonons (a phonon is a quantum mechanical version of a special type of vibrational motion), inducing one of the major drawbacks of this process because it reduces the efficiency of the photocatalytic process (Krishna *et al.*, 2006). The band gap energies of some semiconductors are given in Table 2.1.

Table 2.1: Band gap energies for some semiconductor materials at 0K (Bhatkhande *et al.*, 2001; Thiruvenkatachari *et al.*, 2008).

Semiconductor	Band gap energy (eV)	Semiconductor	Band gap energy (eV)
Diamond	5.4	Fe_2O_3	2.3
CdS	2.42	PbS	0.286
ZnS	3.6	ZrO_2	3.87
ZnO	3.436	Cu_2O	2.172
TiO_2	3.03	CdSe	1.7
CdS	2.582	PbSe	0.165
SnO_2	3.54	Si	1.17
WO_3	2.76	Ge	0.744

During heterogeneous photocatalysis in water treatment, the electronic excitation of a polycrystalline semiconductor, caused by light absorption, drastically alters its ability to lose or gain electrons, promoting decomposition of pollutants to harmless products (Ray, 1998; Lehr *et al.*, 2005). Therefore, the photoreaction acceleration, by the action of the solid catalyst, will depend on the reaction mechanism, that itself depends on the interaction between the species to be degraded and/or the intermediates (Lehr *et al.*, 2005).

The classical heterogeneous photocatalytic process can be divided to seven independent steps, as is detailed below (Herrmann, 1999):

1. Transfer of the reactants from the fluid phase to the catalyst surface (external diffusion)

2. Mass transfer of reactants from the catalyst surface into its pore structure (internal diffusion)
3. Adsorption of at least one of the reactants
4. Reaction on the surface
5. Desorption of the product(s)
6. Mass transfer of the products out of the pore structures of the catalyst
7. Removal of the products from the interface region

The photocatalytic reaction occurs mainly on the adsorbed surface (step 4) and the only difference with conventional catalysis is the mode of activation of the catalyst. That is, the thermal activation is replaced by photonic activation. This activation is not concerned with steps 1, 2, 3, 5, 6 and 7, although photoadsorption and photodesorption of reactants (mainly oxygen) do exist (Herrmann, 1999).

The sequence of chain reactions that can take place during the adsorption step have been described (Gaya and Abdullah, 2008):

- Photoexitation: $hv + semiconductor \rightarrow h^+ + e^-$ (2.1)
- Oxygen ionosorption: $(O_2)_{ads} + e^- \rightarrow O_2^{\bullet -}$ (2.2)
- Ionization of water: $H_2O \rightarrow OH^- + H^+$ (2.3)
- Protonation of superoxides: $O_2^{\bullet -} + H^+ \rightarrow HOO^{\bullet}$ (2.4)

The hydroperoxyl radical formed in Equation 2.4 also has scavenging properties that help prolong the lifetime of photon hole (preventing the recombination between h^+ and e^-) because it can react with electrons to produce HO_2^- and subsequently H_2O_2:

$$HOO^{\bullet} + e^- \rightarrow HO_2^- \quad (2.5)$$

$$HOO^- + H^+ \rightarrow H_2O_2 \quad (2.6)$$

Considering that hydroxyl radical (•OH) is the primary oxidant in a photocatalytic system, Turchi and Ollis (1989) proposed a route where four possible mechanisms take place. This sequence is listed in Table 2.2, where P_1 represents an organic molecule and $P_{1,ads}$ represents the absorbed organic molecule. As was already pointed out, the initiating step in photocatalysis is the excitation of the semiconductor by irradiation to produce electron-hole pairs (Equations 2.1 and 2.7). The typically low quantum yield of photocatalytic reactions is due to high rate of recombination between the electron-hole pairs (Equation 2.11). Recombination can be avoided if these species are separated and "trapped" by surface absorbents. For instance, the photogenerated electrons can be trapped by oxygen to form superoxides ($O_2^{\cdot-}$) and hydroperoxyl radical ($HO_2\cdot$) and subsequently H_2O_2, as shown in Equations 2.2 and 2.5, respectively (Okamoto *et al.*, 1985; Gaya and Abdullah, 2008). Besides, one of the principal hole traps is the adsorbed hydroxide ions or water molecules (Equations 2.8) that proceed to form hydroxyl radicals as shown in Equation 2.12 (Turchi and Ollis, 1989). Another possibility to avoid the recombination between e^- and h^+ is to mix noble metals such as silver, gold, platinum, with the semiconductor photocatalyst (Chao *et al.*, 2003; Falaras, *et al.*, 2003; Aprile *et al.*, 2008).

The direct hole-organic reaction (Equation 2.14), while thermodynamically possible, is not believed to be significant because of the lack of reactivity shown in water-free organic solutions. For example, it has been demonstrated that aromatic molecules preferably adsorb to surface hydroxyls rather than directly to the TiO_2 lattice. For this case, the oxidative attack of these molecules would be analogous to Equation 2.19 (Turchi and Ollis, 1989).

Photo-excited electrons are trapped by Ti^{IV} centres to form Ti^{III} as is shown in Equation 2.15. In systems without a reducible adsorbate, conduction band electrons remain on the semiconductor resulting in the formation of a blue colour, which is characteristic of Ti^{III}. When oxygen is in the system, the surface Ti^{III} is readily oxidized by molecular oxygen to form the superoxide ion radical (Equation 2.16). These ions may be further reduced to H_2O_2 (Equation 2.21). Under acidic conditions, H^+ may protonate the superoxide to form perhydroxyl radical (Equation 2.22).

Equations 2.17 to 2.20 represent four different possible pathways for •OH attack on organics, depending on the photocatalyst surface or the fluid phase (Turchi and Ollis, 1990; Mattews, 1992; Hoffman, *et al.*, 1995).

Table 2.2: Photocatalytic reaction scheme for the TiO_2 (Turchi and Ollis, 1989; Turchi and Ollis, 1990; Kabir, 2006).

Sequence	Reaction	
Excitation of the catalyst by photon energy greater than the band gap	$TiO_2 \xrightarrow{h\nu} e^- + h^+$	(2.7)
Adsorption on the catalyst surface and lattice oxygen (O_L^{-2})	$O_L^{-2} + Ti^{IV} + H_2O \leftrightarrow O_L H^- + Ti^{IV} \cdots OH^-$	(2.8)
	$Ti^{IV} + H_2O \leftrightarrow Ti^{IV} \cdots H_2O$	(2.9)
	$site + P_1 \leftrightarrow P_{1,ads}$	(2.10)
Recombination of the e^- - h^+ pair, releasing heat	$e^- + h^+ \rightarrow heat$	(2.11)
Trapping of the hole and the electron	$Ti^{IV} \cdots OH^- + h^+ \leftrightarrow Ti^{IV} \cdots OH^\bullet$	(2.12)
	$Ti^{IV} \cdots H_2O + h^+ \leftrightarrow Ti^{IV} \cdots OH^\bullet + H^+$	(2.13)
	$P_{1,ads} + h^+ \leftrightarrow P_{1,ads}^{\bullet+}$	(2.14)
	$Ti^{IV} + e^- \leftrightarrow Ti^{III}$	(2.15)
	$Ti^{III} + O_2 \leftrightarrow Ti^{IV} \cdots O_2^{\bullet-}$	(2.16)
Attack by hydroxyl radical (adsorbed or free) under	Case I: $Ti^{IV} \cdots OH^\bullet + P_{1,ads} \leftrightarrow Ti^{IV} + P_{2,ads}$	(2.17)
	Case II: $OH^\bullet + P_{1,ads} \leftrightarrow P_{2,ads}$	(2.18)
	Case III: $Ti^{IV} \cdots OH^\bullet + P_1 \leftrightarrow Ti^{IV} + P_2$	(2.19)
	Case IV: $OH^\bullet + P_1 \leftrightarrow P_2$	(2.20)
Reaction of other radicals	$e^- + Ti^{IV} \cdots O_2^{\bullet-} + 2H^+ \leftrightarrow Ti^{IV}(H_2O_2)$	(2.21)
	$Ti^{IV} \cdots O_2^{\bullet-} + H^+ \leftrightarrow Ti^{IV}(HO_2^\bullet)$	(2.22)
	$H_2O_2 + OH^\bullet \leftrightarrow HO_2^{\bullet-} + H_2O$	(2.23)

Both oxidation and reduction can take place at the surface of the photoexcited semiconductor photocatalyst, as is shown in Figure 2.1. The generation

of electron-hole pairs takes place in the semiconductor particle due to the excitation of an electron from the valence band to the conduction band initiated by light absorption. Upon excitation, the fate of separated electron and hole can follow several pathways; while at the surface, the semiconductor can donate electrons to reduce an electron acceptor (usually oxygen) (pathway b). Also, a hole can migrate to the surface where an electron from a donor species can combine with the surface hole oxidizing the donor species (pathway a). In competition with the charge transfer to adsorbed species is the electron and hole recombination; a separate electron-hole recombination can occur in the volume of the semiconductor particle (pathway c) or at the surface (pathway d) with the release of heat (Linsebigler *et al.*, 1995).

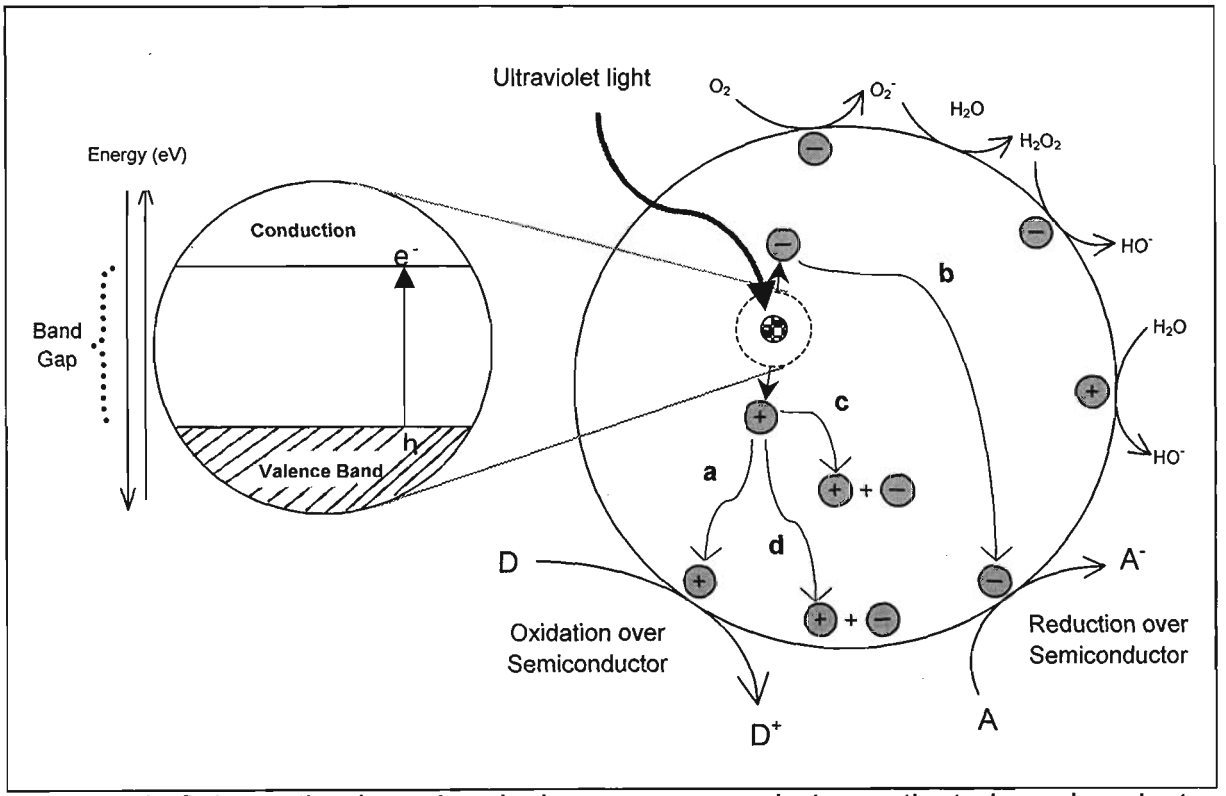

Figure 2.1: Schematic photochemical process over photon activated semiconductor showing the photogeneration of electron/hole pair: (a) oxidation of donor on the surface of the semiconductor particle; (b) diffusion of acceptor and reduction on the surface of the semiconductor; (c) recombination in the bulk, and (d) surface recombination.

As depicted in Figure 2.1, if an electron donor, D, adsorbs on the surface of the semiconductor particles, it can react with the photogenerated holes to generate an oxidized product, D^+. Similarly, an electron acceptor present at the surface, A, can react with the photogenerated conduction band electrons to generate product A^-. In the application of semiconductor photocatalysis to the purification of water, the electron acceptor, A, is invariably dissolved oxygen, and the electron donor, D, is the pollutant (Parsons, 2004).

The activity of the photocatalyst to degrade pollutants can be defined as the relative or absolute rate of photocatalytic reaction (Kaneko and Okura, 2002). Based on the mechanism involved in a photocatalytic process, the photocatalytic activity of semiconductor materials must be controlled by the following parameters: i) light absorption properties, which are mostly governed by the bulk structure of the semiconductor and difficult to modify; ii) rate of reduction and oxidation of the substrate by e^- and h^+, respectively, which is dependent on the catalyst surface; and iii) rate of e^- and h^+ recombination (Kabir, 2006). During the illumination of the photocatalyst, only a portion of the photocatalyst particles can absorb incident photons and the remainder of the photocatalyst does not take part in the reaction. The total number of the absorbed photons should be constant if a sufficient amount of catalyst absorbs all the incident photons. Large catalyst surface area leads to faster reaction of e^- - h^+ with substrate because more substrate molecules are available to participate in the reaction (Ohtani *et al.*, 1987; Su *et al.*, 2004; Kabir, 2006). However, literature reports suggested that e^- and h^+ recombination is dependent on the crystallinity of the catalyst, which increases with the crystal defects in the semiconductor surface. The crystal defects are higher with larger surface area; hence, the appropriate surface area should be determined based on its influence on the catalyst activity (Kabir, 2006).

2.3.2 Titanium Dioxide (TiO_2) as a photocatalyst

Photocatalytic activity of titanium dioxide (TiO_2) was first reported by Fujishima and Honda (1972) for light induced water splitting on TiO_2 surface. A

complete electrochemical circuit with a rutile form of TiO_2 and platinum black, as the two electrodes, allowed water to be decomposed using UV-visible light, into oxygen and hydrogen, without the application of an external voltage (Macak *et al.*, 2007; Fujishima and Zhang, 2006). This result, which is referred to as the "Honda-Fujishima effect", has opened novel approaches in heterogeneous catalysis and TiO_2 applications (Gaya and Abdullah, 2008). The worldwide interest in photocatalysis has increased significantly ever since and much research has been done in this area.

Titanium dioxide exists in three main crystallographic forms: rutile, anatase and brookite. The anatase type has been selectively used for photocatalytic applications because it is the most active form of TiO_2 (Wetchakun and Phanichphant, 2008). The octahedron (TiO_6) is the fundamental structure units in the TiO_2 crystals. In the rutile structure, each octahedron is in contact with ten neighbour octahedrons (two sharing edge oxygen pairs and eight sharing corner oxygen atoms), while in the anatase structure each octahedron is in contact with eight neighbours (four sharing an edge and four sharing a corner). As can be seen in Figure 2.2, each Ti^{4+} ion is surrounded by an octahedron of six O^{2-} ions. This octahedron in rutile is not regular, showing a slight orthorhombic distortion. On the other hand, the octahedron in anatase is significantly distorted so that its symmetry is lower than orthorhombic. The *Ti - Ti* distances in anatase are greater than those in rutile (3.79 and 3.04Å versus 3.57 and 2.96 Å) whereas the *Ti - O* distances are shorter than those in rutile (1.934 and 1.980 Å in anatase versus 1.949 and 1.980 Å in rutile). These differences in lattice structures cause different mass densities and electronic band structures between anatase and rutile, possible reason why the former is more active than the latter (Linsebigler *et al.*, 1995; Gao *et al.*, 2006; Bojinova *et al.*, 2007).

In general, TiO_2 is a material of great importance due to its useful electrochemical, dielectric, electroconductive and optical properties. It is widely used in cosmetics, pigments, photocatalysis, adsorbents and catalytic supports (Gao *et al.*, 2006). As a photocatalyst, TiO_2 is well known because of several reasons: low cost, easy to produce, high chemical stability, and highly oxidizing photogenerated

holes. The redox potential for photogenerated holes is +2.53V versus the standard hydrogen electrode in pH 7 solution and the redox potential for conduction band electrons is -0.52V, which is negative enough to reduce dyoxygen to superoxygen or to hydrogen peroxide (Fujishima and Zhang, 2006). Besides, TiO_2 has biological and environmental safety advantages that give it particular characteristics (Fujishima *et al.*, 2000; Hashimoto *et al.*, 2005; Fujishima and Zhang, 2006).

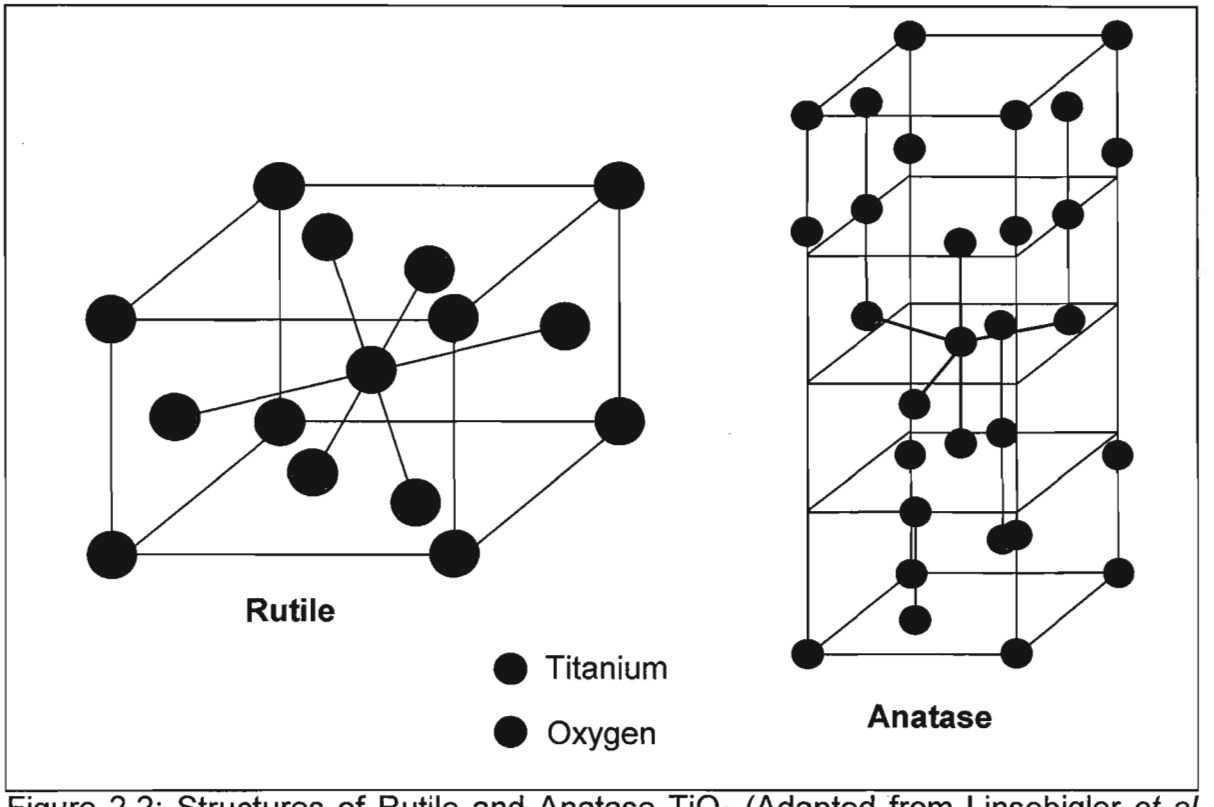

Figure 2.2: Structures of Rutile and Anatase TiO_2 (Adapted from Linsebigler *et al.*, 1995).

The mineralization process by the TiO_2 photocatalytic oxidation of organic compounds is shown in Equation 2.24 where *P* represents the organic compounds (pollutant) and *MA* the mineral acids produced in the process:

$$P + O_2 + hv \xrightarrow{TiO_2} CO_2 + H_2O + MA \qquad (2.24)$$

Since 1977, when Frank and Bard examined the possibilities of using TiO_2 to decompose cyanide in water, there has been increasing interest in environmental applications of photocatalysis (Frank and Bard, 1977; Fujishima *et al.*, 2000). In the last few decades, suspensions of TiO_2 powder have been used for photocatalytic oxidation of organic and inorganic compounds in aqueous solutions to remove the impurities from water. Many organic compounds, such as aromatics, haloaromatics, aliphatics, dyes, dioxins, etc., have been demonstrated to be oxidized through this process to carbon dioxide (CO_2) and water, which are categorized as harmless compounds (Matthews, 1987; Kosanic, 1998; Kabra *et al.*, 2004; Mrowetz and Selli, 2006; Belapounkar *et al.*, 2006; Bojinova *et al.*, 2007; Osajima *et al.*, 2008).

2.4. Photocatalytic efficiency and kinetic overview

2.4.1 Photocatalytic efficiency

The efficiency of the photocatalytic process is measured by quantum yield, ϕ, which is defined as the number of events occurring in the system per photon absorbed (Herrmann, 1999; Rahn *et al.*, 2003). In heterogeneous catalysis, the quantum yield is difficult to measure since the semiconductor particles absorb, scatter and transmit radiation. It may vary on a wide range of conditions including: a) the nature of the catalyst; b) the experimental conditions such as temperature, concentrations, etc.; and c) the nature of the reaction itself. Nonetheless, the knowledge of this parameter is essential because it allows one to compare the activity of different catalysts for the same reaction, to estimate the relative feasibility of different reactions, and to calculate the energetic yield of the process and the associated cost (Hermann, 1999). Given that it is difficult to measure the absorbed light in heterogeneous photocatalysis, it is assumed that all the light is absorbed and the efficiency is quoted as an apparent quantum yield (Linsebigler *et al.*, 1995). Hence, to determine the efficiency of the process, a combination of all the pathway probabilities for the electron and hole must be considered.

Ideally, ϕ is proportional to the rate of the charge transfer process (k_{CT}) and inversely proportional to the sum of the charge transfer rate (k_{CT}) and the electron-hole recombination rate (k_R) (bulk and surface). Mathematically, this relation is given by (Linsebigler *et al.*, 1995):

$$\phi \propto \frac{k_{CT}}{k_{CT} + k_R} \tag{2.25}$$

Equation 2.25, assumes that diffusion of the products into the solution occurs quickly without the reverse reaction of electrons recombining with donors and holes recombining with acceptors. Without recombination, the quantum yield would take on the ideal value of 1. However, in a real system recombination does occur and the concentration of electrons and holes at the surface is not equal (Linsebigler *et al.*, 1995).

One way to improve the yield in a photocatalytic process is to select a semiconducting material that should be capable of reversibly changing its valence state to accommodate a hole without decomposing the semiconductor. In addition, the semiconductor should also have suitable band-gap energies, stability toward photocorrosion, nontoxic nature, low cost, and physical characteristics that enable them to act as catalyst (Kabra *et al.*, 2004).

2.4.2 Kinetic of photocatalyzed reactions

In heterogeneous systems, the reaction kinetics relied for many years on the Langmuir-Hinshelwood (L-H) model to interpret experimental observations. Considering Equation 2.24, the observed variation in the initial degradation rate of the organic compound ($-r$) with organic concentration (P) can be described by Equation 2.26 (L-H kinetics) where k_{LH} is the apparent LH rate constant and K_L is the L adsorption constant.

$$-r = \frac{k_{LH} K_L P}{1 + K_L P} \tag{2.26}$$

This kinetic model, in its simplest form, assumes a relatively rapid reaction achieving adsorption equilibrium, followed by a single, slow surface reaction step (rate determining step) (Emeline *et al.*, 2005; Ollis, 2005). The following equations describe the mechanism where *P* represents the organic pollutant either in bulk solution (*liq*) or adsorbed on the catalyst surface (*ads*) (Mills *et al.*, 2006):

$$P_{liq} \xleftrightarrow{k_1 / k_{-1}} P_{ads} \tag{2.27}$$

$$P_{ads} \xrightarrow{k_2} Products \tag{2.28}$$

The L-H adsorption/kinetic model assumes the following statements: i) at equilibrium, the number of surface adsorption sites is fixed; ii) only one substrate may bind at each surface site; iii) the heat of adsorption by the substrate is identical for each site and is independent of surface coverage; iv) there is no interaction between adjacent adsorbed molecules; v) the rate of surface adsorption of the substrate is greater than the rate of any subsequent chemical reactions; and vi) no irreversible blocking of active sites by binding to product occurs (Fox and Dulay, 1993). Based on these assumptions, the reactant equilibrium coverage, θ, is related to the concentration of the pollutant *P*, and to the apparent adsorption equilibrium constant ($K_{ads} = \frac{k_1}{k_{-1}}$) by:

$$\theta_P = \frac{K_{ads} P}{1 + K_{ads} P} \tag{2.29}$$

Hence, the reaction rate could be:

$$-r = k_{LH} \theta_P = \frac{k_{LH} K_{ads} P}{1 + K_{ads} P} \tag{2.30}$$

where $k_{LH} = k_2$ is the reaction rate constant, which is expected to be dependent on the photon flux (I) incident over the catalyst surface (TiO_2 for example). However, during the last decade, some key experiments have brought evidence that this dependency is not consistent with the obtained results (Ollis, 2005). Some of the flaws of the L-H kinetic model discussed by Ollis (2005) are the followings: i) while adsorption isotherm and reaction rate may each follow the same analytic form, i.e., a saturation function of the Langmuir adsorption isotherm form, the dark adsorption equilibrium constant, K_{ads}, is not found to be the same as the apparent adsorption constant, K_{ads}^{app}, in the rate equation; ii) some reaction and adsorption systems have different analytic forms, iii) the L-H parameters k_{LH} and K_{ads}^{app} collected from different experiments using phenol and 4-chlorophenol have positive correlations, iv) a significant numbers of papers have explored the influence of the reactant concentration (in this case P) and light intensity, I, in the same photocatalyzed reaction, v) Emeline et al., (2000) found that the L-H rate parameters for phenol oxidation vary as follows: k_{LH} proportional to intensity and K_{ads}^{app} inversely with intensity. Therefore, a different approach was proposed to define a new simple model that can be described with the same Equations 2.26 and 2.27. Instead of assuming equilibrium adsorption of reactants and, correspondingly, a slow rate-controlling surface step, the revised model assumes a pseudo-steady-state hypothesis to the surface coverage ($d\theta/dt = 0$). Under these assumptions, the reaction rate expression is (Ollis, 2005):

$$-r = \frac{k_{LH} K_{ads}^{app} P}{1 + K_{ads}^{app} P} \tag{2.31}$$

where

$$K_{ads}^{app} = \frac{k_1}{k_{-1} + k_{LH}} \tag{2.32}$$

As it can be easily identified, Equation 2.31 has exactly the same mathematical form as the L-H model; however, it can explain the dependence of $K_{a,ads}$ on the incident light intensity (I). One important contribution is that k is related to I based on the following expression (Mills *et al.*, 2006):

$$k_{LH} = \alpha I^{\beta} \tag{2.33}$$

where α is a proportional constant and β has been traditionally reported with a value of 0.5 under high-photon-flux conditions when the surface reaction dominates. Nonetheless, Emeline *et al.* (2005) stated that the dependence of the reaction rate to the photon flux, depending on the concentration of the reactant molecules, varies from zero-order kinetics at low concentration to first order kinetics at high concentration. Therefore, at intermediate concentrations, the order of the reaction on photon flux is between 0 and 1, and then, the square root dependence is a particular case lying within this range.

Another important aspect in photocatalytic reactions is the availability of oxygen which plays an important role in the photooxidation process. Oxygen acts as an electron sink for photogenerated carriers, mainly electrons (Kabra *et al.*, 2004). Therefore, the dependence of the photocatalytic degradation rate on oxygen concentration can be also modeled by non-competitive Langmuir adsorption relation (Turchi *et al.*, 1989):

$$r \propto \frac{K_{O_2} C_{O_2}}{1 + K_{O_2} C_{O_2}} \tag{2.34}$$

where K_{O2} is the apparent constant for oxygen and C_{O2} is the dissolved oxygen concentration. Hence, a complete model of the photocatalytic system should consider not only Equation 2.31, but also the dependence on oxygen concentration given by Equation 2.34.

2.5 Overview of photocatalytic reactors

Photocatalytic reactors constitute an important part of every photocatalytic process. The reactor will not only affect the overall rate of photocatalytic degradation of the organic/inorganic compounds, but also define aspects such as irradiation distribution, mass transfer phenomena, among others (Bouchy and Zahraa, 2003). While some of the physic-chemical principles of photocatalysis (e.g. production process, photoactivity, etc.) are relatively well understood, reactor design and reactor engineering of photocatalytic units still require a lot of considerations (Fox and Dulay, 1993; Linsebigler *et al.*, 1995). In particular, this lack of knowledge is true for scaled reactors processing large volumes of water and using high levels of irradiation (De Lasa *et al.*, 2005).

There are several important factors affecting the efficiency of photocatalytic reactors with heterogeneous photocatalyst. These include mode of operation, flow characteristics, reactor geometry, selection of irradiation source, contact between the catalyst and the reactants, the durability of the photocatalyst, etc. (Vaisman *et al.*, 2005; Kabir, 2006). There is a general agreement that controlling and improving all these factors will help establish intermediate and large scale reactors, as demanded by industrial and commercial applications (De Lasa *et al.*, 2005).

Photocatalytic reactors can be classified in terms of the type of illumination (artificial or natural) and in terms of the amount of the irradiation applied (number and kind of lamps to be used). However, a classification based on the state of the photocatalyst is more frequently used. In general, two main groups of reactors can be defined: when the solid phase (the catalyst) is stationary within the reactor (immobilized photocatalyst), and when the catalyst is dispersed within the reactor (suspension or slurry reactors). In the latter case, fine powdered photocatalyst (e.g., TiO_2) is freely dispersed in water providing high efficiency due to the large surface area available for reaction and efficient mass transfer within such systems (Bouchy and Zahraa, 2003). However, due to the small size of the TiO_2 particles (30-200 nm), it is difficult to separate them from water after used, making the post-treatment catalyst recovery stage necessary. This post-treatment catalyst recovery would be undesirable at larger scales as it would add to the overall cost of the treatment

process (De Lasa *et al.*, 2005). Thus, there is a practical necessity to immobilize the photocatalyst to overcome this issue. Immobilization, on the other hand, leads to mass transfer resistance which results in the reduction of reactor efficiency and in the accuracy of measured catalyst efficiency and kinetics (Kulas *et al.*, 1998; Lee and Lee, 2004; McMurray *et al.*, 2004). Table 2.3 summarizes the advantages and disadvantages of slurry and immobilized photocatalytic reactors.

Table 2.3: Comparison between suspended and immobilized photocatalytic systems (De Lasa *et al.*, 2005; Kabir, 2006).

Reactor	Advantages	Disadvantages
Slurry reactors	Uniform catalyst distribution	Requires filtration
	High surface area	Light scattering and adsorption in the suspended medium
	No mass transfer effects	Operational costs are high
	Well mixed particles suspension	
	Low pressure drop through the reactor	
	Initial cost is low	
Immobilized reactors	If the catalyst has good attrition resistance, there is no need of an additional separation operation	Low light utilization efficiencies due to light scattering
	Operation cost are generally cheaper	Mass transfer limitations
		Possible catalyst deactivation and catalyst wash out
		Initial cost is high due to the catalyst immobilization

One alternative to the above mentioned photocatalytic reactors is the fluidized bed reactor (FBPR). The catalyst, which is usually immobilized on a support material, is highly agitated while the fluid is passed up through a bed of catalyst. Some of the support materials frequently used in FBPR are ceramic particles (Kanki *et al.*, 2005), glass beads and silica gel particles (Bideau *et al.,* 1995; Zhang *et al.*, 2006; Choi *et al.*, 2007; Qiu and Zheng, 2007), zeolites (Haque *et al.*, 2005), activated carbon (Lee *et al.*, 2004; Dong *et al.*, 2008), etc. In general, it is reported that fluidized bed photoreactors provide an efficient contact between the catalyst and the pollutants, low mass transfer resistance, and better surface exposure to UV radiation (Satterfield, 1980; Haarstrick *et al.*, 1996; Pozzo *et al.*, 1999, 2000; Bouchy and Zahraa, 2003; Imoberdorf *et al.*, 2008). It is also possible to control and to improve the penetration of light into the fluidized bed by varying its expansion (Haarstrick *et al.*, 1996).

Among different configurations of FBPR, an annular photoreactor (two co-axial cylinders that define the reaction zone with the lamp usually placed on the axis) has been suggested as a very convenient one because the light is absorbed entirely by the reactive system in the annular region (Vaisman *et al.*, 2005). In addition, this configuration meets the requirements of higher surface area-to-volume ratio, which is typically much lower in fix-bed configurations.

Attrition of particles is a serious concern in fluidized bed reactors. The particle motion inside the reactor causes the catalyst attrition due to interparticle collisions and bed-to-wall impacts. It is one of the major obstacles in the development of large scale applications and/or for existing processes whenever the catalyst is changed (Werther and Reppenhagen, 1999). The main consequence of the attrition is the generation of fines or smaller particles due to the severe impacts which occurs in a fluidized bed and the elutriation of these fine particles from the bed results in high catalyst losses, with the subsequent activity decays. Also, potential downstream line blockage with the generated fines will happen and additional filtration stage would be necessary (Werther and Reppenhagen, 1999; Qiu and Zheng, 2007). Catalysts containing major quantities of TiO_2 have reported to have the disadvantage of poor

physical integrity and attrition resistance when used in fluidized bed photocatalytic reactors (Cullo *et al.*, 1986).

2.6 Sol-gel Process

2.6.1 Background and fundamentals

The interest in the sol-gel (solution – gelation) processing of different inorganic, ceramic and glasses materials, began as early as the mid-1800s with the study on silica gels by Ebelman (1846 and 1847) and Graham (1864) who reported that the hydrolysis of tetraethyl orthosilicate (TEOS) yielded SiO_2 under acidic conditions (Hench and West, 1989). Since early 1970's, this technology has gained much attention, especially in glass and ceramics fields, after a borosilicate glass lens was produced by heating a compact mass formed from sol-gel derivate oxide powders (Sakka, 2006).

The most important reason for the significant growth and popularity of the sol-gel technology may be attributed to its low temperature processing. In comparison to other methods that require much higher temperatures, the sol-gel process allows better homogeneity of multi-components materials. Also, the rheological properties of sols or gels allow the formation of fibres, films or composites materials (Livage *et al.*, 1988; Livage *et al.*, 1989; Wen and Wilkes, 1996; Campanati *et al.*, 2003).

The sol-gel process, which is based mainly on inorganic polymeralization reactions, is defined as a sequence of chemical synthesis method that involves the low temperature synthesis of an inorganic network (Bischoff and Anderson, 1995; Wen and Wilkes, 1996). A *sol* is defined as a colloidal (suspension in which the dispersed phase is so small that gravitational forces are negligible and interactions are dominated by short-range forces) of solid particles in a liquid. On the other hand, a *gel* is defined as a semirigid mass formed when the colloidal particles are linked to form a network or when the polymer molecules are cross-linked or interlinked. Therefore, in the sol – gel process, the precursors or starting compounds for the preparation of a colloid consist of a metal or metalloid element surrounded by

various ligands (Brinker and Scherer, 1990; Rahaman, 2007). During the sol-gel process, hydrolysis and polycondensation of the metal-organic compounds, such as metal alkoxide $M(OR)_n$ where M represents a network-forming element such as Si, Ti, Zr, Al, etc., and R is typically an alkyl group (C_xH_{2x+1}), occur to form oxopolymers, which are then transformed into an oxide network (Su *et al.*, 2004; Gao *et al.*, 2006). Metal alkoxides are the most common precursors used in sol-gel process because they react readily with water (Brinker and Scherer, 1990; Rahaman, 2007).

Sol-gel method is one of the most important techniques for preparing nanosized metallic oxide materials with high photocatalytic activities (Su *et al.*, 2004). During the photocatalyst production, the morphology, average particle size and particle size distribution, porosity, phase composition and crystallinity are important factors to be controlled (Gao *et al.*, 2006). Therefore, by tailoring the chemical structure of the primary precursor and carefully controlling the different process steps and variables during the sol-gel preparation, all those parameters can be controlled, giving a final product with good homogeneity, purity and desired microstructure (Su *et al.*, 2004; Gao *et al.*, 2006; Keshmiri *et al.*, 2006).

2.6.2 Sol-gel process steps

The sol-gel process has a number of stages that will define the properties of the final product. Figure 2.3 shows different stages of the process and the sequence in which they are carried out.

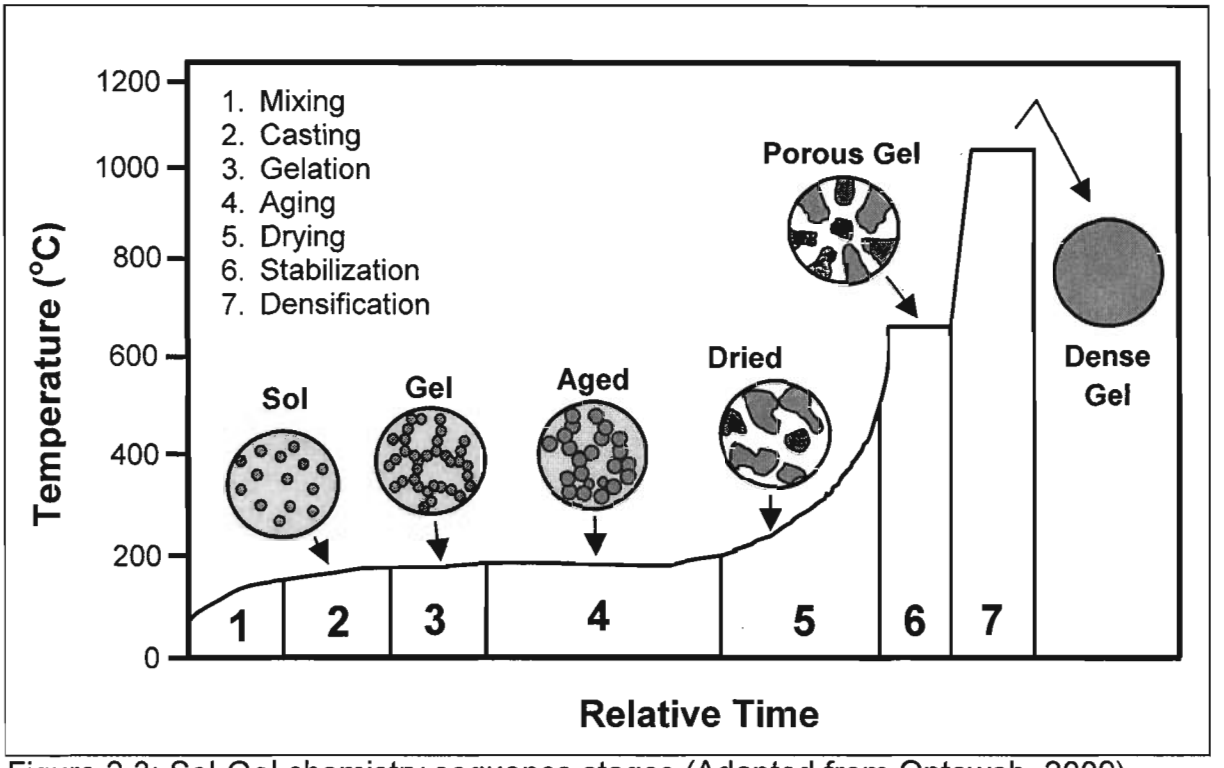

Figure 2.3: Sol-Gel chemistry sequence stages (Adapted from Optoweb, 2009).

The properties of the final product depend on how well controlled are the seven steps involved during the sol-gel process (Figure 2.3). The main characteristics of some of these steps are described below (Hench and West, 1989; Brinker and Scherer, 1990; Scherer, 1990; Richerson, 2006; Rahaman, 2007):

- *Mixing*: a suspension of colloidal powders is formed by mechanical mixing of colloidal particles in water at a pH that prevents precipitation. In general, the liquid alkoxide precursor is hydrolyzed by mixing with water. The hydrated product interacts in a condensation reaction producing an oxide network. The water and the alcohol expelled from the reaction remain in the pores of the network. The size of the sol particles and the cross-linking within the particles depend upon the pH and the ratio between water and the precursor added to form the sol, among other variables.

- *Gelation*: During the gelation, the colloidal particles and condensed species link together to become a three-dimensional network. As the *sol* particles grow and collide, condensation occurs and macroparticles are formed; the *sol* becomes a *gel* when it can support a stress elastically, which is typically defined as the gelation point or gelation time. This change is gradual as more and more particles become interconnected. The physical characteristics of the gel network depend greatly upon the size of particles and cross-linking before gelation. It is believed that the sharp increase in viscosity that accompanies gelation essentially freezes in a particular polymer structure at the gel point.

- *Aging*: During the aging process, the *gel* is maintained in contact with the liquid and its structure and properties continue to change long after the gel point. Four different processes can occur, separately or simultaneously, during aging. These include polycondensation, syneresis, coarsening, and phase transformation. Polycondensation reactions continue to occur along with localized solution and reprecipitation of the *gel* network, increasing the thickness of interparticle necks and decreasing the porosity. Syneresis is defined as the spontaneous shrinkage of the gel and the resulting expulsion of liquid from the pores is expected. Coarsening is the irreversible decrease in surface area through dissolution and reprecipitation processes. In general, it is expected that the strength of the *gel* increases with aging.

- *Drying*: During drying, the liquid is removed from the interconnected pore network. Large stresses can be developed during this process causing the *gels* to crack unless the drying process is controlled via decreasing the liquid surface energy, hypercritical evaporation, or obtaining monodisperse pore sizes by controlling the rates of hydrolysis and condensation. There are three main stages during the drying process. *Stage 1* is characterized by the decrease in volume of the gel and the gel network is deformed by the large capillary forces which cause shrinkage of the object. This stage ends when shrinkage ceases. *Stage 2* begins when the critical point is reached; this critical point occurs when

the strength of the network has increased, due to the greater packing density of the solid phase, sufficient to resist further shrinkage. *Stage 3* is reached when the pores have substantially emptied and the remaining liquid can be released only by evaporation from within the pores and diffusion to the surface.

- *Densification*: Heating the porous *gel* at high temperature induces its densification. This stage is also called sintering and it is essentially the removal of the pores between the starting particles, combined with the growth and strong bonding between adjacent particles.

Based on the process conditions, such as the starting solution, pH, and temperature, different products, in terms of *gel* physical characteristics, are formed. These products can be classified as particle networks, aggregate networks, and polymer networks. The polymer network results in a three dimensional gel structure which can be transformed to a monolithic specimen through the control of drying and heat treatments. When the aggregate clusters formed in the sol exhibit low and nonuniform density distribution, a precipitation of the solid phase occurs (aggregate network). High and nonuniform density distribution of particle aggregates result in a particle network which is considerably uniform and monosized (Ring, 1996). Figure 2.4 represents these three products.

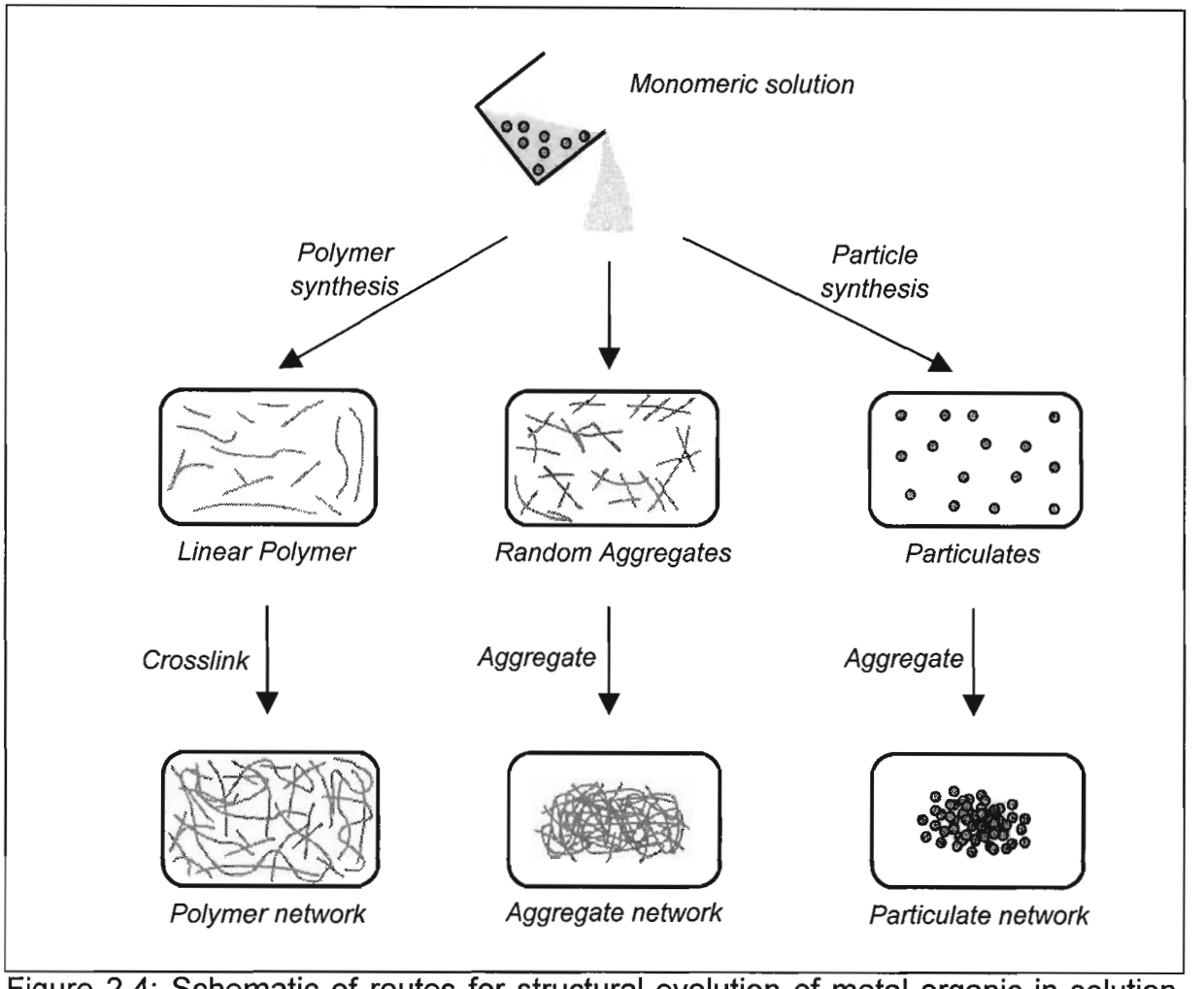

Figure 2.4: Schematic of routes for structural evolution of metal organic in solution (Adapted from Ring, 1996).

As was already pointed out, the concept of sol-gel processing covers a large variety of materials, specially glasses and ceramics. Nonetheless, modifying the sequence or even the conditions of one or more than one of the stages shown in Figure 2.3, leads to different products in different forms. Some of these are xerogel, which is just a dried gel (*xero* means dry), aerogel which is a gel where the liquid component has been replaced with a gas, uniform particles (powders), films and self-supported products (Figure 2.5).

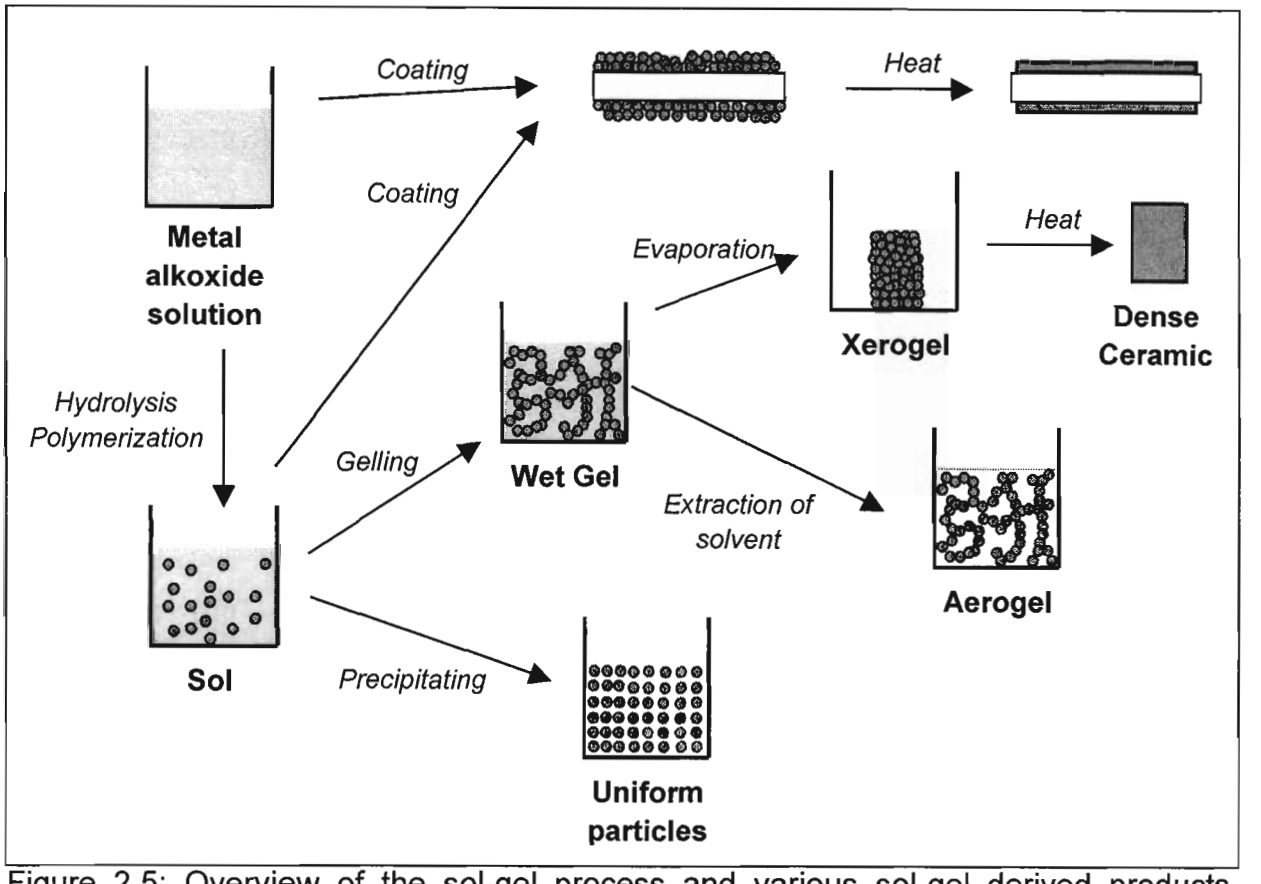

Figure 2.5: Overview of the sol-gel process and various sol-gel derived products (Adapted from Brinker and Scherer, 1990).

2.6.3 Reactions and chemical characteristics

Many chemical reactions have been found along the seven stages described in Section 2.6.2. The sol-gel chemistry is based on inorganic polymerization reactions and two routes are usually described depending on whether the precursor is an aqueous solution of an inorganic salt or an alkoxide in an organic solvent (Livage *et al.*, 1989). In either case, the solid network is formed, from the solution, via the hydrolysis and condensation of the molecular precursors in solution (Livage *et al.*, 1998).

The sol-gel process generally starts with alcoholic or other low molecular weight organic solutions of monomeric, metal or semimetal alkoxide precursors. Once these solutions are mixed with water, hydrolysis and condensation reactions

occur simultaneously (Wen and Wilkes, 1996). Hydrolysis and condensation occur by nucleophilic substitution (S_N) mechanism which involves three steps:

1. Nucleophilic addition (A_N)
2. Proton transfer within the transition states
3. Removal of the protonated species as either alcohol or water.

These two reactions (hydrolysis and condensation) usually proceed with either an acid or base as catalyst; therefore, the structure and morphology of the resulting network strongly depend on the nature of the catalyst. Other important factors are the pH of the reaction, the solvent used, the amount of water added, the sequence of mixing, and the size of the alkoxy group because of its steric effect (Nazeri *et al.*, 1993; Wen and Wilkes, 1996).

The structure of a gel is established at the time of gelation. Subsequent processes such as aging, drying, stabilization and densification depend upon the gel structure. Since it is the rate of hydrolysis and condensation that determine the structure of the gel, it is important to understand the kinetics of the hydrolysis and condensation reactions:

Hydrolysis:

Hydrolysis of the alkoxide occurs upon adding water or a water/alcohol solution, and a reactive *M–OH* hydroxo group is generated. The general hydrolysis reactions can be detailed as follows:

$$M(OR)_n + nH_2O \rightarrow M(OH)_n + nROH \qquad (2.35)$$

However, this reaction is more complex and can be represented with Equation 2.36 (Livage *et al.*, 1989):

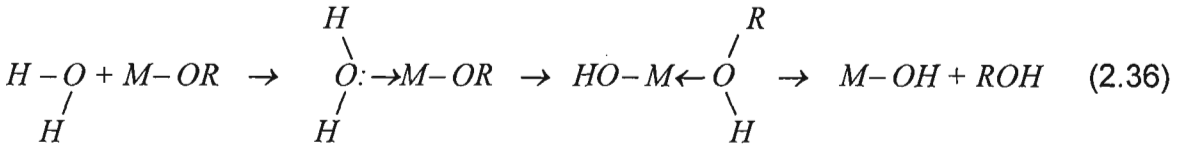

(a) (b) (c) (d) (2.36)

The first step (a) is a nucleophilic addition of a water molecule to the positively charged metal atom M. This leads to a transition state (b) where the coordination number of M has increased by one. The second step involves a proton transfer within (b) leading to the intermediate (c). Then, a proton from the entering water molecule is transferred to the negatively charged oxygen of an adjacent OR group. The last step is the departure of the living group which should be the most positively charged species within the transition state (c). All these processes follow a nucleophilic substitution mechanism and the charge distribution governs the thermodynamics of these reactions (Livage *et al.*, 1988).

Condensation:

Condensation occurs as soon as hydroxo groups, $M(OH)_n$, are formed. Depending on the experimental conditions, three competitive mechanisms are considered (Livage *et al.*, 1988; Livage *et al.*, 1989):

- Alcoxolation: This is a reaction by which the bridging oxo group is formed through the elimination of an alcohol molecule. The mechanism is basically the same as that for hydrolysis with M replacing H in the entering group.

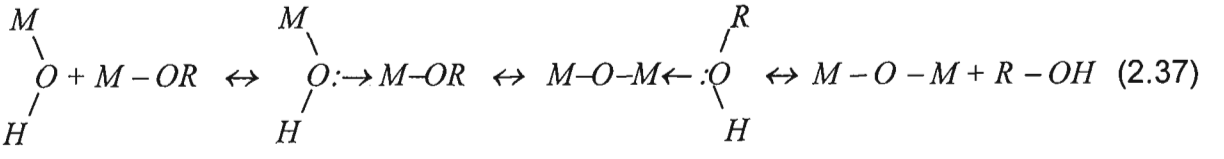

(2.37)

- Oxolation: Follows the same mechanism as alcoxolation, but the R group of the leaving species is a proton (water molecule).

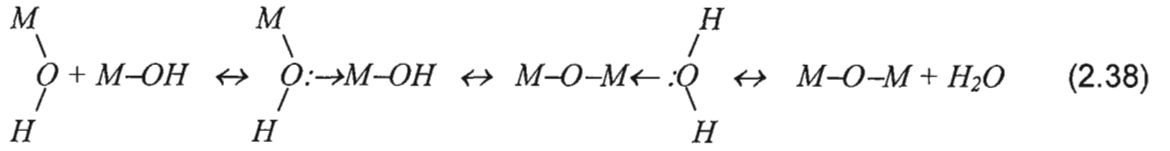

(2.38)

- Olation: It can occur when the full coordination of the metal atom is not satisfied in the alkoxide (N-z ≠ 0). In this case, bridging hydroxo groups can be formed through the elimination of the solvent molecule which will be water or alcohol, depending on the water concentration.

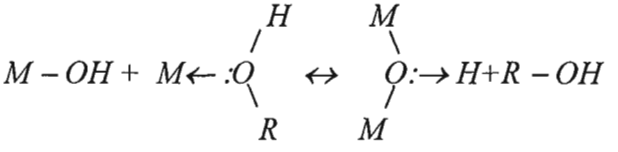

(2.39)

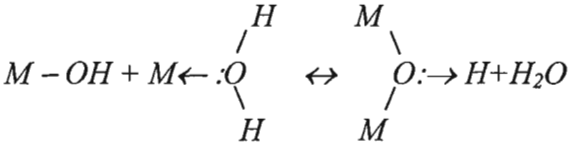

(2.40)

Titanium alkoxide, particularly titanium isopropoxide ($Ti(OC_3H_7)_4$), is one of the typical starting precursors for TiO_2 photocatalysts. Therefore, the overall chemical reaction is as follows:

$$Ti(OC_3H_7)_4 + 2H_2O \rightarrow TiO_2 + 4(C_3H_7)OH \quad (2.41)$$

Figure 2.6 shows the hydrolysis and condensation of this alkoxide in the presence of water. In general, Ti (IV) alkoxides form pentacoordinate and hexacoordinate complexes in the presence of water. Then, condensation happens once the M-OH bonds are formed. The resulting tetrahedral $Ti(OR)_{(4-n)}(OH)_n$ groups can form linear polymers as shown in Figure 2.6 (Laine, 1990).

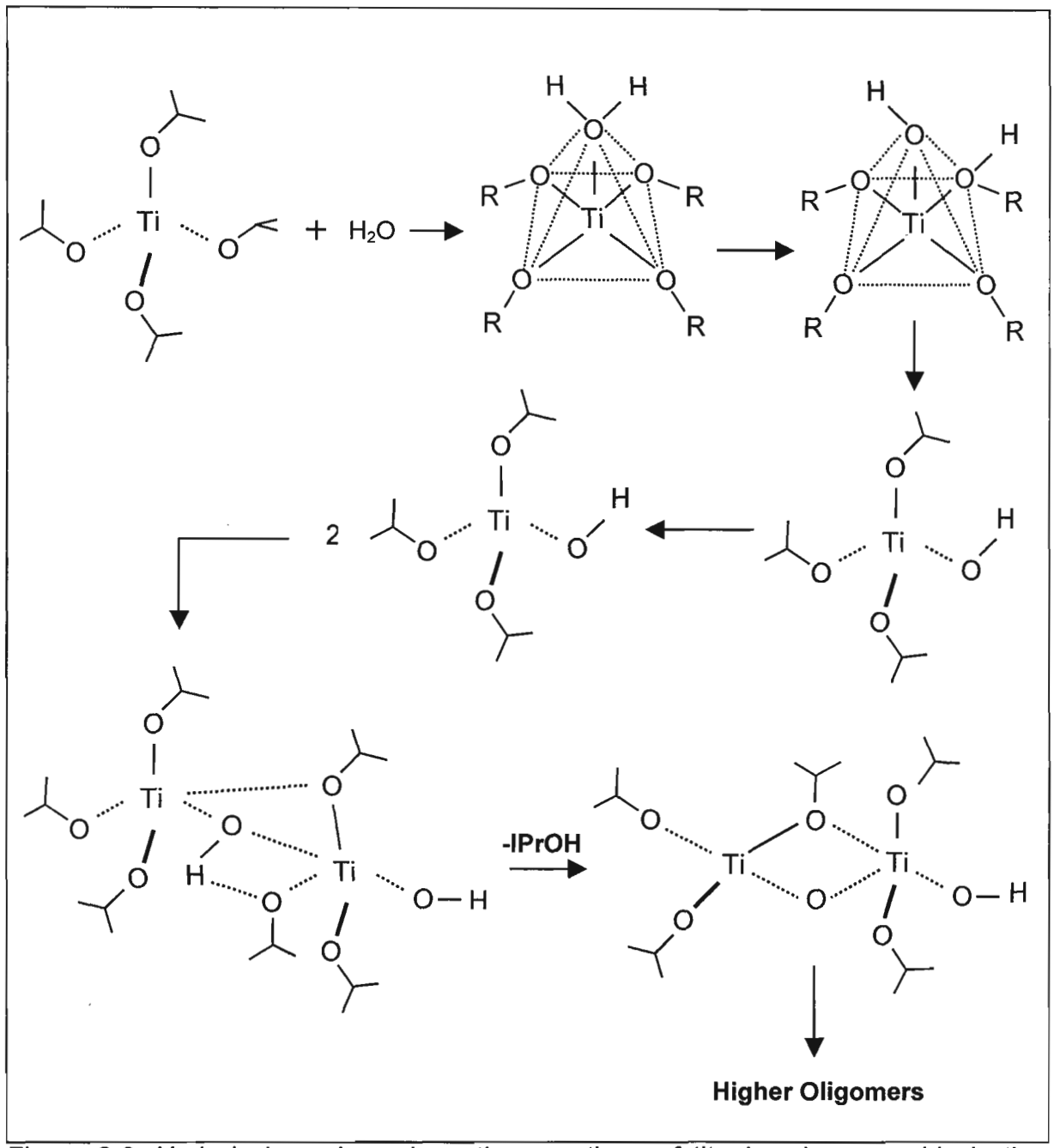

Figure 2.6: Hydrolysis and condensation reactions of titanium isopropoxide in the presence of water (Adapted from Laine, 1990).

Because of the high reactivity of transition metal alkoxides with water, precipitation is usually observed instead of gelation. However, this can be modified by introducing additives such as solvents, acidic or basic catalysts, etc. In many cases, nucleophilic molecules, e.g. XOH, react with alkoxides resulting in a new

molecular precursor. The new molecular precursor reacts differently with the nucleophilic agent. The more electronegative ligands are removed during the condensation reactions, while the less electronegative ones are quickly removed at the initial stages of hydrolysis. Then, instead of having a fast precipitation, a controlled formation of polymeric gels is expected (Danuwila *et al.*, 1994)

In some cases, like in this investigation, the hydrolysis of the alkoxide is performed in the presence of an acid catalyst (e.g., HCl, HNO_3) that allows for controlling the rate and the extent of the hydrolysis reaction. At the same time, polycondensation reactions can be delayed either by the use of titanium organic compounds with high molecular weight alkyl groups or through the reactions which are acid catalyzed increasing the rate of hydrolysis.

2.6.4 Sol– gel advantages and disadvantages

The advantages of the sol-gel processing over other conventional processes can be listed as follows (Brinker *et al.*, 1984; Brinker *et al.*, 1986; Brinker *et al.*, 1988; Brinker and Scherer, 1990; Wen and Wilkes, 1996; Livage, 1998; Sakka, 2006):

- High purity materials can be obtained if the necessary care is exercised during the sol-gel process.
- Processed materials can be very reactive and hence, the sintering temperatures are much lower than those employed for conventional by prepared powders. This is mainly because of the high surface energy of the sol-gel-derivated colloidal particles.
- Lower temperature process leads to products with large specific surface area and high porosity and macro pore ranges.
- Low calcination temperatures, needed for the sol-gel-derived materials, help to better control the size and crystallinity of the resulting particles. At the same time, lower temperatures mean lower energy costs.
- Special materials or configurations have been developed altering the sol conditions, e.g., thin films, controlled-size spherical powders, fibres, among other.

- Mixing of multiple components to produce a variety of organic/inorganic hybrid materials.
- Gelation permits the moulding of near-net shapes in applications where machining of those shapes is expensive. The shape and surface configuration will be retained in the body, despite the large dimensional change due to shrinkage.
- Improved homogeneity of multicomponent species can be obtained by blending a variety of metal alkoxides, colloidal dispersions or easily diffused soluble salts.

On the other hand, the disadvantages of the sol-gel processing are the followings (Brinker *et al.*, 1984; Yang, 1999; Keshmiri, 2004):

- The high-purity alkoxides are relatively expensive raw materials.
- The process is time consuming and multi-step.
- Generation of a significant amount of waste of some chemicals (e.g. alcohol).
- The shrinkage of the resulting gel during drying and heat treatment is high (as high as 90% for materials with high solvent content), potentially causing micro and macro cracks within the dried and calcined body.
- If the thermal processing is not properly completed, the remaining solvent and carbonaceous residues, if not properly removed, can lead to defects such as bloating, residual bubbles or crystal formation.

2.6.5 Sol-gel applications

Because of its multiple advantages, the sol-gel process is one of the most important techniques for preparing nanosized metallic oxide materials with high photocatalytic activities (Su *et al.*, 2004). In recent years, different materials have been coated with photocatalyst using sol-gel principles. Examples of these include activated carbon (Lee *et al.*, 2004; Dong *et al.*, 2008), ceramic particles (Kanki *et al.*, 2005), glass beads and silica gel particles (Bideau *et al.*, 1995; Choi *et al.*, 2007), zeolites (Hisanaga and Tanaka, 2002; Haque *et al.*, 2005), glass slides (Kumara *et*

al., 1999; Guillard *et al.*, 2004), stainless steel (Fernández *et al.*, 1995) among others. Also, many other materials have been produced for photocatalytic purposes, such as membranes, powders, nanoparticles, microspheres, etc. (Bessekhouad *et al.*, 2003; Su *et al.*, 2004; Choi *et al.*, 2006; Choi *et al.*, 2007; Junin *et al.*, 2008; Wetchakum and Phanichphant, 2008; Xu *et al.*, 2008; Shi *et al.*, 2009).

There are also a significant number of other materials produced using sol-gel principles for different applications. Some of those materials include different kinds of composite materials, aerogels, plastic ophthalmic lenses, water repellent coatings etc., (Que *et al.*, 2001; Mackenzie, 2003; Chen *et al.*, 2004). Among all those materials, composite materials have gained a lot of attention because of their advantages and properties.

2.6.6 Composite materials

One of the main applications of sol – gel process is related to the production of the sol-gel-derived composites. Generally speaking, materials formed by the sol-gel process have a relatively high rate of volume shrinkage, which causes considerable cracking and subsequent mechanical failure of the final products. At the same time, it is well known that the dried gel structure is usually weak due to continuous pores with unreacted and trapped organics, water, and other compounds. These problems can be overcome by the introduction of a secondary phase (e.g., pre-calcined powder) as a filler to reinforce the material structure, producing a material with a composite structure.

Composite materials, by definition, usually contain two (or more) distinct materials as a unified combination. The principal material of a composite that envelopes the reinforcement is called *matrix* and the reinforcement is usually called a *filler* or *inclusion* (Keshmiri, 2004).

Through this process, not only is the shrinkage of the *gel* expected to decrease because of the presence of a significant amount of inert ceramic powder, but also the sol-gel-derived material acts as a binder to bond the entire structure. The sol-gel-derived material, present in between the neighbouring particles, also acts as a sintering aid to decrease the sintering temperature (Keshmiri, 2004).

There are various pathways for processing sol-gel-derivated composites; Figure 2.7 shows these pathways (Nazeri *et al.*, 1993):

1. Mixing of two or more sols to form a homogeneous solution (Figure 2.7 (a)). The different components may be tailored so that they do not react with each other to form a new component. This method allows uniformity of the composites.
2. Dispersion of a solid phase, such as fine powders or fibres, in a sol before gelation, which leads to a composite with good homogeneity and good contact between particles and matrix (Figure 2.7 (b)).
3. Impregnation of the fine interconnecting pores by organic or inorganic phases (Figure 2.7 (c)).
4. Infiltration of the fine interconnecting pores by organic or inorganic phases (Figure 2.7 (d)).
5. Combination of # 2 and # 3 in to give a "triphasic" composite.

While preparing a sol-gel composite material, there are some limitations to take into account, like the ones listed below (Lutz and Swain, 1991; Yang, 1999):

1. Agglomeration of ceramic particles in sol precursor becomes critical to further improve the technology of composite-gels.
2. Different thermal expansion coefficients between the inclusions and sol-gel matrices inducing additional stresses in the composite material. Hence, cracks may be formed from small pre-existing defects at or near the filler/matrix interfaces.
3. Composite sol-gel coatings cannot be densified enough to gain high strength and hardness at curing temperature below 1000°C

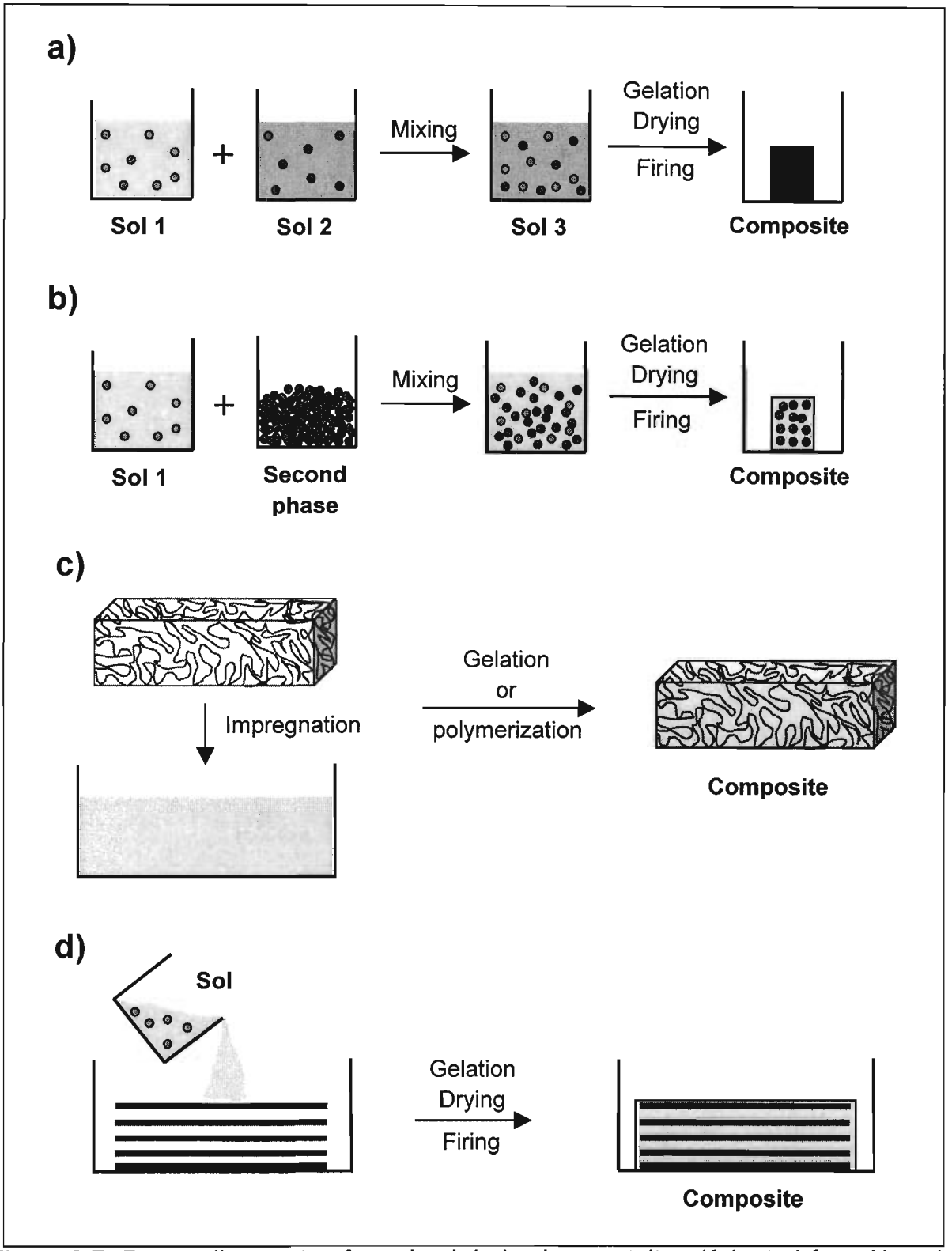

Figure 2.7: Proceeding routes for sol-gel-derived composites (Adapted from Nazeri *et al.*, 1993).

The novel catalyst that is evaluated in this investigation is based in the principles described above. Basically a sol-gel matrix is produced to bond together pre-calcined particles together (TiO_2 powder). Then, the formation of the catalyst is done by the combination of the sol-gel-composite material with a polymeric solution leading to a fast and uniform formation of TiO_2 catalyst.

Chapter Three

Scope and Objectives

3.1 Scope

Over the past two decades, significant efforts have been made towards the applications of photocatalytic TiO_2 in various forms such as coatings on different surfaces and supports, fibres and powders with a wide range of particle sizes and surface areas. However, there are still important number of unsolved problems or drawbacks with respect to the photocatalyst itself and its large scale applications. Some of these challenges are:

- the separation and filtration of the catalyst from the processed fluid (e.g., treated water) when a powder form of photocatalyst is used,
- the diffusive mass transfer resistance and low surface area being limiting factors for the effectiveness of the processes involving supported photocatalyst,
- relatively low photoactivity and significant attrition issue, producing low photoefficiency of the system and process complications such as downstream filtration and separation of the suspended particles, for the fluidized bed photocatalytic process.

This research focuses on the development and standardization of template free composite titania photocatalysts, in the form of spheres, to be used in a fluidized bed photoreactor. The photocatalyst is synthesized using sol–gel principles to bond TiO_2 precalcined particles (Degussa P-25) together, which produced a composite TiO_2 spheres with high photoefficiency and high attrition resistance. These spheres are evaluated in a laboratory scale fluidized bed photocatalytic reactor treating two model compounds.

3.2 Objectives

The specific objectives of this research were to:

1. Examine the effect of parameters such as:
    a. *sol* composition
    b. amount of catalyst to be added to the *sol*
    c. calcination temperature and duration of the heat treatment
    d. drying process conditions (temperature and time)

    in order to determine their effects on the photocatalytic activity and attrition resistance of the TiO_2 spheres.
2. Evaluate the attrition resistance of the TiO_2 spheres, developing a method to determine the amount of TiO_2 particles released in water after the normal operation of the fluidized bed photoreactor.
3. Evaluate the ability of the composite TiO_2 spheres to degrade water contaminated with
    a. Formic Acid (FA) as a model organic compound
    b. 2,4-Dichlorophenoacetic acid (2,4-D) as a model micropollutant
    c. Natural Organic Matter (preliminary tests)
4. Improve the formulation and synthesis process of the photocatalytic spheres considering the results obtained in objectives 1-3.
5. Characterize the TiO_2 spheres in terms of
    a. specific surface area of the TiO_2 spheres (BET)
    b. change in weight with respect to the drying process and heat treatment using thermo gravimetric analysis (TGA)
    c. phase evolution of the photocatalyst using X-ray diffraction (XRD)
    d. microstructure analysis of the catalyst using Scanning Electron Microscope (SEM)

3.3 Significance of this work

This research with its objectives provides the first steps towards the development and standardization of the novel template-free composite TiO_2 photocatalyst. The photocatalyst, with its high attrition resistance and high photoactivity, will significantly contribute to the research and development activities performed towards the implementation of large-scale commercial photocatalytic treatment systems.

Although the treatment of contaminated water by means of heterogeneous photocatalysis has been demonstrated to be a promising technology, the development of commercial systems has not been successfully achieved. Depending on the type of application, a number of limitations and challenges, contributing to this issue, include low photo-efficiency and quantum yield of the catalyst, expensive separation of the catalyst from treated water, and weak adhesion of the catalyst on the support materials. Nonetheless, the development of such commercial systems would be a great improvement to the water treatment industry, since i) many organic compounds can be mineralized during photocatalysis, ii) a significant amount of the degradation by-products are environmentally benign, iii) in most cases low energy UV would be needed for the catalyst activation. The development of composite TiO_2 spheres, that possess good attrition resistance and provide high photo-efficiency, address some of the outstanding challenges and will contribute significantly to the implementation of large-scale commercial photocatalytic systems. The whole photocatalyst is made of pure TiO_2 (no support required), has good photoactivity to degrade pollutants in water, and has high mechanical stability (attrition resistance) that reduces the amount of TiO_2 particles that need to be filtrated downstream.

3.4 Layout

The abovementioned objectives were achieved at different stages along the project. A detailed description of how each objective has been met with respect to their presentation in the following chapters is shown below:

Chapter Four: describes the experimental methodology that was followed to meet all the objectives described above. A detailed description of the procedure to produce the catalyst and the variables involved during the process is presented. Additionally, a detailed explanation of the characterization of the catalyst in terms of the surface area (BET), microstructure (SEM), phase evolution (XRD) and TGA analyses are provided giving the necessary background to all these techniques. Finally, the procedures to determine the activity of the catalysts (using FA, 2,4-D and natural organic matter), the attrition resistance of the catalyst and the fluence rate in the system are explained.

Chapter Five: describes primarily the preliminary experimental results that were obtained with the spheres using the formulation before any modification. Aspects such as catalyst loadings in the reactor, bed expansion, mass transfer within the system, and the impact of the calcination temperature on the FA degradation are some of the points developed and presented along this chapter. The original level of attrition of the spheres is presented as reference and benchmark for additional improvement. Preliminary characterization of the spheres was done in terms of microstructure (SEM), specific surface area (BET) and polymorphic phases determination (XRD).

Chapter Six: covers the analysis of the effect of different variables on the attrition resistance and activity of the catalyst (objective 1) and the determination of the final formulation to produce the composite TiO_2 spheres (objective 5). Detailed characterization of the catalyst produced with the new formulation was performed and the results are presented.

Chapter Seven: presents the results of the experiments performed with the composite TiO_2 spheres to degrade FA under different UV irradiations. Also, 2,4-D was used as a contaminant to evaluate the ability of the photocatalyst to degrade more complex organic molecules in water. Preliminary results with NOM are presented and discussed as well. In addition, a detailed study of the fluence rate determination in the reaction system used in this research is included in this chapter.

Chapter Eight: provides the main conclusions of this research as well as recommendations for future work.

Chapter Four

Experimental Methodology

4.1 Introduction

This chapter provides a detailed description of the experimental work performed during the course of this investigation. Detailed explanations of the production process of the photocatalyst as well as different techniques used to characterize the photocatalyst are discussed. Moreover, analytical techniques used during the experimentation, e.g., the protocol to monitor TiO_2 in suspension are presented. Finally, a detailed description of the fluidized bed photoreactor (FBPR) and its operational procedure are presented.

4.2 Composite TiO_2 spheres preparation

4.2.1 Chemicals and reagents

The list of chemicals that used to prepare the photocatalyst is provided in Table 4.1. Most of the chemicals were obtained from Sigma-Aldrich (Ontario, Canada) and Fisher Scientific (Ontario and Edmonton, Canada). The TiO_2 Degussa P-25 was obtained from Degussa, Germany.

Table 4.1: Specifications of the chemicals used during the preparation of the composite TiO_2 photocatalyst.

Chemicals	Chemical formula	Purity
Ethyl Alcohol Denatured	C_2H_6O / CH_3OH	85% / 15%
Hydrochloric Acid	HCl	38%
Titanium (IV) Isopropoxide	$Ti(OCH(CH_3)_2)_4$	97%
Titanium Dioxide	TiO_2	----
Chitosan	$C_{12}H_{24}N_2O_9$	Medium Molecular Weight
Glacial Acetic Acid	$C_2H_4O_2$	99.7%
Ammonium Hydroxide	NH_4OH	30%

4.2.2 Composite sol-gel material (CSG)

To prepare the composite sol-gel (CSG) material, anhydrous ethyl alcohol denatured was used as a solvent to prevent fast hydrolysis of the titanium alkoxide. Since water content of the sol has a critical role in the hydrolysis and polycondensation reactions during the sol-gel process, the amount of water needs to be well controlled. Milli-Q water was added to the alcohol followed by the addition of the catalyst, in this case HCl, while the solution was magnetically stirred. The catalyst is used to prevent fast gelation of the sol, control the rate of condensation, and eliminate the possibility of precipitate formation due to uncontrolled hydrolysis reaction. Hydrolysis was carried out by the addition of the precursor. Titanium (IV) isopropoxide was used as a precursor without further purification, and it was added to the prepared solution (alcohol with water and HCl) while stirring. Different molar ratios of the chemicals were investigated.

The mixture was stirred for 2 h and a clear and stable alkoxide sol was obtained using this process. Pre-calcined commercial TiO_2 powder, Degussa P-25, was used as a filler material. This material was used because it exhibits high photoefficiency, high surface area (54 m^2 g^{-1}) and low charge recombination rate. Characteristics and properties of Degussa P-25 (e.g., specific surface area and phase composition) have been evaluated prior to incorporating it to the composite preparation process (Section 6.3). Good agitation was required to dissolve the powder into the solution and create a homogeneous solution called Composite Sol–Gel (CSG). A similar procedure was reported before by Keshmiri *et al.* (2004).

4.2.3 Polymeric solution

The polymeric solution was prepared by dissolving chitosan in water. Chitosan is a natural, non-toxic, biodegradable, high molecular weight polymer that was first described in 1811 and named by Odier in 1823. From the commercial point of view, chitosan is obtained by deacetylation of chitin, which is the structural element in the exoskeleton of crustaceans (e.g., crabs, shrimps, etc.) and the cell walls of fungi and certain yeasts, among other sources (Ayers and Hunt, 2001).

Chitosan is a linear cationic polysaccharide made out of two kinds β(1→4)-linked monosaccharide residues, namely N-acetyl-D-glucosamine (A) and D-glucosamine (D). It is established that D-residues at acidic pH provide protonated – NH_3 groups which render chitosan soluble, whereas A-residues have an important role on the stiffness of the chains (Arguelles-Monal *et al.*, 1998) determined by hydrogen bonding between two adjacent hexopyranose rings along the chain, hindering the free rotation around glycosidic bonds and reinforced by an increment on the hydrophobic macromolecular interactions (Skjak-Braek *et al.*, 1989; Arguelles-Monal *et al.*, 1998). Therefore, chitosan was dissolved in Milli-Q water that was acidified with glacial acetic acid. To ensure a homogeneous solution, the solution was stirred for at least 24 h. Different molar ratios of chitosan-water-glacial acetic acid were investigated. The pH of the solution was measured using a pH meter from Denver Instruments – UB5. The viscosity was measured using a viscometer from Cambridge Viscosity – VISCOlab 3000.

4.2.4 Composite TiO_2 spheres formation

Once the CSG material was ready to be used (after approximately 14 hours of agitation), it was mixed with the chitosan solution to create a solution with the desired viscosity needed for the spheres formation. Chitosan also acted as a binder of the CSG material. The CSG material was added to the chitosan solution while the solution was magnetically stirred. This new solution was agitated for 2 h before it was added drop wise to the ammonia solution to form the TiO_2 spheres. The formation of the spheres was based on the principle that the CSG – chitosan solution would undergo a fast gelation when in contact with basic pH.

After the sphere formation, drying was required to remove the liquids contained in the body of the spheres. Different drying conditions were studied during this investigation; specifically, TiO_2 spheres were placed in a furnace for 20 h at 80°C or they were left at room temperature (23°C) for 15 days. After the completion of the drying process, heat treatment was applied to densify the composite TiO_2 spheres. The heat treatment was carried out at the Materials Engineering Ceramic Laboratory using high temperature furnaces. The composite TiO_2 spheres were

placed in ceramic crucibles to be able to heat them up to high temperature (600°C to 900°C). The heating rate for all the samples were approximately 9.5°C min^{-1} up to 470 °C and 4.4°C min^{-1} up to the final temperatures. Among different calcination temperatures and heat treatment conditions, the best conditions were selected to give a product with the desirable characteristics.

Figure 4.1 shows the schematic and sequence of the abovementioned procedure for the production of the composite TiO_2 spheres.

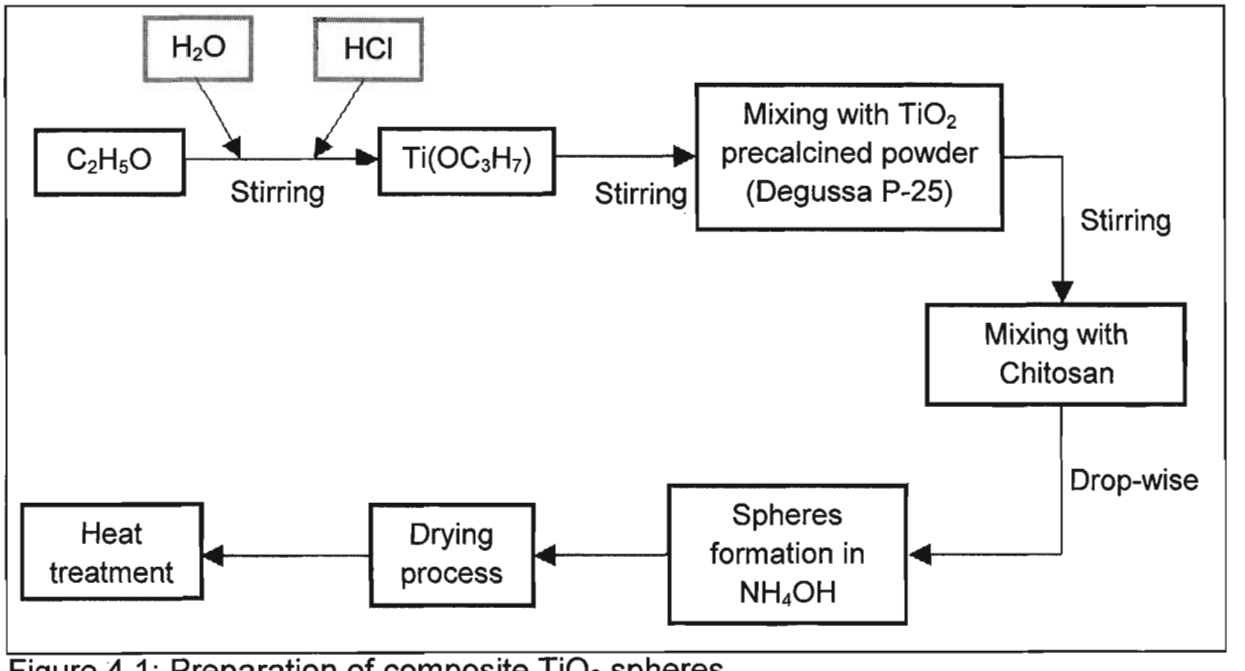

Figure 4.1: Preparation of composite TiO_2 spheres.

4.3 Composite TiO_2 spheres characterization

The objective of catalyst characterization was to examine the catalyst surface and its bulk properties that offer substantial information about the catalyst attributes. The information obtained from all the different characterization tools will significantly improve the understanding of how the physicochemical properties and catalytic performance are related.

In this section, brief reviews of the basic concepts of various catalyst characterization techniques are provided. In particular, BET surface area, pore volume, pore size distribution, X-ray diffraction (XRD), scanning electron microscope (SEM) and thermogravimetric analysis (TGA) are described.

4.3.1 Surface area, pore volume and pore size determination

The determination of total surface area, not only external but also internal, is generally considered an important catalyst characterization (Haber, 1991). Nowadays, adsorption is one of the most widely used methods to determine the surface area and pore size distribution (Gregg and Sing, 1982). When a gas is in contact with a solid surface, physical adsorption will occur. Of course, the amount of gas adsorbed depends on many variables such as equilibrium pressure, temperature, and the specific characteristics of the gas-solid system.

Brunauer-Emmet-Teller (BET) method is a well known technique for the determination of physical adsorption of gas molecules on a solid surface (Brunauer *et al.*, 1938). The theory is an extension of the Langmuir theory, developed based on the monolayer molecular adsorption on a catalyst surface. BET equation was derived for multilayer adsorption and its fundaments are on the relation between the volume of gas physically adsorbed and the total area of adsorbent, which is given in Equation 4.1:

$$\frac{1}{\nu\left(\frac{P_o}{P}\right)-1} = \frac{c-1}{\nu_m c}\left(\frac{P}{P_o}\right) + \frac{1}{\nu_m c} \tag{4.1}$$

where P is the gas pressure; P_o is the saturation pressure of the adsorbate gas, ν is the volume of gas adsorbed, ν_m is the volume of gas adsorbed corresponding to monolayer coverage, and c is a characteristic constant of the adsorbate.

The total surface area was determined using a multipoint BET method using Micromeritics ASAP 2020 equipment (Figure 4.2) located at the Department of

Chemical and Biological Engineering. The pore volume and the pore size distribution were calculated as well using the same equipment.

To determine the porosity of most solid materials, nitrogen (N_2) at 77K is usually utilized as a suitable adsorbate. Thus, by constructing an adsorption isotherm, a better understanding of the porosity of the materials can be obtained. This isotherm is made by measuring the quantity of adsorbate on the surface of the solid over a wide range of relative pressures at constant temperature (Gregg and Sing, 1982). Similarly, desorption isotherm can be obtained by measuring the amounts of gas removed from the sample as the relative pressure is lowered. The isotherm shapes, which is recognized as BDDT (Brunauer, Deming, Deming and Teller) classification, depends on the kind of pores that the solid has (e.g. micropores, mesopores and macropores) (Gregg and Sing, 1982; Sing *et al.*, 1985; Hosokawa, 2007).

Figure 4.2: Multipoint BET equipment – Micrometrics ASAP 2020

The total pore volume is derived from the amount of vapour adsorbed at a relative pressure close to one, assuming that the pores are filled with liquid nitrogen. Pores which would not be filled below P/Po of one are considered negligible to the total pore volume; then, the average pore size can be estimated from the pore volume.

The distribution of pore volume with respect to pore size is known as a pore size distribution. The pore size distribution was calculated using the method proposed by Barrett, Joyner and Halenda (BJH). This method is based on the emptying of the pores by a step-wise reduction of P/Po (Barrett *et al.*, 1951). In general, the desorption isotherm is more appropriate than the adsorption isotherm for the evaluation of the pore size distribution of a solid material because it exhibits a lower relative pressure resulting in a lower free energy state; therefore, the desorption isotherm is closer to the true thermodynamic stability (Gregg and Sing, 1982).

Pore size calculations are made assuming cylindrical pore geometry using the Kelvin Equation (Sing *et al.*, 1985):

$$r_K = \frac{-2\gamma v_m}{RT \ln\left(\frac{P}{P_o}\right)} \tag{4.2}$$

where γ represents the surface tension of N_2 at its boiling point (8.85 mN m^{-1} at 77K); v_m is the molar volume of liquid N_2 (34.7 cm^3 mol^{-1}), T is the N_2 boiling point, P/P_o is the relative pressure of N_2 and r_K is the Kelvin radius of the pore.

The Kelvin radius is the radius of the pore in which condensation happens at *P/Po.* Nonetheless, the r_K does not represent the actual pore radius because some adsorption has taken place prior to condensation on the walls of the pores. Besides, during desorption an adsorbed layer remains on the walls when evaporation occurs. Therefore, the real pore radius (r_p) is given by Equation 4.3:

$$r_p = r_k + t \tag{4.3}$$

where t is the thickness of the adsorbed layer that can be estimated using the Equation 4.4 (DeBoer *et al.*, 1966):

$$t = \left[\frac{13.99}{\log\left(\frac{P}{P_o}\right) + 0.034} \right]^{\frac{1}{2}} \tag{4.4}$$

The measurements with BET equipment were conducted by placing few grams of the catalyst (usually around 0.4 g) in the degasser section for at least 3 h at 100°C. The degassing was done prior to the analysis in order to eliminate any physisorbed species from the surface of the adsorbent. Then, the BET analysis was done using N_2 as an adsorbate and liquid N_2 to keep the temperature constant.

4.3.2 X-Ray diffraction spectroscopy (XRD)

X-ray diffraction (XRD) spectroscopy has been commonly used for crystalline phase identification and for the average crystalline size determination in a catalyst sample. It depends on the fact that crystalline matter is composed of periodic arrays of atoms in three dimensions. As the wavelength of X-rays is of the same order of magnitude as the spacing between the atoms in crystals (~1 Å), crystals behave as a diffraction grating for X-rays. Then, by passing a monochromatic bean of X-rays through a crystal and by measuring the intensities and angles of the diffracted beams at specific orientation of the crystal, the symmetry of the atomic arrangement of the crystal may be deduced and the nature of the atomic structure of the crystal can be solved and quantified (Raudsepp and Pani, 2003).

In catalyst characterization, the catalyst sample is irradiated with X-ray of a known wavelength (λ). This condition results in the reflection of X-rays by atomic layers with interplanar spacing d at a certain angle of incidence and reflection known as the Bragg angle (θ). The relationship between these variables is given by Bragg's Law (Reed, 2005):

$$n\lambda = 2d\sin\theta \tag{4.5}$$

This equation follows directly from the difference in path lengths between successive planes where the integer *n* is the order of diffraction.

The XRD measurements were performed on a Siemens D5000 X-ray diffractometer (Figure 4.3) at 40kV, 40mA. X-ray diffraction patterns were recorded using CoKα radiation (λ= 1.7889Å) over the range 2θ from 3 to 80°, with a scanning speed of 3°/min. The peaks obtained from the analysis were identified using the Diffracplus XRD identification method to determine the crystalline phases present in the sample. This equipment is located at the Department of Earth and Ocean Science at UBC.

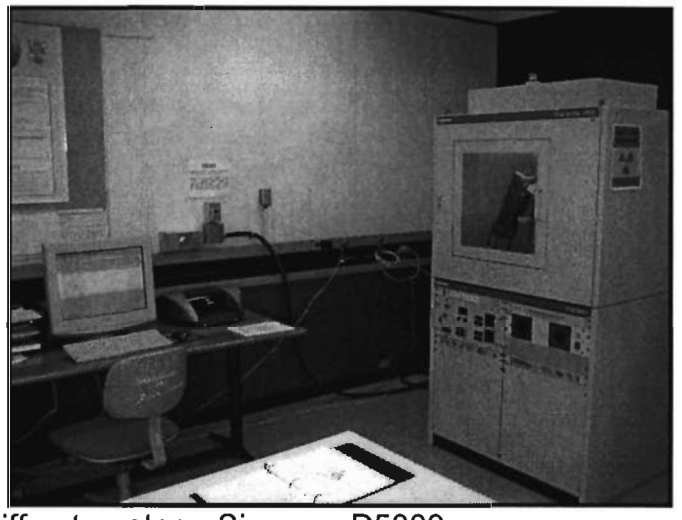

Figure 4.3: X-ray diffractometer – Siemens D5000

To prepare a sample, approximately 4 g of spheres were crushed to a fine powder (less than 10μm) and then placed on a specimen holder and pressed using a glass slide. If the sample was not smaller than 10μm inaccurate intensities of the diffraction peaks could result because of extinction, micro-absorption contrast among the phases, prefer orientation of particles, etc. (Raudsepp and Pani, 2003).

Rietveld refinement was carried out as well to determine the quantitative composition of the phases formed during the calcination processes. In Rietveld method, a model for the shapes and widths of the diffraction peaks, a model for any aberrations in the shapes and positions of the peaks and a model for the background are defined for the crystal-structure of each phase. These models were used to

calculate a simulated powder diffraction pattern for each phase. The sum of the individual calculated patterns was then fitted to the digital experimental diffraction pattern. The fitting was done by least-squares refinement of structural parameters of each phase (Raudsepp *et al.*, 1990; Raudsepp and Pani, 2003).

4.3.3 Scanning Electron microscopy (SEM)

Scanning Electron Microscope (SEM) was used to analyze the morphology (size and shape), topography (surface features) and crystallographic (atomic arrangements) of the photocatalyst. In the SEM unit, an electron gun is used to generate an electron beam with high intensity. Once the beam bombard the metal/carbon coated specimen, secondary (SE) and backscattered electrons (BSE) are emitted from highlighted area. Local variation in surface topography, e.g. orientation of surface with respect to the electron beam, gives rise to contrast and then, images are produced by scanning the beam while displaying the signal from an electron detector (Haber, 1991; Reed, 2005). SE are produced by inelastic interactions of high energy electrons with valence electrons of atoms in the specimen which cause the ejection of the electrons from the atoms; on the other hand, BSE consist of high-energy electrons originated in the electron beam, that are reflected or back-scattered out of the specimen interaction volume by elastic scaterring interaction with specimen atoms (Bozzola and Russell, 1998).

A Philips XL-30 SEM unit, located at the Materials Engineering Analytical Laboratory, was used (Figure 4.4). SEM samples were prepared by placing few spheres, randomly picked, on the surface of the specimen, and then either gold or carbon was used as coating to enhance the conductivity of the sample. The majority of the images were taken using SE with an approximate distance of 14 mm from the sample.

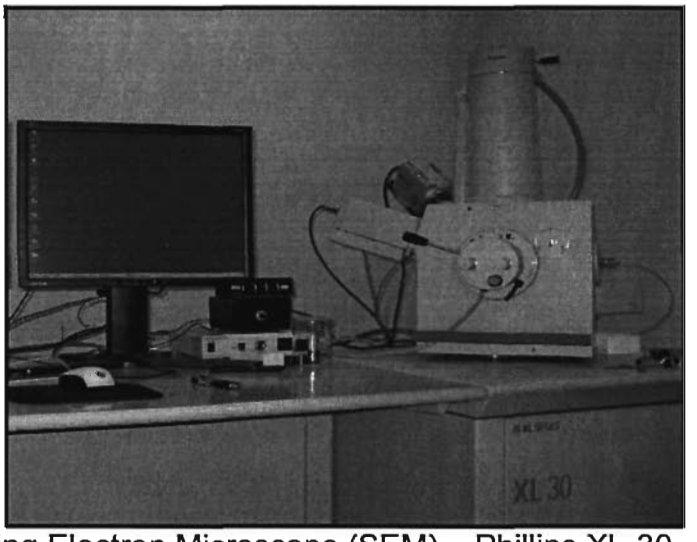

Figure 4.4: Scanning Electron Microscope (SEM) – Phillips XL-30

4.3.4 Thermogravimetric analysis (TGA)

Thermogravimetric analysis (TGA) is an analytical technique used to determine either the material's thermal stability or the change of sample mass with change of temperature. This loss of mass is due to the amount of volatile components or solvents that are released from the sample when the specimen is heated up (Hill, 2005).

TGA analysis relies on a high degree of precision in three different measurements: weight, temperature and temperature change. In general, the analyzer consists of a high-precision balance with a pan, generally made of platinum, where the sample is placed. This pan is placed inside the electrically heated oven with a thermocouple to accurately measure the temperature. The measurement is normally carried out in air or in an inert atmosphere, such as Helium or Argon, to prevent oxidation or other undesirable reactions and the weight is recorded as a function of increasing temperature.

In addition to weight changes, some instruments record the temperature difference between the specimen and one or more reference pans (differential thermal analysis, or DTA) or the heat flow into the specimen pan compared to that of the reference pan (differential scanning calorimetry, or DSC). The latter can be used

to monitor the energy released or absorbed via chemical reactions during the heating process (Hill, 2005).

A TA Instruments - Q600 thermo gravimetric analyzer, located at the Department of Chemical and Biological Engineering (Figure 4.5), with N_2 flow of 100 cm^3 min^{-1} and temperature range of 20°C to 600°C was used. Heating rates of 12°C min^{-1} up to 80°C (an isothermal study was done for 1200 min), 9.6°C min^{-1} up to 473°C and 4.4°C min^{-1} to 600°C (an isothermal study was done for 180 min) were utilized.

Right after the production process, a single composite TiO_2 sphere was placed in the pan for 23 hours. The change in the weight of the TiO_2 with system temperature was used to determine the adsorbed moisture and solvent content of the catalyst.

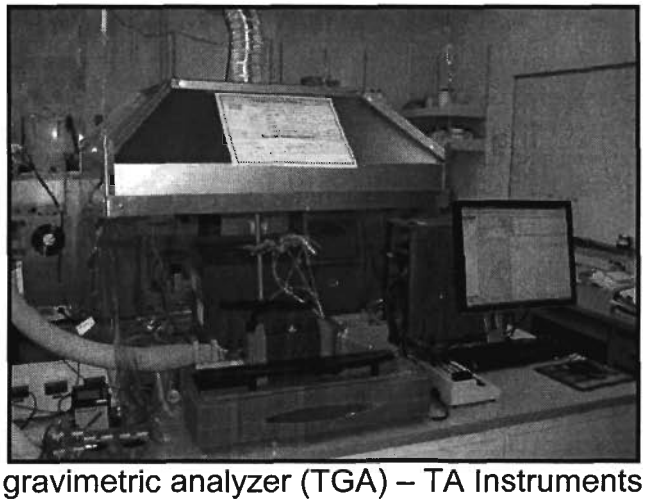

Figure 4.5: Thermo gravimetric analyzer (TGA) – TA Instruments

4.4 Fluidized Bed Photoreactor Setup

The fluidized bed photoreactor was built using an 80 mL quartz tube (15 cm height and 2.6 cm of internal diameter) as is shown in Figure 4.6. Two acrylic pieces, held together with three threaded rods, were part of the main body of the reactor. The conic shape in the bottom piece (calming section) helps develop the

fluid to have a better catalyst expansion. The catalyst inside the quartz tube was irradiated by three UV-Hg lamps (5.7 W at 254 nm output, GPH357T5L/4P, Light Sources Inc.) that were longitudinally placed surrounding the reactor. The position of the lamps could be changed in order to adjust the level of irradiation. A cylindrical reflector was also included in some experiments surrounding the lamps to improve the radiation to the reactor.

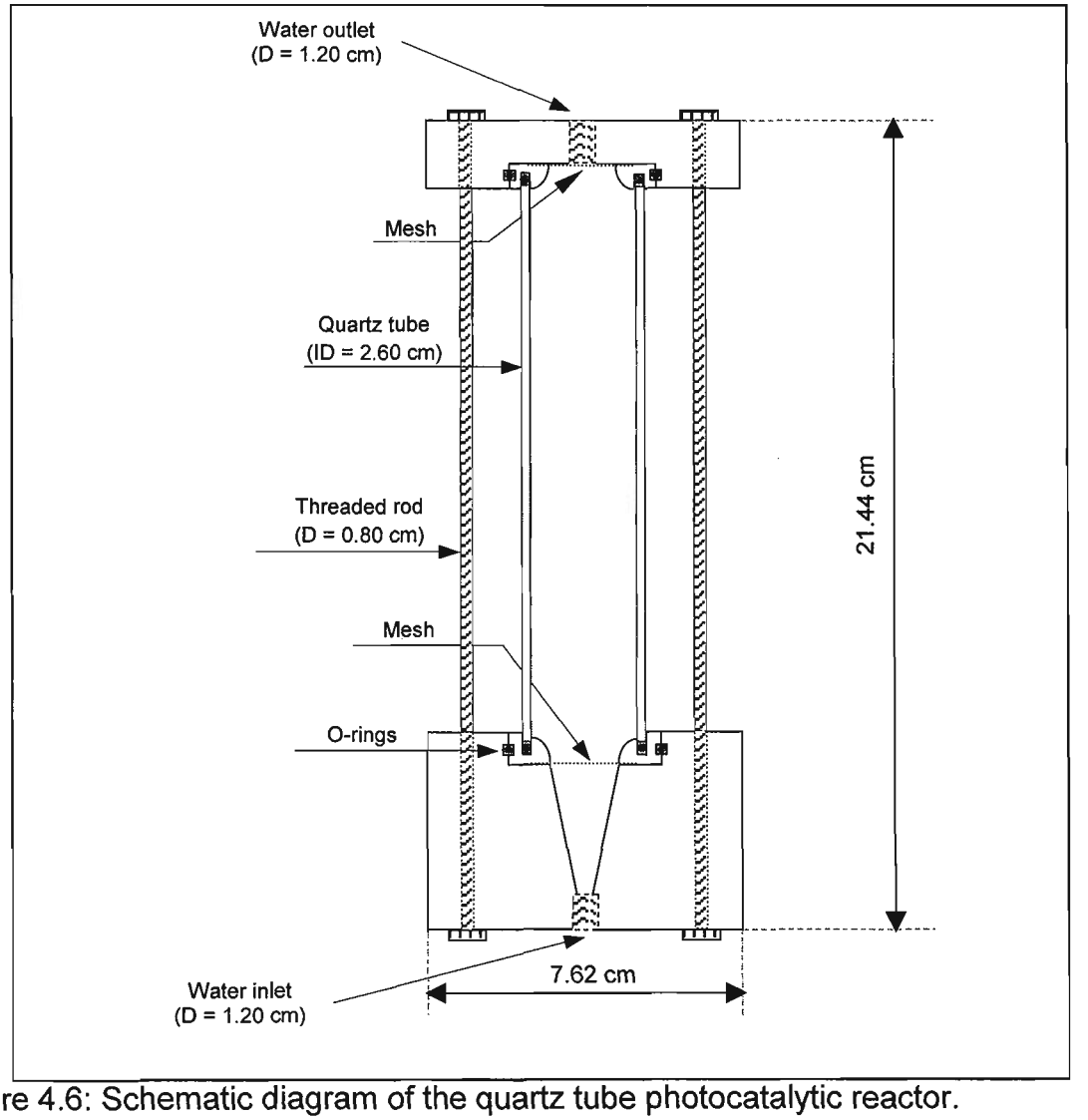

Figure 4.6: Schematic diagram of the quartz tube photocatalytic reactor.

4.5 Photocatalyst activity test

In order to measure the activity of the composite TiO_2 photocatalyst spheres, two different model organic pollutants were put in contact with the spheres in the presence of UV lamps. In both cases, the reaction proceeded at 27°C and at ambient pressure and the changes in concentration were monitored using High Performance Liquid Chromatography (HPLC). The list of chemicals use for these experiments is provided in Table 4.2.

Table 4.2: Specifications of chemicals used during the activity test of the CSG photocatalyst

Chemicals	Chemical formula	Purity	Supplier[a]	Role
Formic acid	$HCOOH$	99%	AO	Model organic contaminant
Acetonitrile	CH_3CN	HPLC - 99%	S-A	HPLC eluent
Methanol	CH_3OH	HPLC - 99%	FS	HPLC eluent
Glacial Acetic Acid	CH_3COOH	99.7%	FS	HPLC eluent
2,4-Dichlorophenoacetic acid	$C_8H_6Cl_2O_3$	98%	S-A	Model micropollutant
2,4-Dichlorophenol	$C_6H_4Cl_2O$	99%	S-A	2,4-D by-product
4-Chlorophenol	C_6H_5ClO	99%	S-A	2,4-D by-product
2-Chloro-1,4-benzoquinone	$C_6H_3ClO_2$	95%	S-A	2,4-D by-product
4-Chlorocatechol	$C_6H_5ClO_2$	97%	S-A	2,4-D by-product
Chlorohydroquinone	$C_6H_5ClO_2$	85%	S-A	2,4-D by-product

[a] AO: Acros Organics; S-A: Sigma Aldrich; FS: Fisher Scientific

In addition to the experiments with FA and 2,4-D, preliminary tests were conducted with raw drinking water containing natural organic matter (NOM) to determine the ability of the composite spheres to degrade NOM. Total organic carbon analyzer (Shimatzu, TOC - V_{CPH}) were used to monitored the change in

concentration with respect to time. Same as above, these experiments were run at 27°C and ambient pressure.

The optimum amount of catalyst to be loaded on the photocatalytic reactor was experimentally determined monitoring the apparent rate constant of FA with respect to time for a given bed expansion. The optimum mass of catalyst was chosen based on the highest degradation rate constant.

The photocatalytic reactor was placed inside a wooded box to avoid any direct contact with UV light and to be able to change the level of irradiation applied to the reactor by changing the position of the UV lamps (Figure 4.7). The photoreactor was fed from a storage tank (Figure 4.8) that was equipped with a porous diffuser, sparging air through the solution in order to maintain relatively constant dissolved oxygen needed for the reaction. The recycling flow rate was relatively high (3.4 L min^{-1}), and the bed expansion of the TiO_2 photocatalyst was approximately 500%.

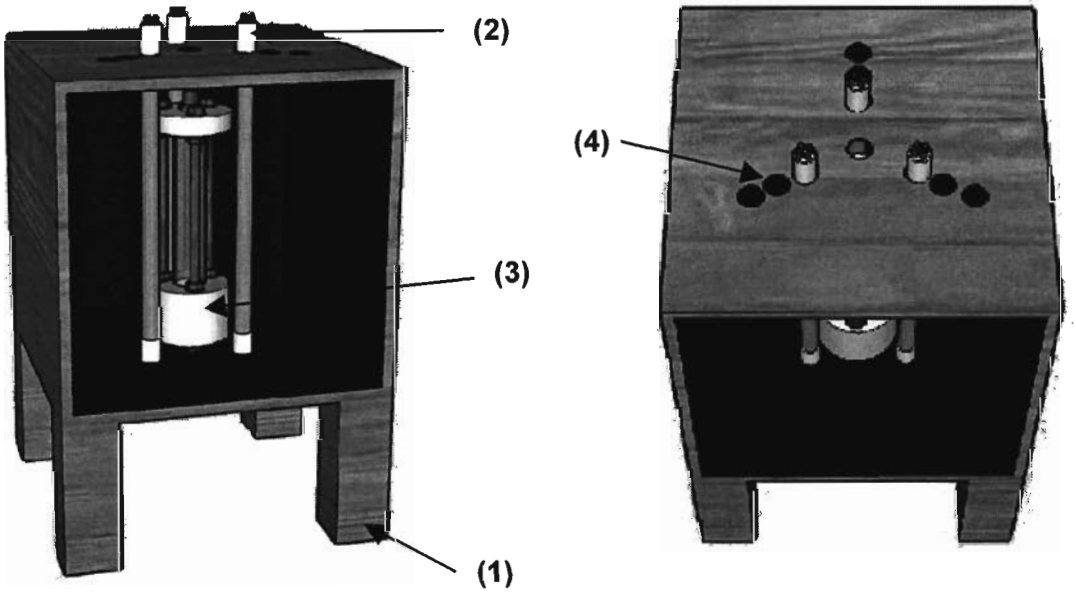

Figure 4.7: Experimental setup: (1) wooden box, (2) UV lamps, (3) fluidized bed photocatalytic reactor (FBPR), (4) different lamp positions.

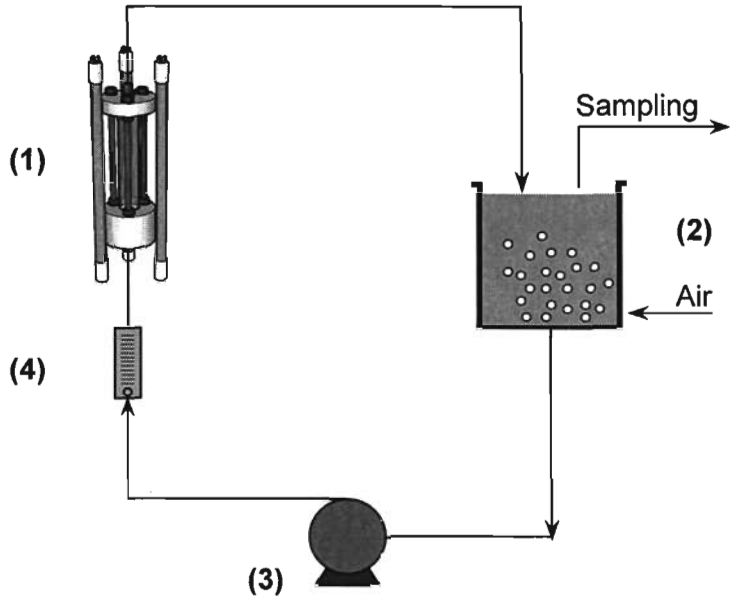

Figure 4.8: Experimental setup: (1) fluidized bed photocatalytic reactor (FBPR), (2) tank, (3) pump, (4) Flowmeter.

As mentioned before, in all of the experiments carried out in this investigation, the High Performance Liquid Chromatography (HPLC) and the Total Organic Carbon analyzer (TOC) were used. Therefore, a brief explanation of these two equipments is necessary to have a brief background about them.

4.5.1 High Performance Liquid Chromatography analysis (HPLC)

HPLC is a widely used analysis to separate, identify and quantify compounds because of the multiple advantages such as high precision and low volume of samples.

In this investigation, a Water HPLC Instrument (WATERS 2695), equipped with a Symmetry C-18 column (4-μm particle diameter) was used for the purpose of analyzing FA and 2,4-D. This equipment has degasser chamber to degas the mobile phase in the system, reducing the amount of dissolved air from the mobile phase and preventing air bubbles and consequent drift or other baseline irregularities. The mobile phase changed depending on the organic pollutant that was analyzed. Other

variables such as column temperature, flow rate, among others change also depending of the nature of the pollutant as is going to be explained later.

4.5.2 Total Organic Carbon Analysis (TOC)

TOC analysis has been recognized as non-specific analytical technique to measure the water quality during the water purification process, because it represents the amount of carbon bound in an organic compound. Typically, when the TOC is measured, the total carbon and the inorganic carbon are measured at the same time. Then, subtracting the inorganic carbon from the total carbon yields the TOC.

For this particular work, samples of 25 mL were analyzed in a Shimadzu TOC-VCPH combustion oxidation TOC analyzer. This equipment employs combustion oxidation at 680°C to improve the detection regardless the type of organic matter. Calibration curve of two points using Milli-Q water and a standard solution of Benzoic Acid was used.

4.5.3 Organic pollutants degradation

Two different organic pollutants were used to determine the photoactivity of the composite TiO_2 spheres. Formic Acid (FA) and 2,4-Dichlorophenoacetic acid (2,4-D) were selected.

As a general procedure, catalyst washing was needed to eliminate any small particles of TiO_2 adhered to the surface of the catalyst spheres and to remove any contamination on the surface of the catalyst. At the same time washing helped clean the system itself. One L of milli-Q water was used to wash the catalyst for 60 min. This water was changed in the first 30 min.

4.5.3.1 Formic acid (FA) degradation

Formic acid was selected as a model pollutant because it is oxidized directly to CO_2 without the formation of any stable intermediate products and because it has

been used extensively in other photocatalytic studies (Ha and Anderson, 1996; Kim and Anderson, 1996; Muggli and Backes, 2002; McMurray *et al.*, 2004; Krysa, 2006).

After the washing process, 1 L of water was re-circulated through the reactor for 15 min, with the UV lamps. This ensured that the UV lamps were warm and reached their maximum output prior to the start of the experiment. After this time, a concentrated FA solution (10 g L^{-1}) was added to the water, the amount of this solution determined the initial FA concentration in the system.

The concentrations of FA were quantified using the HPLC with Acetonitrile / water (40:60% v/v) as the mobile phase. The flow rate of mobile phase for the analysis was kept at 1mL min^{-1} using λ=214 nm for UV detention. The temperature of the column was kept at 25°C during the detection. Reagent grade standard was used to calibrate the HPLC for the model organic compound.

4.5.3.2 Micro-pollutant degradation (2,4 Dichlorophenoxyacetic acid)

2,4-Dichlorophenoxyacetic acid (2,4-D) is the third most commonly used herbicide in the United States and Canada. Worldwide, 2,4-D and different salts derivatives and ester forms are used in a variety of places including home lawns, cereal and grain crops, commercial areas, commercial turf, rights-of-way, and forest (Trillas *et al.*, 1995). This widespread use of 2,4-D leads to certain environmental impact due to the fact that during its application it could be easily spread within the environment. Once on the ground, it can be incorporated in the natural aqueous stream showing different half-lifes, depending on factors such as oxygen concentration, acidity, solar light, among others (EPA, 2008).

Therefore, evaluating the photocatalytic activity of composite TiO_2 spheres using 2,4-D as a micro-pollutant is important for real large scale applications. Prior to these experiments, an adsorption study was done to determine the amount of 2,4-D that is being adsorbed in the TiO_2 spheres.

After the initial washing of the photocatalyst (as discussed above), 500 mL of 2,4-D solution, at different initial concentrations (1 - 10 mg L^{-1}), was re-circulated through the reactor with the UV Lamps off. This process was allowed for approximately 1 h, ensuring that the adsorption of the 2,4-D on the catalyst reached

equilibrium. Immediately after that, the UV lamps were turned on for about 1 h. Samples were collected at different intervals and the concentrations of 2,4-D and its photodegradation by-products were quantified using HPLC with methanol / water / glacial acetic acid (58:40:2% v/v) as a mobile phase. The flow rate of mobile phase for analysis was kept at 1.23 mL min^{-1} using λ=280 nm for UV detention. The temperature of the column was kept at 35°C during the detection. Reagent grade standards were used to calibrate the HPLC for the parent contaminant and its oxidation by-products.

4.5.4 Natural Organic Matter (NOM) degradation

Natural organic matter (NOM) is defined as a complex mixture of organic compounds present in surface water, with a composition that changes with respect to season and location (Bursill *et al.*, 2002). Therefore, testing TiO_2 spheres with NOM will give us a good understanding about the photocatalytic effect of CSG titania in complex mixture of compounds.

Water from Trepanier Creek in the Peachland area in central British Columbia (with the initial TOC of approximately 5 mg L^{-1}) was treated in the fluidized bed reactor using 25 g of titania photocatalyst spheres. The photodegradation study was performed running 1 L of raw water through the FBPR for 1 h. Prior to these experiments, an adsorption study was done to determine the amount of NOM that is being adsorbed in the TiO_2 spheres At each intervals, 25 mL of water sample was collected and analyzed by the TOC

4.6 Attrition resistance determination

Photocatalyst attrition was determined by measuring and monitoring the amount TiO_2 in the solution. A spectrophotometric technique was adopted and used for this purpose (Jackson, 1883; Jackson *et al.*, 1991). The list of chemicals required to perform this analysis is provided in Table 4.3.

Table 4.3: Specifications of chemicals used for the attrition resistant of the composite TiO_2 spheres.

Chemicals	Chemical formula	Purity	Supplier
Ammonium Sulfate	$(NH_4)_2SO_4$	100%	Fisher Scientific
Sulfuric acid	H_2SO_4	98%	Fisher Scientific
Hydrogen Peroxide	H_2O_2	30%	Fisher Scientific

In this technique, 10 mL of the solution after the photocatalytic treatment (containing TiO_2 in suspension) and 10 mL of solution of ammonium sulfate, $(NH_4)_2SO_4$ in sulfuric acid, H_2SO_4, (3 M) was heated up to approximately 100°C in a porcelain dish for approximately 10 min to produce an homogeneous solution. This solution was then transferred to a 25 mL volumetric flask which was filled to exactly 25 mL with 6 mL of H_2O and with a H_2SO_4 solution in water (1.1 M). Three drops of hydrogen peroxide, H_2O_2, were added to the sample to produce a yellow-orange colored complex ions ($TiO_2 \cdot H_2O_2$) (Eisenberg, 1943; Charlot, 1964; Marczenko, 1986):

$$Ti^{4+} + H_2O_2 + 2H_2O \Leftrightarrow TiO_2 \cdot H_2O_2 + 4H^+ \quad (4.5)$$

The amount of Ti^{4+} present in the solution was determined using a spectrophotometer (Shimadzu 1240) at λ = 410 nm.

4.7 Photocatalyst deactivation and attrition evolution

For the FA, 2,4-D and NOM, some tests were performed to determine and quantify photocatalyst deactivation. In each case, the same photocatalyst samples were used for several consecutive runs to determine if there was a change in the activity of the catalyst with respect o the degradation of each contaminant. A change in the photocatalytic degradation for any of those compounds was considered as and indicator for photocatalyst deactivation.

4.8 Fluence rate determination

As discussed before, a photocatalyst is activated by light that is provided to generate the electron and holes (e^- - h^+) pairs. Therefore, identifing the amount of light or irradiation supplied to the reactor is required to understand thoroughly the phenomena behind the photocatalysis process.

The fluence rate is defined as the energy provided by the UV lamps per unit time per illuminated area of the reactor (J s^{-1} m^{-2}). For the purpose of this research, the irradiation flux to the photoreactor was measured using two different methods: potassium ferrioxalate and iodite-iodate actinometry techniques. The chemicals required for carrying out these measurements, with both actinometric solutions, are listed in Table 4.4.

In the case of potassium ferrioxalate, the photochemical reaction that describes the chemical change in the actinometer is given by Equation 4.6. As can be seen, the Fe^{3+} is converted to Fe^{2+} in the presence of UV irradiation (Zalazar *et al.*, 2005):

$$2Fe^{3+} + C_2O_4^{2-} \xrightarrow{h\nu} 2Fe^{2+} + 2CO_2 \qquad (4.6)$$

Table 4.4: Specifications of chemicals used for the fluence rate determination.

Chemicals	Chemical formula	Purity	Supplier
Sodium Acetate anhydrous	$C_2H_3O_2Na$	----	Sigma Aldrich
Sulfuric acid	H_2SO_4	98%	Fisher Scientific
Iron (III) Sulfate pentahydrate	$Fe_2O_{12}S_3 \cdot 5H_2O$	97%	Acros Organics
Potassium oxalate monohydrate	$K_2C_2O_4 \cdot H_2O$	----	Sigma Aldrich
1,10 Phenantroline	$C_{12}H_8N_2$	99%	Acros Organics
Potassium Iodate	KIO_3	100%	Fisher Scientific
Potassium Iodide	KI	99%	Fisher Scientific

The potassium ferrioxalate method involved a solution of ($Fe_2(SO_4)_3$) (98.02 g $Fe_2O_{12}S_3 \cdot 5H_2O$ + 55 mL of H_2SO_4 made up to 1 L) that was prepared from the hydrate compound. Then, the actinometry solution was prepared mixing 50 mL of iron sulfate solution with 50 mL of potassium oxalate ($K_2C_2O_4$) (1.2 M) solution. This new solution was diluted with water up to 1 L.

Prior to each experiment, UV lamps were warmed up for 15 min to reach stable radiation. Then, the actinometry solution was pumped through the system shown in Figure 4.8. Different lamp positions were used to measure the irradiation reaching the reactor. In every case, 2 mL of sample was taken. Each sample was mixed with 8 mL of phenantroline (0.2 % w/w), 1 mL of buffer solution (49.43 g $C_2H_3O_2Na$ + 10 mL of H_2SO_4 made up to 1 L) and 9 mL of water. This final solution was left under dark conditions for 30 min. Finally, the amount of ferrous ions produced was measured via spectrophotometric measurement of the concentration of complex formed with 1,10 phenantroline ($[(C_{12}H_8N_2)_3Fe]^{2+}$) at λ = 510 nm.

The fluence rate was proportional to the absorbance measured at 510 nm (Parker, 1953) and was calculated as follows:

$$H_{PF} = \frac{7.8478 \cdot Abs \cdot V_{irrad} \cdot V_{dil}}{\varepsilon \cdot \phi \cdot t \cdot V_{samp} \cdot Area} \tag{4.7}$$

where H_{PF} is in mW cm^{-2}, V_{irrad} is the irradiated volume in mL, V_{dil} is the volume of the dilution in mL, ε is the molar extinction coefficient (1.11 x 10^4 L gmol^{-1} cm^{-1}), ϕ is the quantum yield (~1.48 according with Golsdtein and Rabani (2008)), t is the irradiation time in min and V_{samp} is the volume of the sample taken for analysis in mL. The *Area* is the irradiated area of the reactor (127 cm^2)

In the case of the Iodite-Iodate actinometry, the reaction that describes the process is the following (Rahn *et al.*, 2003):

$$8KI + KIO_3 + 3H_2O + h\nu \rightarrow 3I_3^- + 6OH^- + 9K^+ \tag{4.8}$$

According to this reaction, the triiodide could be determined spectrophotometrically at λ = 450 nm. A 0.01 M solution of sodium borate buffer was required to prepare 0.1 M solution of potassium iodate in the borate buffer. Finally, 0.6 M of potassium iodide was needed to be prepared in borate-iodate solution. Additional details that was followed could be obtained elsewhere (Rahn, 1997; Rahn *et al.*, 2003; Rahn *et al.*, 2006).

Finally, the quantum yield was determined using Equation 4.8:

$$\phi = 0.75\left[1 + 0.02\left(T - 20.7\right)\right]\left[1 + 0.23\left(C - 0.577\right)\right] \tag{4.9}$$

where the quantum yield (ϕ) is given in mol einstein^{-1} and T is the temperature of the solution in °C and C is the molar concentration of the iodide solution. Then, the fluence rate was calculated as follows:

$$H_{II} = \frac{4.72x10^{5} \cdot \Delta A_{450} \cdot V \cdot 1000}{\varepsilon_{450} \cdot \phi \cdot Area \cdot t} \tag{4.10}$$

where H_{II} is the fluence in mW cm^{-2}, ΔA_{450} is the change in the absorbance at λ = 450 nm, V is the solution volume in L, ε_{450} is the molar absorption coefficient of triodide at λ = 450 nm (M^{-1} cm^{-1}), ϕ is quantum yield calculated with Equation 4.9, *Area* is the irradiated area (127 cm^{2}) and *t* is the time of sampling in s.

Chapter Five

Preliminary Evaluation of Composite TiO_2 Photocatalyst

5.1 Introduction

The photocatalytic activity of a photocatalyst is one of the most important parameters in photocatalyst development. High activity is always desirable because it translates into better photodegradation of pollutants in contaminated water. Another important parameter to evaluate, in the case of FBPR, is the mechanical strength of the particles because it will ensure good durability and stability of the catalyst. Therefore, this section describes the preliminary evaluation of the photocatalyst activity, using Formic acid (FA) as a model organic compound, and the attrition resistance of the CSG TiO_2 spheres as a reference and benchmark for additional improvement.

Preliminary characterization of the original composite photocatalyst was performed using BET method to measure the surface area of the catalyst, X-ray diffraction (XRD) to identify the polymorphic phases present in the TiO_2 spheres, and scanning electron microscopy (SEM) to identify the microstructural characteristics of the catalyst.

5.2 Composite TiO_2 photocatalyst activity

In order to evaluate the activity of the catalyst, photocatalytic degradation of Formic Acid (FA) was investigated. FA was selected as a model pollutant because it is oxidized directly to CO_2 and H_2O without the formation of any stable intermediate products (McMurray *et al.*, 2004). As was described in Section 4.5, HPLC was used to analyze the change in FA concentration with respect to the reaction time.

As part of this preliminary evaluation, spheres calcined at different temperatures were used, mainly because it is well known that the calcination temperature plays a critical role defining the crystalline phases, the surface area and most importantly, the activity of the photocatalyst (So *et al.* 1997; Pozzo *et al.*, 2000; Yin *et al.*, 2001; Su *et al.*, 2004; Qiu and Zheng, 2007). In general, it is expected that the activity of the photocatalyst will decrease with an increment in the calcination temperature because the surface area will decrease, and the anatase will be converted to rutile. Therefore, calcination temperatures between 600ºC and 1300ºC were studied to ensure that a wide range of temperatures were covered and its impact was studied thoroughly.

It is also known that physical characteristics of the spheres, such as size and density, changed with the calcination temperature. Therefore, to have a constant height of the expanded bed in the FBPR (to have a similar light distribution in the system), certain parameters such as flow rate and mass of catalyst should be adjusted for spheres produced under different temperatures. The height of the bed is an important characteristic of the FBPR that needs to be maintained constant from one test to another, in order to allow comparison between the experiments. Inconsistent bed's heights may lead to different photon distributions, flow behaviour, and mass transfer within the reactor. Hence, prior to any photocatalytic experiments a thorough assessment of the bed expansion was performed as discussed in the following section.

5.2.1 Bed expansion estimation

The bed expansion of the composite TiO_2 spheres within the reactor was calculated based on the terminal velocity (v_t) and bed voidage (ε) of the TiO_2 spheres. In this approach, the fluidization velocity (U) can be calculated with Equation 5.1 where Q is the volumetric flow rate and $R_{reactor}$ is the radius of the quartz tube (0.012 m).

$$U = \frac{Q}{\pi (R_{reactor})^2} \tag{5.1}$$

The v_t is calculated using a correlation proposed by Haider and Levenspield (1989) (Equation 5.2) were d^* is the dimensionless particle diameter, ρ_{H2O} and ρ_{sph} are the density of the water (1000 kg m^{-3}) and the spheres respectively; μ_{H2O} is the viscosity of the water (0.001 kg m^{-1} s^{-1}), r_{sph} is the radius of the spheres, and g is the gravitational force.

$$v_t = \left(\frac{{\rho_{H_2O}}^2}{g(\rho_{sph} - \rho_{H_2O})\mu_{H_2O}} \right)^{-\frac{1}{3}} \left(\frac{18}{d^{*2}} + \frac{0.5909}{\sqrt{d^*}} \right)^{-1} \tag{5.2}$$

$$d^* = 2r_{sph} \left(\frac{g(\rho_{sph} - \rho_{H_2O})\rho_{H_2O}}{{\mu_{H2O}}^2} \right)^{\frac{1}{3}} \tag{5.3}$$

The terminal velocity of isolated single particles, v_e, is calculated by Equation 5.4 (Khan and Richardson, 1987). The bed voidage, ε, is predicted using Equation 5.5 which is the correlation given by Richardson and Zaki (1954). The exponent e is known as the expansion index and can be calculated by Equation 5.6.

$$\frac{v_e}{v_t} = 1 - 1.15 \left(\frac{r_{sph}}{R_{reactor}} \right)^{0.6} \tag{5.4}$$

$$\frac{U}{v_e} = \varepsilon^e \tag{5.5}$$

$$\frac{4.8 - e}{e - 2.4} = 0.043(Ar)^{0.57} \tag{5.6}$$

where Ar is known as the Archimedes number, defined by

$$Ar = \left(\frac{8g\left(\rho_{sph} - \rho_{H_2O}\right)\rho_{H_2O} r_{sph}^{\ 3}}{\mu_{H_2O}^{\ 2}} \right) \tag{5.7}$$

With the bed voidage for the catalyst, it is possible to predict the expansion of the bed in the reactor using Equation 5.8. The value of ε_0 is calculated based on the physical characteristics of the catalyst and it is estimated to be equal to 0.39 for the spheres calcined at 600°C and 0.37 for the spheres calcined at 900°C (Benenati and Brosilow, 1962; Mueller, 1997):

$$B_{\exp} = \frac{1-\varepsilon_0}{1-\varepsilon} \tag{5.8}$$

The height of the static bed in the reactor, $H_{bed,0}$, and the bed height (H_{bed}) corresponding to a given bed expansion can be evaluated applying Equations 5.9 and 5.10 (Imoberdorf *et al.*, 2008):

$$H_{bed,0} = \frac{m_{sph}}{\pi\rho_{sph}\left(1-\varepsilon_0\right)R_{reactor}^{\ 2}} \tag{5.9}$$

$$H_{bed} = H_{bed,0} B_{\exp} \tag{5.10}$$

As shown in Equation 5.9, the mass of catalyst is an important parameter for defining the expansion of the bed. In addition, the amount of catalyst influences the efficiency of the system to degrade contaminants, mainly because the light distribution in the reactor might change with the amount of catalyst loaded in the reactor. Therefore, the optimum mass of catalyst that should be loaded in the reactor (for a given catalyst characteristics such as size and density) needs to be determined.

Spheres at 600°C were selected as a baseline because it was expected that they would show higher activity. Table 5.1 shows different masses of catalyst calcined at 600°C and the flow rates required to obtain a fairly constant height of the

expanded bed (the bed was expanded up to approximately 93% of the 15 cm height of the quartz tube). As can be seen, the greater the amount of catalyst, the lower the volumetric flow rate for a constant height of the bed.

Table 5.1: Data to calculate the height of the expanded bed in the fluidized bed photocatalytic reactor (FBPR) of spheres at 600°C (r_{sph} = 5.75 x 10^{-4} m; ρ_{sph} = 3109 kg m^{-3})

Mass of Catalyst loaded in the FBPR (kg)	Volumetric flow rate (m^3 s^{-1})
0.015	6.5 x 10^{-5}
0.025	5.7 x 10^{-5}
0.035	4.8 x 10^{-5}
0.040	4.5 x 10^{-5}

Figure 5.1 shows the dependence of the FA degradation on the photocatalyst loadings in the reactor using spheres calcined at 600°C. The voidage of the bed for all the cases is also specified. At catalyst loading of above 25 g, the reaction rate constant was approximately constant for FA degradation considering a relatively constant height of the expanded bed ($H_{bed} \approx$ 14cm). In addition, the change in the rate constant between 25 g and 35 or 40 g was almost negligible, but the difference in the amount of spheres loaded in the reactor was very significant. Therefore, 25 g was used as the loading used for all the experiments in this study, giving a bed expansion of 500% with respect to the height of the static bed (~2.8 cm)

It is important to mention that increasing the amount of catalyst in the reactor, the light penetration might change within the reactor. Therefore, the light distribution might be different for different catalyst loadings. Even though this could affect the FA degradation, this effect was not considered because this analysis was done as a preliminary test of the system with composite TiO_2 spheres.

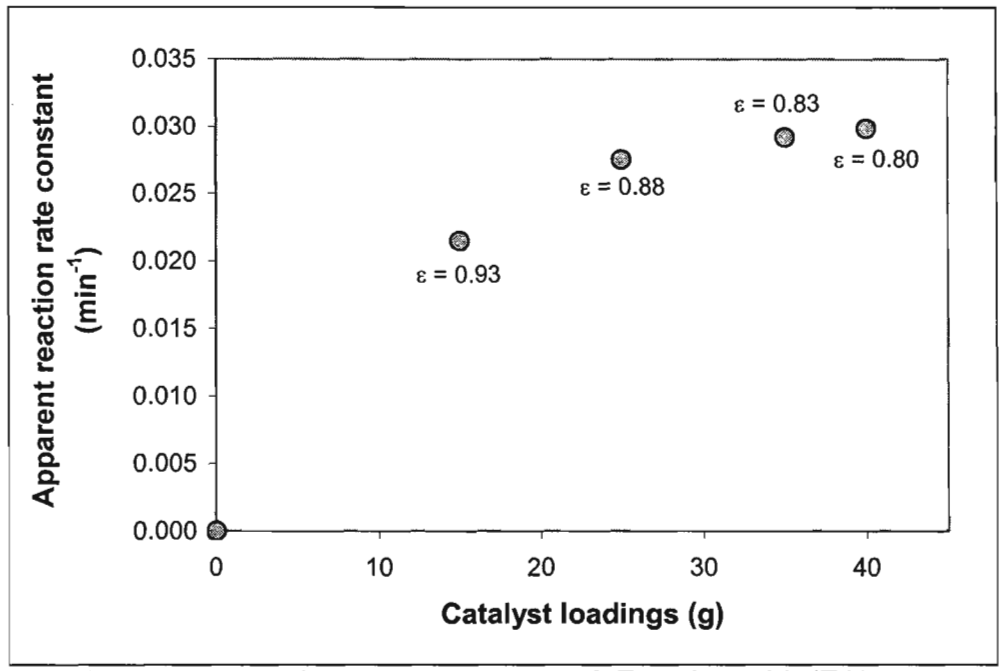

Figure 5.1: Apparent reaction rate constant of Formic acid (FA) versus catalyst loadings in the FBPR using spheres calcined at 600°C (ε = voidage of the bed)

5.2.2 Photocatalyst activity at different calcination temperatures

To compare the activity of spheres calcined at different temperatures, the same mass of spheres determined with spheres at 600°C (25 g) was used for the other spheres (calcined at different temperatures) and the flow rate was adjusted as is detailed in Table 5.2 to have a similar height of the expanded bed ($H_{bed} \approx$ 14cm) in all cases. This criterion was followed just for the preliminary comparative studies, even though it was recognized that changing either the mass of the catalyst or the flow rate in the system would change the dynamic of the system.

As expected, spheres at 600°C showed the highest activity to degrade FA. Figure 5.2 shows the effect of the calcination temperature on the FA degradation using the TiO_2 spheres. First order degradation reaction was determined for the cases at 600°C, 700°C and 800°C. As is shown, there is a strong relation between the heat treatment and the activity of the catalyst. For the catalyst calcined at 900°C or higher temperatures, there was no or little FA degradation after three hours of operation. On the other hand, for the catalyst calcined at 600°C the FA degradation was completed after 3 h. Table 5.3 shows the rate constants for the experiments

presented in Figure 5.2. To calculate this rate constant, the apparent rate constant was normalized multiplying it by the ratio of the total volume (1000 mL) to the active volume (80 mL) according with the approach followed by Turchi and Wolfrum (1992). The rate constant was the highest at 0.315 min^{-1} for the catalyst calcined at 600°C, but it decreased with increasing temperature. At 800°C, for example, the rate constant decreased by 92%. These results can be explained from the point of view that higher calcination temperatures induce higher amount of rutile in the catalyst and lower surface area.

Table 5.2: Data to determine the activity of spheres at different calcination temperatures (m_{sph} = 0.025 kg)

Parameter	Nomenclature	Value at different temperatures			
		600°C	700°C	800°C	900°C
Volumetric flow rate ($m^3\ s^{-1}$)	Q	5.7×10^{-5}	7.3×10^{-5}	7.8×10^{-5}	8.0×10^{-5}
Density of spheres ($kg\ m^{-3}$)	ρ_{sph}	3109	4020	4399	4527
Radius of spheres (m)	r_{sph}	5.75×10^{-4}	5.59×10^{-4}	5.25×10^{-4}	4.65×10^{-4}

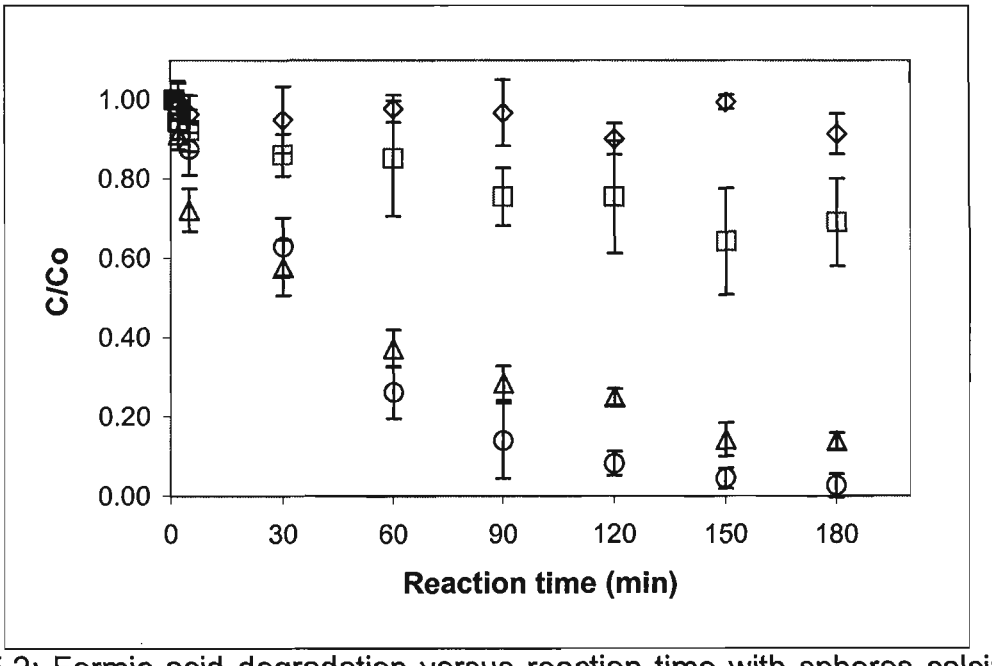

Figure 5.2: Formic acid degradation versus reaction time with spheres calcined at: (◊) 900°C, (□) 800°C, (Δ) 700°C, (o) 600°C; error bars represent 95% CI of the triplicate runs)

The calcination temperature had an impact on the spheres ability to degrade organic compound (in this case FA) because it defined characteristics such as the surface area, pore size, pore volume and the amount of anatase in the catalyst (Section 5.4).

Table 5.3: FA photodegradation rate constants (k_r) of composite TiO_2 spheres produced at different calcination temperatures (mass of catalyst loaded to the reactor equal to 0.025 kg)

Calcination temperature (°C)	Degradation rate constant (min^{-1})	Standard error of the parameter
600	0.315	0.061
700	0.164	0.008
800	0.025	0.013
900	N/A	N/A

5.2.3 Mass transfer resistance calculations

In a heterogeneous reaction sequence, mass transfer of reactants first takes place from the bulk to the external surface of the catalyst. Occurrence and completion of the photocatalytic reaction is then followed by the mass transfer of the products from the catalyst surface to the solution. Hence, mass transfers of the reactants and products significantly affect and sometime hinder the overall reaction rates.

In fluidized bed reactors, it is well known that the mass transfer resistance is negligible. Nonetheless, calculations were done to confirm that the reaction rate was not limited by mass transfer. In that regards, the catalyst-liquid mass transfer coefficient was calculated using mass transfer correlations proposed in the literature (Tournié *et al.*, 1979; Arters and Fan, 1984; Prakash *et al.*, 1987) and the Sherwood number (*Sh*):

$$Sh = \frac{k_{MT} d_{sph}}{D_{FA-W}} \tag{5.11}$$

$$Sh = 0.228\phi^{1.35} Ga^{0.323} M_v^{0.3} Sc^{0.4} \quad (5.12)$$

where *Ga* is the Galileo number, M_v is the density number, *Sc* is the Schmidt number, ϕ_s is the sphericity (in this case considered equal to 1), k_{MT} is the mass transfer coefficient and $D_{FA\text{-}W}$ is the diffusive coefficient for FA in water. These three dimensionless numbers can be calculated by:

$$Ga = \frac{d_{sph}^{3} \rho_{H_2O} g}{\mu_{H_2O}} \quad (5.13)$$

$$M_v = \frac{\rho_{sph} - \rho_{H_2O}}{\rho_{H_2O}} \quad (5.14)$$

$$Sc = \frac{\mu_{H_2O}}{\rho_{H_2O} D_{FA-W}} \quad (5.15)$$

Using some of the data listed in Table 5.2 for the spheres at 600ºC and the diffusivity of FA in water equal to 1.45 x 10^{-9} m^2 s^{-1} (Perry and Green, 1997), Equations 5.13 to 5.15 could be solved. Thus, the mass transfer coefficient was calculated, using Equation 5.11, to 1.09 x10^{-4} m s^{-1}.

To compare the mass transfer coefficient with the reaction rate constant (k_r) at 600ºC (0.315 min^{-1}), Equation 5.16 was applied:

$$k_r' = \frac{k_r}{a} \quad (5.16)$$

Where k_r' is the reaction rate constant expressed in m s^{-1} and a is the external surface to volume ratio of the catalyst particle and it can be calculated by:

$$a = \frac{4\pi r_{sph}^{\ 2}}{\frac{4}{3}\pi r_{sph}^{\ 3}} = \frac{3}{r_{sph}} \tag{5.17}$$

Knowing a, the value of k_r' was calculated to be 1.01 x 10^{-6} m s^{-1}, which can be compared with the mass transfer coefficient using a criterion similar to that developed by Mears (1971). In this approach, the reaction rate constant needs to be:

$$\frac{k_r C_{FA} r_{sph}}{k_{MT} C_{FA}} \leq \frac{0.15}{i} \tag{5.18}$$

where i is the integer exponent in power law rate expression. In the case of this work i was equal to 1 because the degradation followed first order kinetics. Simplifying Equation 5.18, gives:

$$\frac{k_r'}{k_{MT}} \leq 0.05 \tag{5.19}$$

According to Equation 5.19, the reaction rate constant should be smaller than 5% of the mass transfer coefficient in order to neglect mass transfer resistance. With the values of k_r' and k_{MT} being 1.01 x 10^{-6} m s^{-1} and 1.09 x10^{-4} m s^{-1}, respectively, it is concluded that mass transfer resistance was negligible in the system used in this investigation.

5.3 Attrition determination

The motion of particles in a fluidized bed reactor usually causes catalyst attrition due to the collision between particles and bed-to-wall impacts (Vaisman *et al.*, 2005; Qiu and Zheng, 2007). One of the main consequences of attrition in any system, and particularly in water treatment processes, is the loss of catalyst and generation of fines that are difficult to separate downstream.

Figure 5.3 shows the amount of TiO_2 detached into water after 3 h of operation for catalyst produced at different calcination temperatures. As expected, the resistance of the catalyst improves when the calcination temperature increases because the structure of the spheres becomes harder and more compact. At 600°C, the amount of TiO_2 in suspension after 3 h of continuous operation was approximately 22 mg L^{-1}; while at 800°C this value dropped to nearly 8 mg L^{-1}.

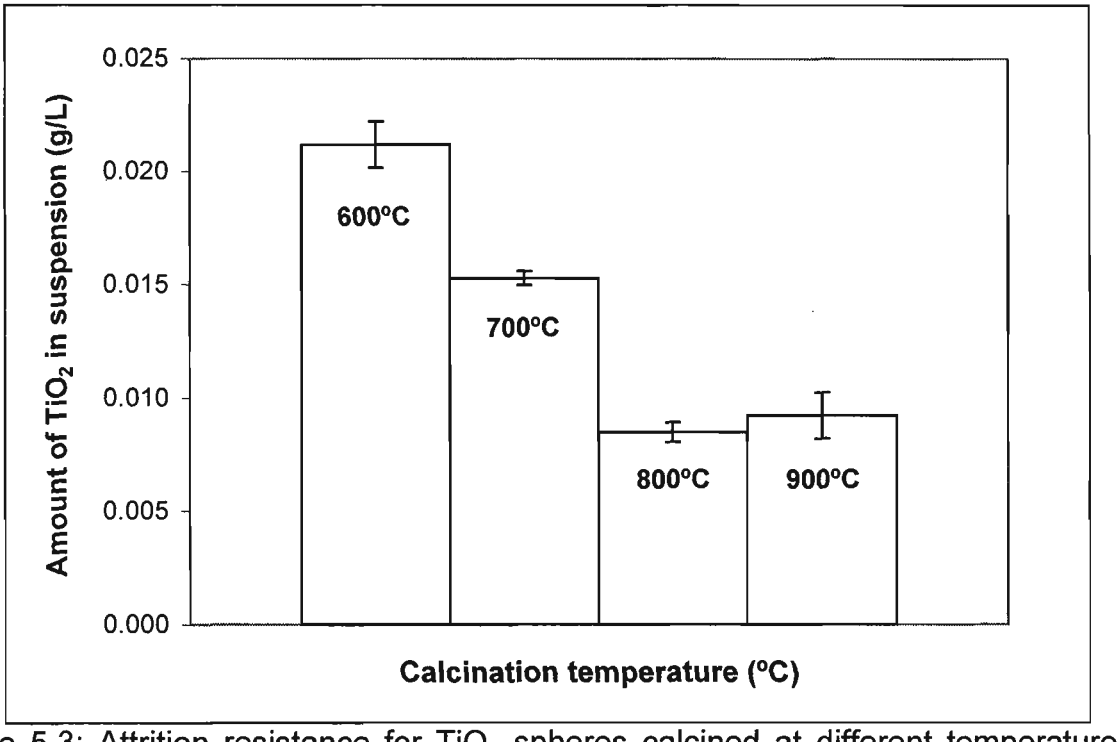

Figure 5.3: Attrition resistance for TiO_2 spheres calcined at different temperatures (Error bars represent 95% CI of triplicate runs)

5.4 Composite photocatalyst characterization

Microstructure of the produced TiO_2 spheres was analyzed by using SEM. Images of the composite TiO_2 spheres calcined at 600°C and 900°C are shown in Figure 5.4. As it can be seen, there are no significant differences between these two batches. The spheres at 700°C and 800°C showed similar characteristics as well.

In all the cases, the TiO_2 spheres had a relatively smooth surface despite the presence of some roughness along the surface of the catalyst. No cracks were found

after heat treatment confirming that there were not extreme stresses during the catalyst production process. Grooves around the equator of the sphere as well as the crater shown in Figure 5.4a, 5.4c & 5.4d are the result of the production process.

Spheres calcined at 600°C had an average diameter of 1.17 mm. At higher calcination temperature, e.g. 900°C, the average diameter was reduced to 0.930 mm. In either case, the catalyst particles showed consistency in size and shape.

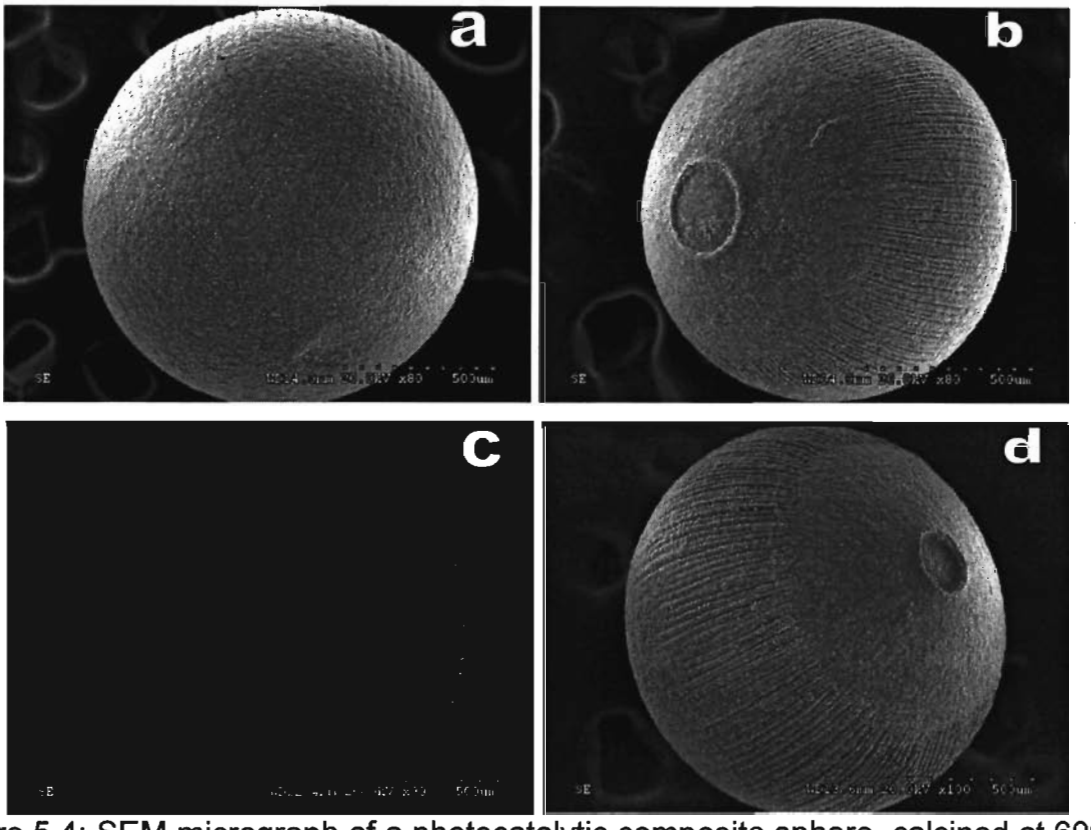

Figure 5.4: SEM micrograph of a photocatalytic composite sphere, calcined at 600°C (a and b) and calcined at 900°C (c and d)

As briefly discussed before, the calcination temperature played a significant role in the activity of the catalyst. It defined many of the photocatalyst characteristics, e.g., the surface area, pore volume, pore size, percentage of anatase, among others. From Table 5.4 it is clear that the higher the temperature, the smaller the surface area and the pore volume, but the higher the pore size. The percentage of anatase in the catalyst also changed with calcination temperature; the amount of

anatase was reduced significantly when the calcination temperature increased from 600ºC to 700ºC (from approximately 72% to 1.9%). At higher temperatures there was no anatase in the catalyst.

Table 5.4: Surface area and anatase composition (using BET and XRD respectively) of the composite TiO_2 spheres calcined at different temperatures.

Calcination temperature (°C)	Anatase (%)	Surface area ($m^2\ g^{-1}$)	Pore size (nm)	Pore volume ($cm^3\ g^{-1}$)
600	72.23	36.93	22.03	0.2577
700	1.86	6.58	30.43	0.0995
800	0	3.79	42.73	0.0425
900	0	N/A	N/A	N/A

Figure 5.5 shows the X-ray diffraction patterns of TiO_2 spheres, at different calcination temperatures. When the spheres were calcined at 600°C, there was a broad peak at $2\theta = 30°$, which is identified as the most intensive peak (1 0 1) for anatase. Another characteristic peak was found at $2\theta = 32°$ which represents the rutile (1 1 0) phase. The peak intensity of anatase (1 0 1) decreased dramatically and the peak intensity of rutile (1 1 0) increased significantly when the calcination temperature increased from 600°C to 700°C. This demonstrates that increasing the temperature of heat treatment accelerated phase transformation from thermodynamically metastable anatase to more stable and more condense rutile phase (So *et al.* 1997).

BET was used for the surface area, pore size distribution and pore volume analyses of the composite TiO_2 spheres at different calcination temperatures. As shown in Table 5.4, a strong dependence was observed for the surface area, pore size and pore volume to the calcination temperature of the composite TiO_2 spheres. The specific surface area and pore volume shifted towards smaller values at higher calcination temperatures, but the average pore diameters increased upon heat treatment, which is consistent with the literature (Bischoff and Anderson, 1995; Xu *et al.*, 2008). The reduction in surface area with the calcination temperature was

significant. At 700°C the specific surface area decreased to 6.58 $m^2 g^{-1}$ and the pore volume reduced almost by 60% with respect to the value reported when the catalyst was calcined at 600°C (36.93 $m^2 g^{-1}$). Although a large portion of the mesoporous structure was maintained at 700°C (Figure 5.7), the pore volume was reduced significantly, likely because higher calcination temperatures induce crystallization of TiO_2, followed by crystal growth, and collapse of the pores (Peng *et al.*, 2005).

The isotherms and pore size distributions of the composite TiO_2 spheres, calcined at different temperatures, are shown in Figures 5.6 and 5.7. It is clear that spheres calcined at 600°C have higher surface area than those calcined at higher temperatures. According to the BDDT (Brunauer, Deming, Deming and Teller) classification, the spheres showed isotherm type IV, exhibiting H2 hysteresis loops. This result indicates that the composite photocatalyst porosity is in the meso - range (2~50nm) (Sink *et al.*, 1985).

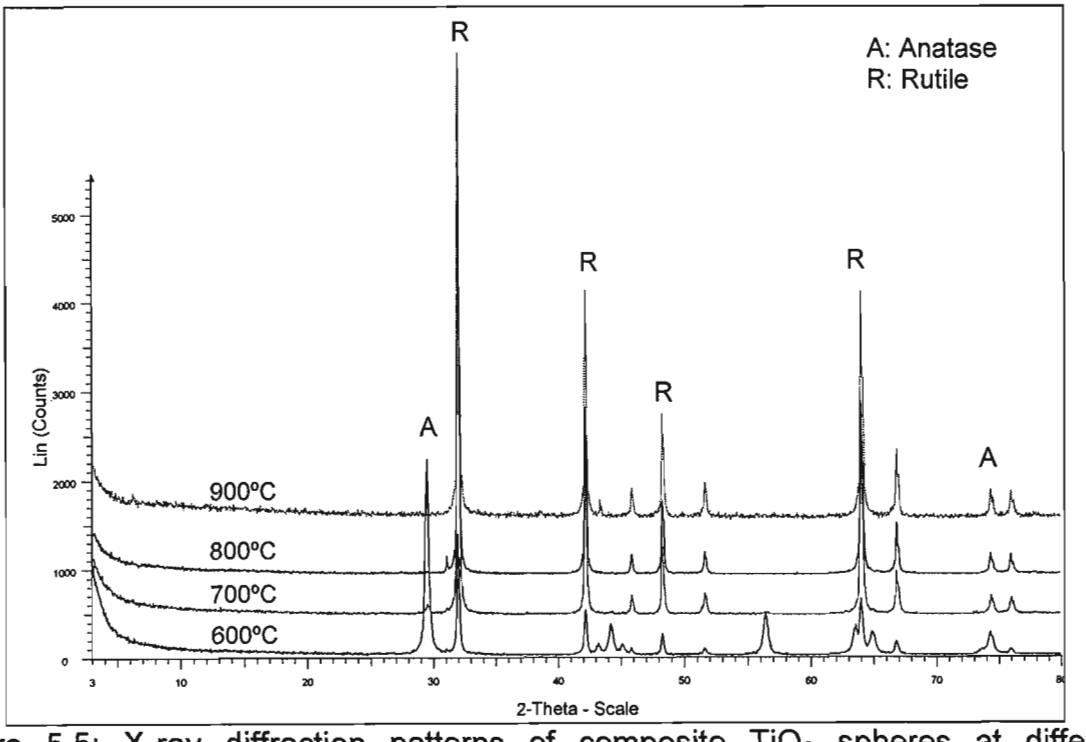

Figure 5.5: X-ray diffraction patterns of composite TiO_2 spheres at different temperatures.

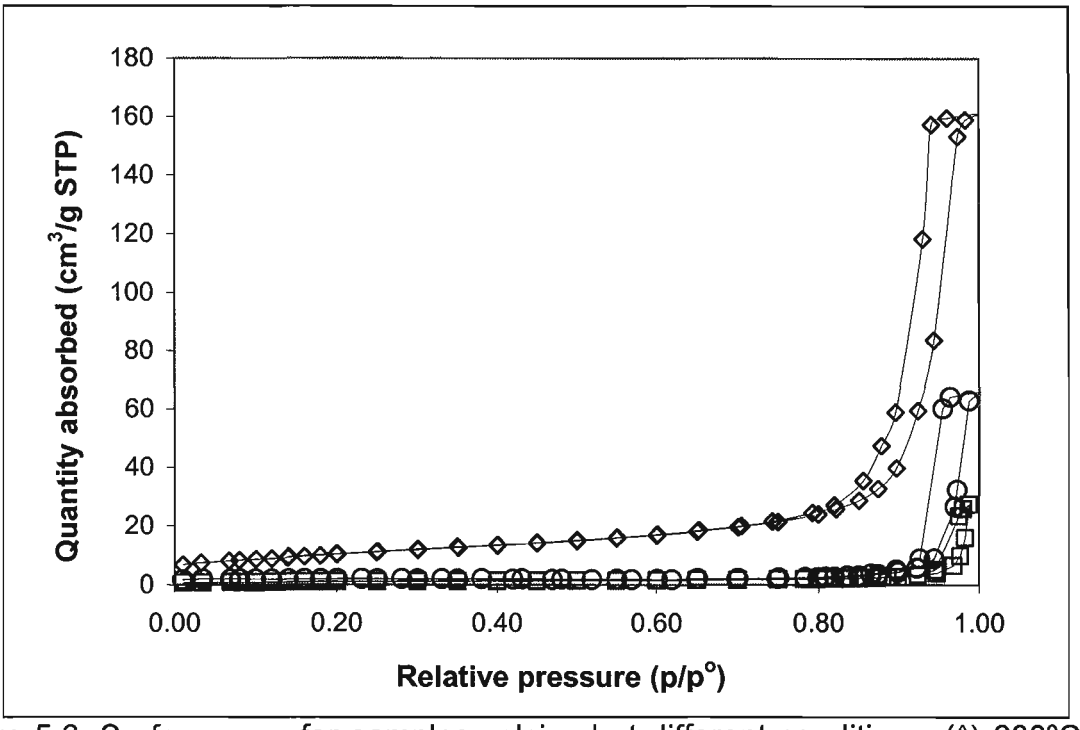

Figure 5.6: Surface area for samples calcined at different conditions, (◊) 600°C, (o) 700°C, (□) 800°C.

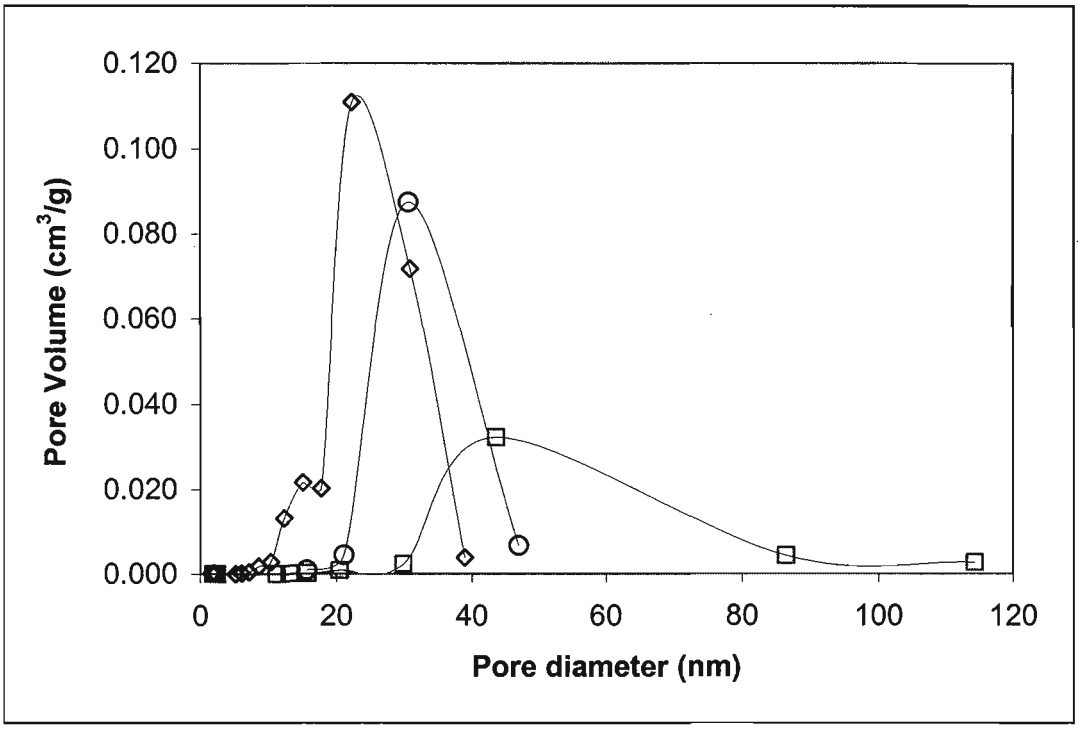

Figure 5.7: Pore size distribution for samples calcined at different temperatures, (◊) 600°C, (o) 700°C, (□) 800°C

5.5 Final remarks

Based on the results presented in this section, 25 g of TiO_2 spheres calcined at 600ºC was selected as a practical loading for the fluidized bed reactor experiments carried out in the rest of the research. This calcination temperature was selected for further study because the activity of the catalyst prepared at this temperature was superior.

At 600ºC, the percentage of anatase (72%) and the surface area (~37 m^2 g) of the TiO_2 spheres were higher than those of the other samples, which can explain the difference in activity. High percentages of anatase and high surface area have been reported as desirable characteristics that lead to more efficient photocatalyst with greater degradation of contaminants (Berry and Mueller, 1994; Thiruvenkatachari *et al.*, 2008).

In terms of attrition resistance of the catalyst, it has been demonstrated that the higher the calcination temperature, the higher the resistance of the catalyst. However, when the temperature increases, the activity drops significantly. At 600°C, the attrition in the system was determined to be 22 mg L^{-1} of TiO_2 particles in suspension while at 800°C this value dropped to nearly 8 mg L^{-1}. However, the degradation rate constant dropped from 0.315 ± 0.061 min^{-1} at 600°C to 0.025 ± 0.013 min^{-1} at 800°C. Hence, it was decided to use 600°C as the appropriate calcination temperature, but to perform further optimization on different variables that lead to improve attrition resistance.

Chapter Six

Photocatalyst Improvement and Characterization

6.1 Introduction

Attrition of the catalyst particles within a photoreactor is a key challenge requiring attention. Catalyst attrition in a system will induce low photoefficiency of the system and process complications such as downstream filtration and separation of the suspended particles, with the subsequent increment in cost.

This chapter describes the results of the work performed to improve the attrition resistance of the composite TiO_2 spheres. Variables such as the rate of hydrolysis and condensation during the sol-gel processing, the spheres formation process, and drying and heat treatment conditions were studied. At the same time, the activity of the spheres to degrade formic acid (FA) was determined. Photocatalyst characterization was performed using BET method to measure the surface area of the spheres, X-ray diffraction (XRD) to identify the polymorphic phases present in the TiO_2 spheres, and scanning electron microscopy (SEM) to identify the microstructural characteristics of the catalyst.

6.2 Compositional study of the TiO_2 spheres formulation

The preparation of the composite TiO_2 spheres involves a series of variables that affect not only the chemical composition of the spheres, but also their physical characteristics, such as the size and shape of the catalyst. Table 6.1 shows some of the variables involved during the preparation process of the composite TiO_2 spheres. These are variables that may influence the chemical composition of the sol-gel, the shape of the spheres and their production process.

Table 6.1: Variables involved during the production process of the composite TiO_2 spheres.

Variable – Composite TiO_2 production	**Effect / Purpose of the variable**
Amount of Alcohol	Solvent
Amount of water	Induce hydrolysis reactions
Amount and type of catalyst	Control hydrolysis and polycondensation reactions
Amount of TTIP	Precursor of Titanium
Stirring time	Homogenize the solution
Mass Degussa P-25	Filler material
Chitosan solution characteristics	Helps with the spheres formation and aging
pH of the Ammonia solution	Helps with the spheres formation
Size of the droppers used to produce the spheres	Size of the TiO_2 spheres
Height of the droppers	Shape of the spheres
Volume of solution in the droppers	Production of the spheres (define shape of the spheres)
Drying conditions (temperature and time)	Define the characteristics of the xerogel
Heat treatment conditions (temperature and time)	Densification of the spheres

Despite many variables involved in the process, only some have direct and significant impact on the attrition resistance of the catalyst. For example, the sol-gel matrix properties, as well as the drying and heat treatment conditions could have important contributions to the properties of the spheres. Particularly, the hydrolysis and condensation reactions that take place during the sol-gel process may influence the attrition resistance of the catalyst since the condensation reactions are responsible of the network construction (bonds between particles) along the gel. In general, hydrolysis and condensation occur simultaneously once the hydrolysis reaction has been initiated. Many factors that can influence these two processes include the amount of water added, the nature and concentration of the catalyst, the

solvent used and the sequence of mixing (Hench and West, 1990; Nazeri *et al.*, 1993; Wen and Wilkes, 1996). These condensation reactions continue through the drying stage. Therefore, the drying conditions of the spheres should be adequate to promote these reactions to continue. Finally, the heat treatment is necessary to densify the gel and produce a body dense enough to give the spheres strength.

Preliminary tests with these and other variables were done to determine their effects on the attrition resistance and the activity of the catalyst. The activity was monitored using FA as a model organic compound.

6.2.1 Preliminary tests and effects of various parameters

The photocatalyst had originally been developed in the Advance Oxidation Research Laboratory at the Department of Chemical and Biological Engineering at UBC. Nonetheless, the original development did not focus on the attrition resistance of the catalyst. Therefore, experiments were performed modifying the original formulation of the spheres to determine the impact of some of the variables involved during the production process of the catalyst. The response variables for this study were the level of attrition after 3 h of continuous use in the reaction system, shown in Figure 4.8, and the photocatalytic activity of the spheres to degrade FA. In all the cases, 25 g of catalyst were used.

Among all the variables listed in Table 6.1, the following were selected for this stage of the investigation: i) amount of water used to prepare the sol; ii) type and concentration of the catalyst for sol preparation; iii) amount of filler material (Degussa P-25) used to produce the CSG; iv) pH of the chitosan solution and its concentration; and v) drying and heat treatment conditions.

As pointed out before, it was believed that the characteristics of the sol (and eventually of the gel) have an impact on the attrition resistance of the catalyst. This is because the hydrolysis and condensation reactions that take place during the whole process are responsible for the network formed during gelation. Thus, the proper amount of water and catalyst are key factors to investigate. At the same time, the chitosan solution could play an important role in the spheres characteristics since

it is used as a binder during the spheres formation. In addition, chitosan solution is responsible for the hardening process of the spheres once they are produced. The drying process and the heat treatment are needed to remove the liquid that is trapped inside the spheres and to densify the photocatalyst.

Table 6.2 lists the range of variables explored in this stage of the research. For each experiment, only the indicated variable was changed while all the other variables were kept constant, according to the original formulation of the catalyst. The main focus was to determine if the variable has an impact on the response variables.

Table 6.2: Range of the variables to be studied during the preliminary tests with the composite TiO_2.

Experiment	Variable	Original Formulation	Range of study
1	Amount of water (g H_20 mL^{-1} TTIP)	0.040	0.053 - 0.070
2	Type of the catalyst	HCl	----
3	Amount of catalyst (mL mL^{-1} TTIP)	0.20	0.10 - 0.13
4	Amount of filler (g P-25 mL^{-1} TTIP)	0.40	0.30 - 0.50
5	pH of the Chitosan solution (adim)	4.94	4.01 - 4.58
6	Concentration of Chitosan in the polymeric solution (g L^{-1})	10	15
7	Drying conditions	15 days - 23°C	20 h - 80°C
8	Calcination time (h)	1	3

6.2.1.1 Type of catalyst used during the sol-gel preparation

As mentioned above, the type of catalyst could affect the properties of the gel. Hence, different acid catalysts were tested to determine the effect on hydrolysis and condensation reactions. Phosphoric acid (H_3PO_4), acetic acid (CH_3COOH) and nitric acid (HNO_3) were used in the same ratio as HCl (0.20 mL mL^{-1} TTIP), which was used as the catalyst in the original formulation of the spheres, as shown in Table 6.2. Detailed studies on the impact of the catalyst, performed by Brinker and Scherer (1990), Livage (1998) and Hench and West (1990) for different sols, e.g. silica sols, showed that the catalyst used during the process has a clear impact on the gelation time, syneresis and the change of the isoelectric point (IEP).

In this research, the use of H_3PO_4 significantly increased the viscosity of the solution producing some clusters when the solution was in contact with titanium (IV) isopropoxide (TTIP). With CH_3COOH, the clusters were formed when the CSG was mixed with the chitosan solution. In both cases, the spheres were not produced because of the rapid increase in the viscosity of the solution. Using HNO_3, on the other hand, no significant changes were observed with respect to the original formulation because the characteristics of HCl and HNO_3 are similar, e.g., pKa. In this case, the spheres were formed and the attrition was measured showing a value of 20 mg L^{-1} which represents no change with respect to the original formulation (Figure 6.1).

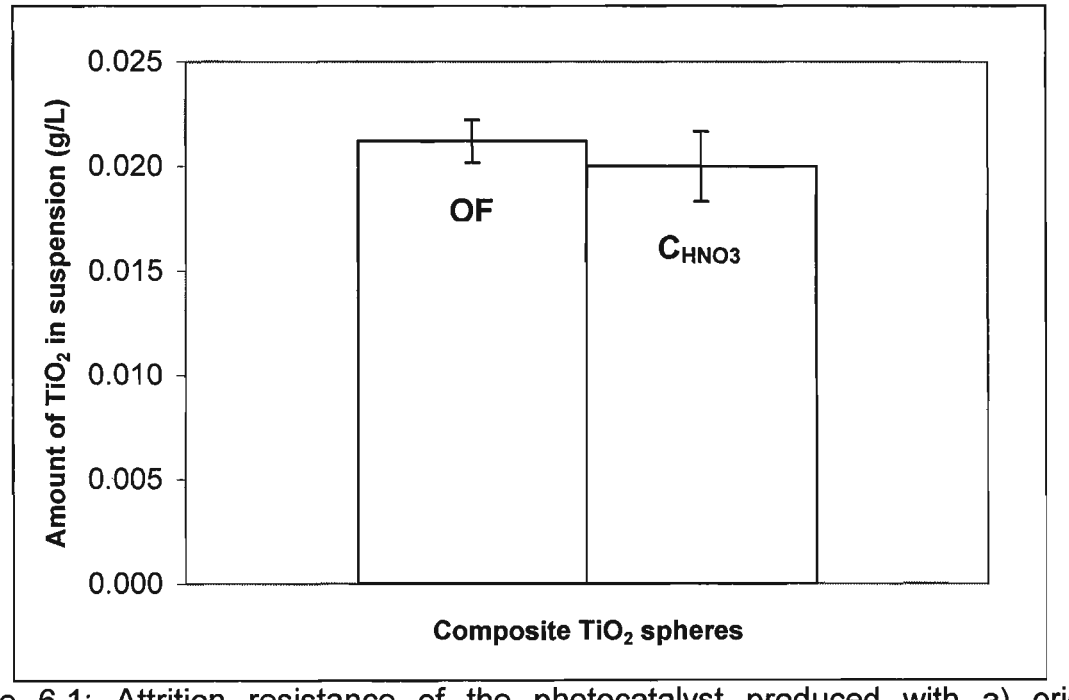

Figure 6.1: Attrition resistance of the photocatalyst produced with a) original formulation (OF); b) using HNO_3 as a catalyst instead of HCl (C_{HNO3}). Error bars represent 95% CI of triplicate runs.

The results with HNO_3 are consistent with theory, as it is well known that more acidic conditions strongly delay condensation processes. Thus, it could be expected that a weaker acid would lead to faster condensation reactions, resulting in

a different gelation time. In other words, it is expected that the higher the pH, the smaller the gelation time (Livage *et al.*, 1988; Brinker and Scherer, 1990). When no acid is added, the result is not a gel but a precipitate. Based on the results obtained here, and because HNO_3 did not give significant improvements, HCl was kept as the catalyst for this application.

6.2.1.2 Water and catalyst (HCl) concentration

Water is one of the key reagents during sol-gel processing. It is partially responsible for the hydrolysis reactions that take place during the sol-gel formation. At the same time, the structure of the final gel depends on the contribution of the hydrolysis and condensation reactions, which define the structure and morphology of the resulting oxide. Hence, the characteristics of the final product depend on the relative contribution of these two reactions.

With water content and acid concentration being very important, their impact on the attrition resistance of the catalyst was investigated. First, the effect of increasing the amount of water in the system was investigated by changing the water content from 0.040 g H_2O per mL TTIP to 0.053 g H_2O per mL TTIP and 0.070 g H_2O per mL TTIP. When 0.070 g H_2O per mL TTIP was used, the viscosity of the solution increased and a lot of clusters were formed in the reaction media. Therefore the spheres could not be produced at this concentration of water. On the other hand, the effect of acid was studied by reducing its concentration from 0.20 mL HCl to 0.13 mL HCl and 0.10 mL HCl per mL TTIP. With 0.10 mL HCl per mL TTIP, immediately after the addition of TTIP, clusters were formed and the spheres could not be produced.

Figure 6.2 shows the effect of using 0.053 g H_2O per mL TTIP in one formulation and 0.13 mL HCl per mL TTIP in another formulation. As shown, there was around 32% reduction in attrition (i.e., the amount of TiO_2 particles released in the water) for each of the abovementioned conditions. Even though there could be an interaction between these two variables, only the individual contribution to the

attrition resistance is shown in Figure 6.2. The interaction between these two variables will be discussed later.

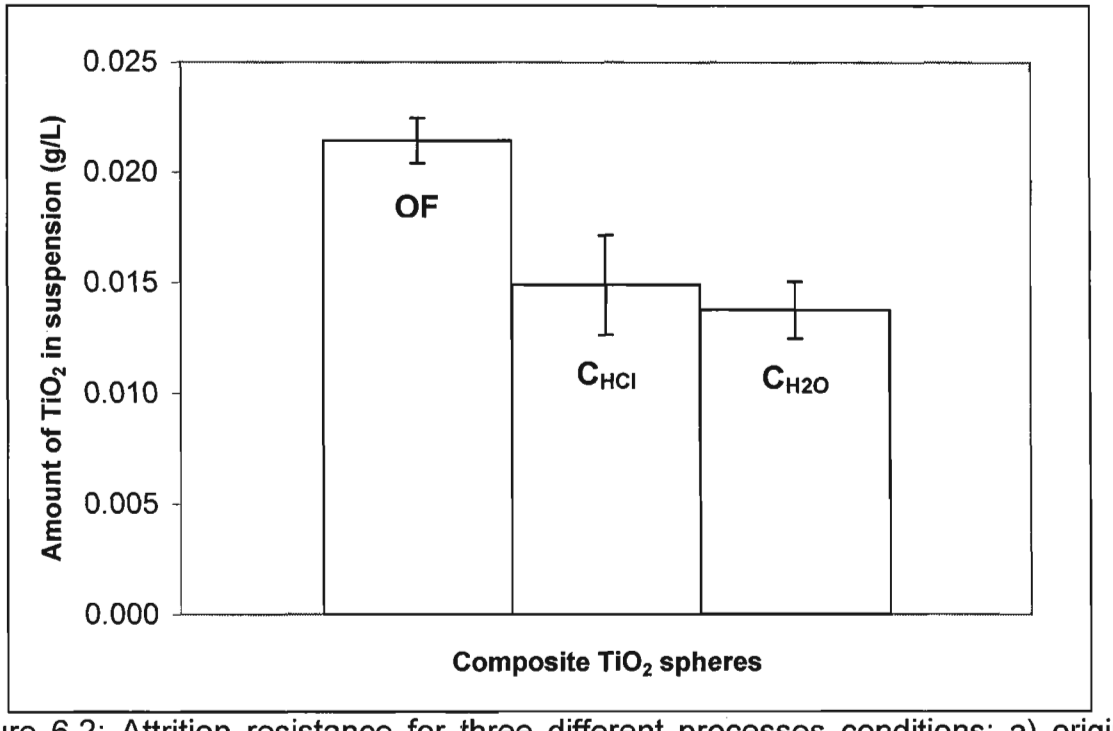

Figure 6.2: Attrition resistance for three different processes conditions; a) original formulation (OF); b) increased amount of water (C_{H2O}) in the sol-gel matrix; c) reduced the amount of HCl (C_{HCl}) in the sol-gel matrix. Error bars represent 95% CI of triplicate runs.

The viscosity of the sol-gel changed with respect to the amount of water and acid added. With 0.053 g H_2O per mL TTIP the viscosity at 25°C was 5.55 cP (compared with the 4.83 cP of the sol-gel used for the OF). On the other hand, when the amount of acid was 0.13 mL HCl per mL TTIP the viscosity was 5.39 cP. As expected, the viscosity in both cases increased compared to that in the OF, an indication that the hydrolysis and condensation reactions were promoted by adding more water and less acid.

6.2.1.3 Amount of filler material (Degussa P-25)

Commercial TiO_2 (Degussa P-25) was dispersed in the sol as filler to fabricate composite high performance sol-gel materials. P-25 was chosen because of its demonstrated high photoefficiency to degrade organic pollutants (Porter *et al.*, 1999; Araña *et al.*, 2009). Figure 6.3 shows the effect of the amount of Degussa P-25. It is shown that reducing the amount of P-25 from 0.40 g P-25 per mL TTIP to 0.30 g P-25 per mL TTIP led to slightly lower attrition. The amount of TiO_2 particles released to the solution was reduced by about 9%. On the other hand, increasing the amount of P-25 added (i.e., 0.40 g P-25 to 0.50 g P-25 per mL TTIP) showed similar level of attrition compared to the original formulation.

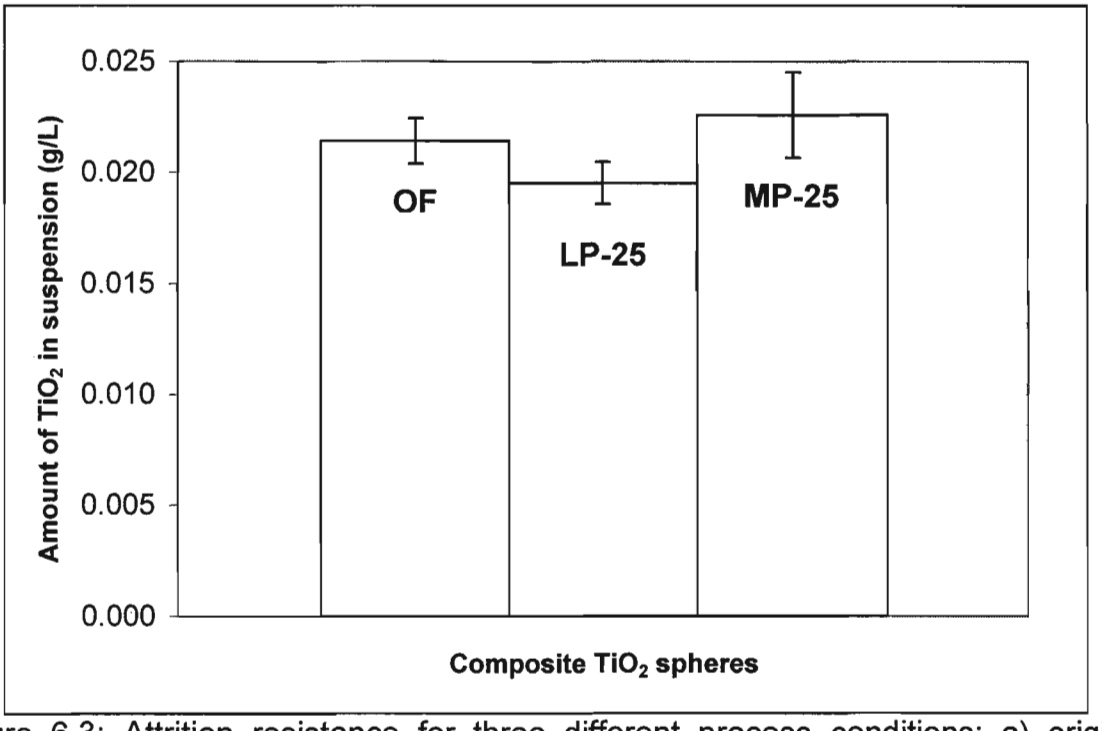

Figure 6.3: Attrition resistance for three different process conditions; a) original formulation (OF); b) using 0.30 g P-25 mL^{-1} TTIP (LP-25); c) using 0.50 g P-25 mL^{-1} TTIP (MP-25). Error bars represent 95% CI of triplicate runs.

These results showed that the amount of filler material did not have a significant impact on the attrition of the composite TiO_2 spheres. However, some

impacts would be observed on the production process of the spheres. With the amount of Degussa P-25 reduced significantly, the viscosity of the solution changes as well. Therefore, lower amounts of P-25 could result in a solution that has low viscosity, making it difficult to produce the spheres. On the contrary, higher amounts of P-25 would increase the viscosity of the CSG and the process to produce the spheres would take longer than that of the OF.

6.2.1.4 pH of the chitosan solution

The polymeric matrix (chitosan solution) was used in this application because it has a certain viscosity needed for the formation of spheres and also for the fast hardening property that chitosan has upon contact with basic solution. As discussed earlier, chitosan is soluble in dilute acids. Therefore, for this application glacial acetic acid was used to acidify the water and propitiate the solution of the polymer. Then, by modifying the amount of acid added to the water, the pH of the final solution could be adjusted.

Figure 6.4 shows the effect of the pH of the chitosan solution on the attrition resistance of the spheres. Reducing the pH to 4.58 (the original pH was 4.94) induced a reduction in the level of attrition in the system. After 3 h of continuous operation, approximately 14 mg L^{-1} of TiO_2 was measured in the solution, representing a 32% reduction compared to that in the original formulation (OF). With further reduction of the pH to 4.01, no additional improvement was observed, but the viscosity of the TiO_2-chitosan solution increased significantly.

These results suggest that decreasing the pH of the chitosan solution resulted in a lower pH for the polymeric matrix-TiO_2 CSG solution inducing a harder structure when it came in contact with the ammonia solution. The difference between the pH of the chitosan-TiO_2 CSG solution and the ammonia solution helped to increase the strength of TiO_2 spheres, producing a harder three-dimensional structure. The reports from literature suggested that chitosan shows chemical high cross-linked gels when it is in contact with Glutaraldehyde and that the gelation of this chitosan chains depends on parameters such as pH, chitosan concentration,

ionic strength, etc. (Arguelles-Monal *et al.*, 1998). It is believed that the degree of gelation of chitosan in ammonia solution depends on the pH difference between these two solutions, making stronger structure when the difference increases. It is important to note that more acidic condition in the chitosan solution could also retard the condensation reactions of the TiO_2 CSG material.

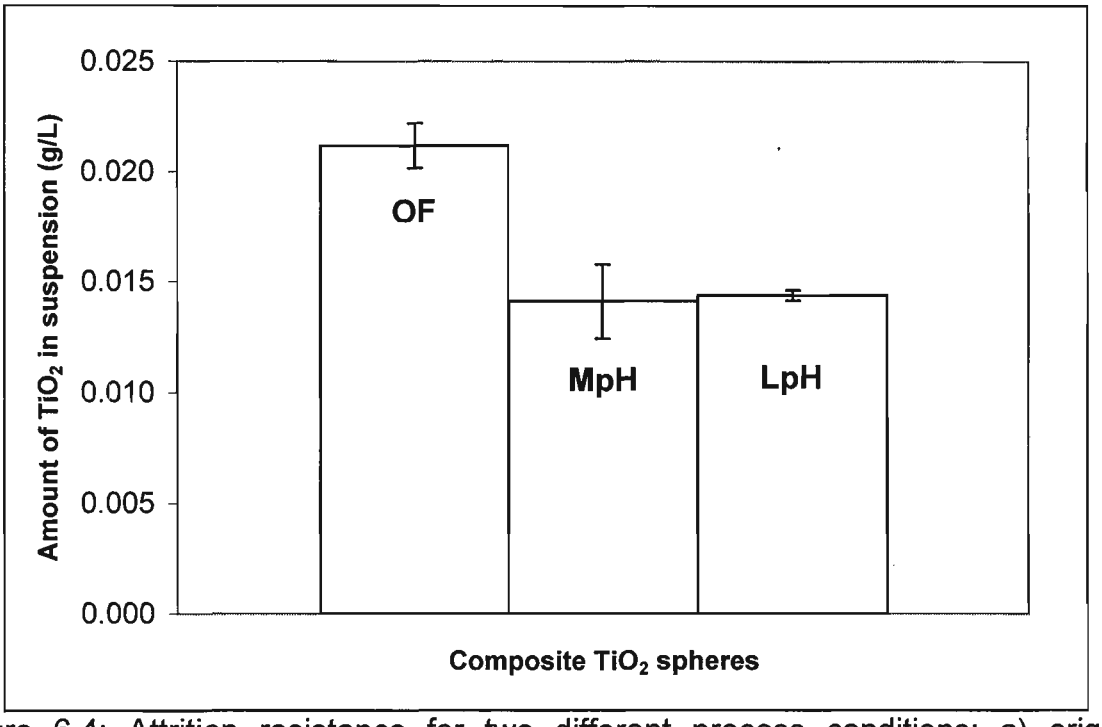

Figure 6.4: Attrition resistance for two different process conditions; a) original formulation (OF); b) when the pH of the chitosan solution was 4.58 (MpH); c) when the pH of the chitosan solution was 4.01 (LpH). Error bars represent 95% CI of triplicate runs.

6.2.1.5 Concentration of chitosan in the polymeric solution

The main purpose of chitosan in this application was to propitiate the necessary conditions to form the spheres. The effect of chitosan concentration on the attrition resistance of the catalyst is shown in Figure 6.5. In general, increasing the concentration of chitosan to 15 g L^{-1} (in the original formulation the concentration of chitosan was 10 g L^{-1}) induced a reduction in the attrition by 38% compared to that in the original formulation. With this increment in the chitosan concentration, the

viscosity of the solution increased from 135 cP to 206 cP (measured at 25ºC) and the pH of the solution increased to 5.52. As mentioned before, condensation reactions continued to happen during the aging, drying and heat treatment stages. It is expected that less acidic conditions in the chitosan–TiO_2 CSG solution (based on the increment in pH of the chitosan solution) might promote those reactions to continue and to do so even faster. As mentioned in Chapter 2, condensation reactions are responsible to build bridges between chains; hence, this change in acidic conditions of the chitosan–TiO_2 CSG solution might be the cause of a strong structure in the spheres showing a reduction in the amount of TiO_2 particles in suspension.

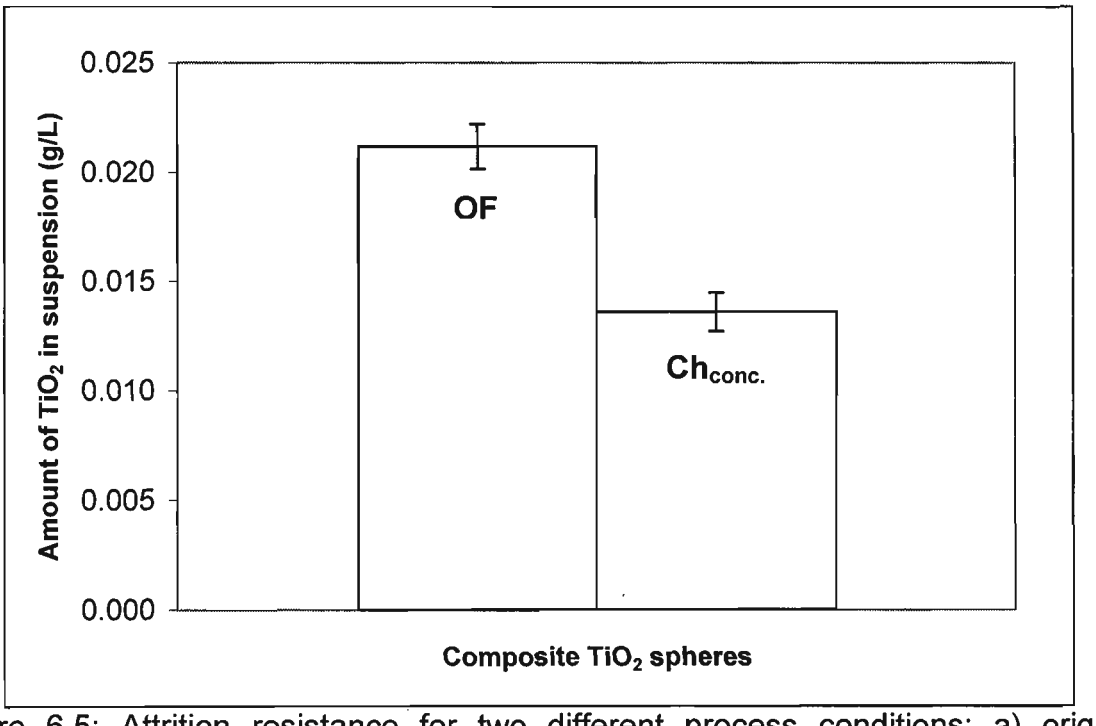

Figure 6.5: Attrition resistance for two different process conditions; a) original formulation (OF); b) when the chitosan solution had a concentration of 15 g chitosan L^{-1} (Ch_{conc}). Error bars represent 95% CI of triplicate runs.

As mentioned before, chitosan is used in this application due to the fast hardening property that it has upon contact with basic solution. Therefore, increasing the concentration of chitosan in solution, might lead to a harder structure in the

spheres. Nonetheless, it is important to mention that increasing the concentration of chitosan also increases the viscosity of the polymer-CSG solution. If the viscosity of this solution increases by a significant degree, the production process of the spheres will be more difficult and take longer time because the solution flows slowly.

6.2.1.6 Drying process of the spheres

The fresh spheres contain significant amount of liquid (alcohol, water, ammonia solution, etc.) that must be removed from the structure. That is, the gel must be dried before the appropriate heat treatment is applied. As the drying process proceeds, the network formed during the gelation process becomes stiffer because of the formation of new bonds due to condensation reactions (Rahaman, 2007). Thus, an accelerated drying process increases the solid network matrix which has an impact on the mechanical strength of TiO_2 spheres. However, if the drying process is too aggressive, cracks can be induced in the body of the gel.

The relation between the drying process and the attrition resistance can be observed on Figure 6.6. As can be seen, when the drying process was done at 80°C for 20 h, instead of 15 days at room temperature (RT - 23°C), the amount of TiO_2 particles in suspension was reduced. When the temperature of the furnace was increased to 600°C for 1h immediately after the drying process, the amount of TiO_2 in suspension dropped further to 11 mg L^{-1} from around 22 mg L^{-1} in the OF ($D_{cont.}$). However, when the catalyst was first cooled down to RT and then placed in the furnace for 1h at 600°C, the amount of TiO_2 in suspension was 15 mg L^{-1} (D_{cool}). This effect could be explained in terms of the polycondensation reactions that take place during the drying and heat treatment. If the temperature of the catalyst is decreased after the drying process, many of those reactions would slow or stop and the solid network will not be as compact as the case where such reactions continue with immediate heat treatment after drying.

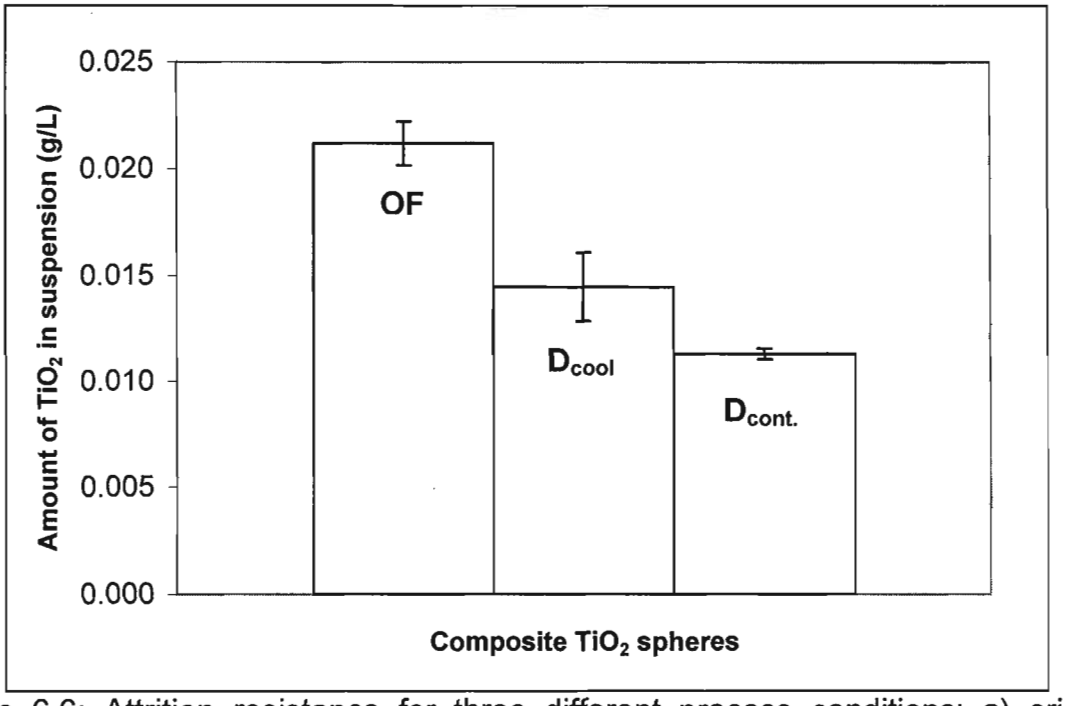

Figure 6.6: Attrition resistance for three different process conditions; a) original formulation (OF); b) catalyst dried for 20 h at 80°C, cooled down, and then placed in the furnance at 600°C for 1 h (D_{cool}); b) catalyst dried in the furnace at 80°C for 20 h, followed by immediate temperature increase to 600°C for 1 h ($D_{cont.}$). Error bars represent 95% CI for triplicate runs.

6.2.1.7 Heat treatment conditions

The main purpose of heat treatment is to densify the gel and produce a strong body. The relation between heat treatment and the attrition resistance of TiO_2 spheres has already been demonstrated in section 5.3 (Figure 5.3). An increase in the calcination temperature of the spheres reduced the attrition, i.e., the amount of particles released from the catalyst to the water. Nonetheless, the activity is reduced by increasing the heat treatment temperature (Figure 5.2 in Section 5.2.2).

Another important factor affecting photocatalyst attrition is the length (or time) of heat treatment. Figure 6.7 shows the effect of increasing the calcination time from 1 h to 3 h at 600°C. As shown, the amount of TiO_2 in suspension drops to 13 mg L^{-1} from around 22 mg L^{-1} in the OF. The effect of these two conditions (time and temperature) can be explained based on the impact that higher temperatures and/or longer exposure to a given temperature induce tighter solid network that will resist

better the attrition effect. The higher the temperature and/or the longer the calcination time, the denser the spheres would be, which means the solid network is tighter and more compact. Therefore, the strength of the composite TiO_2 spheres increases, improving the attrition resistance of the photocatalyst.

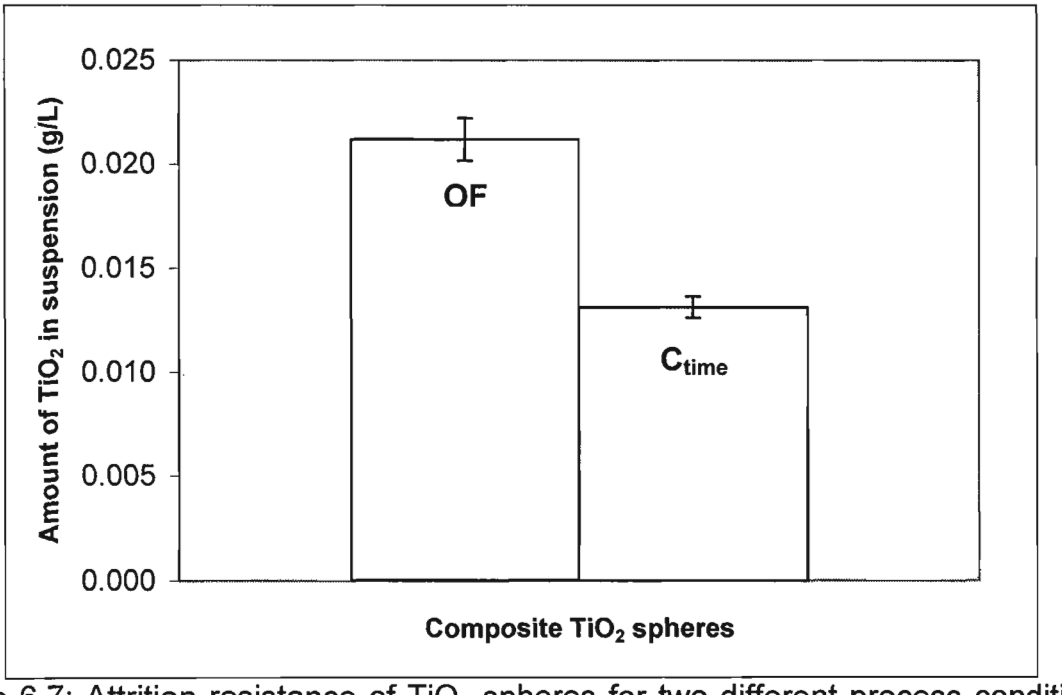

Figure 6.7: Attrition resistance of TiO_2 spheres for two different process conditions; a) original formulation (OF); b) catalyst fired for 3 h at 600°C instead of 1 h at 600°C (C_{time}). Error bars represent 95% CI for triplicate runs.

In all the above mentioned cases, the activity of the catalyst was not drastically impacted by the changes in the spheres formulation or synthesis procedure. Indeed, there was no statistical difference between the apparent rates constants obtained in all the experimental runs involving different batches of spheres. This inference was based on the comparison between F values obtained for the apparent rate constants obtained from every experimental run ($F = 2.47$) and the $F_{9,20}$ of 4.57 (at 99% confidence level). Appendix A provides more details on these analyses.

6.2.2 Experimental design

Based on the results obtained in Section 6.2.1, an experimental design was developed to study the effects and interactions of some of the variables involved in the production process of the spheres. These tests were performed to complement the earlier results on the effect of each individual parameter (determined independently).

As discussed earlier, the amount of water and catalyst, the drying and heat treatment conditions, and the pH and concentration of chitosan had a positive impact on the spheres resistance to attrition. However, the pH of the chitosan solution and its concentration had a strong impact on the production process of the catalyst because of the changes in the viscosity of the solution, which represent a change in the production process. Thus, in order to have a similar effect, the pH of the ammonia solution can be increased from 11.75 to 12.0 (increasing the percentage of ammonium hydroxide from 10% to 20%) to increase the pH difference between the chitosan-TiO_2 CSG solution and the ammonia solution. Higher concentrations of ammonia made the production of the spheres more difficult because the presence of vapours induced a fast hardening of the chitosan-TiO_2 CSG solution in the droppers. With respect to the amount of filler (Degussa P-25) added to the sol-gel, 0.30 g P-25 per mL TTIP was used to produce the catalyst.

A fractional factorial experimental design (2^{5-1}) was set-up to determine the effect of each variable and the interactions among variables. This approach is useful in an investigation of a multivariable system since it can indicate major trends with promising directions using relatively fewer runs (16 runs instead of the 32 runs for the complete 2^5 factorial design) in the factor space (Box *et al.*, 1978). At the same time, the effects and interactions among variables can be identified. Table 6.3 shows the experimental design distribution and the levels of the variables investigated.

The experimental runs were carried out using the FBPR and the system shown in Figure 4.8. In all the experiment, attrition was determined using the procedure detailed in Chapter 4 (Section 4.7) and the activity was measured using FA as a model organic compound.

Table 6.3: Fractional factorial design (2^{5-1}) to study the effects of and interactions among variables involved in the production of the composite TiO_2 spheres.

Runs	Amount of Water (g mL^{-1} TTIP)	Amount of HCl (mL mL^{-1} TTIP)	Concentration of NH_4OH solution (%)	Drying process	Calcination time (h)	Experimental order
1	0.040	0.133	10	RT-15 days	3	5
2	0.053	0.133	10	RT-15 days	1	6
3	0.040	0.200	10	RT-15 days	1	7
4	0.053	0.200	10	RT-15 days	3	4
5	0.040	0.133	20	RT-15 days	1	3
6	0.053	0.133	20	RT-15 days	3	8
7	0.040	0.200	20	RT-15 days	3	2
8	0.053	0.200	20	RT-15 days	1	1
9	0.040	0.133	10	80°C – 20 h	1	12
10	0.053	0.133	10	80°C – 20 h	3	16
11	0.040	0.200	10	80°C – 20 h	3	9
12	0.053	0.200	10	80°C – 20 h	1	15
13	0.040	0.133	20	80°C – 20 h	3	14
14	0.053	0.133	20	80°C – 20 h	1	11
15	0.040	0.200	20	80°C – 20 h	1	13
16	0.053	0.200	20	80°C – 20 h	3	10

The results obtained from the factorial experiments are shown in Table 6.4. The amount of particles in suspension reduced from 22 mg L^{-1} (run # 3 which represents the original formulation) to a minimum 6.73 mg L^{-1}, representing a 70% reduction in attrition. In terms of photocatalytic activity to degrade FA (with the initial concentration of 100 mg L^{-1}), the results indicated that the degradation rate constants were not statistically different in all cases. The effects and interactions among variables were calculated using Yates algorithm (Box *et al.*, 1978; Riedwyl, 1998). The analysis was done to determine the combination of variables that led to the lowest attrition and highest activity. Detailed calculations are presented in Appendix A.

Table 6.4: Response variables of the fractional factorial design (2^{5-1}) for the composite TiO_2 spheres (mass of catalyst equal to 0.025 kg)

Runs	Amount of TiO_2 particles in suspension (mg L^{-1})	Reaction rate constant (min^{-1})
1	8.63	0.286
2	9.65	0.283
3	21.92	0.281
4	9.78	0.297
5	8.51	0.314
6	6.73	0.325
7	14.19	0.306
8	13.53	0.323
9	7.68	0.338
10	15.71	0.336
11	16.55	0.345
12	12.68	0.344
13	8.81	0.316
14	7.39	0.344
15	11.97	0.330
16	13.23	0.305

6.2.3 Modified formulation to produce the TiO_2 composite spheres

Considering the results obtained in the previous section, the level of the variables giving the best result in terms of mechanical strength and photoefficiency of the photocatalyst are listed in Table 6.5. As can be seen, higher amount of water, lower amount of acid, higher concentration of ammonia in solution, faster drying process and longer time at 600°C gave the best combination of variables. Those variables were then used for the production of photocatalytic spheres in all the remaining experiments in this research.

Table 6.5: Variables chosen from the experimental design analysis.

Variables studied	Level
Amount of water	0.053 g H_2O mL^{-1} TTIP
Amount of HCl	0.13 mL HCl mL^{-1} TTIP
Concentration of NH_4OH solution	20% v/v
Drying process conditions	80°C – 20 h
Calcination time	3 h

Considering the variables listed in Table 6.5, a batch of catalyst was prepared and tested in the FBPR. Figure 6.8 shows the effect of all these variables collectively in one formulation (modified formulation - MF) versus the original formulation (OF). As shown in the figure, the combination of all these variables gave an attrition of 7 mg L^{-1} (with a particle size distribution around 15 μm, as can be seen in Appendix B) which represents approximately 70% reduction in the amount of TiO_2 particles released in the water.

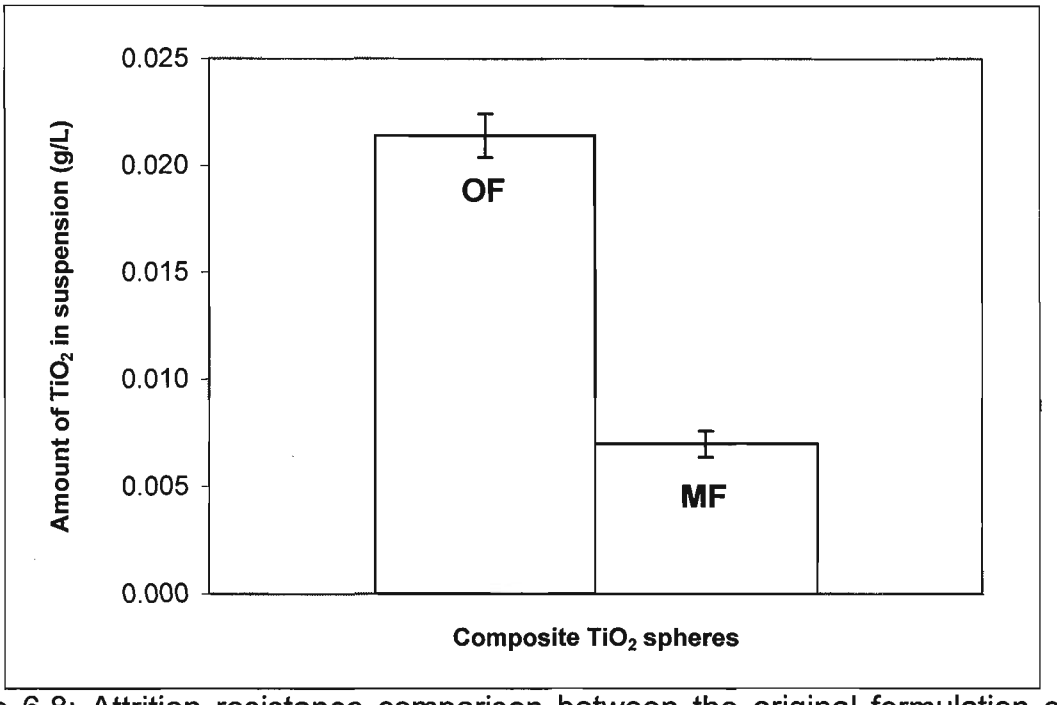

Figure 6.8: Attrition resistance comparison between the original formulation of the catalyst (OF) and the modified formulation (MF) considering variables listed in Table 6.5. Error bars represent 95% CI of triplicate runs.

It is important to mention that the viscosity of the sol-gel used in the MF was 7.94 cP, which is higher than the viscosity of the sol-gel solution in the OF (4.83 cP). Hence, increasing the amount of water and reducing the amount of acid in one formulation induce a 64% increment in the viscosity of the sol-gel. As discussed before, this increase in viscosity is a reflection of the condensation reactions that take place in the solution.

To further confirm the results obtained in Figure 6.8, some additional tests were performed by varying some variables in the modified formulation (MF). As shown in Figure 6.9, reducing the concentration of NH_4OH (from 20% to 10%) increased the attrition by 80% to13 mg L^{-1}. Reducing the amount of water during the preparation of sol-gel (from 0.053 g H_2O to 0.040 g H_2O per mL TTIP) gave 43% more attrition in the system (10 mg L^{-1}). Finally, drying the catalyst at 80ºC for 20 h followed by cooling down to room temperature, before heat treatment, led to higher attrition (14 mg of TiO_2 L^{-1} in a litre of solution).

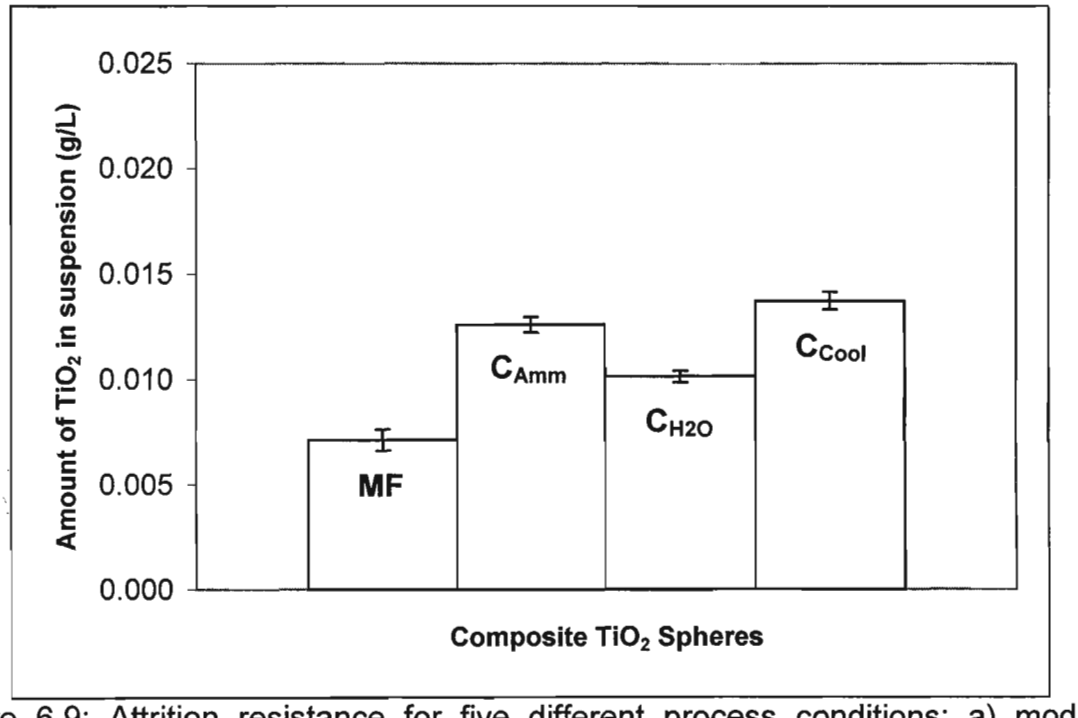

Figure 6.9: Attrition resistance for five different process conditions; a) modified formulation (MF); b) reducing the ammonia concentration to 10% (C_{Amm}); c) reducing the amount of water to 0.040 g H_2O mL^{-1} TTIP (C_{H2O}); d) the catalyst was cooled down to RT after the drying process and before the heat treatment at 600ºC for 3 h (C_{Cool}). Error bars represent 95% CI for triplicate runs.

There are few literature reports for the quantitative determination of TiO_2 particles in suspension in a fluidized bed system. Nonetheless, it has been reported that using silica-gel as a support, the amount of TiO_2 in suspension varies from 6 mg L^{-1} to 312 mg L^{-1}, mainly due to the preparation of photocatalyst and its

interaction with the support itself (Bideau et al., 1995). Also, using soda-lime glass beads, the TiO_2 in suspension was identified between 1 mg L^{-1} to 130 mg L^{-1}, depending on the catalyst preparation procedure (Qiu and Zheng, 2007). Comparing the literature results with those obtained in this study for the composite TiO_2 spheres, it is clear that the level of attrition is certainly low with the advantage that the activity is not hindered due to the catalyst detachment.

6.3 Catalyst characterization

As mentioned before, one of the most important parameters in the synthesis of the TiO_2 spheres is the calcination temperature, mainly because it plays a critical role defining the crystalline phases, the surface area and most importantly, the activity of the catalyst. Even though the calcination temperature used in this application is 600°C, the following discusses four different temperatures (600°C – 900°C) in order to analyze different characteristics of the catalyst (prepared using modified formulation). As shown in Table 6.6, commercial TiO_2 (Degussa P-25) had the highest surface area (54.03 m^2 g^{-1}) and the highest percentage of anatase (87.76%). Even though the composite TiO_2 spheres showed a significantly high percentage of anatase (84.20%) and a very high surface area (187.3 m^2 g^{-1}) before the heat treatment, once the heat treatment was applied, the surface area, percentage of anatase, pore volume dropped noticeably. The same tendency was shown when the temperature during the heat treatment increased from 600°C to 900°C

6.3.1 XRD analysis

Figures 6.10 shows the X-ray diffraction patterns of the pre-calcined TiO_2 powder (Degussa P-25) and the composite spheres calcined at 600°C. There are broad peaks at $2\theta = 30°$ (identify as the most intensive peak (1 0 1) for the anatase) and at $2\theta = 32°$ which represents the rutile (1 1 0) phase. As shown, in both cases the peaks were located in exactly the same position, but Degussa P-25 has a

smaller rutile peak than the composite spheres which explains the high percentage of anatase in the commercial titania.

Table 6.6: Surface area and anatase composition (using BET and XRD respectively) of pre-calcined powder (Degussa P-25 – as received) and composite TiO_2 spheres prepared using the new formulation and calcined at different temperatures.

Material	Heat treatment (°C)	Anatase (%)	Surface area ($m^2 g^{-1}$)	Pore volume ($cm^3 g^{-1}$)	Pore size (nm)
Degussa P-25	----	87.76	54.03	0.2275	16.56
TiO_2 Spheres	----	84.20	187.32	0.2707	7.17
	600	64.69	29.37	0.1680	18.16
	700	0.0	6.44	0.0671	31.31
	800	0.0	2.13	0.0315	38.68
	900	0.0	N/A	N/A	N/A

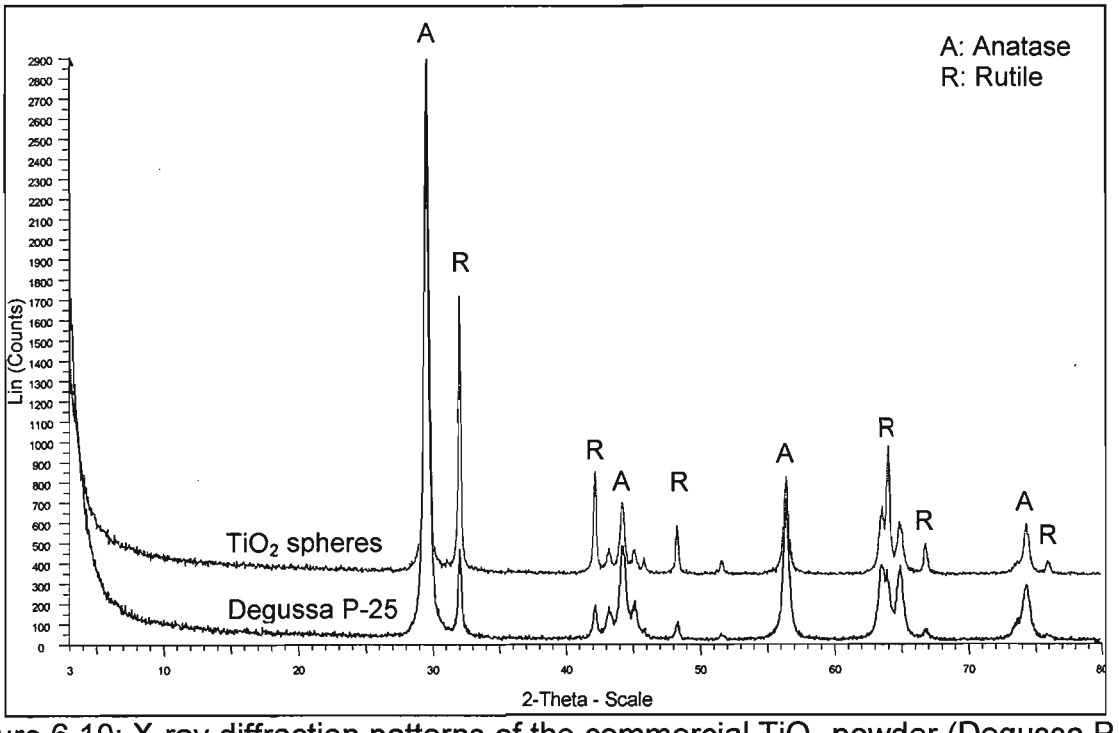

Figure 6.10: X-ray diffraction patterns of the commercial TiO_2 powder (Degussa P-25 as received) and the composite TiO_2 spheres produced with the modified formulation (MF) calcined at 600°C.

Figure 6.11 shows the effect of calcination temperatures on the X-ray diffraction patterns of the photocatalyst spheres calcined at different temperatures (600 – 900°C). The peak intensity of anatase (1 0 1) dramatically disappeared and the peak intensity of rutile (1 1 0) significantly increased when higher temperatures were applied, demonstrating that increasing heat treatment temperature accelerates phase transformation from thermodynamically metastable anatase to the most stable and more condense rutile phase (So *et al.* 1997). In general, the primary formed TiO_2 particles usually contain large portions of defect sites and because at high temperature some bond breaking and atom arrangements are induced, the transformation of anatase to rutile is facilitated. Because anatase has a structural similarity to rutile this transformation is initiated by forming the rutile nuclei along the anatase interface. Thus, the rutile structure can be developed at the expense of anatase crystals (Yin *et al.*, 2001; Su *et al.*, 2004).

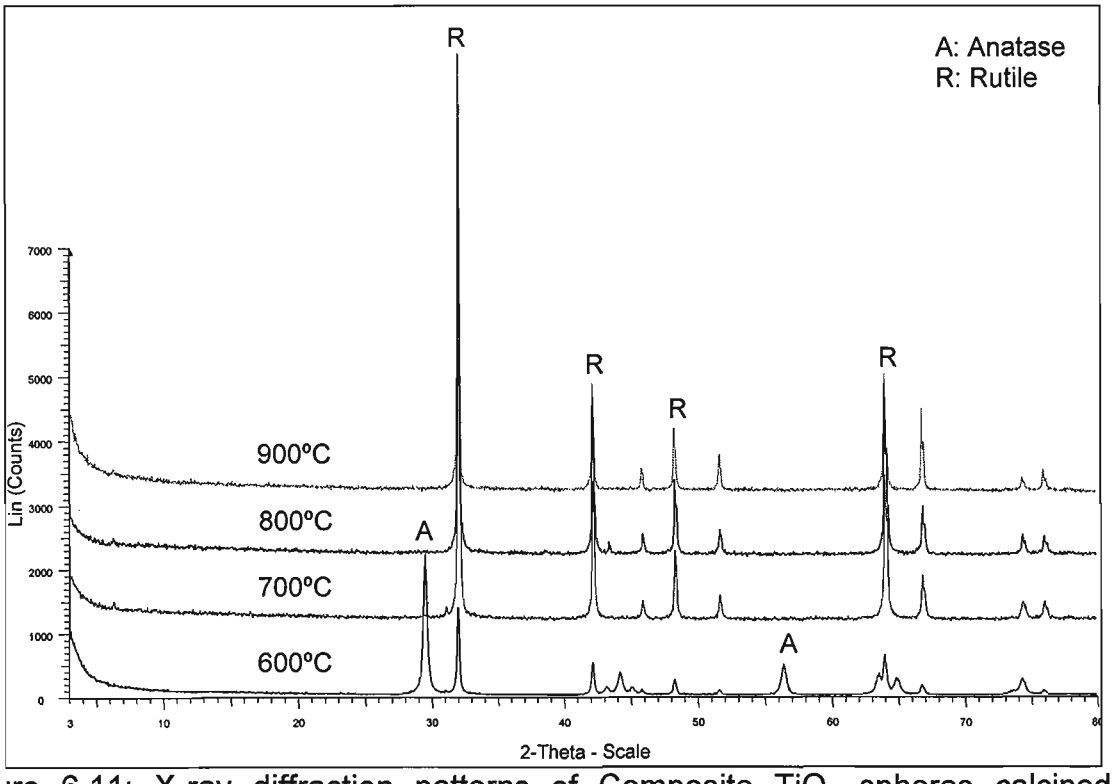

Figure 6.11: X-ray diffraction patterns of Composite TiO_2 spheres calcined at different temperatures (600, 700, 800 and 900°C).

Using Rietveld refinement method, the amount of anatase and rutile in the composite photocatalyst was determined. The weight fractions of anatase and rutile for spheres calcined at 600°C were 64.69% and 35.31%, respectively. In comparison, the commercial TiO_2 (Degussa P-25) has a weight fraction of 87.76% for anatase and 12.24% for rutile. A 100% phase transformation from anatase to rutile took place at a temperature between 600°C and 700°C. Increasing the calcination temperature by 100°C (from 600°C to 700°C) led to the complete disappearance of anatase as shown in Figure 6.11 (no peak is present for 700°C).

6.3.2 BET analysis

BET was used for the surface area, pore size distribution and pore volume analysis of the composite TiO_2 spheres. Table 6.6 shows the dependence of the surface area, pore size and pore volume on the calcination temperature of the composite TiO_2 spheres. The specific surface area and pore volume shifted towards smaller values at higher calcination temperatures. At 700°C the specific surface area decreased to 6.44 $m^2 g^{-1}$ and the pore volume reduced by 60% with respect to the value reported when the catalyst was calcined at 600°C. Although a large portion of the mesoporous structure was maintained at 700°C, the pore volume was reduced significantly, likely because higher calcination temperatures induce crystallization of TiO_2, subsequent crystal growth, and shrinkage of the pores (Peng *et al.*, 2005). At 800°C, the mesoporous structure has significantly disappeared, mainly due to the particle size of the catalyst. In general, the specific surface area and the pore volume decreased with the increase of calcination temperature; at the same time, the average pore diameter increased. On the other hand, the average pore diameters increased upon heat treatment, which is consistent with the literature reports (Xu *et al.*, 2008; Bischoff and Anderson, 1995).

The isotherms and pore size distributions of the composite TiO_2 spheres calcined at 600°C, and commercial TiO_2 powder (Degussa P-25) are shown in Figure 6.12. It is clear that Degussa P-25 has a higher surface area than the composite photocatalyst, with a value of 54.03 $m^2 g^{-1}$ for the powder and

29.37 m^2 g^{-1} for the composite TiO_2 spheres calcined at 600°C. According to the BDDT (Brunauer, Deming, Deming and Teller) classification, the powder and the spheres show isotherm type IV, exhibiting hysteresis loops mostly of H2 and H3. This result indicates that the composite photocatalyst porosity in the meso-range (2~50nm) (Sink *et al.*, 1985).

In the sol-gel process, nanosize particles are formed by hydrolysis and condensation processes. If gelation occurs, these particles are connected together to form three dimensional aggregates. During heat treatment (sintering), the primary particles are grown into larger ones and bond together to form a solid network, which exhibits a narrow pore size distribution and smaller surface area at higher temperature (Brinker and Scherer, 1990) (see Figure 6.12). On the other hand, Degussa P-25 powder is prepared at elevated temperature (>1000°C) by flame synthesis, containing larger crystalline anatase and rutile particles. As a result, Degussa P-25 has the widest pore diameter region.

Comparing the BET results and XRD analysis with the ones obtained for the spheres produced using the original formulation (Table 5.3), it is clear that the accelerated drying process, the calcination time and/or the sol-gel composition had an impact not only on the percentage of anatase, but also on surface area, pore size and pore volume. In general, higher percentages of anatase and higher surface area have been determined for the spheres produced with the original formulation.

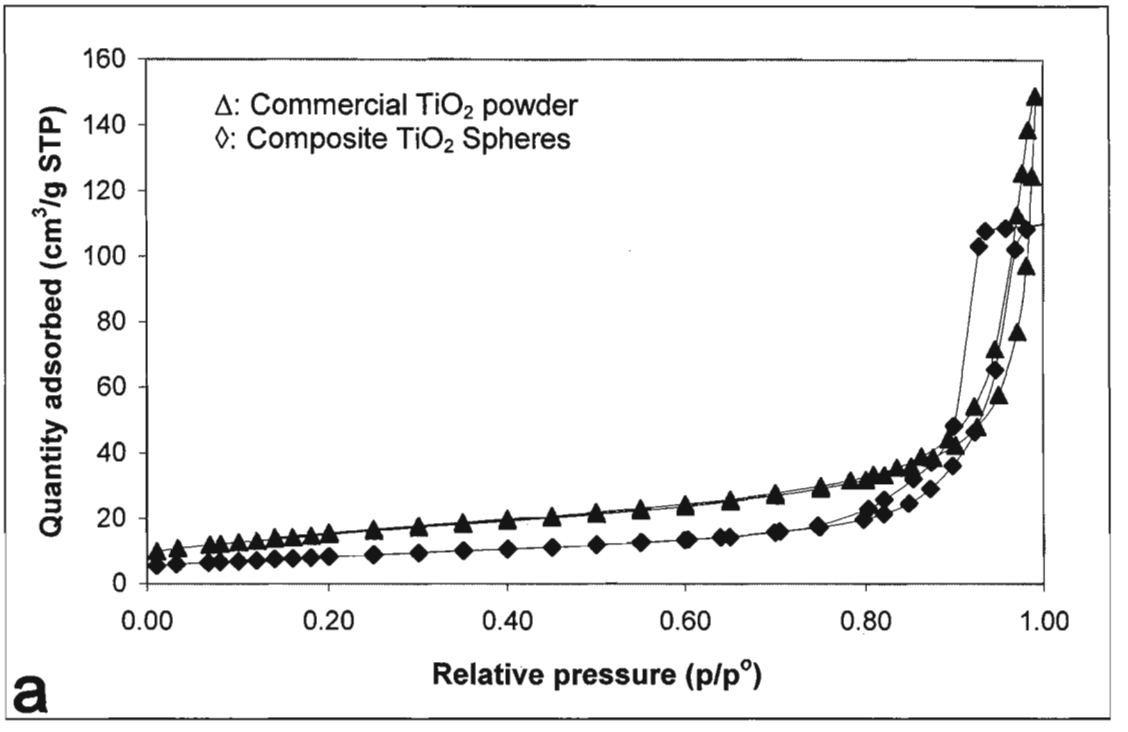

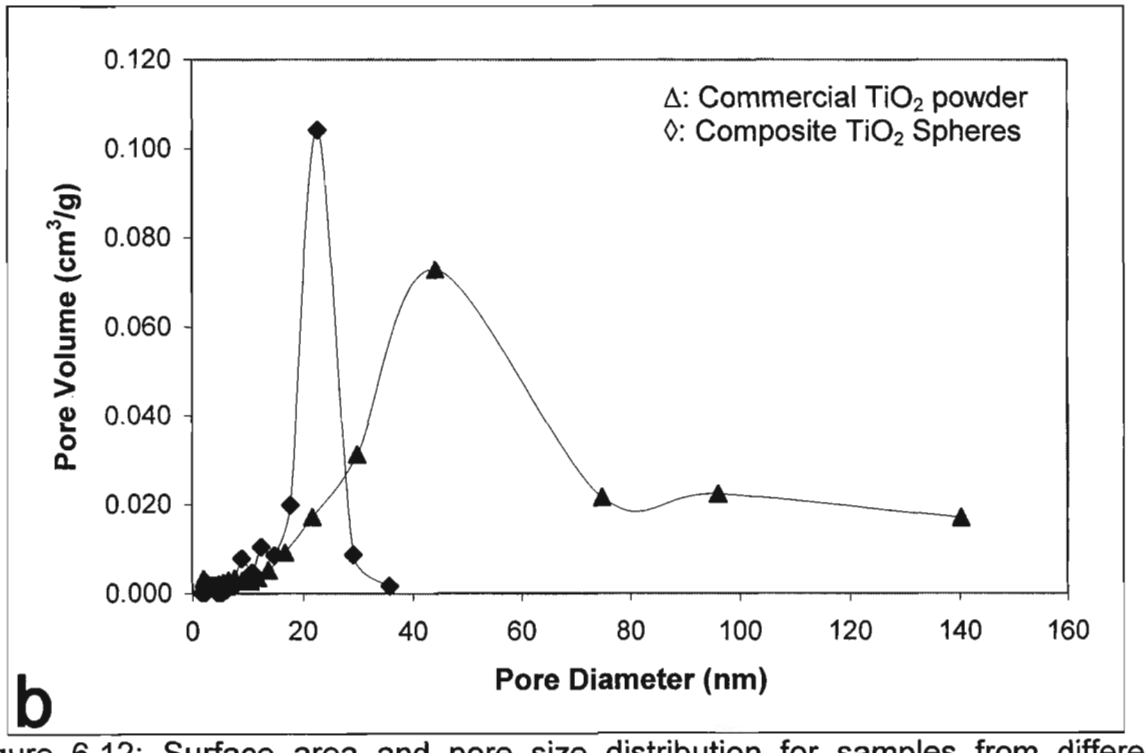

Figure 6.12: Surface area and pore size distribution for samples from different conditions, (a) surface area of commercial TiO_2 powder (Degussa P-25) and the composite TiO_2 spheres calcined at 600°C, (b) pore size distribution of Degussa P-25 and composite TiO_2 spheres calcined at 600°C.

6.3.3 TGA analysis

In order to better understand the thermal behaviour of the composite TiO_2 spheres during different drying and heat treatment conditions the catalyst was analyzed using TGA at different heating rates to emulate the actual process. The TGA analysis was performed in three stages. The first stage was from room temperature to 80°C as shown in Figure 6.13a. The sample weight was reduced by 87% within the 25 min analysis. The second stage involved maintaining the temperature constant (80°C) for 20 h, showing an additional reduction of 7.6% with a final value of 1.59 mg (Figure 6.13b). Finally, the third stage constituted heat treatment, for which the temperature increased from 80°C to 600°C, showing a final catalyst weight of 1.38 mg (Figure 6.13c).

The loss of mass for the TiO_2 spheres was mainly due to the evaporation of the residual water, alcohol, chitosan decomposition and ammonia that had been trapped in composite structure. Weight reduction of the sample was as high as 91% resulted by the sintering and densification of the composite.

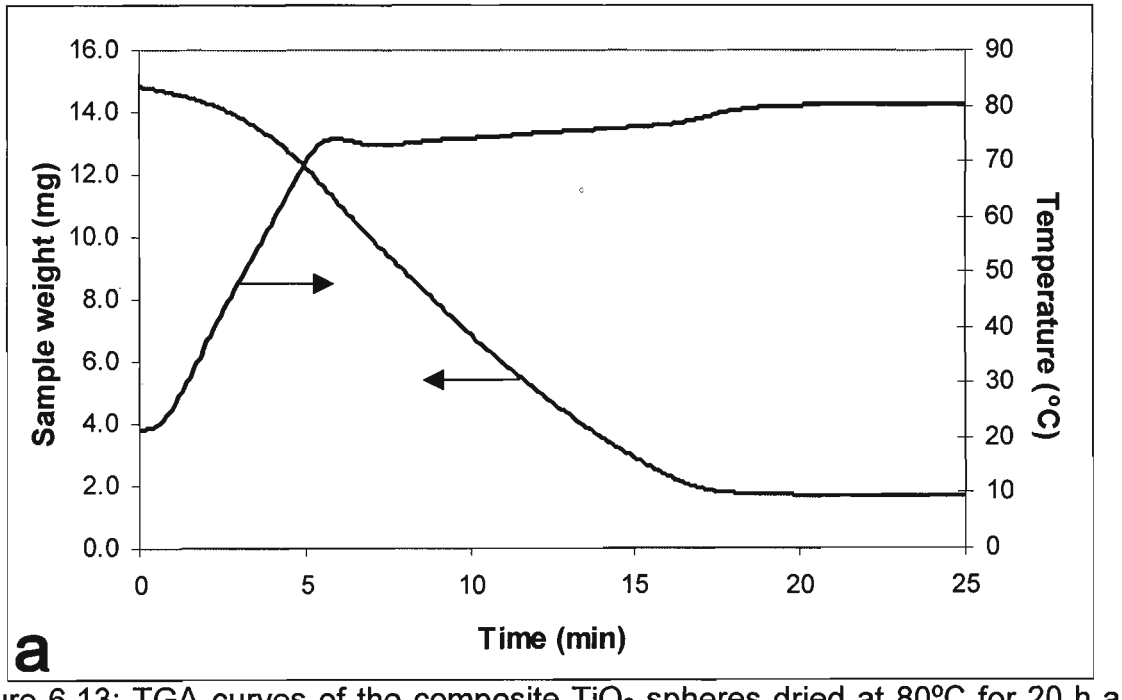

Figure 6.13: TGA curves of the composite TiO_2 spheres dried at 80°C for 20 h and calcined at 600°C for 3 h, (a) first 25 min of the drying process, (b) isotherm drying process, (c) heat treatment for 3 h.

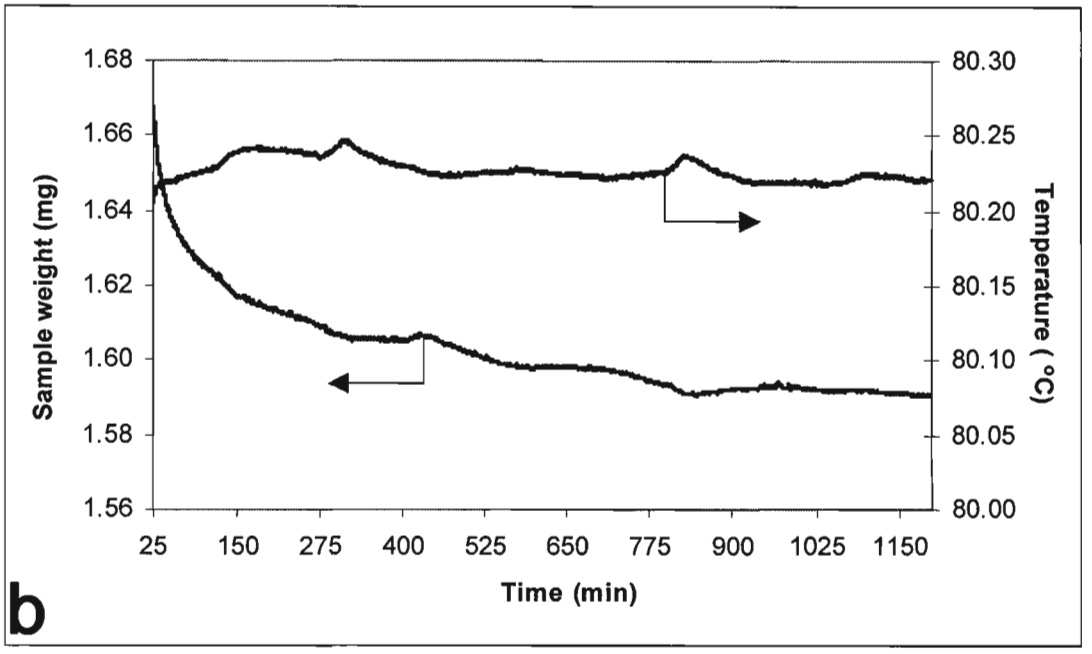

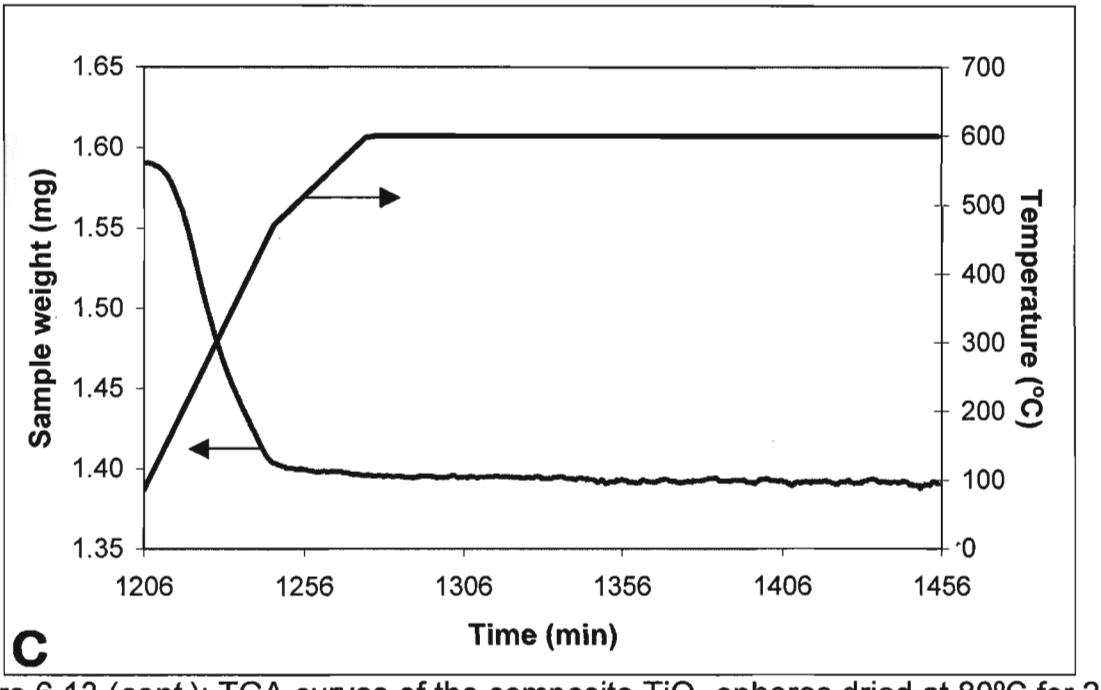

Figure 6.13 (*cont.*): TGA curves of the composite TiO_2 spheres dried at 80°C for 20 h and calcined at 600°C for 3 h, (a) first 25 min of the drying process, (b) isothermal drying process, (c) heat treatment for 3 h.

6.3.4 SEM analysis

Microstructure of the produced TiO_2 spheres was analyzed using SEM (Figure 6.14). Composite TiO_2 spheres using the new formulation had an average

diameter of 1.15 mm. At higher calcination temperature, i.e. 900°C, the average diameter was reduced to 0.90 mm. In either case, the catalyst particles showed consistency in size and shape.

Figure 6.14 shows that the composite TiO_2 spheres had a relatively smooth surface despite the presence of some roughness along the surface of the catalyst. No cracks were found after heat treatment, confirming that there were no extreme stresses during the catalyst production process. Grooves around the sphere (Figure 6.13b & 6.13d) as well as the crater shown in Figures 6.13b & 6.13c are the result of the production process; the same for all the spheres.

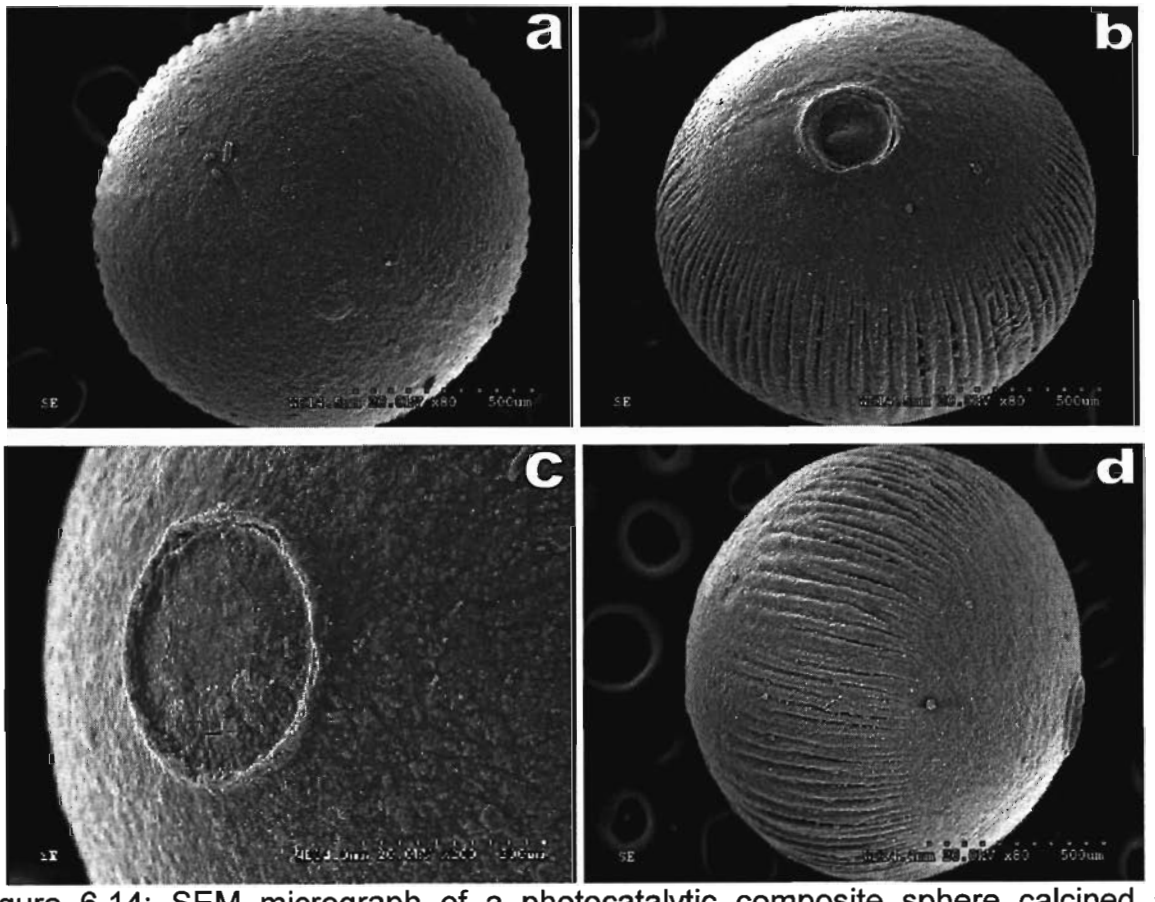

Figure 6.14: SEM micrograph of a photocatalytic composite sphere calcined at 600°C for 3 h.

6.4 TiO_2 spheres durability and attrition determination over time

A batch of composite TiO_2 spheres (25 g) was used for 25 h in a fluidized bed photocatalytic reactor to determine how the attrition was changing over time. Every 3 h a sample was collected to determine the amount of TiO_2 in water as a measure of attrition, as shown in Table 6.7. The attrition increment was reduced with respect to the initial value (7 mg L^{-1}) showing a maximum value of 6 mg L^{-1} after 18 h of use.

Table 6.7: Evolution of the TiO_2 particles released from the composite TiO_2 spheres over time.

Duration (h)	Cumulative attrition (mg L^{-1})	Attrition increment (mg L^{-1})
3	7.392	----
6	11.073	3.681
9	14.285	3.212
12	19.076	4.791
15	23.137	4.061
18	29.197	6.060
21	34.845	5.648
25	39.859	5.014

Figure 6.15 shows the cumulative attrition versus time. As can be seen, there is a linear increment of the attrition with approximately 40 mg L^{-1} of TiO_2 particles after 25 h of continuous operation. As listed in Table 6.7, the increment every three hours was between 3.2 and 6.1 mg L^{-1}.

SEM micrographs of the catalyst after 25 h of continuous use are shown in Figure 6.16 showing that the surface of the catalyst is smoother than that of the catalyst right after the heat treatment. Comparing these images with the micrograph shown in Figure 6.14, the catalyst after 25 h of continuous use shows practically no roughness.

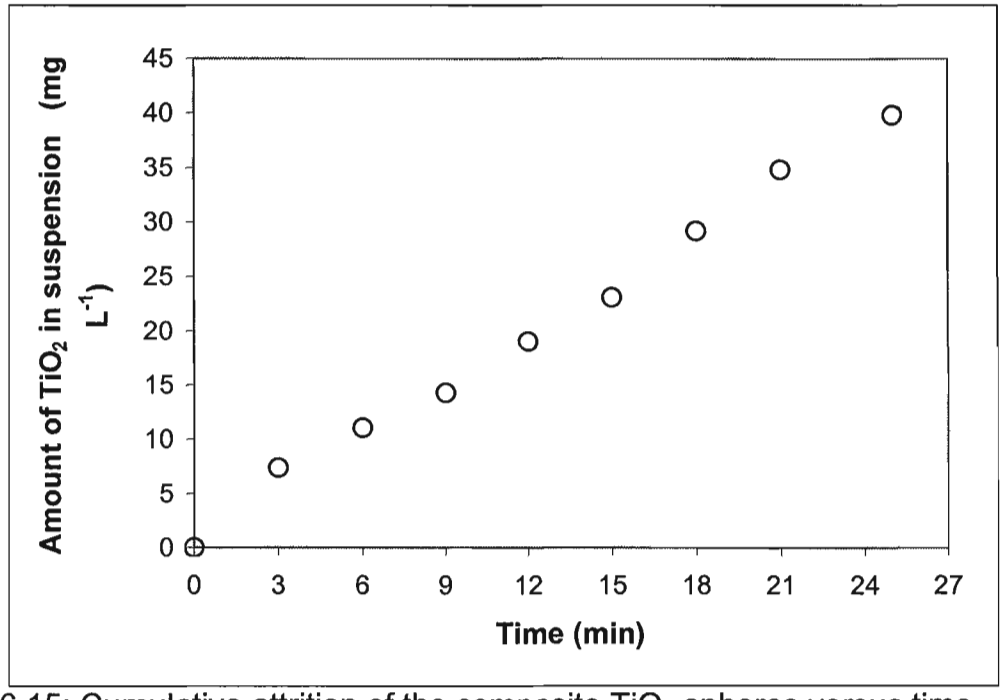

Figure 6.15: Cumulative attrition of the composite TiO_2 spheres versus time.

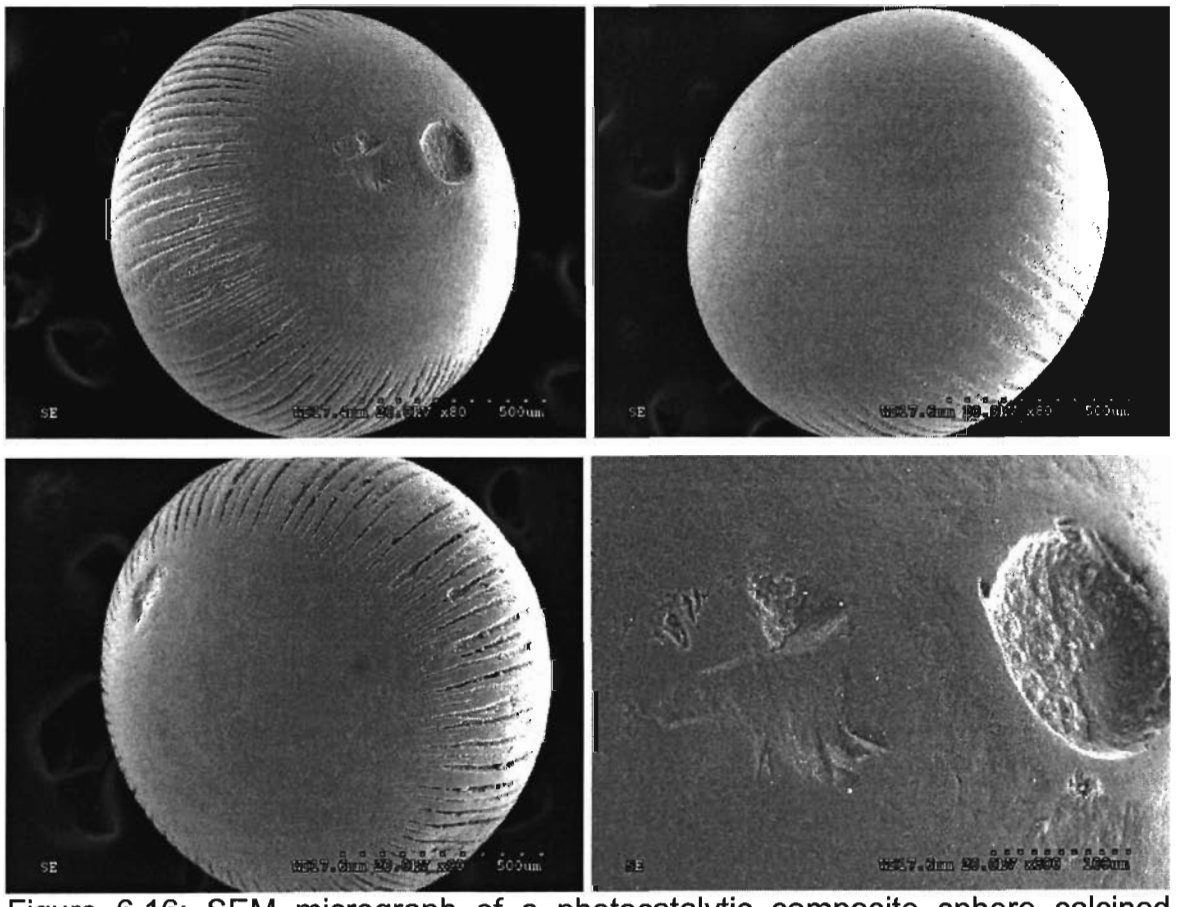

Figure 6.16: SEM micrograph of a photocatalytic composite sphere calcined at 600°C after 25 h of continuous use.

6.5 Final remarks

This section demonstrated the significant improvement obtained on the attrition resistance of the TiO_2 spheres through modifications made in the formulation and synthesis procedure. The amount of TiO_2 particles in suspension were reduced from 22 mg L^{-1} to 7 mg L^{-1} based on the following changes in the procedure/formulation: a) inducing more hydrolysis and condensation reactions by increasing the amount of water from 0.040 g H_2O to 0.053 g H_2O per mL TTIP and reducing the amount of HCl from 0.20 mL HCl to 0.13 mL HCl per mL TTIP during the sol-gel production; b) increasing the pH of the ammonia solution from 11.75 to 12 (increasing the percentage of ammonia from 10% to 20% v/v); c) accelerating the drying process conditions to 80°C for 20 h; and d) increasing the calcination time from 1 h to 3 h at 600°C.

The activity of the catalyst prepared with MF, was similar to that of spheres prepared with the OF (i.e., with none of the abovementioned modifications). Using the MF, the FA degradation rate constant was between 0.281 min^{-1} and 0.344 min^{-1} and using the OF, the degradation rate constant was 0.315 ± 0.061 min^{-1}.

In terms of the characteristics of the spheres, the modifications in the spheres at 600°C resulted in a surface area of 29.37 $m^2 g^{-1}$ (compared with 37 $m^2 g^{-1}$ for that of OF) and a percentage anatase of 65% (compared with 72% for that of OF). The shape and size of the spheres were similar to those in the original formulation.

Besides the better attrition resistance and the good activity of the photocatalyst, this new formulation to produce the composite TiO_2 spheres are more efficient in terms of the spheres formation because less time would be needed to prepare the final product.

Chapter Seven

Activity of Composite TiO_2 Spheres

7.1 Introduction

Titanium Dioxide is a photocatalyst studied extensively in the last three decades because of its ability to destroy organic pollutants in liquid and gas effluents. It has been shown that under UV irradiation, TiO_2 photocatalyst can degrade many organic pollutants into harmless substances such as CO_2, H_2O and mineral acids as a result of oxidative redox reactions on the surface of the photocatalyst (Bhatkhande *et al.*, 2002; Kabra *et al.*, 2004; Syoufian *et al.*, 2007; Gaya and Abdullah, 2008; Higgins *et al.*, 2009).

This investigation has focused on the development of a composite photocatalyst with high attrition resistance and good photoactivity. As shown in Chapter Six, the catalyst formulation and synthesis were improved, resulting in better attrition resistance. The improvement came through the modification of the hydrolysis and condensation rates during sol-gel preparation, aging time, spheres formation, drying process, and calcination conditions. This chapter focuses specifically on the photocatalytic activity of the catalyst spheres in a fluidized bed photoreactor. Formic acid (FA) and 2,4-Dichlorophenoacetic acid (2,4-D) were selected as model compounds, representing simple and more complex organic contaminants, respectively. In addition, preliminary tests were carried out for the degradation of natural organic matter (NOM). Experimental conditions involved different initial concentrations and fluence rates within the reactor.

The performance of the composite TiO_2 spheres at degrading the organic molecules was also compared with that of Degussa P-25, known as a standard photocatalyst with many literature data (Porter *et al.*, 1999; Araña *et al.*, 2009). Experiments with P-25 were conducted with the amount of powder P-25 (catalyst loading) that gave the maximum activity.

7.2 Fluence rate determination

The fluence rate applied to the photocatalytic reactor was determined for the experimental set up showed in Figure 4.7. The fluence rate is defined as the energy provided by the UV lamps per unit time per irradiated area of the reactor ($J\ s^{-1}\ m^{-2}$). For this experimental setup, there were three possible lamp positions around the reactor, located at 5, 7.5 and 10 cm from the centre of the reactor. Therefore, the fluence rate was determined for each of those positions, so the effect of distance on the amount of irradiation in the reactor could be determined. It is important to clarify that for the initial fluence rate determinations, the cylindrical reflector was not used.

Potassium ferrioxalate and iodide-iodate actinometers were used to determine the fluence rate in the system. Potassium ferrioxalate actinometer was first introduced by Hatchard and Parker (1956) and it is probably the most commonly used. Iodide-iodate actinometer was introduced by Rahn (1997) and it has the advantange that it is optically opaque to light below 290 nm and it is optically transparent to wavelengths greater than 330 nm. In other words, it absorbs practically all of the light below 290 nm but little of the ambient light normally present in the laboratory, which represents a difference from the potassium ferrioxalate actinometer that absorbs slightly in visible region (Goldstein and Rabani, 2008). Nonetheless, the experiments with potassium ferrioxalate were performed under dark conditions to avoid any interference in the results.

Figure 7.1 shows the difference between the two actinometers. As is shown, this difference was significant especially when the irradiation was high. Potassium ferrioxalate actinometer showed higher fluence rate values at two different lamp positions (5 cm and 7.5 cm). However, there was no statistical difference between the two actinometers when the lamps were located 10 cm from the reactor. In addition, the iodide-iodate actinometer seemed to show a "saturation effect", meaning that the fluence rate only increased by 16% when the lamps were moved closer to the reactor (from 10 cm to 5 cm). This "saturation effect", as it suggests, was likely due to the saturation of the actinometric solution at very high photon flux that prevents proper differentiation between different levels of irradiation.

To determine which actinometer represented better the actual irradiation and fluence rate in the system, the fluence rate was converted into the lamp output. This effective output was then compared with the nominal output provided by the manufacturer.

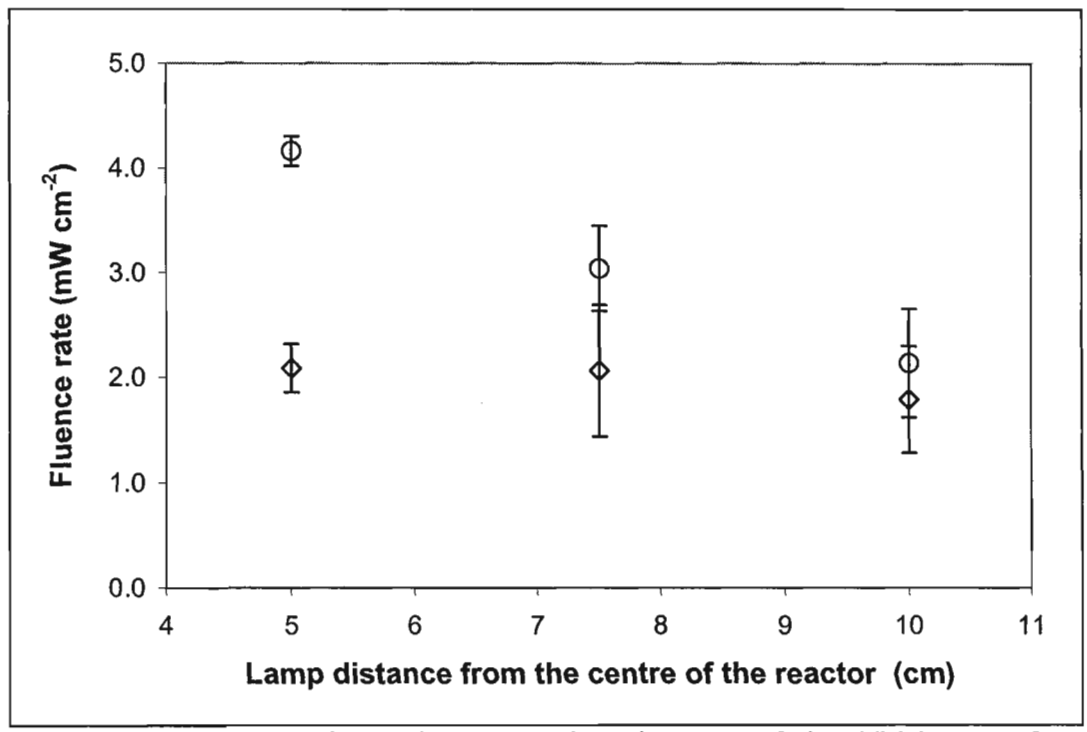

Figure 7.1: Fluence rate dependence on the distance of the UV Lamps from the centre of the quartz tube using two different actinometers: (o) Potassium Ferrioxalate; (◊) Iodide-iodate actinometer. Error bars represent 95% CI of the triplicate runs.

To calculate the effective output of the UV lamps, a model was developed in collaboration with Dr. Gustavo Imoberdorf (of the Advance Oxidation Research Laboratories) based on the data obtained from the actinometrical measurements and the photon absorption distribution in the system. Monte Carlo (MC) algorithm was used in this model considering the trajectories of a large number of photons, as well as possible locations where they are absorbed in the reactor (Imoberdorf *et al.*, 2008). The model considers two main parts: i) the photon emission and ii) the photon propagation in the system. The photon emission in the lamp is modeled according to

two stochastic rules, i) the probability for a photon to be emitted is uniform in all the lamp volume, and (ii) the photon emission is considered isotropic. Once a plausible emission point inside the lamp and a plausible propagation direction of a given photon are evaluated, the photon trajectory is tracked until it leaves the lamp. In addition, the optical properties of the reactor quartz tube are considered to discount the reflection of some of the photons. This procedure is repeated until all the photons are tracked. Finally, once the photon trajectories are known, the local net spectral radiation flux (q_λ) is evaluated as is shown in Equation 7.1:

$$q_\lambda(r) = P_{lamp,\lambda} \frac{n_{ph,trans}(r)}{n_{ph,tot}} \frac{1}{2L_R \pi R_{reactor}} \tag{7.1}$$

where $P_{lamp,\lambda}$ is the power of the lamp at 254 nm, $n_{ph,trans}$ is the number of photons entering into the reactor volume, and $n_{ph,tot}$ is the total number of photons considered in the MC model. Figure 7.2 shows a representation of the possible photon paths for the MC method.

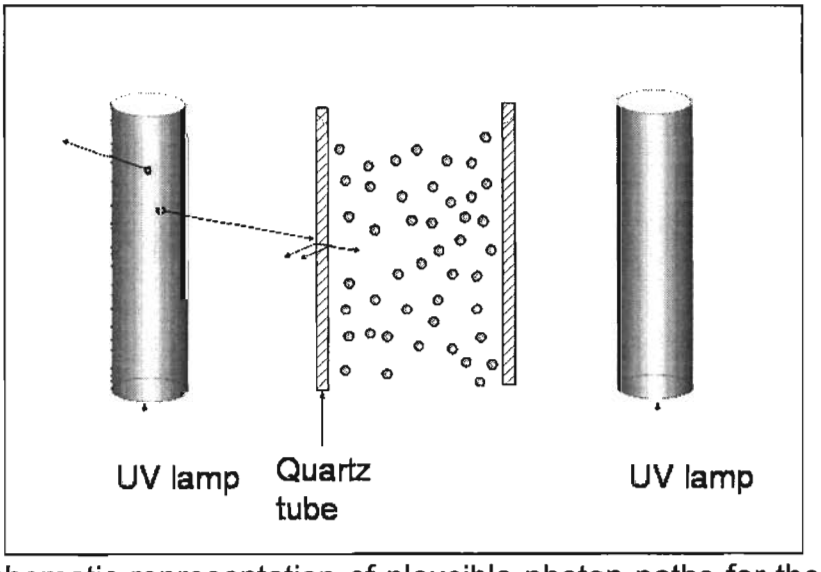

Figure 7.2: Schematic representation of plausible photon paths for the Monte Carlo (MC) Method in the reaction system shown in Figure 4.7.

Table 7.1 shows the experimental results and the predicted values for the fluence rate using the above mentioned model. At the same time, the effective output of each UV lamp is shown. It is important to mention that the nominal output of the lamp, according to the manufacturer, is 5.7 W (LightSources & LightTech technical sheet, 2005).

Table 7.1: Computed and experimental fluence rates obtained for the reaction system shown in Figure 4.7.

Actinometer	Lamp positions from the centre of the reactor (cm)	Fluence rate (mW cm^{-2})		Predicted UV lamps output (W)[a]
		Experiment	Model	
Potassium Ferrioxalate	5	4.16	4.44	4.73
	7.5	3.04	2.83	
	10	2.14	2.04	
Iodide - Iodate	5	2.09	2.61	2.80
	7.5	2.06	1.50	
	10	1.79	1.20	

[a] According with the manufacturer the output at 254 nm is 5.7 W

Based on these results, it is clear that potassium ferrioxalate provided a more realistic prediction of the nominal output of the lamps. The difference between the effective and the nominal output of the lamps is 17% using potassium ferrioxalate actinometer, while using iodide-iodate actinometer the difference is 51%, the later being high and likely not representing the real output of the lamps. A radiometer (International Light - IL 1700) was used to verify the emission of the lamps at 1 m distance from the lamp, as recommended by the manufacturer. These measurements showed that the output of each of these lamps were similar to the value reported by the manufacturer, with a maximum deviation of 7%.

The differences between the effective and the nominal output of the lamps can be explained in terms of the temperature variations inside the wooden enclosure. When the UV lamps were on, the temperature inside the box increased due to the lack of fresh air circulating through the system. This led to the increase in the temperature of the UV lamps, thereby affecting their real output. A change in the UV lamp temperature would change the vapour pressure of the mercury inside the lamp, changing the equilibrium between the gas and liquid phases that affect the

emission of the lamp (this phenomenon is commonly called "wind chill" effect) (Lau *et al.*, 2009; UVTA technical sheet, 1999).

Potassium ferrioxalate was proven to better represent the actual fluence rate within the FBPR. Figure 7.3 shows the correlation between the experimental results obtained using potassium ferrioxalate actinometer and the results obtained using the proposed model with the effective output of each UV lamp being 4.73 W.

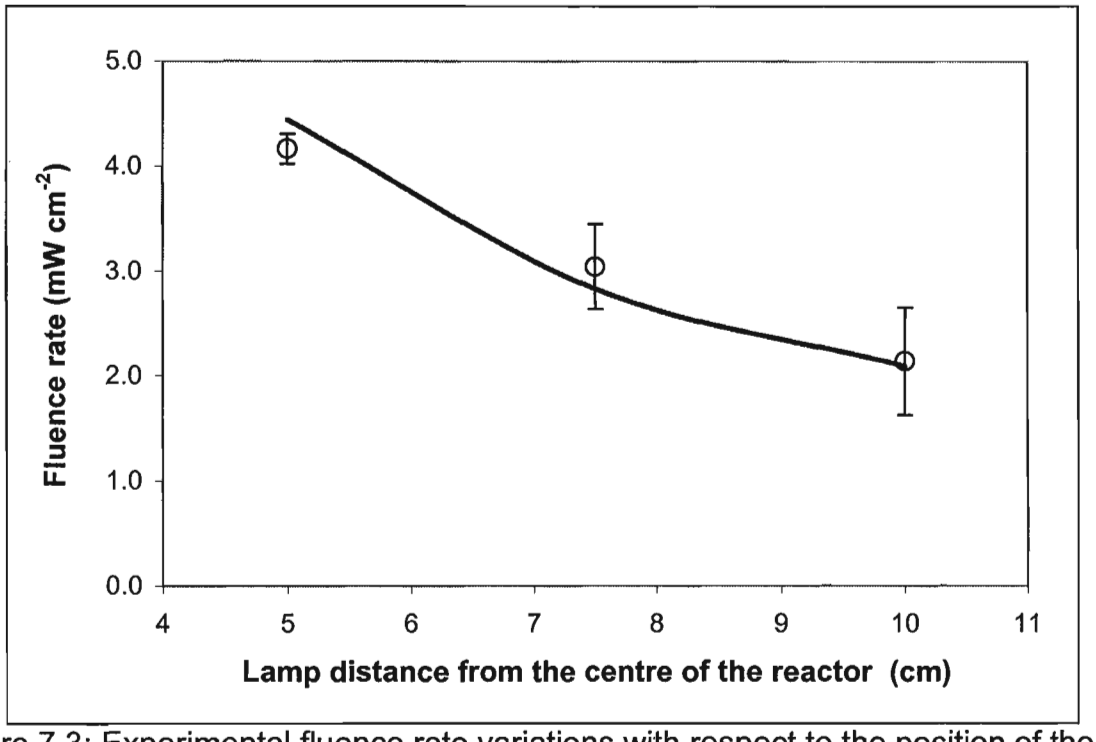

Figure 7.3: Experimental fluence rate variations with respect to the position of the UV lamps using Potassium Ferrioxalate actinometer and the predicted behaviour using Monte Carlo (MC) model. Error bars represent 95% CI for the triplicate runs.

Potassium ferrioxalate actinometer was then used to determine the fluence rate when the cylindrical reflector was placed around the lamps. In this case, all the lamps were located at 5 cm from the centre of the reactor. A value of 5.32 mW cm^{-2} was determined using the reflector, which is 26% higher than the value obtained without the reflector (4.16 mW cm^{-2}). As expected, the fluence rate was higher using the reflector, mainly because more photons reached the reactor.

7.3 Photocatalytic degradation of Formic Acid (FA)

The degradation of FA was studied under different irradiation levels (i.e., lamps positioned at different distances from the reactor) as is shown below.

7.3.1 Effect of the radiation flux on FA degradation

The effect of radiation flux was investigated by changing the position of the UV lamps or taking out the reflector (cylinder covered with aluminum foil). The experimental setup was exactly the same as the one described in Chapter 4. FA concentration was monitored with respect to time to determine the effect of different levels of irradiation on the degradation pathway of the pollutant. Figure 7.4 shows the impact of the different irradiation levels in the FA degradation showing that the higher the irradiation, the faster the FA degradation. Therefore, when the reflector was used, the degradation was the fastest.

Table 7.2 shows the rate constants (k_r) of the FA photodegradation under different fluence rates. In all the cases pseudo-first order kinetics was assumed. The normalized rate constants were calculated multiplying the apparent rate constant by the ratio of the total volume (1000 mL) to the active volume (80 mL) according to the approach followed by Turchi and Wolfrum (1992). The value of k_r was the highest for the highest fluence rate, i.e., when the lamps were closer to the reactor and the cylindrical reflector was used (0.317 min^{-1}). At 5 cm from the reactor, but without the reflector, the rate constant dropped by 36% (0.205 min^{-1}). As expected, for the other positions of the lamps, the rate constants were smaller, because rate constant depends on the amount of irradiation available in the system as was described in Chapter 2. On the other hand, the lower the irradiation, the smaller the amount of electron-hole (e^- - h^+) pairs that are generated on the surface of the catalyst and, as a consequence, the smaller the rate of degradation of the organic pollutants (in this case FA).

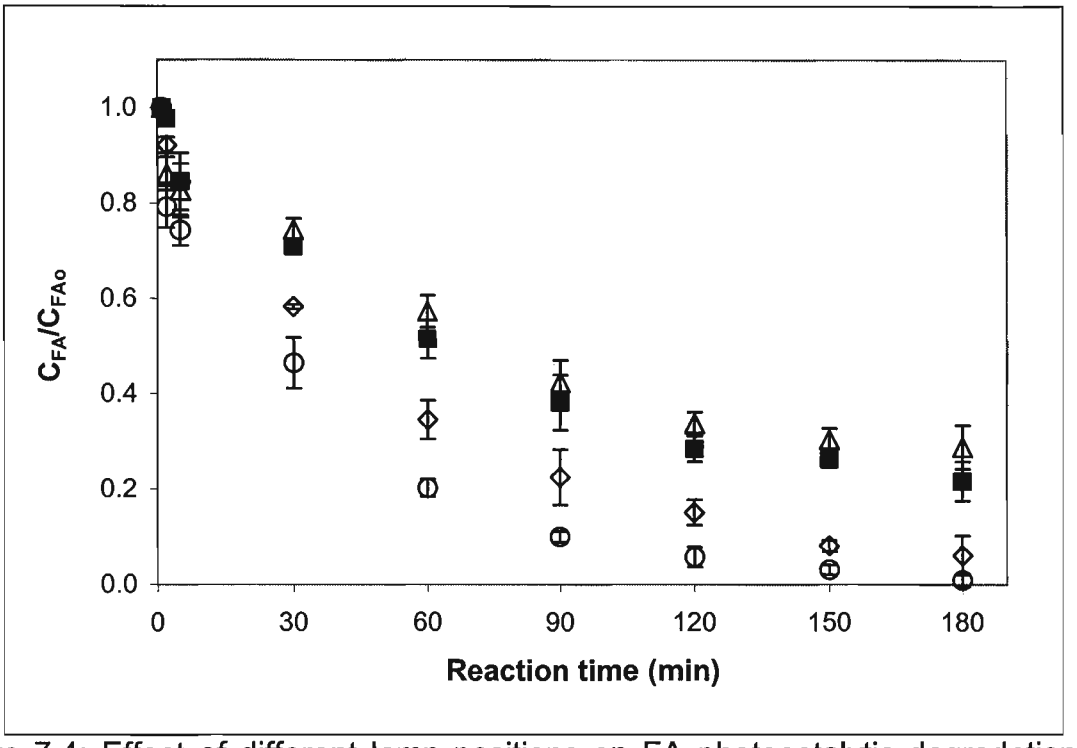

Figure 7.4: Effect of different lamp positions on FA photocatalytic degradation, (o) 5.32 mW cm^{-2}, (◊) 4.16 mW cm^{-2}, (■) 3.04 mW cm^{-2}, (Δ) 2.14 mW cm^{-2}. Error bars represents 95% CI for the triplicate runs.

Table 7.2: FA photodegradation rate constants (k_r) of composite TiO_2 spheres at different fluence rates using 100 mg L^{-1} as initial concentration of FA and 0.025 kg of composite TiO_2 spheres

Lamp position (cm)	Fluence rate (mW cm^{-2})	Degradation rate constant (min^{-1})	Standard error of the parameter
5 (reflector)	5.32	0.317	0.038
5 (no reflector)	4.16	0.205	0.048
7.5 (no reflector)	3.04	0.114	0.014
10 (no reflector)	2.14	0.094	0.025

7.3.2 Deactivation of the TiO_2 spheres

Deactivation of the photocatalyst is one of the main concerns in heterogeneous photocatalytic processes. As was discussed before, photocatalytic reactions mainly take place on the surface of the photocatalyst; therefore, adsorption of pollutants is one of the most important steps in photocatalytic reactions. If the

products of the photocatalytic reactions adsorb firmly on the surface of the photocatalyst, the surface charge carrier transportation and pollutant adsorption can be altered, resulting in the loss of photocatalyst activity (Liqiang *et al.*, 2004). One way to determine this effect is to run the same catalyst more than once and to calculate changes in the degradation rate as a function of time and use. The degradation rates of the reuse catalyst can be compared with that of the fresh catalyst to determine if there was any change in the activity.

The deactivation of the composite TiO_2 spheres, *a(t)*, was calculated using the same approach as shown in Equation 7.2.

$$a_{cat}(t) = \frac{k_r(t)}{k_r(t=0)} \tag{7.2}$$

A similar approach has been used elsewhere (Szépe and Levenspiel, 1968; Fogler, 2006). Nonetheless, it is important to clarify that this approach was used here just to show the effect of FA, or any other possible contaminant, on the deactivation of the catalyst. Figure 7.5 shows the results after 27 h of continuous use, using FA (100 mg L^{-1}) as a pollutant. The level of FA was maintained by adding fresh quantities every 3 h. As can be seen, the activity of the catalyst remained practically constant after 27 h of use. That is, FA degradation was not affected with repeated use of the catalyst. This implies that no contamination or fouling happened on the CSG photocatalyst and hence there was no inhibition or photocatalytic activity loss.

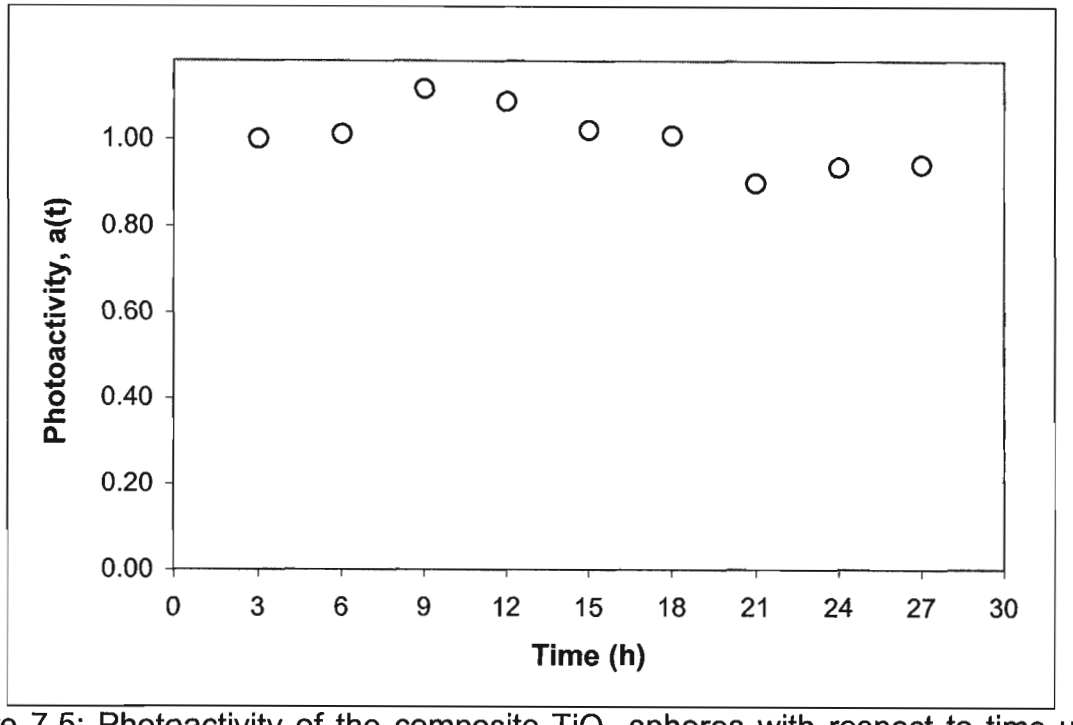

Figure 7.5: Photoactivity of the composite TiO_2 spheres with respect to time using 100 mg L^{-1} of FA.

7.3.3 Comparison with Degussa P-25

The performance of the composite TiO_2 spheres at degrading FA was compared with that of particulate TiO_2 (Degussa P-25). In both cases, the experiments were performed under exactly identical conditions, e.g., initial concentration of FA, irradiation flux, and flow rate.

Prior to the comparative investigation, the set ups shown in Figure 4.7 and 4.8 were operated with different amounts of P-25 to determine the impact of P-25 loading on FA degradation. As shown in Figure 7.6, the reaction rate constant changed with P-25 loadings. The rate constant increased with increasing the TiO_2 loading until a plateau was reached after a concentration of 0.4 g of P-25 in 1 L of water. This indicates that photon absorption starts to be the limiting factor as the amount of P-25 powder goes beyond 0.4 g L^{-1}. With further increase in catalyst concentration (i.e., beyond 1 g L^{-1}), FA degradation rate decreases since suspended particles absorb photons and block the illumination path. At the same time, diffusion and mass transfer limitations could also dominate since the radiation is higher at the

wall and most reactions take place in this region. For the purpose of this research and given that P-25 loadings of between 0.4 g L^{-1} and 1 g L^{-1} gave similar FA degradation rates, a loading of 0.75 g L^{-1} was selected.

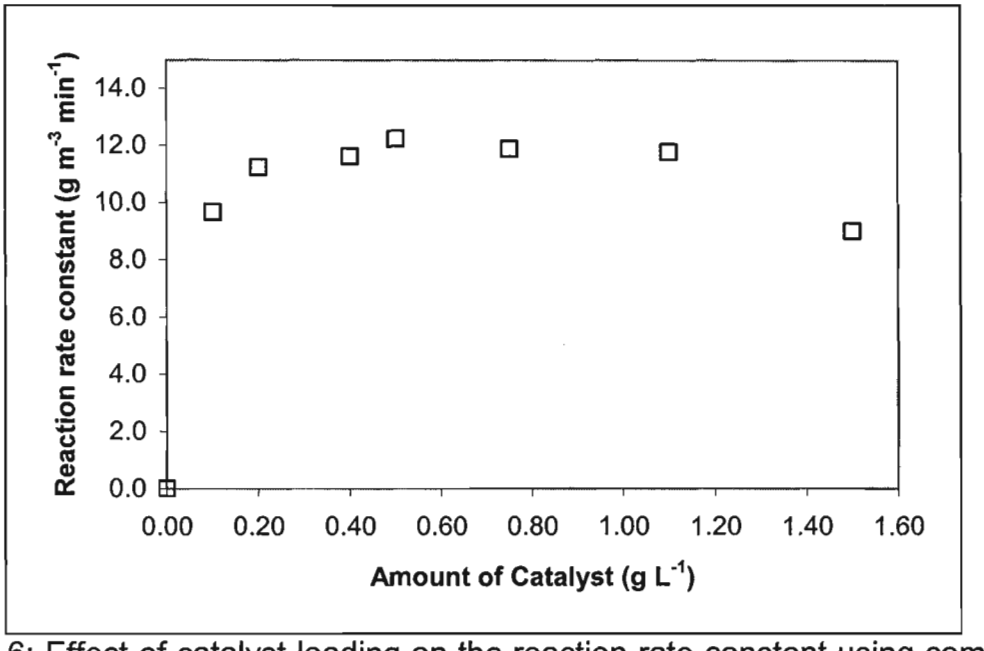

Figure 7.6: Effect of catalyst loading on the reaction rate constant using commercial TiO_2 powder (Degussa P-25) as a photocatalyst: C_{FAo} = 100 mg L^{-1}, V_{tot} = 1L.

It should be noted that these results depend on the photoreactor geometry, characteristics of UV radiation (power and wavelength), pollutant concentration, and also the kind of photocatalyst used (Minero and Vione, 2006; Muruganandham and Swaminathan, 2006). Chen *et al.* (2008) found that 3 g L^{-1} was the most efficient for the degradation of FA. Dijkstra *et al.* (2001) reported that a catalyst loading of 2 g L^{-1} was found to be optimum for FA degradation. All those literature studies were performed in set-ups different from that used in this investigation.

A significant reduction in the concentration of FA was observed when the reactor was loaded with Degussa P-25 and treated with UV irradiation (Figure 7.7a). Langmuir-Hinshelwood kinetic model was used to describe the FA degradation, giving an average reaction rate constant of 11.87 g_{FA} m^{-3} min^{-1}. Similar to the case with composite TiO_2 spheres (Figure 7.7b), there was no significant photolytic

degradation when the reactor was operated with the UV lamps on, but without the P-25. At the same time, when there was no UV-irradiation, no reduction of FA was observed, showing that there was neither adsorption nor catalytic oxidation in the reaction system. Note that Figure 7.10 presents one set of data from three replicate experiments with the same P-25 loading of 0.75 g L^{-1}.

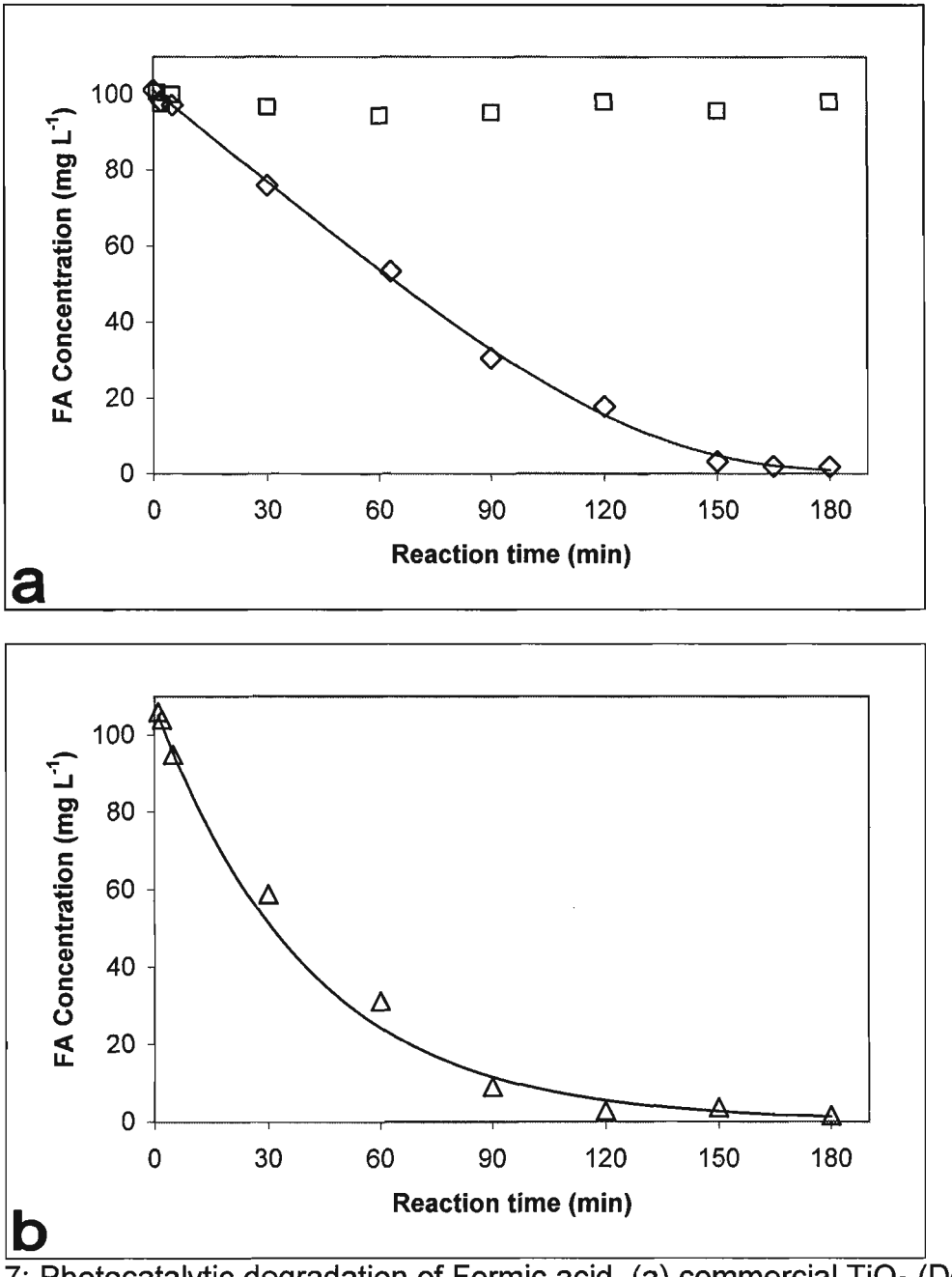

Figure 7.7: Photocatalytic degradation of Formic acid, (a) commercial TiO_2 (Degussa P-25): (□) with UV lamps off (◊) with UV irradiation; (b) composite TiO_2 spheres.

For a better comparison between the composite TiO_2 spheres and the commercial TiO_2 (Degussa P-25), the relative efficiency (ξ) was determined for the experiments performed with both photocatalysts. This criterion is useful for comparing quantitatively the efficiency of different photocatalysts under the same experimental conditions. Even though the mass of photocatalyst was not the same, the amount of irradiation that was applied to the catalyst and other experimental conditions were the same.

The initial reaction rates were used to compare the two photocatalysts (composite TiO_2 spheres and Degussa P-25). The relative efficiency was calculated following a similar approach described by Serpone (1996 and 1997) and Shankar *et al.* (2006). However, FA degradation using Degussa P-25 was used as the benchmark because P-25 has been known as a standard photocatalyst for many years:

$$\xi = \frac{\left(-r_{FA,0}\right)_{spheres}}{\left(-r_{FA,0}\right)_{P-25}} \tag{7.3}$$

where $-r_{FA,0}$ is the initial reaction rate for the spheres and for the P-25 (shown in Table 7.3) calculated in the first 30 min of reaction.

Table 7.3: Initial reaction rate for the FA degradation in the presence of composite TiO_2 spheres and Degussa P-25.

Photocatalyst	**Initial reaction rate, $-r_{FA,0}$ (g_{FA} m^{-3} min^{-1})**
Composite TiO_2 spheres	1.78
Degussa P-25	0.84

Using the results shown in Table 7.3, and through Equation 7.3, the relative efficiency (ξ) came to be equal to 2.12. This result indicates that the initial oxidative degradation process for FA is more effective with the composite TiO_2 spheres than with Degussa P-25. Analyzing the degradation pattern using the spheres and

Degussa P-25 (Figure 7.10), it is clear that the composite TiO_2 spheres provides faster degradation of the FA.

Another way to compare the TiO_2 spheres with P-25, using FA as a model pollutant, is using the apparent quantum yield (Φ_{app}). One assumption for the calculation of quantum yield was that all the light that is emitted from the lamp is absorbed by the catalyst. Therefore, using Equation 7.4, the quantum yield was calculated:

$$\phi_{app} = \frac{\left(-r_{FA,0}\right)_{spheres\,/\,P-25}}{I_o} \cdot V \qquad (7.4)$$

where $-r_{FA,0}$ is the initial degradation rate (mol m^{-3} s^{-1}) per unit of reaction volume V, and I_o the amount of photons entering the reactor (Einsteins s^{-1}). The value of I_o was determined using Potassium Ferrioxalate Actinometry as 1 x 10^{-4} Einsteins s^{-1} (with the lamps at 5 cm from the centre of the reactor using the cylindrical reflector). The quantum yield for the spheres was determined to be 0.60 and for the Degussa P-25 was 0.18, which is comparable to the one reported in other studies under similar conditions (McMurray *et al.*, 2004). These results indicated that more molecules of FA were degraded per photon of light absorbed using the composite TiO_2 than using the commercial TiO_2.

In terms of the characteristics of these two photocatalysts, the composite TiO_2 spheres had smaller surface area (29.37 m^2 g^{-1}) than the commercial TiO_2 powder (54 m^2 g^{-1}), but the pore volume and pore size were not that different (Table 6.6 – Section 6.3). In terms of the percentage of anatase, P-25 had 87% in comparison with 65% for the TiO_2 spheres. Based on these data, P-25 was expected to provide higher degradation than the CSG titania. However, it is postulated that light distribution in the reactor might have played a factor in bridging higher performance for the CSG catalyst, as is confirmed with the apparent quantum yield value.

7.4 Photocatalytic degradation of 2,4-D

A pesticide and related products are defined as any substance or mixture of substances, e.g. insecticide, herbicide, fungicide, etc., and any product related to any of these including any growth regulators, and their relevant metabolites, degradation and reaction products (Sinclair *et al.*, 2006). Phenoxyalkanoic acid herbicides are extensively used around the world mainly for the control of annual and perennial weeds. They are also used in lakes, ponds and ditches for aquatic weed control. One of the most frequently used herbicides in this group is 2,4-Dichlorophenoxyacetic acid (2,4-D) (Djebbar *et al.*, 2006). This widespread use of 2,4-D leads to certain environmental impacts due to the fact that during its application it could be easily spread within the environment. Once on the ground, it can be incorporated in the natural aqueous stream showing different half-lifes, depending on factors such as oxygen concentration, acidity, solar light, among others (EPA, 2008).

2,4-Dichlorophenoxyacetic acid degradation has been studied in aquatic environments by different methods such as microbial, chemical and photochemical processes with varying success (Bell, 1956; Greer *et al.*, 1990; Veeh *et al.*, 1996; Ghertner *et al.*, 2001; MacAdam and Parsons, 2009). Photocatalytic degradation has also been used as a potential technology to degrade 2,4-D. Different photocatalysts, such as ZrO_2, WO_x, MnO_2, TiO_2, Iron (II) Sulfate, among other, have been investigated and showed different results (Kwan and Chu, 2003; Alvarez *et al.*, 2007; Alvarez *et al.*, 2008; Zhang *et al.*, 2008). Among the metal oxide semiconductors suitable for photocatalytic processes, titanium dioxide (TiO_2) has received more attention because of all the advantages that this photocatalyst has such as its high photocatalytic activity, its low price, etc.

Photocatalytic decomposition of 2,4-D has been investigated using different reactor configurations such as solar reactors (Kamble *et al.*, 2006; Bandala *et al.*, 2007) and with different catalyst configurations like slurry systems (Trillas *et al.*, 1995; Djebbar and Sehili, 1998; Kamble *et al.*, 2006; Galindo *et al.*, 2008; Rodriguez – Gonzalez *et al.*, 2008) and supported catalyst on different surfaces (Trillas *et al.*, 1996; Modestov and Lev, 1998; Shankar *et al.*, 2006; Giri *et al.*, 2008) showing a

variety of results. At the same time, different mechanisms have been proposed to describe the photocatalytic degradation of 2,4-D; however, it has been reported that the action of •OH radicals contribute in about 70% to the conversion of 2,4-D and the other 30% can be attributed to the capture of positive holes by the adsorbed 2,4-D on the surface of the photocatalyst (Djebbar and Sehili, 1998). Figure 7.8 shows the mechanism and pathway of 2,4-D degradation with its intermediates, including the more predominant 2,4-Dicholorophenol (2,4-DCP).

For the purpose of this work and prior to any photocatalytic oxidation tests, it was necessary to determine the adsorption of this pollutant on the composite photocatalyst. Hence, a detailed adsorption study was performed first. The photocatalytic degradation was then performed with three different irradiation levels (i.e., fluence rates) and three different initial concentrations of 2,4-D. In addition, a comparison between the composite TiO_2 spheres and Degussa P-25 was done to determine the performance of TiO_2 spheres with respect to the standard photocatalyst.

7.4.1 Adsorption study of 2,4-D on the composite TiO_2 spheres

Adsorption equilibrium studies were conducted under dark conditions using 30 mL aliquots of 2,4-D solution (concentrations up to 20 mg L^{-1}) in contact with 1.5 g of TiO_2 spheres for about 2 h to allow equilibrium. The ratio of 20 mL of 2,4-D solution g^{-1} catalyst was the same as that used in the photocatalytic reactor. The equilibrium was established when the amount of solute being adsorbed onto the adsorbent was equal to the amount being desorbed, i.e., there was no further change in the concentration of 2,4-D in the solution.

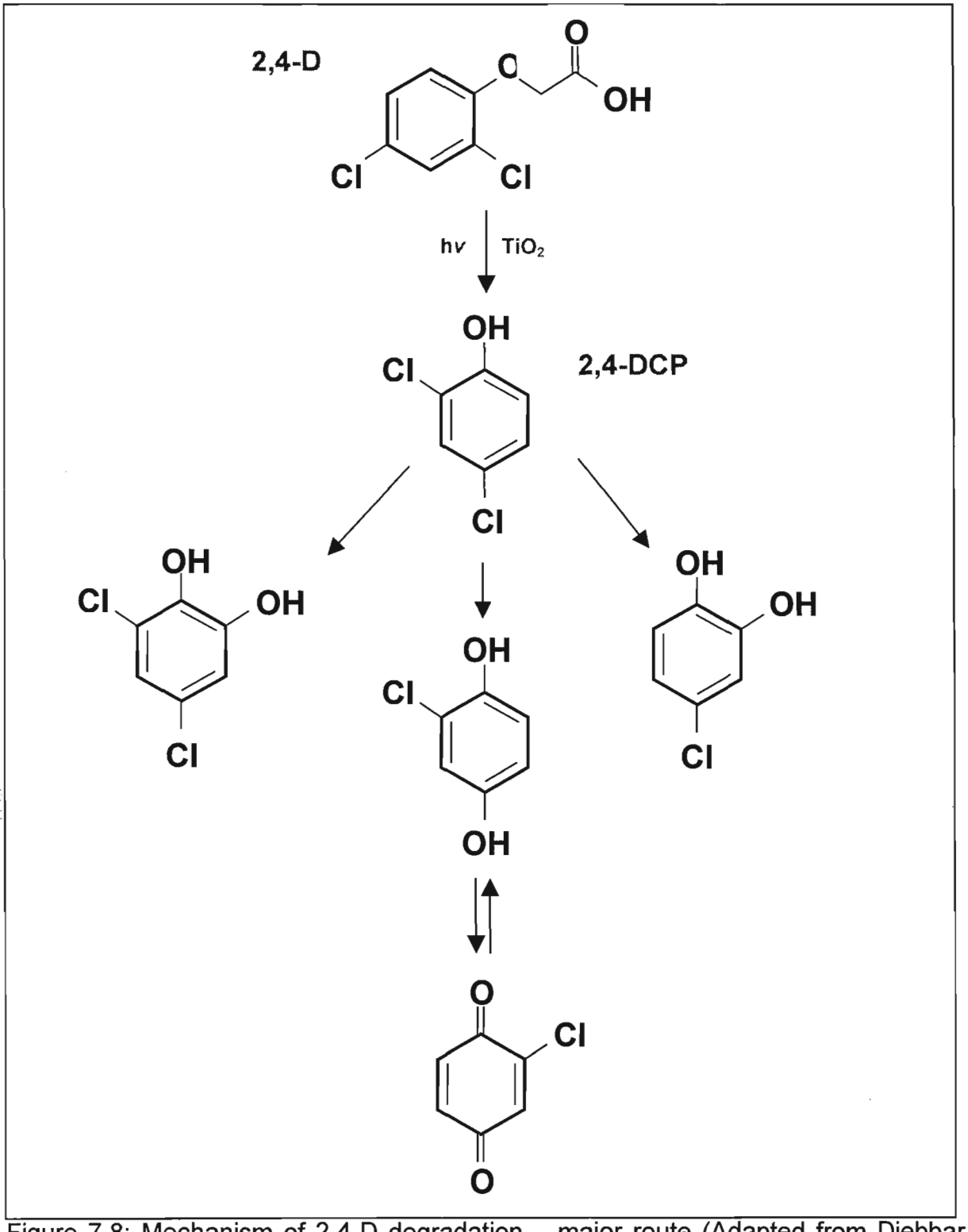

Figure 7.8: Mechanism of 2,4-D degradation – major route (Adapted from Djebbar and Sehili, 1998).

Figure 7.9 shows the amount of contaminant adsorbed per mass of catalyst plotted against the concentration of the contaminant in the bulk solution upon the attainment of the equilibrium. According to the results and in the range of concentrations studied, the adsorption isotherm follows a linear relation, as shown in Equation 7.5, which is in agreement with literature reports (Allen et al., 2004, Goetz et al., 2009):

$$C_{ads} = K \cdot C_{eq} \tag{7.6}$$

which K being equal to 2.1 x 10^{-6} m^3 g^{-1}.

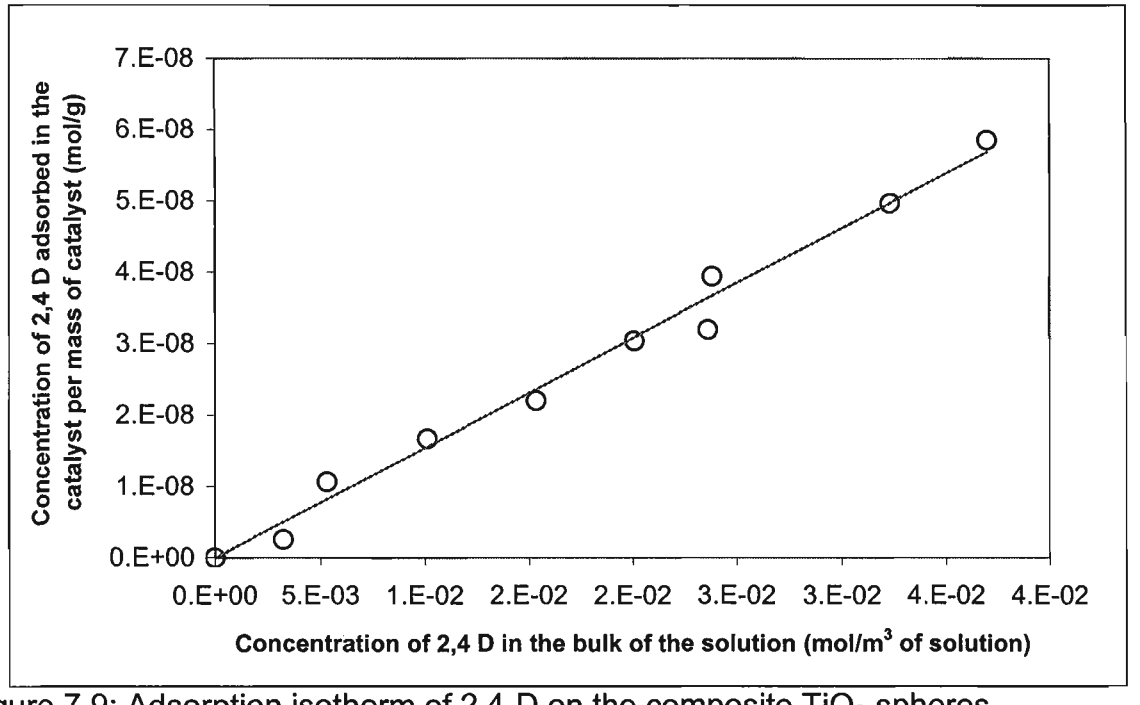

Figure 7.9: Adsorption isotherm of 2,4-D on the composite TiO_2 spheres.

Figure 7.10 shows the relation between the above mentioned isotherm (obtained in 30 mL aliquots) and some of the measurements obtained in the fluidized bed photoreactor operating under dark. All these measurements were conducted using different batches of the composite TiO_2 spheres. As can be seen, there is a

close agreement between the data obtained from the isotherm tests and those obtained during real experiments in the FBR. Nonetheless, it is worth indicating that there were some variations between different batches of TiO_2 spheres, in terms of the adsorption of 2,4-D on the catalyst, but the overall trend was very similar and consistent as shown in Figure 7.9.

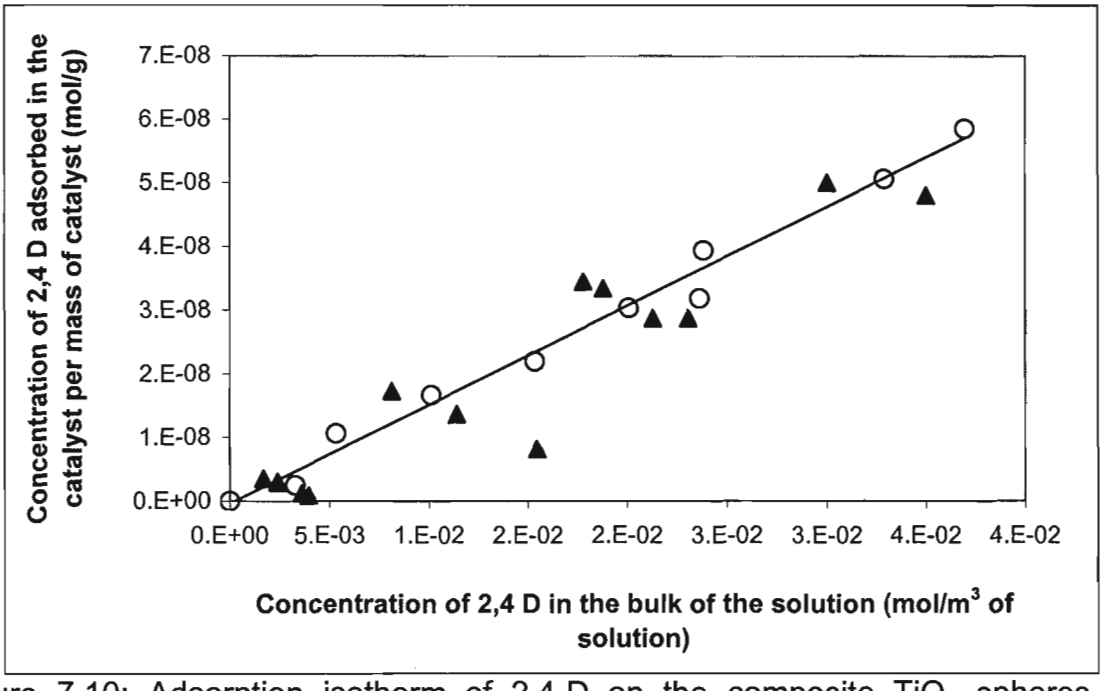

Figure 7.10: Adsorption isotherm of 2,4-D on the composite TiO_2 spheres, (o) isotherm study, (▲) measurements at the FBPR with different batches of spheres.

The adsorption phenomenon and its impact on the removal of 2,4-D from the contaminated water are further demonstrated in Figure 7.11. The concentration of 2,4-D decreases rapidly upon the start of the experiment, reaching a plateau after about 30 min. No further change in the concentration of 2,4-D demonstrates the establishment of adsorption equilibrium. Hence, all the photodegradation studies were carried out after 75 min, ensuring that there was no adsorption taking place. When the UV lamps were turned on, the photocatalytic degradation of 2,4-D and the formation of the main intermediate (2,4-DCP) started.

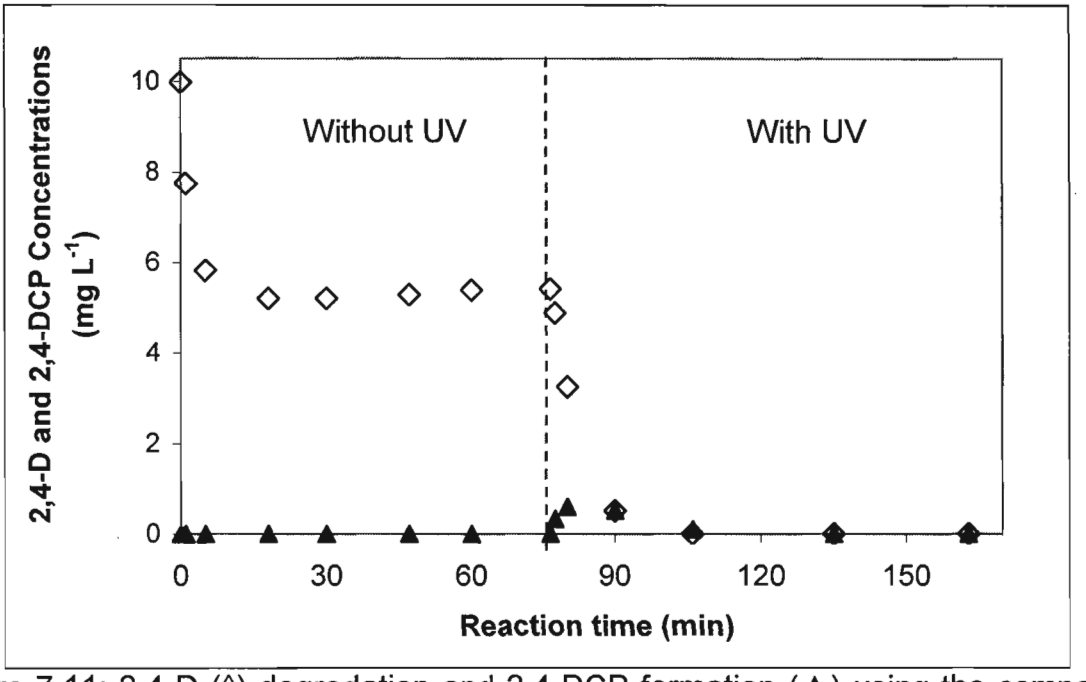

Figure 7.11: 2,4-D (◊) degradation and 2,4-DCP formation (▲) using the composite TiO_2 spheres.

7.4.2 Effect of different levels of irradiation on 2,4-D degradation

The effect of three different lamp positions (i.e., fluence rates) on the degradation of 2,4-D was studied. As shown in Figure 7.12, different levels of irradiation induced a difference in the degradation pathway. When the UV lamps were placed farthest from the centre of the reactor (i.e., the fluence was the lowest), the degradation was slower than when the lamps were in closer positions. Therefore, after 30 min of irradiation the conversion of 2,4-D (with respect to the equilibrium concentration at 75 min) was 50% when the fluence rate was 2.14 mW cm^{-2} and 90% when the fluence rate was 4.16 mW cm^{-2}.

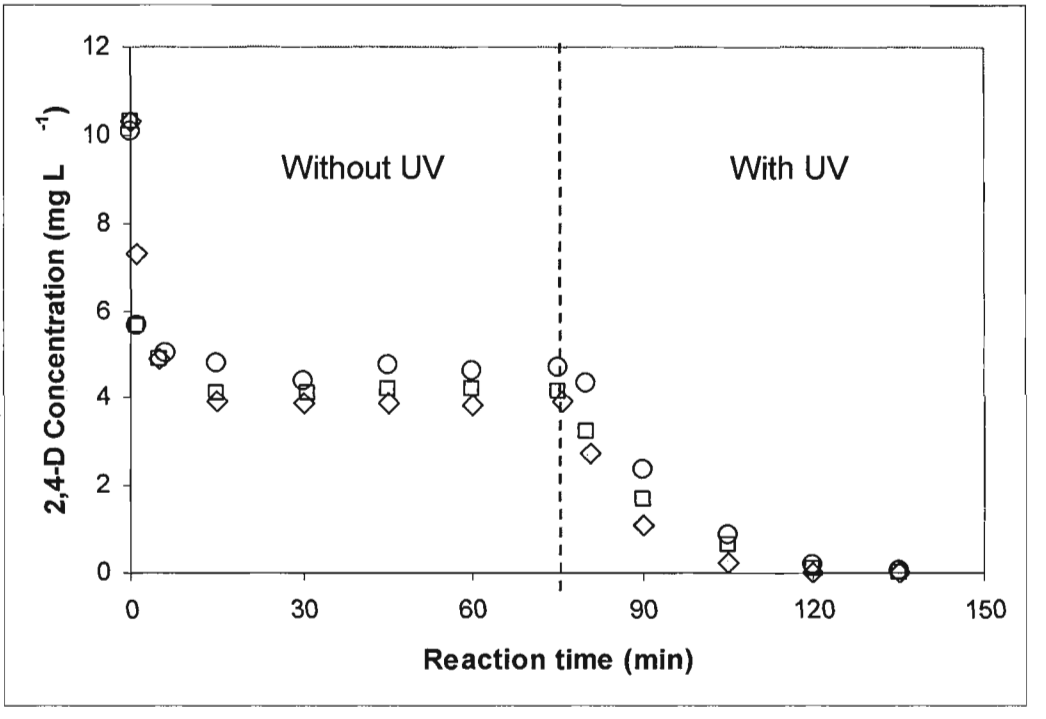

Figure 7.12: Degradation of 2,4-D using the composite TiO_2 spheres under difference fluence rates, (◊) 4.16 mW cm^{-2}, (□) 3.04 mW cm^{-2}, (o) 2.14 mW cm^{-2}. The initial concentration of 2,4-D was 10 mg L^{-1}.

The degradation of 2,4-D followed pseudo-first-order kinetics at low 2,4-D concentration (Figure 7.13), which is in agreement with the literature (Shankar *et al.*, 2006; Terashima *et al.*, 2006; Giri *et al.*, 2007; Giri *et al.*, 2008). Therefore, the influence of different levels of irradiation on the degradation rate constant was determined as is shown in Table 7.4. It is observed that the degradation rate decreased with decreasing the fluence rate or increasing the distance of the lamps from the centre of the reactor.

Table 7.4: 2,4-D photodegradation rate constants ($k_{2,4\text{-}D}$) of composite TiO_2 spheres at different fluence rates using 10 mg L^{-1} of initial concentration and 25 g of composite TiO_2 spheres

Fluence rate (mW cm^{-2})	$k_{2,4\text{-}D}$ (min^{-1})	Standard error of the parameter
4.16	0.736	0.022
3.04	0.555	0.014
2.14	0.330	0.089

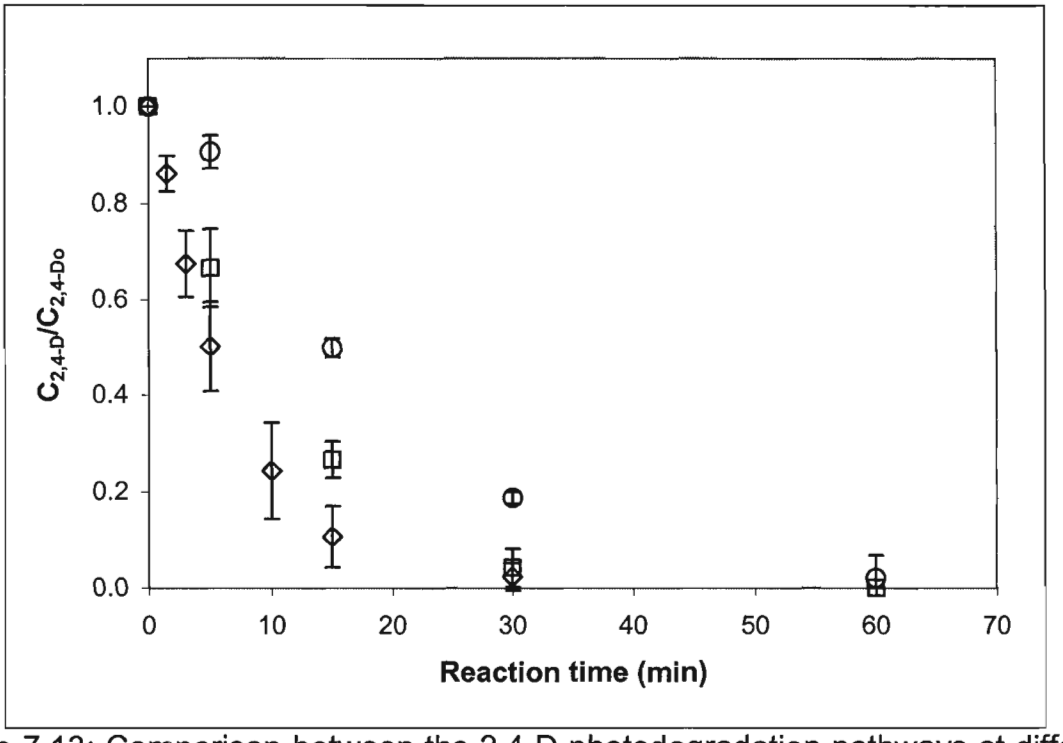

Figure 7.13: Comparison between the 2,4-D photodegradation pathways at different irradiation levels with fluences of: (◊) 4.16 mW cm^{-2}, (□) 3.04 mW cm^{-2}, (o) 2.14 mW cm^{-2}. Error bars represent 95% CI of the triplicate runs.

The reaction rate constants listed in Table 7.4 were normalized multiplying the apparent rate constant by the ratio of the total volume (500 mL) to the active volume (80 mL) according to the approach followed by Turchi and Wolfrum (1992). As shown in Table 7.4, the degradation rate constant changed with respect to the fluence rate. For high fluence rates (e.g., 4.16 mW cm^{-2}), the reaction rate constant (0.736 min^{-1}) was more than 2 times higher than the reaction rate constant (0.330 min^{-1}) at lower fluence rate (2.14 mW cm^{-2}). This result is expected since the reaction rate constant is related to the incident light intensity as was previously discussed in Chapter 2.

Once the degradation of 2,4-D started with the UV lamps turned on, 2,4-DCP (an aromatic intermediate of the 2,4-D degradation) was detected. As can be seen in Figure 7.14, the maximum amount of this intermediate was found when the fluence rate was 2.14 mW cm^{-2} (lamps at 10 cm from the centre of the reactor) mainly because with less irradiation, longer time was required to degrade the generated

2,4-DCP into other compounds. After 20 min of irradiation, with lamps at 10 cm distance, there was more than 60% more of 2,4-DCP in the system than when the lamps were in the closest position. Other four intermediates (Chlorohydroquinone, 4-Chloropyrocatechol, 2,4-Dichloropyrocatechol and Chlorobenzoquinone) were present in the system, but in very small quantities and were not tracked in this investigation. All the intermediates, including 2,4-DCP, were removed with further irradiation (e.g., over 80% removal of 2,4-DCP after 90 min).

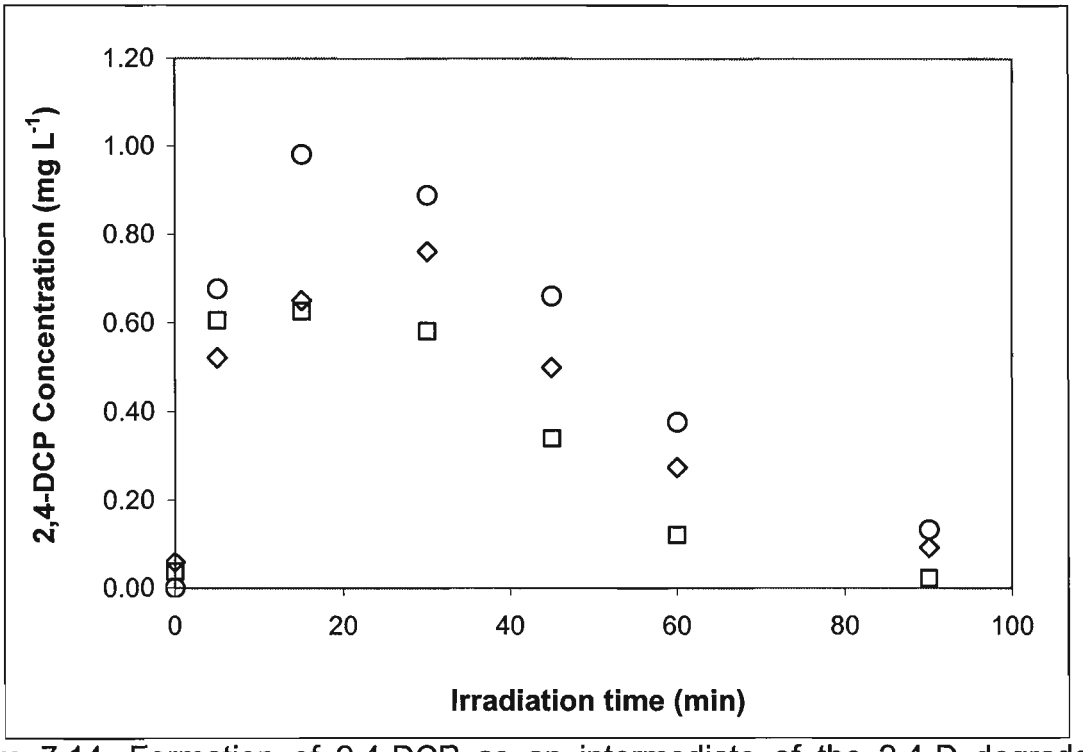

Figure 7.14: Formation of 2,4-DCP as an intermediate of the 2,4-D degradation using the composite TiO_2 spheres at different fluence rates: (□) 4.16 mW cm^{-2}, (◊) 3.04 mW cm^{-2}, (o) 2.14 mW cm^{-2}. The initial concentration of 2,4-D was 10 mg L^{-1}.

7.4.3 Effect of initial concentration of 2,4-D in its degradation

The influence of initial concentration of 2,4-D on its photodegradation rate was studied for 1, 5 and 10 mg L^{-1} using 25 g of TiO_2 spheres (Figure 7.15). The adsorption equilibrium was achieved after 30 min but the system was run under dark

up to 75 min. After this point, the UV irradiation was applied for all the concentrations.

Figure 7.16 shows the effect of the initial concentration on the photocatalytic degradation of 2,4-D. As shown, the lower the initial concentration of 2,4-D, the faster its degradation (Table 7.5). In all the cases, pseudo-first order reaction was found for the different initial concentrations, with a kinetic constant that increased as the initial reactant concentration decreases.

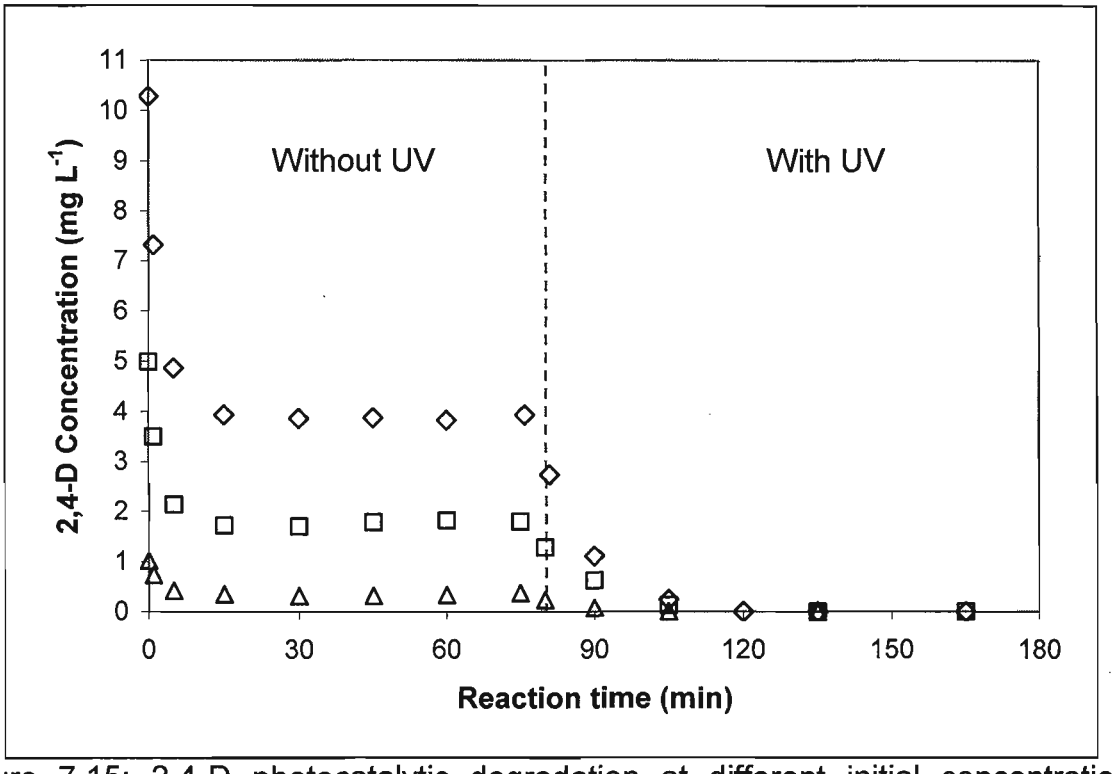

Figure 7.15: 2,4-D photocatalytic degradation at different initial concentrations, (◊) 10 mg L^{-1}, (□) 5 mg L^{-1}, (Δ) 1 mg L^{-1}. Fluence rate of 4.16 mW cm^{-2} (lamps at 5 cm from the centre of the reactor).

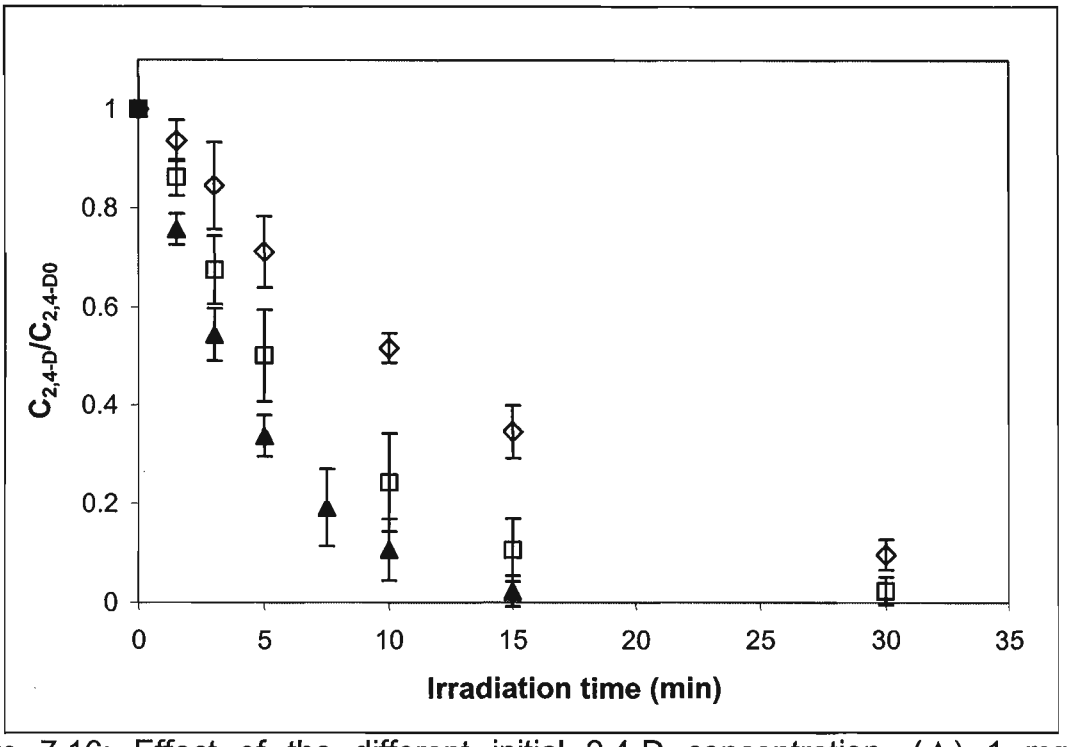

Figure 7.16: Effect of the different initial 2,4-D concentration, (▲) 1 mg L^{-1}, (□) 5 mg L^{-1}, (◊) 10 mg L^{-1}. Fluence rate equal to 4.16 mW cm^{-2} (lamps at 5 cm from the centre of the reactor).

Table 7.5: Pseudo-first-order kinetic rate constants ($k_{2,4\text{-}Dobs}$) in photocatalytic degradation of 2,4-D with different initial concentration (fluence rate = 4.16 mW cm^{-2}) using 25 g of composite TiO_2 spheres

2,4-D initial concentration (mg L^{-1})	$k_{2,4\text{-}Dobs}$ (min^{-1})	Standard error of the parameter
1	1.383	0.195
5	0.984	0.084
10	0.736	0.022

In pure first order kinetics, it is expected to see a linear relation between the concentration and the reaction rate. In other words, the higher the concentration, the faster the reaction rate. At the same time, the reaction rate constant should be relatively constant no matter which concentration of pollutant is used. However, the experimental results showed that the reaction rate constant changed with the initial concentration of 2,4-D (the lower the initial concentration, the higher the rate

constant). Beltran-Heredia *et al.* (2001) proposed a model to explain similar results considering that the rate determining step of the catalyzed reaction is the reaction between •OH radicals and organic molecules over the catalyst surface. The proposed hypothesis was based on the theory that TiO_2 surface possesses both acidic and basic sites. The acidic sites are associated with coordinatively unsaturated surface metal ions while the basic sites are associated with surface anions or anion vacancies. These two types of sites can be involved in the adsorption process of the reacting species. One will adsorb the reacting specie (2,4-D) and its degradation products; the other one will be able to adsorb oxygen (Beltran-Heredia *et al.*, 2001). Therefore, the reaction rate for second order surface decomposition might be written in terms of Langmuir-Hinshelwood kinetics as is shown in Equation 7.6:

$$r = k''\theta_{OH}\theta_{2,4-D} \tag{7.6}$$

in which k'' is the surface second order rate constant, θ_{OH} is the fractional site coverage by hydroxyl radicals and $\theta_{2,4\text{-}D}$ is the fraction of sites covered by 2,4-D. These last two variables can be written as follows:

$$\theta_{OH} = \frac{K_{O_2a}P_{O_2}}{1+K_{O_2a}P_{O2}} \tag{7.7}$$

$$\theta_{2,4-D} = \frac{K_{2,4-D}C_{2,4-D}}{1+K_{2,4-D}C_{2,4-D}+\sum_i K_i I_i} \tag{7.8}$$

where K_{O2}, $K_{2,4\text{-}D}$ and K_i are equilibrium adsorption constants and I refers to the various intermediate products of 2,4-D. Turchi and Ollis (1989) proposed a kinetic simplification that helps to explain results from several researchers investigating degradation of aromatics compounds. In this simplification it is assumed that the degradation is a step-wise process (more than one intermediate is involved in the

degradation pathway of an aromatic compound) where the K_i values of the generated intermediates are fairly similar to the reactant $K_{2,4\text{-}D}$ value ($K_i \approx K_{2,4\text{-}D}$). Thus, simplifying Equation 7.8, the following relation can be obtained:

$$\theta_{2,4-D} = \frac{K_{2,4-D} C_{2,4-D}}{1 + K_{2,4-D} C_{2,4-D_0}} \tag{7.9}$$

where $C_{2,4\text{-}D0}$ is the initial concentration of 2,4-D, that is equal to the concentration of 2,4-D plus the intermediates present in the system ($C_{2,4\text{-}D0} \approx C_{2,4\text{-}D} + \Sigma I_i$). In addition, considering that the partial pressure of oxygen is constant during the photocatalytic run, the fractional site coverage by hydroxyl radicals was constant and equal to k_c. Then, Equation 7.6 can be written as:

$$r = k'' \cdot k_c \frac{K_{2,4-D} C_{2,4-D}}{1 + K_{2,4-D} C_{2,4-D_0}} = k_{obs} C_{2,4-D} \tag{7.10}$$

which is a pseudo-first order kinetic equation with respect to the pollutant concentration. In this way, the results listed in Table 7.6 can be explained in terms of the Langmuir-Hinshelwood kinetic model in which the degradation rate of 2,4-D would be faster for the more dilute solution. In dilute solutions there will be more active sites available for the adsorption of 2,4-D and, at the same time, less amount of degradation intermediates will compete with the 2,4-D for the active sites of the photocatalyst.

The formation of 2,4-DCP at different initial concentrations is shown in Figure 7.17. As can be seen, the maximum amount of this intermediate was found when the initial concentration was 10 mg L^{-1}. This result was expected because the higher the concentration of 2,4-D, the higher the concentration of the intermediates that are formed (for a given fluence rate) along the photocatalytic degradation of the parent compound.

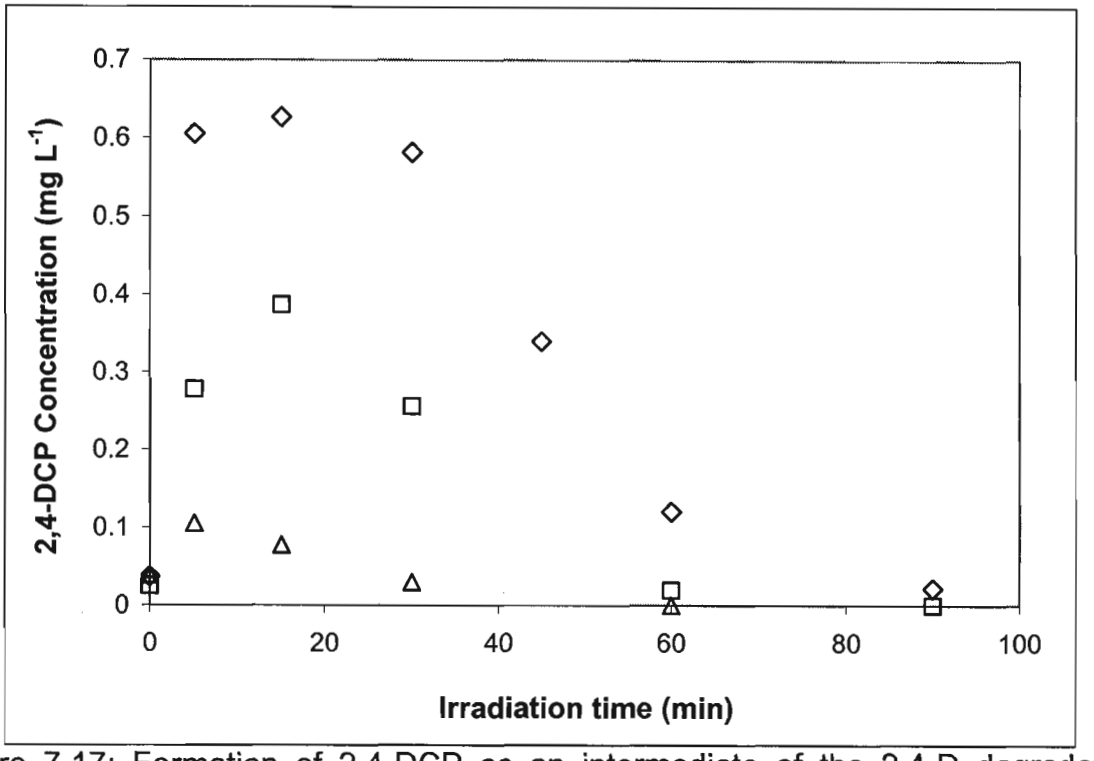

Figure 7.17: Formation of 2,4-DCP as an intermediate of the 2,4-D degradation using the composite TiO_2 spheres at different initial concentration of 2,4-D: (◊) 10 mg L^{-1}, (□) 5 mg L^{-1}, (Δ) 1 mg L^{-1}. The lamp position in all the cases was 5 cm from the centre of the reactor (fluence rate equal to 4.16 mW cm^{-2}).

The pH evolution was monitored during the 2,4-D degradation with the initial concentration of 5 mg L^{-1}. As shown in Figure 7.18, the pH increased rapidly in a short period of time from 4.70 to 5.10, and then remained stable up to 80 min (which is consistent with the start of the irradiation). Upon the start of irradiation, pH increased again to a value of 5.40 (possibly due to the formation of the intermediates, specially 2,4-DCP) and then remained constant until the end of the experiment. The initial pH and its evolution along the photocatalytic process need to be carefully determined because pH might affect the surface charge on the photocatalyst and the state of the ionization of the substrate, and hence its adsorption (Marczewska and Marczewski, 1997; Kamble *et al.*, 2004). This change in pH might explain some of the variability that was found during the adsorption study as was discussed by Marczewska and Marczewski (1997) and Pettibone et al.

(2008) where different organic compounds showed different adsorption behaviours on different adsorbents, such as TiO_2 nanoparticles, at different pH.

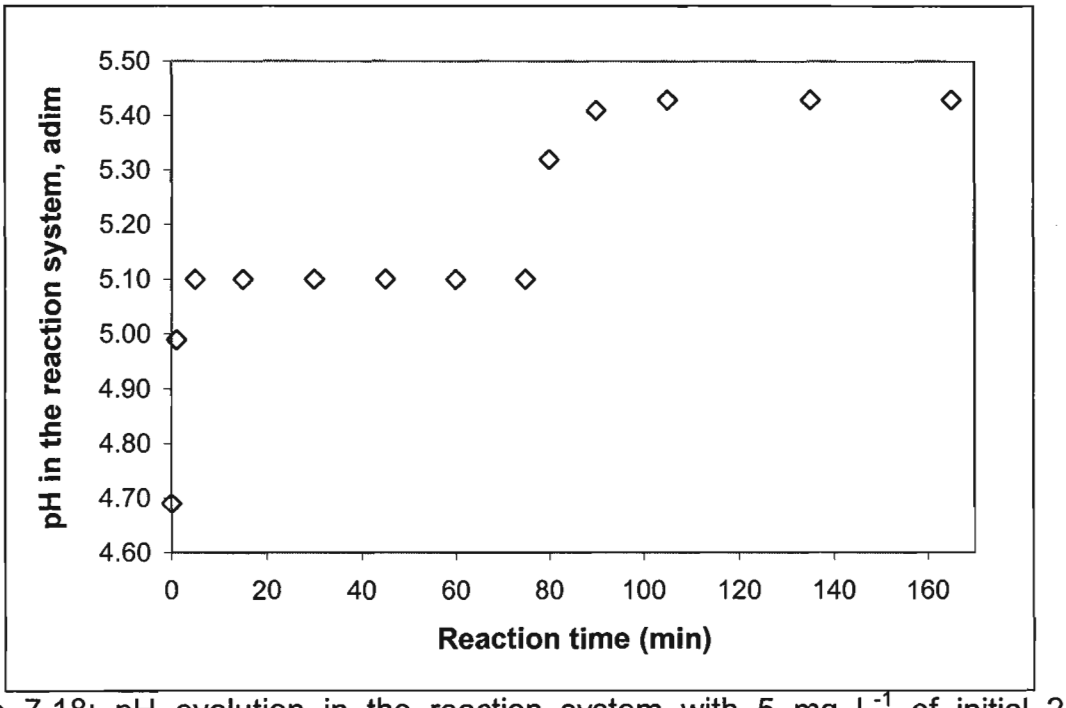

Figure 7.18: pH evolution in the reaction system with 5 mg L^{-1} of initial 2,4-D concentration.

7.4.4 Deactivation of the TiO_2 spheres

Photocatalytic deactivation was investigated through repeated use of the TiO_2 spheres for the degradation of 2,4-D. Figure 7.19 shows the removal of 2,4-D over three runs. After each run was completed, the reaction system was charged with 2,4-D to bring the concentration to the original level. From the results, it is evident that the activity of the catalyst remained the same and the pollutant was removed completely within 60 min of irradiation. The same was observed for the adsorption capacity of the photocatalytic spheres.

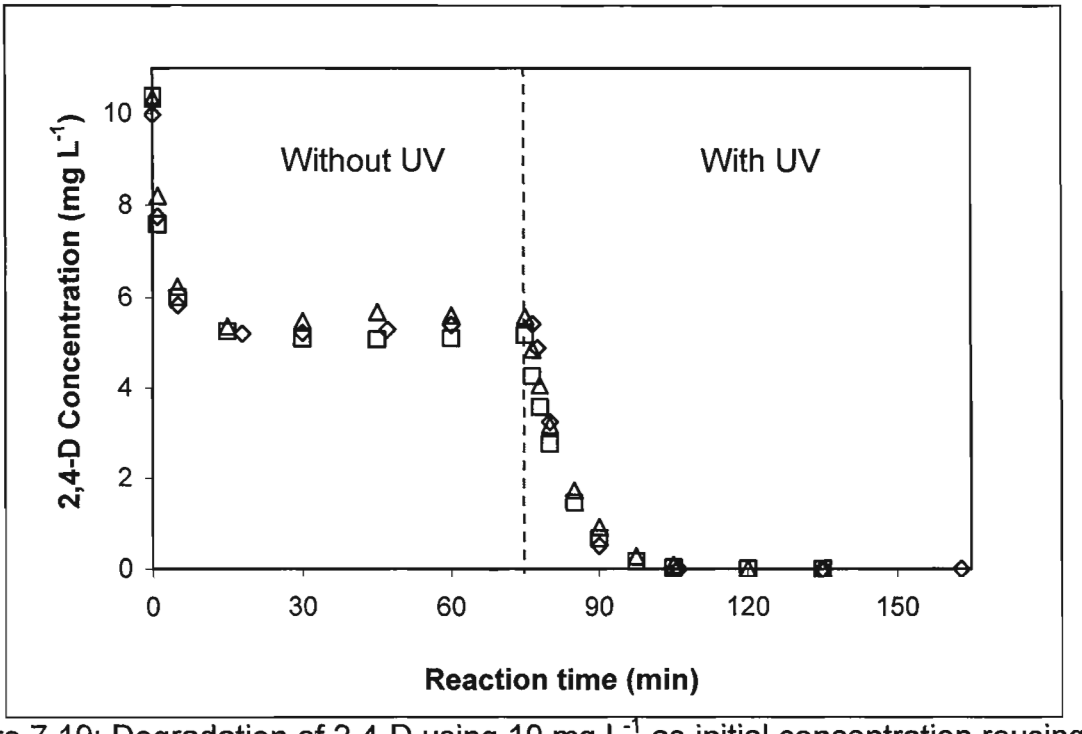

Figure 7.19: Degradation of 2,4-D using 10 mg L^{-1} as initial concentration reusing the TiO_2 spheres, (◊) 3 h, (□) 8 h, (Δ) 15 h.

The experiments shown in Figure 7.19 were performed in batch modes, that is, each run was done independently (after the first run, the UV lamps were turned off and the concentration of 2,4-D was re-established). Nonetheless, it was important to perform the same experiment with continuous irradiation, meaning that immediately after the first run, the concentration of 2,4-D was re-established (without turning off the UV lamps). Figure 7.20 shows the results of such experiments with 10 mg L^{-1} of 2,4-D added to the solution each time when the concentration depleted in the solution. As shown, 2,4-D degradation did not change with subsequent additions of 2,4-D. At the same time, the 2,4-DCP, as the main intermediate, was formed and degraded in all of the above mentioned runs.

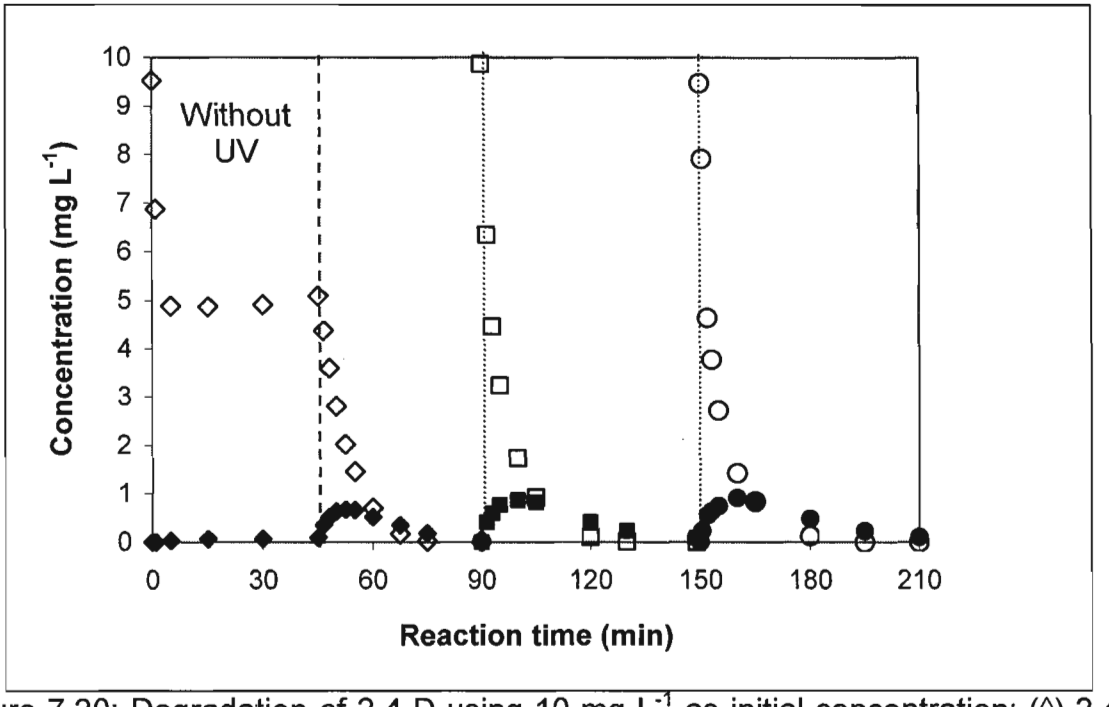

Figure 7.20: Degradation of 2,4-D using 10 mg L^{-1} as initial concentration: (◊) 2,4-D for the first run; (♦) 2,4-DCP generation during the first run; (□)2,4-D for the second run; (■) 2,4-DCP generation during the second run; (o) 2,4-D for the third run; (●)2,4-DCP generation during the third run.

7.4.5 Comparison with Degussa P-25

The performance of the composite TiO_2 spheres at degrading 2,4-D was compared with that of particulate TiO_2 (Degussa P-25). In both cases, the experiments were conducted under exactly identical conditions, e.g. initial concentration of 2,4-D and same irradiation to the reactor.

Similar to the case for FA (described in Section 7.3.4), the P-25 catalyst loading was 0.75 g L^{-1}. Also, this analysis was done just for the lamps at 5 cm from the centre of the reactor and without the cylindrical reflector (fluence rate equal to 4.16 mW cm^{-2}). Other lamp positions were not investigated.

Figure 7.21 shows the degradation of 2,4-D with 0.75 g L^{-1} using 10 mg L^{-1} initial concentration of the pollutant. The concentration of 2,4-D decreased upon the start of the experiment, reaching a plateau after 30 min. No further change in the concentration of 2,4-D demonstrate the establishment of adsorption equilibrium. No

significant photolytic degradation was observed when the reactor was operated with the UV lamps on, but without the P-25.

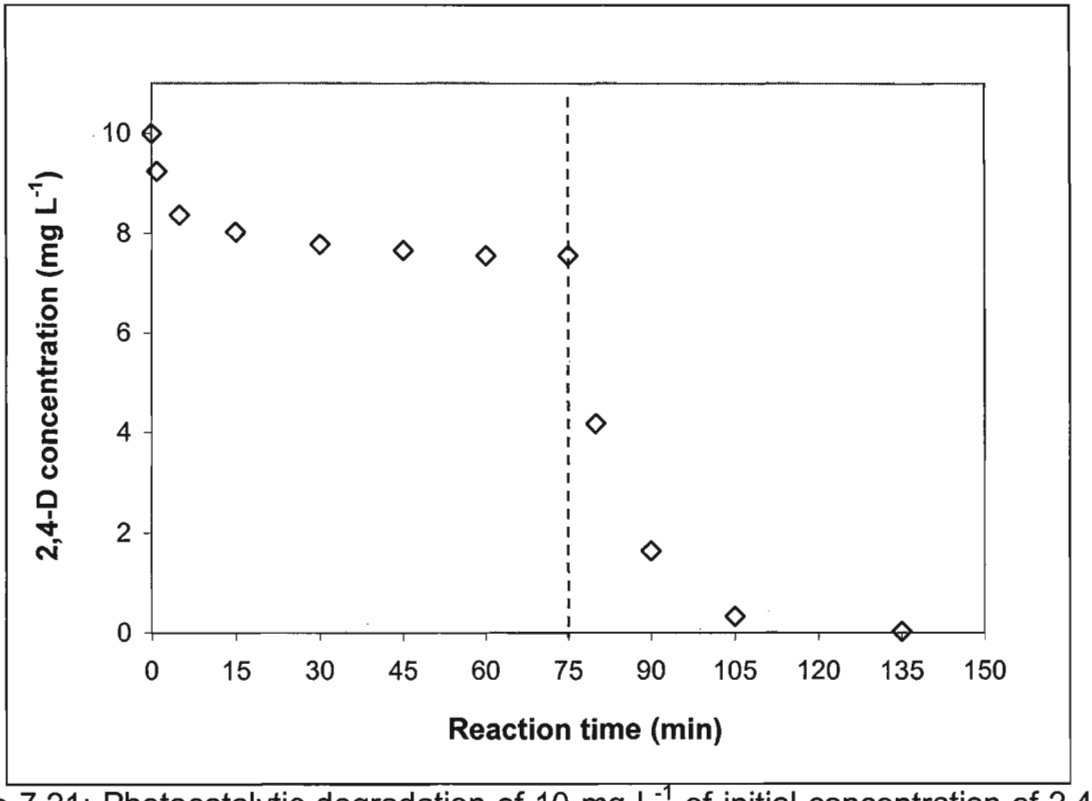

Figure 7.21: Photocatalytic degradation of 10 mg L^{-1} of initial concentration of 2,4-D (fluence rate equal to 4.16 mW cm^{-2}).

As can be seen in Figure 7.21, the degradation follows a pseudo-first-order kinetics with an average reaction rate constant of 0.09 min^{-1}. Figure 7.22 shows the photocatalytic degradation of 2,4-D using the commercial TiO_2 and the composite TiO_2 spheres. As shown, the spheres degraded the 2,4-D faster than the other catalyst, i.e., after 15 min of irradiation there was 50% less 2,4-D using the spheres than with Degussa P-25.

For a better comparison between the composite TiO_2 spheres and the commercial TiO_2 powder (Degussa P-25), the relative efficiency (ξ) was determined for the experiments performed with both catalysts. Even though the mass of the catalyst was not the same, the amount of irradiation that was applied to the catalysts and other experimental conditions were the same.

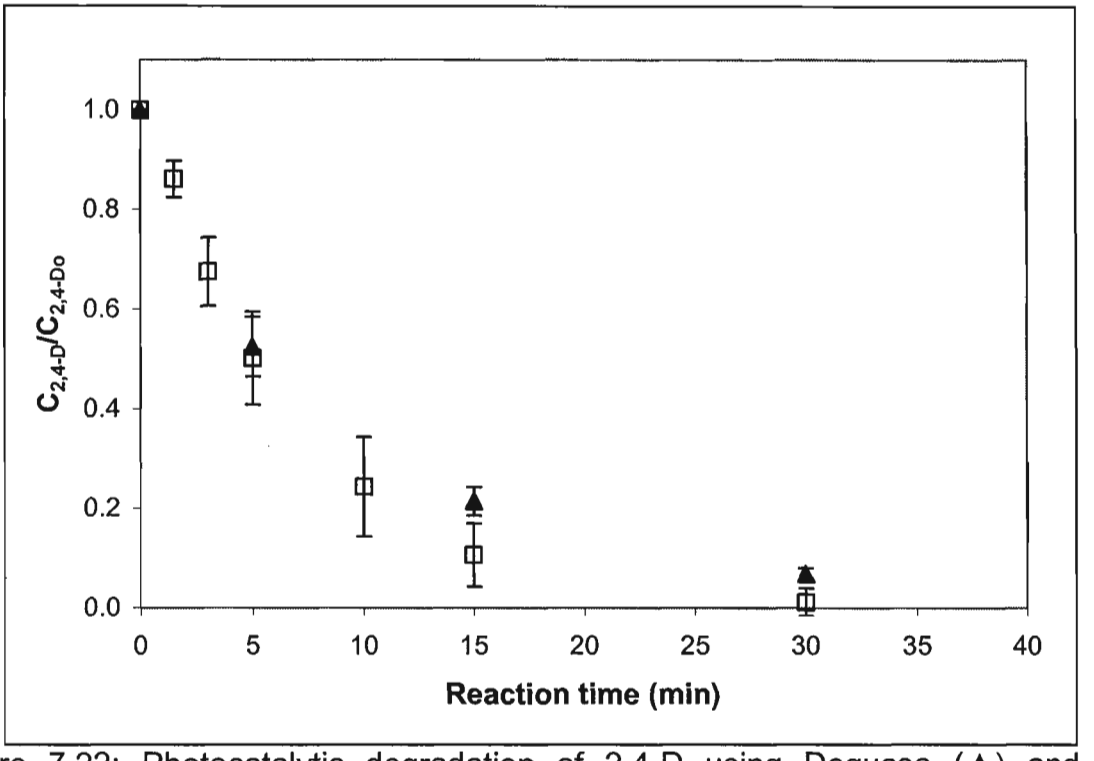

Figure 7.22: Photocatalytic degradation of 2,4-D using Degussa (▲) and the composite TiO_2 spheres (□) with an initial concentration of 10 mg L^{-1}. Lamps position at 5 cm from the centre of the reactor (fluence rate equal to 4.16 mW cm^{-2}).

The relative efficiency is defined as the ratio of the initial rates of the pollutants for the two photocatalysts as shown in Equation 7.11. In this equation, $-r_{2,4\text{-}D,0}$ is the initial reaction rate for the spheres and for P-25 (shown in Table 7.6), calculated in the first 15 min of reaction.

$$\xi = \frac{\left(-r_{2,4-D,0}\right)_{spheres}}{\left(-r_{2,4-D,0}\right)_{P-25}} \tag{7.11}$$

Table 7.6: Apparent reaction rate constant for the 2,4-D degradation in the presence of composite TiO_2 spheres and Degussa P-25

Photocatalyst	Initial reaction rate, $-r_{2,4\text{-}D}$ x 10^{-2} ($mg_{2,4\text{-}D}$ L^{-1} min^{-1})
Composite TiO_2 spheres	5.58
Degussa P-25	3.91

Using the results shown in Table 7.6, and evaluating Equation 7.11, the relative efficiency (ξ) was equal to 1.26. This indicates that the oxidative degradation process for 2,4-D is more effective with the composite TiO_2 spheres than with Degussa P-25. Analyzing the degradation pattern using the spheres and Degussa P-25 (Figure 7.22), it is also clear that the composite TiO_2 spheres degraded the pollutant (2,4-D) faster.

7.5 Photocatalytic degradation of natural organic matter (NOM)

Natural organic matter (NOM) is defined as a complex mixture of organic compounds present in surface water. The structure and chemical composition of NOM is not well understood due to its complexity and variability with respect to season and location (Bursill *et al.*, 2002). However, it is known that from the chemical point of view, NOM is grouped into non-humic substances and humic substances. The humic substances are non-polar organic acids derived from soil humus and terrestrial aquatic plants and are subdivided into humic acids (that precipitate out of solution at pH<2) and fulvic acids (these do not precipitate) (Thurman, 1985).

NOM brings several challenges to drinking water treatment operations mainly because of its contribution to the formation of disinfection by-products (DBPs) (Nikolaou and Lekkas, 2001). It may also induce subsequent deterioration of water quality due to bacterial re-growth in distribution systems (Zhang and DiGiano, 2002). Therefore, different efforts have been made to eliminate or minimize the level of NOM in source water before treatment. Advanced oxidation processes have been extensively studied for the removal of NOM from natural water, finding that NOM could be mineralized leading to a reduction of DBPs formation (Speitel *et al.*, 2000).

This section presents the results of some preliminary tests with the composite TiO_2 spheres to determine the feasibility of using photocatalysis to reduce the amount of NOM in natural water. Water from Trepanier Creek in the Peachland area in Central British Columbia (initial TOC of approximately 5 mg L^{-1}) was treated in the

fluidized bed reactor (the same setup used for the degradation of FA and 2,4-D). As shown in Figure 7.23, 40% of the initial TOC was eliminated when the FBPR was run just with the composite photocatalyst (no UV). When the reactor was running with the catalyst and UV (photocatalytic process) there was also approximately 40% of reduction in the TOC. Therefore, all the TOC reduction that was detected during the photocatalytic process was probably due to the adsorption of NOM in the composite TiO_2 spheres (Figure 7.23). No significant photocatalytic degradation was observed when the reactor was operated with the UV lamps on, but without the composite TiO_2.

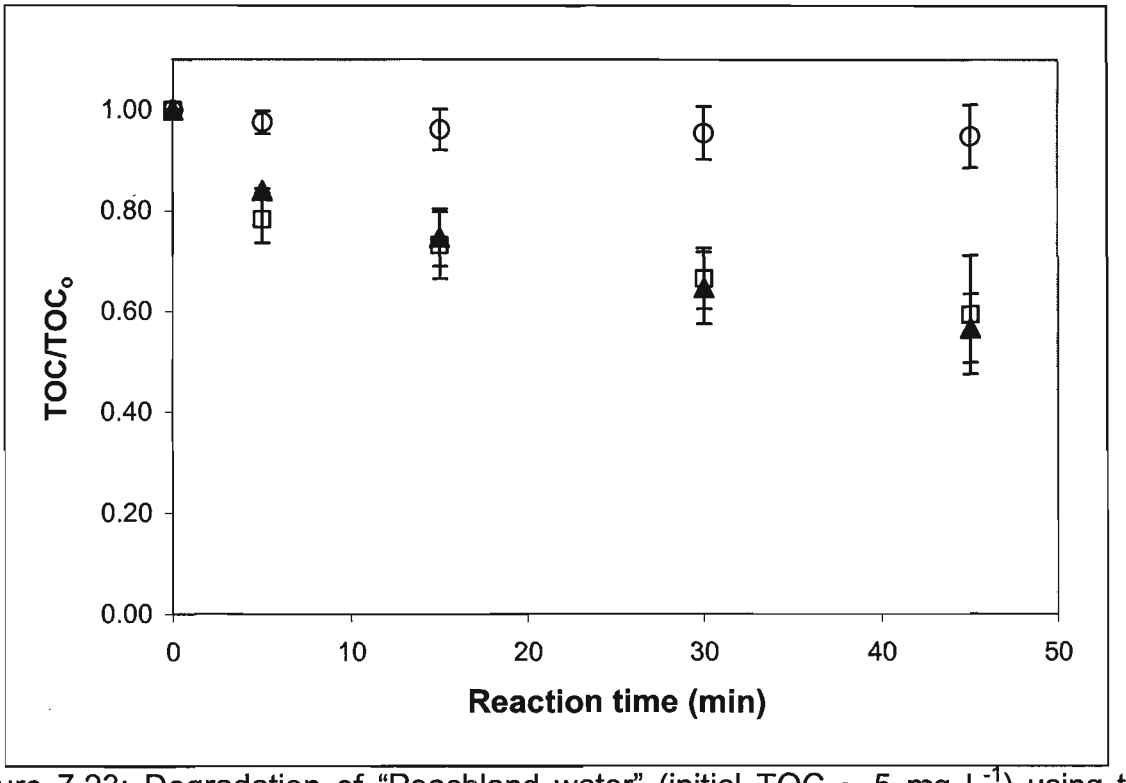

Figure 7.23: Degradation of "Peachland water" (initial TOC ~ 5 mg L^{-1}) using the composite TiO_2 spheres, (o) using only UV (fluence rate of 4.16 mW cm^{-2}) without the TiO_2 spheres, (□) with the TiO_2 spheres without UV light, (▲) with TiO_2 spheres and UV (4.16 mW cm^{-2}). Error bars represent 95% CI of triplicate runs.

An adsorption study was done using the composite TiO_2 spheres and natural organic matter. As can be seen in Figure 7.24, after 60 min approximately 40% of

the NOM was adsorbed on the spheres. After that point, the UV lamps were turned on to determine if there was some photocatalytic degradation. As shown, the concentration of NOM (or TOC) did not decrease any further after the UV lamps were turned on. Based on these preliminary results, can be concluded that under the experimental conditions used in this investigation, there is not significant photocatalytic degradation of Peachland water using CSG titania spheres. Further studies should be done to better understand the mechanism and variables involved during NOM photocatalytic degradation.

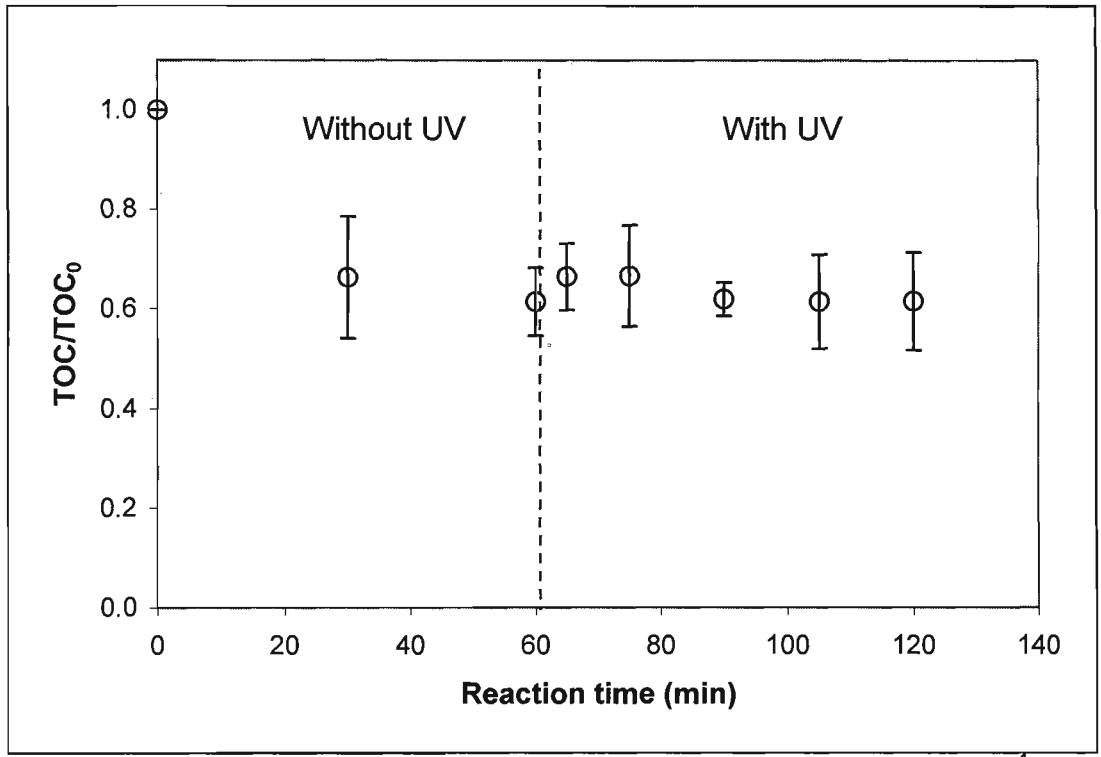

Figure 7.24: Adsorption of "Peachland water" (initial TOC ~ 5 mg L^{-1}) on the composite TiO_2 spheres. Error bars represent 95% CI of duplicate runs.

7.5.1 Effect of NOM on the degradation of 2,4-D

In order to better emulate real applications of photocatalytic processes, 2,4-D degradation was studied in the presence of NOM. The effect of NOM presence on

the degradation of 2,4-D is shown in Figure 7.25. For this study, 2,4-D was added to 500 mL of Peachland water, bringing the concentration of the pollutant to 10 mg L^{-1}. As can be seen, the degradation of 2,4-D was affected significantly and was slower than the degradation of the same concentration of 2,4-D without NOM. After 30 min of irradiation, 40% of 2,4-D was still in the solution when NOM was present as the matrix, while without NOM all the 2,4-D was degraded within the same time.

The presence of NOM, not only hindered the degradation of 2,4-D, but also reduced its adsorption on the CSG catalyst. As was shown in Figures 7.23 and 7.24 approximately 40% of NOM was adsorbed on the TiO_2 spheres; hence, this reduction in 2,4-D adsorption could be due to higher affinity of the NOM to be adsorbed on the catalyst. This clearly demonstrate the competitive effect of NOM for occupying the adsorption sites and also scavenging the •OH radicals formed during the irradiation process.

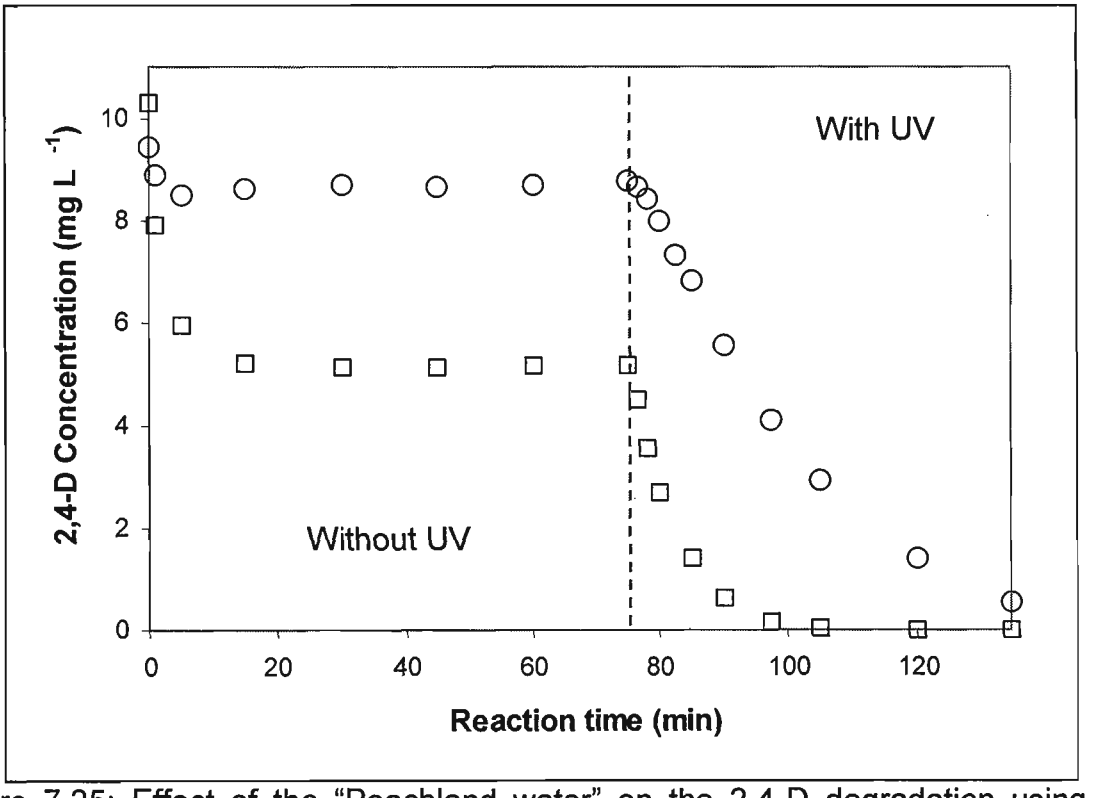

Figure 7.25: Effect of the "Peachland water" on the 2,4-D degradation using the composite TiO_2 spheres, (o) 2,4-D mix with Peahland water, (□) 2,4-D mixed with Milli-Q water.

In terms of the deactivation of the catalyst, the same batch of catalyst was run for 6 h as shown in Figure 7.26. It is shown that the activity of the catalyst was decreased after every run, indicating the consequence and impact of the NOM on the activity of the catalyst. After these three runs, the colour of the catalyst changed to light brown (originally the spheres are white); this could indicate contamination on the surface of the catalyst diminishing its activity.

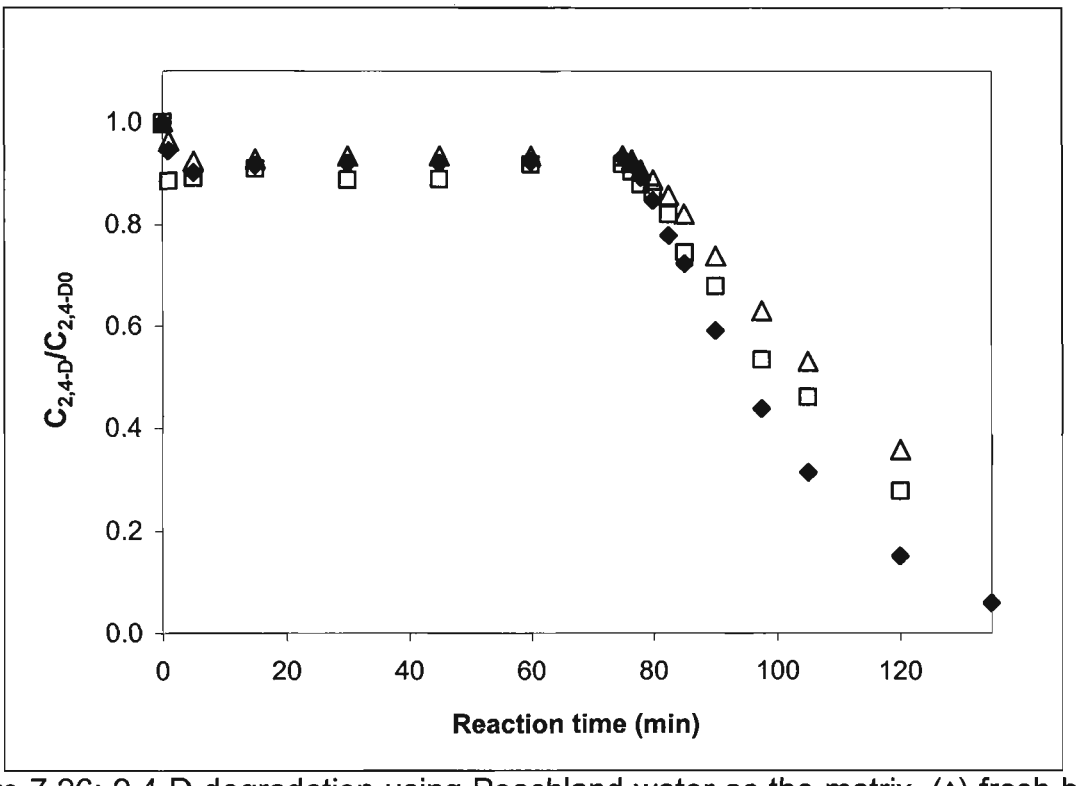

Figure 7.26: 2,4-D degradation using Peachland water as the matrix, (♦) fresh batch of TiO_2 spheres, (□) reusing the same batch of spheres the first time, (Δ) reusing the batch of spheres the second time.

7.6 Final remarks

The fluence rate within the reactor was determined to be 5.32 mW cm^{-2} when the UV lamps were located at 5 cm from the centre of the reactor and when the cylindrical reflector was used. This fluence rate decreased when the cylindrical

reflector was removed (4.16 mW cm^{-2}) and when the lamps were moved away from the reactor.

FA was used as a model organic compound to test the activity of the composite TiO_2 spheres. Using a 100 mg L^{-1} as initial concentration of FA, the degradation (showed a first order kinetics) was complete after 105 min of irradiation applying a fluence rate of 5.32 mW cm^{-2}. The effect of different irradiation levels was studied showing that the degradation rate constant changed from 0.317 ± 0.038 min^{-1} (at 5.32 mW cm^{-2}) to 0.094 ± 0.025 min^{-1} (at 2.14 mW cm^{-2}). No photocatalyst deactivation was found after 27 h of use.

The herbicide 2,4-D showed a significant adsorption on the composite TiO_2 spheres, reaching an adsorption equilibrium after 75 min. The effect of different irradiation levels and different initial concentrations were studied. At different fluence rates, the degradation rate constant (following pseudo-first order kinetics) changed from 0.736 ± 0.022 min^{-1} (at 4.16 mW cm^{-2}) to 0.330 ± 0.089 min^{-1} (at 2.14 mWcm^{-2}). At different initial concentrations, pseudo-first order reaction was found with a kinetic constant that increased as the initial reactant concentration decreased, which can be explained using Langmuir-Hinshelwood kinetic model. No photocatalyst deactivation was found after 6 h of continuous use.

Degussa P-25 (0.75 g L^{-1}) was used to compare the photoactivity of the composite TiO_2 spheres using the above mentioned organic compounds. In both cases the TiO_2 spheres showed higher activity than the commercial TiO_2.

Preliminary tests with NOM ("Peachland water" with an initial TOC of ~5 mg L^{-1}) suggested that using the spheres there was no photocatalytic degradation. On the other hand, ~40% of adsorption was found on the CSG titania. In addition, 2,4-D was mixed with NOM to determine the effect of NOM in the pesticide degradation, showing that the NOM hindered the degradation of 2,4-D and diminished the CSG spheres activity after consecutive runs.

Chapter Eight

Conclusions and Recommendations

8.1 Conclusions

This research investigated the attrition of the composite TiO_2 spheres in FBPR and how attrition can be controlled and reduced by adjusting some of the conditions in the production process of the TiO_2 spheres. In addition, the activity of the spheres to degrade contaminants in water was tested using two model contaminants, formic acid (FA) and 2,4-Dichlorophenoacetic acid (2,4-D). Also, preliminary tests with natural organic matter (in water from Trapanier Creek in Central British Columbia, Canada) were performed.

Based on the experimental work carried out in this study, the following conclusions have been made:

1. The template-free composite TiO_2 spheres were produced by mixing a composite sol-gel (CSG) titania with a viscous acidic solution of chitosan. The CSG material was a sol-derived TiO_2 with fine particles (commercial TiO_2 powder) dispersed in the liquid by high shear mixing. The commercial powder (Degussa P-25) acted as filler material providing higher efficiency of the photocatalyst. The chitosan acidic solution was used to produce the TiO_2 spheres because of its desired viscosity (needed for the spheres formation), and because of its fast hardening when in contact with basic solutions. This composite TiO_2 spheres possessed consistency in their shape and size (with a narrow size distribution around 1.15 mm at 600°C) and relatively smooth surface.

2. Modifying the composite TiO_2 spheres formulation and some of the synthesis procedures, it was possible to reduce the attrition effect of the photocatalyst. Hydrolysis and condensation reactions during the sol-gel production, the pH difference between the chitosan-TiO_2 CSG solution and the ammonia (NH_4OH)

solution, and the drying and heat treatment conditions contributed greatly to a stronger structure of photocatalyst with higher attrition resistance. The amount of TiO_2 particles in suspension were reduced from 22 mg L^{-1} to 7 mg L^{-1} (70% reduction) after 3 h of continuous operation in a FBPR based on the following changes in the procedure/formulation: i) inducing more hydrolysis and condensation reactions by increasing the amount of water from 0.040 g H_2O to 0.053 g H_2O per mL TTIP and reducing the amount of HCl from 0.20 mL HCl to 0.13 mL HCl per mL TTIP during the sol-gel production, ii) increasing the pH of the ammonia solution from 11.75 to 12.0 (increasing the percentage of ammonia from 10% to 20% v/v), iii) accelerating the drying process conditions to 80°C for 20 h, and iv) increasing the calcination time from 1 h to 3 h at 600°C.

3. During the sol-gel preparation of the TiO_2 spheres, the amount of water and catalyst (HCl) used during the gelation stage defined the rates of hydrolysis and condensation reactions in the system. With an increment in the water content and with a reduction in the amount of HCl, the viscosity of the sol increased from 4.83 cP in the original formulation to 7.94 cP. This increment in the viscosity showed that the condensation reactions during the sol-gel preparation were accelerated. These condensation reactions continued occurring even during the drying process of the spheres inducing a stiffer network because of the formation of more *Ti–O–Ti* bonds. Therefore, an accelerated drying process induced stronger spheres structure. At the same time, an increase in the calcination temperature of the spheres reduced the attrition effect of the photocatalyst, i.e., the amount of TiO_2 particles released from the catalyst to the water.

4. The calcination temperature had an enormous impact on catalyst characteristics such as the percentage of anatase and surface area. At 600°C, the surface area of the spheres was 29.37 $m^2 g^{-1}$ and at 700°C, the surface area dropped by 78% (6.44 $m^2 g^{-1}$). The percentage of anatase changed from 64.7% at 600°C to 0% at 700°C, demonstrating that phase transformation from anatase to rutile was accelerated by increasing the temperature of heat treatment. Even though high anatase/rutile ratio had proved to be beneficial for the activity of the

photocatalyst, it was found that surface area had also a significant role in photocatalyst activity, i.e., at 800°C and with 100% of rutile, the composite TiO_2 spheres showed little degradation of FA (0.025 ± 0.013 min^{-1}) and possessed a surface area of 3.79 m^2 g^{-1}. On the other hand, at 900°C (100% rutile) and no surface area, no FA was degraded. In photocatalytic reactions, larger surface area leads to faster reaction of e^- - h^+ with substrate because more substrate molecules are available to participate in the reaction.

5. The production process of the TiO_2 spheres using the new/modified formulation (MF) was more efficient (i.e., time devoted to obtain the final product was less) than that with the old formulation (OF). Using the original formulation (OF), approximately 20 days were required to produce one batch of spheres, whereas with the MF the same batch could be produced in three days. This reduction in processing time gives an added advantage to the composite TiO_2 spheres for large-scale applications.

6. Spheres at 600°C showed high activities for the degradation of FA (100 mg L^{-1}). Within 105 min of irradiation, FA was degraded in the system (with a fluence rate of 5.32 mW cm^{-2}) showing first-order reaction kinetics with a degradation rate constant of 0.315 ± 0.061 min^{-1}. At higher calcination temperatures, the degradation rate constant significantly dropped, i.e., at 800°C the degradation rate constant was 0.025 ± 0.013 min^{-1}, mainly because there was no anatase in the catalyst and the surface area was 90% smaller than that at 600°C. On the other hand, at lower fluence rates, the degradation rate constant for the FA also decreased, i.e., at 2.14 mW cm^{-2} the degradation rate constant was 0.094 ± 0.025 min^{-1}, confirming that the reaction rate constant depend on the irradiation flux applied to the system. There was no statistical difference between the photocatalytic activity of the spheres produced by the original formulation and by the new formulation.

7. 2,4-D (10 mg L^{-1}) was degraded with composite TiO_2 spheres showing pseudo first-order kinetics (reaction rate constant equal to 0.736 ± 0.022 min^{-1}) when the

fluence rate was 4.16 mW cm^{-2}. At lower fluence rates, the degradation rate constant significantly decreased, i.e., at 2.14 mW cm^{-2} the degradation rate constant was reduced by 45% (0.330 ± 0.089 min^{-1}). At different initial concentrations of the pesticide, pseudo-first order reaction was found with a kinetic rate constant that increased as the initial reactant concentration decreased. With an initial concentration of 1 mg L^{-1} the degradation rate constant was 1.383 ± 0.195 min^{-1} and at 5 mg L^{-1} the degradation rate constant was 0.984 ± 0.084 min^{-1}. This effect can be explained based on the hypothesis that in dilute solutions there will be more active sites available for the adsorption of 2,4-D and, at the same time, less amount of degradation intermediates will compete with the 2,4-D for the active sites of the photocatalyst.

8. Reusing the composite TiO_2 spheres more than once, it was found that using FA (100 mg L^{-1}) and 2,4-D (at 1, 5 and 10 mg L^{-1}), the spheres showed the same photocatalytic activity. There was no fouling or contamination of the TiO_2 spheres that led to inhibition or photocatalytic activity loss. On the other hand, when using NOM as matrix for the 2,4-D, it was found that the activity changed and reduced over time. After the third run (6 h of use) with the same batch of spheres, the degradation of 2,4-D was diminished significantly. While 83% of the 2,4-D was degraded using the fresh catalyst and after 45 min of irradiation, only 60% of 2,4-D was eliminated after once the same catalyst was used for the third consecutive run.

9. The relative efficiency parameter (ξ) was used to compare the activity of the composite TiO_2 spheres with the commercial TiO_2 photocatalyst (Degussa P-25 with a concentration of 0.75 g L^{-1}). TiO_2 spheres showed higher activity than the P-25 (ξ = 2.12) when 100 mg L^{-1} of FA was used as a model organic compound. In addition, the apparent quantum yield (Φ_{app}) was calculated for the composite TiO_2 spheres and for the commercial TiO_2 powder (Degussa P-25). For the spheres, a Φ_{app} = 0.60 was determined in contrast with the Φ_{app} = 0.21 for the P-25, confirming that the spheres were more efficient to degrade FA in the FBPR. For the degradation of 2,4-D, the relative efficiency was ξ = 1.26 suggesting that

with more complex molecules (i.e., pesticides) the composite photocatalyst showed slightly higher activity. Even though the composite TiO_2 spheres had a comparable high percentage of anatase and surface area (64% and 29 $m^2 g^{-1}$, respectively) with commercial TiO_2 (88% and 54 $m^2 g^{-1}$), the difference in activity could be due to the differences in terms of the light distribution in the system.

10. Using composite TiO_2 spheres to degrade NOM in raw drinking water (Peachland water), it was found that the spheres had a strong adsorption capacity. However, no significant photocatalytic degradation/mineralization of NOM was observed when the reactor was operated. In the presence of NOM, the degradation of 2,4-D was hindered and its adsorption on the CSG catalyst was reduced.

11. Potassium ferrioxalate actinometer better represented the fluence rate within the FBPR. Iodide-Iodate actinometer, on the other hand, showed a "saturation effect" at different lamp positions, meaning that the fluence rate slightly changed at different lamp positions around the reactor. This "saturation effect", as it suggests, was likely due to the saturation of the actinometric solution at very high photon flux that prevented proper differentiation among different levels of irradiation. The effective output of the UV lamps was calculated based on the fluence rate values of each actinometry showing a value of 4.73 W using potassium ferrioxalate and 2.80 W with iodide-iodate. Comparing these values with the nominal output of the lamps (5.7 W - given by the manufacturer) it was concluded that potassium ferrioxalate better represented the radiation characteristics within the FBPR.

8.2 Recommendations for future work

Although this investigation has shown that the modifications performed in the formulation and synthesis of the composite TiO_2 spheres provided better attrition resistance to the photocatalyst, further studies would be needed to further improve the characteristics and performance of this particular photocatalyst. It is

recommended that further investigations be carried out to quantify any additional changes the formulation and/or preparation process may offer to the mechanical stability and photoefficiency of the photocatalyst.

The following represents some of the specific recommendations for future research on the composite template-free TiO_2 spheres:

1. Study in more detail the effect of hydrolysis and condensation reactions in the attrition resistance of the composite TiO_2 spheres. As was proven in this investigation, the hydrolysis and condensation reactions helped produce a tighter network, improving the attrition resistance of the photocatalyst. Therefore, further studies in the procedure to produce the CSG could lead to a stronger TiO_2 spheres structure.

2. Explore different drying process conditions (temperature and time) to understand the real effect of these conditions on the attrition resistance of the photocatalyst.

3. Investigate the effect of lower calcination temperatures (i.e., 500°C) on the activity and attrition resistance of the composite photocatalyst produced with the new formulation (MF). It is expected that the activity of the photocatalyst would increase at lower calcination temperatures because the surface area and the anatase/rutile ratio would be higher than those at 600°C; nonetheless, the attrition resistance of the spheres might be reduced.

4. Incorporate traces of noble metals (or other materials) to the photocatalyst formulation in order to further improve the activity of the TiO_2 spheres. It is well known that adding materials such as silver, platinum or manganese help to prevent electron-hole recombination, increasing the activity of the photocatalyst. However, the production process of the spheres needs to be carefully assessed to identify the best stage to add these materials. At the same time, the characteristics of the CSG photocatalyst need to be evaluated to determine the impact of these materials on the properties of the spheres (e.g., attrition resistance)

5. Optimize the production process of the composite TiO_2 spheres in order to produce larger amounts of spheres in a more effective way, through the design of equipment with greater throughput.

6. Perform further studies with the composite spheres in the fluidization process to determine the best reactor design and operational conditions.

7. Continue the study with NOM and NOM with 2,4-D to understand better the true photocatalytic mechanism and the performance of composite TiO_2 spheres in setting that include natural water systems. These kinds of assessments are important because they will give a better understanding of the feasibility of photocatalytic process using the CSG photocatalyst under more realistic conditions.

8. Study the performance of the composite TiO_2 spheres (in terms of photoactivity and attrition resistance) in larger scale fluidized bed reactors (e.g., pilot scale reactors).

9. Investigate the deactivation of the photocatalyst (e.g., in the case of NOM and NOM with 2,4-D) and determine possible mechanism to regenerate the photocatalyst particles.

BIBLIOGRAPHY

Allen, S.J., G. Mckay and J.F. Porter. (2004). Adsorption isotherm models for basic dye adsorption by peat in single and binary component systems. J. Colloid Interf. Sci., 280, 322-333.

Alvarez, M., T. López, J.A. Odriozola, M.A. Centeno, M.I. Domínguez, M. Montes, P. Quintana, D.H. Aguilar and R.D. González. (2007). 2,4-Dichlorophenoacetic acid (2,4-D) photodegradation using an M^{n+}/ZrO_2 photocatalyst: XPS, UV-vis, XRD characterization. Appl. Catal. B – Environ., 73 (1-2), 34-41.

Alvarez, M., T. López, S. Recillas, D.M. Frías, M. Montes, J.J. Delgado, M.A. Centeno and J.A. Odriozola. (2008). Photocatalytic degradation of 2,4-dichlorophenoxyacetic acid using nanocrystalline cryptomelane composite catalyst. J. Mol. Catal. A-Chem., 281, 107-112.

Ambrus, Z., K. Mogyorósi, A. Szalai, T. Alapi, K. Demeter, A. Dombi and P. Sipos. (2008). Low temperature synthesis, characterization and substrate-dependent photocatalytic activity of nanocrystalline TiO_2 with tailor-made rutile to anatase ratio. Appl. Catal. A – Gen., 340, 153-161.

Aprile, C., A. Corma and H. Garcia. (2008). Enhancement of the photocatalytic activity of TiO_2 through spatial structuring and particle size control: from subnanometric to submillimetric length scale. Phys. Chem. Chem. Phys., 10, 769-783.

Araña, J., A. Peña Alonso, J.M. Doña Rodríguez, G. Colón, J.A. Navío and J. Pérez Peña. (2009). FTIR study of photocatalytic degradation of 2-propanol in gas phase with different TiO_2 catalyst. Appl. Catal. B – Environ., 89, 204-213.

Arguelles-Monal, W., F.M. Goycoolea, C. Peniche and I. Higuera-Ciapara. (1998). Rheological study of the chitosan/glutaraldehyde chemical gel system. Polym Gels Netw., 6, 429-440.

Arters, D.C. and L. Fan. (1986). Solid-liquid mass transfer in a gas-liquid-solid fluidized Bed. Chem. Eng. Sci., 41(1), 107-115.

Ayers, M. and A. J. Hunt. (2001). Synthesis and properties of chitosan-silica hybrid aerogels. J. Non-cryst solids, 285, 123-127.

Bandala, E.R., M.A. Peláez, D.D. Dionysiou, S. Gelover, J. Garcia and D. Macias. (2007). Degradation of 2,4-dichlorophenoacetic acid (2,4-D) using cobalt-

peroxymonosulfate in Fenton-like process. J. Photoch. Photobio. A., 186 (2-3), 357-363.

Barrett, E., L.G. Joyner and P.P. Halenda. (1951). The determination of pore volume and area distributions in porous substances: computations from nitrogen isotherms. J. Am. Chem. Soc., 73(1), 373-380.

Belapurkar, A.D., P. Sherkhane and S.P. Kale. (2006). Disinfection of drinking water using photocatalytic technique. Curr. Sci. India, 91 (1), 73-76.

Bell, G.R. (1956). On the photochemical degradation of 2,4-Dichlorophenoacetic acid and structurally related compounds in the presence and absence of riboflavin. Botanical Gazzette, 118(2), 132-136.

Beltran-Heredia, J., J. Torregrosa, J.R. Dominguez and J.A. Peres. (2001). Oxidation of p-hydroxybenzoic acid by UV radiation and by TiO_2/UV radiation: comparison and modeling of reaction kinetics. J. Hazard. Mater., B83, 255-264.

Benenati, R.F. and C.B. Brosilow. (1962). Void fraction distribution in beds of spheres. A.I.CH.E. Journal, 8(3), 359-361.

Bessenkhouad, Y., D. Robert and J.V. Weber. (2003). Synthesis of photocatalytic TiO_2 nanoparticles: optimization of the preparation conditions. J. Photoch. Photobio. A., 157, 47-53.

Bhatkhande, D.S., V.G. Pangarkar and A.A.C.M. Beenackers. (2002). Photocatalytic degradation for environmental applications – a review. J. Chem. Technol. Biot., 77 (1), 102-116.

Bideau, M., B. Claudel, C. Dubien, L. Faure, and H. Kozouan. On the "immobilization" of titanium dioxide in the photocatalytic oxidation of spent waters. J. Photoch. Photobio. A., 91, 137-144.

Bischoff, B. and Anderson, M.A. (1995). Peptization process in the sol-gel preparation of porous anatase (TiO_2). Chem. Mater., 7 (10), 1772-1778.

Bojinova, A., R. Kralchevska, I. Poulios and C. Dushkin. (2007). Anatase/rutile TiO_2 composites: Influence of the mixing ratio on the photocatalytic degradation of malachite green and orange II in slurry. Mater. Chem. Phys., 106, 187-192.

Bouchy, M., and O. Zahraa. (2003). Photocatalytic reactors. Int. J. Photoenergy, 05, 191-197.

Box, G., W.G. Hunter and J.S. Hunter. Statistics for experimenters: An introduction to design, data analysis and model building. John Wiley & Sons, Inc., USA.

Boyd, G.R., H. Reemtsma, D.A. Grimm and S. Mitra. (2003). Pharmaceutical and personal care products (PPCPs) in surface and treated waters of Louisiana, USA and Ontario, Canada. Sci. Total. Environ., 311, 135-149.

Bozzola, J.J. and L.D. Russell. (1998). Electron microscopy. Jones and Bartlett Publishers, Second Edition, Canada.

Brinker, C.J., and G. Scherer. (1990). Sol-Gel Science: The physics and chemistry of Sol-Gel processing. Academic Press, USA.

Brinker, C.J., D.E. Clark and D.R. Ulrich. (1984). Better ceramics through chemistry. North-Holland.

Brinker, C.J., D.E. Clark and D.R. Ulrich. (1986). Better ceramics through chemistry II. Materials Research Society.

Brinker, C.J., D.E. Clark and D.R. Ulrich. (1988). Better ceramics through chemistry III. Materials Research Society.

Brunauer, S., P.H. Emmet and E. Teller. (1938). Adsorption of Gases in Multimolecular Layers. J. Am. Chem. Soc., 60, 309-319.

Bursill, D., J. Van Leeuwen and M. Drikas. (2002). Problems related to particulate and dissolved components in water: the importance of organic matter. Water Sci. Technol., 2(1), 155-162.

Campanati, M., G. Fornasari and A. Vaccari. (2003). Fundamentals in the preparation of heterogeneous catalysts. Catal. Today, 77, 299-314.

Catalkaya, E.C. and F. Kargi. (2008). Advanced oxidation treatment of pulp mill effluent for TOC and toxicity removals. J. Environ. Manage., 87, 236-404.

Chao H.E., Y.U. Yun, H.U. Xingfang and A. Larbot. (2003). Effect of silver doping on the phase transformation and grain growth of the sol-gel titania powder. Journal of European Ceramic Socierty, 23, 1457-1464.

Charlot, G. (1964). Colorimetric Determination of Elements: Principles and Methods. Elsevier Pub. Co., NY – USA.

Chen, Q., J. Chang, L. Li and J.Y. Yuan. (2008). A new kinetic model of photocatalytic degradation of formic acid in UV/TiO_2 suspension system with in-situ monitoring. React. Kinet. Catal. L., 93 (1), 157-164.

Chen, W., J. Zhang, Q. Fang, S. Li, J. Wu, F. Li and K. Jiang. (2004). Sol-gel preparation of thick titania coatings aided by organic binder materials. Sensor Actuator, B 100, 195-199.

Choi, J., J. Ban, S. Choung, J. Kim, H. Abimanyu and K. Yoo. (2007). Sol-gel synthesis, characterization and photocatalytic activity of mesoporous TiO_2/γ-Al_2O_3 granules. J. Sol-Gel Sci. Techn., 44, 21-28.

Choi, H., E. Stathatos and D. Dionysiou. (2006). Sol-gel preparation of mesoporous photocatalytic TiO_2 films and TiO_2/Al_2O_3 composite membranes for environmental applications. Appl. Catal. B – Environ., 63, 60-67.

Cullo, L., Jr. Nagle, V. Elliot, Jr. Restelli, F. Edward and T. Yogan. (1987). Method to making anatase-titania attrition resistant catalyst composition. Aristech Chemical Corporation. US Patent 4 705 770.

Cumming, G., F. Fidler and D. L. Vaux. (2007). Error bars in experimental biology. J. Cell. Biol., 177 (1), 7-11.

De Lasa, H., B. Serrano and M. Salaius. (2005). Photocatalytic reaction engineering. Springer, USA.

DeBoer, J.H., B.C. Lippens, B.G. Lippens, J.C.P. Broekhoff, A. Van den Heuvel and Th. V. Osinga. (1966). T-curve of multimolecular N_2-Adsorption. J. Colloid. Interf. Sci., 21(4), 405-414.

Dijkstra, M.F.J., A. Michorius, H. Buwalda, H.J. Panneman, J.G.M. Winkelman and A.A.C.M. Beenackers. (2001). Comparison of the efficiency of immobilized and suspended systems in photocatalytic degradation. Catal. Today, 66, 487-494.

Djebbar, K., and T. Sehili. (1998). Kinetics of heterogeneous photocatalytic decomposition of 2,4-Dichlorophenoxyacetic acid over titanium dioxide and zinc oxide in aqueous solution. Pestic. Sci., 54, 269-276.

Djebbar, K., and T. Sehili. (2006). Photocatalytic degradation of 2,4-Dichlorophenoxyacetic acid and 4-Chloro-2-Methylphenoxyacetic acid in water by using TiO_2. Environ. Technol., 27, 1191-1197.

Dong, S., D. Zhou and X. Bi. (2008). Effect of liquid and gas flow rates on the performance of a fluidized bed photocatalytic reactor. Int. J. Chem. React. Eng., 6, A100.

Dunuwila, D.D., C.D. Gagliardi and K.A. Berglud. (1994). Application of controlled hydrolysis of titanium (IV) Isopropoxide to produce sol-gel-derivate thin films. Chem. Mater., 6, 1556-1562.

Eisenberg, G. (1943). Colorimetric determination of hydrogen peroxide. Ind. Eng. Chem., 15 (5), 327-328.

Emeline, A., V. Ryabachuk and N. Serpone. (2000). Factors affecting the efficiency of photocatalyzed process in aqueous metal-oxide dispersion: Prospect of distinguising between two kinetic models. J. Photoch. Photobio. A., 133, 89-98.

Emeline, A.V., V.K. Ryabchuk and N. Serpone. (2005). Dogmas and misconceptions in heterogeneous photocatalysis. Some Enlightened Reflections. J. Phys. Chem. B., 109, 18515-18521.

EPA (2008). Pesticides: 2,4-D Red Facts. Retrieved on 03/14/2009 from http://www.epa.gov/oppsrrd1/REDs/factsheets/24d_fs.htm

Falaras, P., I.M. Arabatzis, T. Stergiopoulos and M.C. Bernard. (2003). Enhanced activity of silver modified thin-film TiO_2 photocatalysts. Int. J. Photoenergy, 05, 123-130.

Fernández, A., G. Lassaletta, V.M. Jiménez, A. Justo, A.R. González-Elipe, J.M. Herrmann, H. Tahiri and Y. Ait-Ichou. (1995). Preparation and characterization of TiO_2 photocatalyst supported on various rigid supports (glass, quartz and stainless steel). Comparative studies of photocatalytic activity in water purification. Appl. Catal. B – Environ.,7, 49-63.

Fogler, H.S. (2006). Elements of chemical reaction engineering. Fourth Edition. Pearson Education Inc. USA.

Fox, M.A. and M.T. Dulay. (1993). Heterogeneous photocatalysis. Chem. Rev., 83, 341-357.

Frank, S. and A.J. Barn. (1977). Heterogeneous photocatlytic oxidation of cyanide and sulfite in aqueous solutions at semiconductor powders. J. Phys. Chem-US, 81(15), 1484-1488

Fujishima, A., T. Rao, and D. Tryk. (2000). Titanium dioxide photocatalysis. J. Photoch. Photobio. C., 1, 1-21.

Fujishima, A. and X. Zhang. (2006). Titanium dioxide photocatalysis: present situation and future approaches. C.R. Chimie, 9, 750-760.

Galindo, F., R. Gómez and M. Aguilar. (2008). Photodegradation of the herbicide 2,4-dichlorophenoxyacetic acid on nanocrystalline TiO_2-CeO_2 sol-gel catalysts. J. Mol. Catal. A-Chem., 281, 119-125.

Gao, B., Y. Ma, Y. Cao, J. Zhao and J. Yao. (2006). Effect of ultraviolet irradiation on crystallization behaviour and surface microstructure of titania in the sol-gel process. J. Solid State Chem., 179, 41-48.

Gaya, U.I., and A.H. Abdullah. (2008). Heterogeneous photocatalytic degradation of organic contaminants over titanium dioxide: A review of fundamentals, progress and problems. J. Photoch. Photobio. C., 9, 1-12.

Ghertner, D.A., T. Bertram and C. Langelier. (2001). Photochemical degradation of 2,4-D and atrazine in well-defined media. Abstr. Pap. Am. Chem. S., 221, U176.

Giri, R.R., H. Ozaki, T. Ishida, R. Takanami and S. Taniguchi. (2007). Synergy of ozonation and photocatalysis to mineralize low concentration 2,4-dicholorophenoacetic acid in aqueous solutions. CHEMOSPHERE, 66(9), 1610-1617.

Giri, R.R., H. Ozaki, R. Takanami and S. Taniguchi. (2008). Heterogenous photocatalytic ozonation in dilute aqueous solution with TiO_2 fiber. Water Sci. Technol., 58 (1), 207-216.

Goetz, V., J.P. Cambon, D. Sacco and G. Plantard. (2009). Modeling aqueous heterogeneous photocatalytic degradation of organic pollutants with immobilized TiO_2. Chem. Eng. Process, 48, 532-537.

Goldstein, S. and J. Rabani. (2008). The ferrioxalate and iodide-iodate actinometers in the UV region. J. Photoch. Photobio. A., 193, 50-55.

Greer, C.W., J. Hawari and R. Samson. (1990). Influence of environmental factors on 2,4-dichlorophenoxyacetic acid degradation by *Pseudomonas cepacia* isolated from peat. Arch. Microbiol., 154, 317-322.

Gregg, S.J. and K.S.W. Sing. (1982). Adsorption, surface area and porosity. Second Edition, Acemic Press Inc, NY - USA.

Guillard, C., D. Debayle, A. Gagnaire, H. Jaffrezic and J. Herrmann. (2004). Physical properties and photocatalytic efficiencies of TiO_2 films prepared by PECVD and sol-gel methods. Mater. Res. Bull., 39, 1445-1458.

Haarstrick, A., O. Kut, and E. Heinzle. (1996). TiO_2-asisted degradation of environmentally relevant organic compounds in wastewater using a novel fluidized bed photoreactor. Environ. Sci. Technol., 30, 817-824.

Haber, J. (1991). Manual on catalyst characterization. Pure Appl. Chem., 63 (9), 1227-1246.

Haider, A. and O. Levenspield. (1989). Drag coefficient and terminal velocity of spherical and non spherical particles. Powder Technol., 58, 63-70.

Haque, F., E. Vaisman, C. Langford and A. Kantzas. (2005). Preparation and performance of integrated photocatalyst adsorbent (IPCA) employed to degrade model organic compounds in synthetic wastewater. J. Photoch. Photobio. A., 169, 21-27.

Harris, G., M. Asce, V. D. Adams, W.M. Moore and D.L. Sorensen. (1987). Potassium ferrioxalate as chemical actinometer in ultraviolet reactors. J. Environ. Eng.-ASCE., 113 (3), 612-627.

Hashimoto, K., H. Irie, and A. Fujishima. (2005). TiO_2 photocatalyst: A historical overview and future prospects. Jpn. J. Appl. Phys., 44 (12), 8269-8285.

Hatchard, C.G. and C.A Parker. (1956). A new sensitive chemical actinometer. II. Potassium ferrioxalate as a standard chemical actinometer. Proc. R. Soc. A., 235, 518-536.

Hench, L. and J. West. (1990). The Sol-Gel process. Chem. Rev., 90 (1), 33-68.

Herrmann, J.M. (1999). Heterogeneous photocatalysis: fundamentals and applications to the removal of various types of aqueous pollutants. Catal. Today, 53, 115-129.

Higgins, R., B. A. Bishop and R. Goldsmith. A photocatalytic membrane reactor for enhanced destruction of chloro-organics in aqueous media. CeraMem Corporation – Technical document. Retrieved 06-01-2009 from http://www.netl.doe.gov/publications/proceedings/00/ind_part00/em7-4.pdf

Hill, J.O. (2005). Encyclopedia of chemical processing. Taylor & Francis Group.

Hisanaga, T. and K. Tanaka. (2002). Photocatalytic degradation of benzene on zeolite-incorporated TiO_2 film. J. Hazard. Mater. B93, 331-337.

Hoffmann, M., S.T. Martin, W. Choi and D. Bahnemann. (1995). Environmental applications of semiconductor photocatalysis. Chem. Rev., 95, 69-96.

Hosokawa, M., K. Nogi, M. Naito and T. Yokoyama. (2007). Nanoparticle technology handbook. Elsevier, USA.

Imoberdorf, G., F. Taghipour, M. Keshmiri and M. Mohseni. (2008). Predictive radiation field modeling for fluidized bed photocatalytic reactors. Chem. Eng. Sci., 63, 4228-4238.

Jackson, E. (1883). A new test for titanium and the formation of a new oxide of the metal. Chem. News., 47, 157.

Jackson, N.B., C.M. Wang, Z. Luo, J, Schwitzgebel, J. G. Ekerdt, J.R. Brock and A. Heller. (1991). Attachment of TiO_2 powders to hollow glass microbeans: activity of the TiO_2-coated beads in the photoassisted oxidation of ethanol to acetaldehyde. J. Electrochem. Soc., 138 (12), 1991

Junin, C., C. Thanachayanont, C. Euvananont, K. Inpor and P. Limthongkul. (2008). Effects of precipitation, sol-gel synthesis conditions, and drying methods on the properties of nano-TiO_2 for photocatalysis applications. Eur. J. Inorg. Chem., 974-979.

Kabir, M. (2006). Fluidized bed photocatalytic reactor system for disinfection and wastewater treatment. PhD Thesis. Department of Chemical and Petroleum Engineering, University of Calgary, AB – Canada.

Kabra, K., R. Chaudhary and R. Sawhney. (2004). Treatment of hazardous organic and inorganic compounds through aqueous-phase photocatalysis: A Review. Ind. Eng. Chem. Res., 43 (24), 7683-7696.

Kamble, S., S.P. Deosarkar, S.B. Sawant, J.A. Moulijn and V.G. Pangarkar. (2004). Photocatalytic degradation of 2,4-Dichlorophenoxyacetic acid using concentrated solar radiation: batch and continuous operation. Ind. Eng. Chem. Res., 43, 8178-8187.

Kamble, S.P., S.B. Sawat and V.G. Pangarkar. (2006). Photocatalytic mineralization of phenoxyacetic acid using concentrated solar radiation and titanium dioxide in slurry photoreactor. Chem. Eng. Res. Des., 84(A5), 355-362.

Kaneko, M. and I. Okura. (2002). Photocatalysis science and technology. Kodousha, Springer. Japan.

Kanki, T., S. Hamasaki, N. Sano, A. Toyoda and K. Hirano. (2005). Water purification in a fluidized bed photocatalytic reactor using TiO_2-coated ceramic particles. Chem. Eng. J., 108, 155-160.

Khan, R.A. and J.F. Richardson. (1987). The resistance to motion of a solid sphere in a fluid. Chem. Eng. Commun., 62, 135-150.

Keshmiri, M., T. Troczynsky and M. Mohseni. (2006). Oxidation of gas trichloroethylene and toluene using composite sol-gel TiO_2 photocatalytic coatings. J. Hazard. Mater., B128, 130-137.

Keshmiri, M. (2004). Composite sol-gel process for photocatalytic titanium dioxide. PhD thesis. Department of Metals and Materials Engineering - University of British Columbia, BC – Canada.

Keshmiri, M., M. Mohseni and T. Troczynsky. (2004). Development of novel TiO_2 sol-gel derived composite and its photocatalytic activities for trichloroethylene oxidation. Appl. Catal. B – Environ., 53, 209-219.

Kim, D.H. and M.A. Anderson. (1996). Solution factors affecting the photocatalytic and photoelectrocatalytic degradation of formic acid using supprted TiO_2 thin films. J. Photoch. Photobio. A., 94, 221-229.

Kosanic, M. (1998). Photocatalytic degradation of oxalic acid over TiO_2 powder. J. Photoch. Photobio. A., 119, 119-122.

Krishna, V., N. Noguchi, B. Koopman and B. Moudgil. (2006). Enhancement of titanium dioxide photocatalysis by water-soluble fullerenes. J. Colloid Interf. Sci., 304, 166-171.

Krysa, J., G. Waldner, H. Mesťánková, J. Jirkovský and G. Grabner. (2006). Photocatalytic degradation of model organic pollutants on an immobilized particulate TiO_2 layer: Roles of adsorption processes and mechanistic complexity. Appl. Catal. B - Environ., 64, 290-301.

Kuhn, H.J., S.E. Braslavsky and R. Schmidt. (2004). Chemical actinometry. Pure Appl. Chem., 76(2), 2105-2146.

Kulas, J., I. Rousar and J. Krysa. (1998). Photocatalytic degradation rate of oxalic acid on the semiconductive layer of n-TiO_2 particles in the batch mode plate reactor: Mass transfer limits. J. Appl. Electrochem., 28, 843-853.

Kumara, G.R.R.A., F.M. Sultanbawa, V.P.S. Perera, I.R.M. Kottegoda and K. Tennakone. (1999). Continuous flow photochemical reactor for solar decontamination of water using immobilized TiO_2. Sol. Energ. Mat. Sol. C., 58, 167-171.

Kwan, C.Y. and W. Chu. (2003). Photodegradation of 2,4-Dichlorophenoxyacetic acid in various iron-mediated oxidation systems. Water Res., 36(9), 2043-2051.

Laine, R.M. (1990). Chemical processing of glasses. SPIE, vol. 1328, Sol-Gel Optics, 16-28.

Lau, J., W. Bahnfleth and J. Freihaut. (2009). Estimating the effects of ambient conditions on the performance of UVGI air cleaners. Build. Environ., 44, 1362-1370.

Lee, D., S.C. Kim, I.C. Cho, S.J. Kim and S.W. Kim. (2004). Photocatalytic oxidation of microcystin-LR in a fluidized bed reactor having TiO_2-coated activated carbon. Sep. Purif. Technol., 34, 59-66.

Lee, S. and K. Lee. (2004). Mass transfer effect on the photocatalytic activity of UV/TiO_2 packed-bed systems. J. Ind. Eng. Chem., 10 (3), 492-498.

Lehr, J., J. Keelay and J. Lehr. (2005). Water Encyclopedy. John Wiley and Sons, 755-823.

LightSources Inc., and LightTech Lamp Technology. (2005). Technical sheet on germicidal lamps. USA.

Linsebigler, A.L., G. Lu and J.T. Yates. (1995). Photocatalysis on TiO_2 surfaces: principles, mechanisms and selected results. Chem. Rev., 95 (3), 735-758.

Liqiang, J., X. Baifu, Y. Fulong, W. Baiqi, S. Keying, C. Weimin and F. Honggang. (2004). Deactivation and regeneration of ZnO and TiO_2 nanoparticles in the gas phase photocatalytic oxidation of n-C_7H_{16} or SO_2. Appl. Catal. A-Gen., 275, 49-54.

Livage, J. (1998). Sol-gel synthesis of heterogeneous catalyst from aqueous solutions. Catal. Today, 41, 3-19.

Livage, J., C. Sanchez, M. Henry and S. Doeuff. (1989). The chemistry of the sol-gel process. Solid State Ionics, 32(33), 633-638.

Livage, J., M. Henry and C. Sanchez (1988). Sol-gel chemistry of transition metal oxides. Prog. Solid State Ch., 18, 259-341.

Lutz, E.H. and M.V. Swain. (1991). Mechanical and thermal shock properties of duplex-ceramics. A review. Materials Forum, 15, 307-323.

MacAdam, J. and S.A. Parsons. (2009). An investigation into advance oxidation of three chlorophenoxy pesticides in surface water. Water Sci. Technol., 59 (8), 1665-1671.

Macak, J., M. Zlamal, J. Krysa and P. Schmuki. (2007). Self-organized TiO_2 nanotubes layers as highly efficiency photocatalysts. Small, 3(2), 300-304.

Mackenzie, J. (2003). Sol-Gel Research – Achievements since 1981 and Prospects for the Future. J. Sol-Gel Sci. Techn., 26, 23-27.

Marczenko, Z. (1986). Separation and spectrophotometric determination of elements. Halsted Press, NY – USA.

Marczewska, A.D. and Marczewski, A.W. (1997). A general model for adsorption of organic solutes from dilute aqueous solutions on heterogeneous solids: application for prediction of multisolute adsorption. Langmuir, 13, 1245-1250.

McMurray, T.A., J.A. Byrne, P.S.M. Dunlop, J.G.M. Winkelman, B.R. Eggins and E.T. McAdams. (2004). Intrinsec kinetics of photocatalytic oxidation of formic and oxalic acid on immobilised TiO_2 films. Appl. Catal. A – Gen., 262, 105-110.

Matthews, R. (1992). Photocatalytic oxidation of organic contaminants in water: an aid to environmental preservation. Pure & Appl. Chem., 64(9), 1285-1290.

Matthews, R. (1987). Photo-oxidation of organic impurities in water using thin films of titanium dioxide. J. Phys. Chem., 91, 3328-3333.

McMurray, T.A., J.A. Byrne, P.S.M. Dunlop, J.G.M. Winkelman, B.R. Eggins and E.T. McAdams. (2004). Intrinsec kinetics of photocatalytic oxidation of formic and oxalic acid on immobilised TiO_2 films. Appl. Catal. A – Gen., 262, 105-110.

Mears, D.E. (1971). Test for transport limitations in experimental catalytic reactors. Ind. Eng. Chem. Process Des. Dev., 10(4), 541-547.

Muggi, D. and M. J. Backes. (2002). Two active sites for photocatalytic oxidation of formic acid on TiO_2: Effect of H_2O and temperature. J. Catal., 209, 105-113.

Mills, A., R.H. Davies and D. Worsley. (1993). Water purification by semiconductor photocatalysis. Chem. Soc. Rev., 22 (6), 417-425.

Mills, A., J. Wang and D. Ollis. (2006). Dependence of the kinetics of liquid-phase Photocatalyzed reactions on oxygen concentration and light intensity. J. Catal., 243, 1-6.

Minero, C. and D. Vione. (2006). A quantitative evolution of the photocatalytic performance of TiO_2 slurries. Appl. Catal. B – Environ., 67, 257-269.

Modestov, A.D. and O. Lev. Photocatalytic oxidation of 2,4-dichlorophenoxyacetic acid with titania photocatalyst. Comparison of supported and suspended TiO_2. J. Photoch.Photobio. A., 112, 261-270.

Mrowetz, M. and E. Selli. (2006). Photocatalytic degradation of formic and benzoic acids and hydrogen peroxide evolution in TiO_2 and ZnO water suspensions. J. Photoch. Photobio. A., 180, 15-22.

Muller, G.E. (1997). Numerical simulation of packed beds with monosized spheres in cylindrical containers. Powder Technol., 92, 179-183.

Muraganandham, M. and M. Swaminathan. (2006). TiO2 – UV photocatalytic oxidation of reactive Yellow 14: Effect of operational parameters. J. Hazard. Mater. B135, 78-86.

Nazeri, A., Bescher, E. and Mackenzie, J. (1993). Ceramic composites by the sol-gel method: A review. Ceram. Eng. Sci. Proc., 14(11-12), 1-19.

Nelson R.J., C.L. Flakker and D.S. Muggli (2007). Photocatalytic oxidation of methanol using titania-based fluidized beds. Appl. Catal. B - Environ. 69(3-4), 189-195.

Nikolaou, A. and T.D. Lekkas. (2001). The role of natural organic matter during formation of chlorination by-products: A Review. Acta Hydroch. Hydrob., 29, 63-77.

Ohtami, M., M. Kakimoto, S. Nishimoto and T. Kagia. (1993). Photocatalytic reaction of neat alcohols by metal-loaded Titanium (IV) oxide particles. J. Photoch. Photobio. A., 70(3), 265-272.

Okamoto, K., Y. Yamamoto, H. Tanaka and A. Itaya. (1985). Kinetics of heterogenous photocatalytic decomposition of phenol over anatase TiO_2 powder. Bull. Chem. Soc. Jpn., 58, 2023-2028.

Ollis, D.F. and C. Turchi. (1990). Heterogeneous photocatalysis for water purification: contaminant mineralization kinetics and elementary reactor analysis. Environ. Prog. , 9 (4), 229-234.

Ollis, D.F., E. Pelizzetti and N. Serpone. (1991). Photocatalyzed destruction of water contaminants. Environ. Sci. Technol. , 25 (9), 1522-1529.

Ollis, D. (2005). Kinetics of liquid phase photocatalyzed reactions: An Illuminating approach. J. Phys. Chem. B. 109, 2439-2444.

Optoweb (2009). Sol-gel process. Retrieved 02-16-2009 from http://optoweb.fis.uniforma2.it/optp/solgel/

Osajima, J.A., H.M. Ishiki and K. Takashima. (2008). The Photocatalytic degradation of Imazapyr. Monatsh. Chem., 139, 7-11.

Parker, C.A. (1953). A new sensitive chemical actinometer. I. Some trials with potassium ferrioxalate. Proc. R. Soc. A., 220, 104-116.

Parson, S. (2004). Advance oxidation processes for water and wastewater treatment. IWA Publising, USA.

Peng, T., D. Zhao, K. Dai, W. Shi and K. Hirao. Synthesis of titanium dioxide nanoparticles with mesoporous anatase wall and high photocatalytic activity. J. Phys. Chem. B., 109 (11), 4947-4952.

Perry, R.H. and D.W. Green. (1997). Perry's chemical engineering handbook. Seventh Edition, McGraw Hill, USA.

Pettibone, J.M., D.M. Cwiertny, M. Scherer and V.H. Grassian. (2008). Adsorption or Organic acids on TiO2 Nanoparticles: Effect of pH, Nanoparticle Size, and Nanoparticle Aggregation. Langmuir, 24, 6659-6667.

Porter, J.F., Y. Li and C. Chan. (1999). The effect of calcination on the microstructural characteristics and photoreactivity of Degussa P-25 TiO_2. J. Mater. Sci., 34, 1523-1531.

Pozzo, R., M. Baltanás and A. Cassano. (1999). Towards a precise assessment of the performance of supported photocatalysts for water detoxification processes. Catal. Today, 143-157.

Pozzo, R., J. Giombi, M. Baltanás and A. Cassano. (2000). The performance in fluidized bed reactor of photocatalysts immobilized onto inert supports. Catal. Today, 62, 175-187.

Prakash, A., C.L. Briens and M.A. Bergougnou. (1987). Mass transfer between Solid particles and liquid in a three phase fluidized bed. Can. J. Chem. Eng., 65, 228-236.

Qiu, W. and Y. Zheng. (2007). A comprehensive assessment of supported titania photocatalyst in a fluidized bed photoreactor: Photocatalytic activity and adherence stability. Appl. Catal. B - Environ, 71, 151-162.

Que, W., Y. Zhou, Y.L. Lam, Y.C. Chan and C.H. Kam. (2001). Preparation and characterizations of the TiO_2/organically modified silane composite materials Produced by the Sol-Gel Method. J. Sol-Gel Sci. Techn., 20, 187-195.

Rahaman, M. (2007). Ceramic processing. Taylor & Francis Group, USA.

Rahn, R.O. (1997). Potassium iodide as a chemical actinometer for 254 nm radiation: use of iodate as an electron scavenger. Photochem. Photobiol., 66(4), 450-455.

Rahn, R.O., J. Bolton and M.I. Stefan. (2006). The iodide/iodate actinometer in UV disinfection: determination of the fluence rate distribution in UV reactors. Photochem. Photobiol., 82, 611-615.

Rahn, R.O., M.I. Stefan, J.R. Bolton, E. Goren, P. Shaw and K.R. Lykke. (2003). Quantum yield of the iodide-iodate chemical actinometer: dependence on wavelength and concentration. Photochem. Photobiol., 78(2), 146-152.

Raudsepp, M., F.C. Hawthorne and A.C. Turnock. (1990). Evaluation of the Rietveld method for the characterization of fine-grained products of mineral synthesis: the diopside-hedenbergite Join. Can. Mineral., 28, 93-109.

Raudsepp, M. and E. Pani. (2003). Application of Rietveld analysis to environmental mineralogy. In: Mineralogical Association of Canada, Short Courses Series, Volume 31, Chapter 8, 165-180.

Ray, A. (1998). A new photocatalytic reactor for destruction of toxic water pollutants by advanced oxidation process. Catalysis Today, 44, 357-368.

Reed, S.J.B. (2005). Electron microprobe analysis and scanning electron microscopy in geology. Second Edition, Cambridge University Press, UK.

Richardson, J.F. and W.N. Zaki. (1954). Sedimentation and fluidization. Part I. Trans. Inst. Chem. Eng., 32, 35-53.

Richerson, D.W. (2006). Modern ceramic engineering: properties, processing and use in design. Taylor & Francis Group. Third Edition. USA.

Riedwyl, H. (1998). Modifying and using Yates' algorithm. Stat. Pap., 39, 41-60.

Ring, T.A. (1996). Fundamentals of ceramic powder processing and synthesis. Academic Press.

Rodríguez-Gonzáalez, V., A. Moreno-Rodríguez, M. May., F. Tzompantzi and R. Gómez. (2008). Slurry photodegradation of 2,4-dichlorophenoacetic acid: A comparative study of impregnated and sol-gel In_2O_3-TiO_2 mixed oxide catalysts. J. Photoch. Photobio. A., 193, 266-270.

Sakka, S. (2006). Current sol-gel activities in Japan. Sol-Gel Sci. Techn., 37, 135-140.

Satterfield, C.N. (1980). Heterogenous catalysis in practice. McGraw-Hill, Inc. USA.

Scherer, G.W. (1990). Theory of drying. J. Am. Ceram. Soc., 73 (1), 3-14.

Serpone, N., G. Sauvé, R. Koch, H. Tahiri, P. Pichat, P. Piccinini, E. Pelizzeti and H. Hidaka. (1996). Standardization protocol of process efficiencies and activation parameters in heterogenous photocatalysis: relative photonic efficiencies ξ_r. J. Photoch. Photobio. A., 94, 191-203.

Serpone, N. (1997). Relative photonic efficiencies and quantum yields in heterogeneous photocatalysis. J. Photoch. Photobio.A, 104, 1-12.

Shankar, M.V., S. Anandan, N. Venkatachalam, B. Arabindoo, and V. Murugesan. (2006). Fine route for an efficient removal od 2,4-dichlorophenoxyacetic acid (2,4-D) by zeolite-supported TiO_2. Chemosphere, 63, 1014-1021.

Shi, J., J. Zheng and P. Wu. (2009). Preparation, characterization and photocatalytic activities of holmium-doped titanium dioxode nanoparticles. J. Hazard. Mater., 161, 416-422.

Sinclair, C.J., A.B.A. Boxall, S.A. Parsons and M.R. Thomas. (2006). Prioritization of pesticide environmental transformation products in drinking water supplies. Environ. Sci. Technol., 40, 7283-7289.

Sing, K.S.W., R.A.W. Haul, L. Moscou, R.A. Pierotti, J. Rouquerol and T. Siemieniewska. (1985). Reporting physisorption data for gas/solid systems with special reference to the determination of surface area and porosity. Pure Appl. Chem., 57 (4), 603-619.

Sink, K.S.W., R.A.W. Haul, R.A. Pierotti and T. Siemieniewska (1985). Reporting physisorption data for gas/solid systems with special reference to the determination of surface area and porosity. Pure Appl. Chem., 57, 603-619.

Skjak-Braek, G., T. Anthonsen and P. Sandford. (1989). Chitin and chitosan. Elsevier Applied Science, USA.

Stangroom, S.J., C.D. Collins and J.N. Lester. (1998). Sources of organic micropollutants to lowland rivers. Environ. Technol., 19, 643-666.

So, W.W., S.B. Park, K.J. Kim and S.J. Moon. (1997). Phase transformation behavior at low temperature in hydrothermal treatment of stable and unstable titania sol. J. Colloid Interf. Sci., 191, 398-406.

Speitel, G.E., J.M. Symons, J.M. Mialaret and M.M.E. Wanielista. (2000). AOP/biomilm process for DOX precursors. Journal-American Water works Association, 92, 59-73.

Su, C., B.-Y. Hong and C.-M. Tseng (2004). Sol-gel preparation and photocatalysis of titanium dioxide. Catal. Today, 96, 119-126.

Syoufian, A., O. H. Satriya and K. Nakashima. (2007). Photocatalytic activity of titania hollow spheres: Photodecomposition of methylene blue as a target molecule. Catal. Commun., 8, 755-759.

Szépe, S., and O. Levenspiel. (1968). Optimal temperature policies for reactors subject to catalyst deactivation – I Batch reactor. Chem. Eng. Sci., 23, 881-894.

Teichner, S.J. (2008). The origins of photocatalysis. J. Porous Mater., 15, 311-314.

Terashima, Y., H. Ozaki, R.R. Giri, T. Tano, N. Nakatsuji, R. Takanami and S. Taniguchi. (2006). Photocatalytic oxidation of low concentration of 2,4-D solution with new TiO_2 fiber catalyst in a continuous flow reactor. WA. Sci. Technol., 54 (8), 55-63.

Thiruvenkatachari, R., S. Vigneswaran and I.S. Moon. (2008). A review on UV/TiO_2 photocatalytic oxidation process. Korean J. Chem. Eng., 25 (1), 64-72.

Thurman, E.M. (1985). Organic geochemistry of natural waters. Nijhoff & Junk Publ. USA.

Tournié, P., C. Laguerie and J.P. Couderc. (1979). Correlations for mass transfer between fluidized spheres and a liquid. Chem. Eng. Sci., 34, 1247-1255.

Tremblay, K.M.A. (2001). Photocatalytic treatment of wastewater: a model for a fast process monitoring analysis method. M.Sc Thesis. Department of Chemistry, University of Calgary, AB.

Trillas, M., J. Peral and X. Domenech. (1995). Redox photodegradation of 2,4-dichlorophenoxyacetic acid over TiO_2. Appl. Catal. B – Environ.,5, 377-387.

Trillas, M., J. Peral and X. Domenech. (1996). Photocatalyzed degradation of phenol, 2,4-Dichlorophenol, phenoxyacetic acid and 2,4-Dichlorophenoxyacetic acid over supported TiO_2 in a flow system. J. Chem. Tech. Biotechnol., 67, 237-242.

Turchi, C., and D. Ollis. (1989). Mixed reactant photocatalysis: intermediates and mutual rate inhibition. J. Catal., 119, 483-496.

Turchi, C., and D. Ollis. (1990). Photocatalytic degradation of Organic water contaminants: mechanism involving hydroxyl radiacl attack. J. Catal., 122, 178-192.

Turchi, C. and E. Wolfrum. (1992). Letters to the Editors: comments on "Reactor dynamics in the evaluation of photocatalytic oxidation kinetics". J. Catal., 136, 626-628.

Ultraviolet Technology of Australasia PTY LTDA (UVTA). (1999). Technical sheet on critical factors for ultraviolet desinfection systems.

Vaisman, E., M.F. Kabir, A. Kantzas and C.H. Langford. (2005). A fluidized bed photoreactor exploiting a supported photocatalyst with adsorption pre-concentration capacity. J. Appl. Electrochem., 35, 675-681.

Veeh, R.H., W.P. Inskeep and A.K. Camper. (1996). Soil depth and temperature effects on microbial degradation of 2,4-D. J. Environ. Qual., 25, 5-12.

Wen, J. and G. Wilkes (1996). Organic/inorganic hybrid network materials by the sol-gel approach. Chem. Mater., 8, 1667-1681.

Werther, J. and J. Reppenhagen (1999). Catalyst attrition in fluidized-bed systems. AIChE Journal, 45 (9), 2001-2010.

Wetchakun, N. and S. Phanichphant. (2008). Effect of temperature on the degree of anatase-rutile transformation in titanium dioxide nanoparticles synthesized by the modified sol-gel method. Curr. Appl. Phys., 8, 343-346.

WHO (2006). Water. Training Package for the Health Sector. Retrieved 08-27-2008 from http://www.who.int/ceh/capacity/Water.pdf.

WHO (2008). Water and sanitation. Retrieved 08-27-2008 from http://www.euro.who.int/watsan/issues/20030903_1

Xu, J., W. Dai, J. Li, Y. Cao, H. Li and K. Fan. (2008). Novel core-shell structure mesoporous titania microspheres: preparation, characterization and excellent photocatalytic activity in phenol abatement. J. Photoch. Photobio. A., 195, 284-294.

Yang, Q. (1999). Composite sol-gel ceramics. PhD thesis. Department of Metals and Materials Engineering - University of British Columbia, BC - Canada.

Yin, H., Y. Wada, T. Kitamura, S. Kambe, S. Murasawa, H. Mori, T. Sakata and S. Yanagida. (2001). Hydrothermal synthesis of nanosized anatase and rutile TiO_2 using amorphous phase TiO_2. J. Mater. Chem., 11, 1694-1703.

Zalazar, C., M. Labas, C. Martin., R. Brandi, O. Alfano and A. Cassano. (2005). The extended use of actinometry in the interpretation of photochemical reaction engineering data. Chem. Eng. J., 109, 67-81.

Zhang, X., H. Liu, W. Li, G. Cui, H. Xu, K. Han and Q. Long. (2008). Visible-light photocatalytic degradation of aromatic contaminants with simultaneous H_2 generation: comparison of 2,4-Dichlorophenoxyacetic acid and 4-Chlorophenol. Catal. Lett., 125, 371-375.

Zhang, M., T. An, J. Fu, G. Sheng, X. Wang, X. Hu and X. Ding. (2006). Photocatalytic degradation of mixed gaseous carbonyl compounds at low level on adsorptive TiO_2/SiO_2 photocatalyst using a fluidized bed reactor. Chemosphere, 64, 423-431.

Zhang, W. and F. A. DiGiano. (2002). Comparison of bacterial regrowth in distribution systems using free chlorine and chloramine: statistical study of causative factors. Water Res., 36, 1469-1482.

Appendix A

Statistical analysis: Yates effects, F values and CI

The calculation of the effects in the response variables (catalyst attrition and photocatalyst activity) of the different formulation used to prepare the composite TiO_2 spheres will be described in this section.

- **Comparison between different formulation to produce TiO_2 spheres**

To compare the photocatalytic activity of the different catalyst formulations (Section 6.2.1 – Preliminary tests and effects of various parameters), an analysis between different formulations was done by comparing the mean of the reaction rate constant of each of those formulations following the same approach described by Box *et al.* (1978).

For each of the experiments described in Section 6.2.1, three replicates were done per experimental run; therefore, three independent values of the rate constant were determined during the FA degradation in a FBPR. An average ($\hat{y}_t$) was calculated for each of those sets of data as well as the grand average for all the data ($\hat{y}$) obtained during in these preliminary experiments, which is the sum of all the reaction rate constants experimentally obtained divided by the total number of observations.

For the variations within formulations, the sum of squares, S_t (deviations from the average), was calculated by:

$$S_t = \sum_{m=1}^{n} (y_{ti} - \bar{y}_t)^2 \qquad \text{(A.1)}$$

where the y_{tm} is the m^{th} observation (each rate constant) in the t^{th} formulation and $\hat{y}_t$ is the average of the three experimental values. Then, the *within-formulation sum of squares* for all the formulations (*f* in total) was given by:

$$S_R = \sum_{t=1}^{f}\sum_{m=1}^{n}(y_{ti} - \bar{y}_t)^2 \tag{A.2}$$

and the *within-formulation mean square* was given by:

$$s_R{}^2 = \frac{S_R}{N_t - f} \tag{A.3}$$

where *f* is the total number of formulations tested and N_t is the total number of observations (total number of reaction rate constants).

For the variations between formulations, the *between-formulations sum of squares* can be calculated by:

$$S_T = \sum_{i=1}^{f} n_t(\bar{y}_t - \bar{y})^2 \tag{A.4}$$

where n_t is the number of observations (reaction rate constants) per formulation (*f*). Then, the *between-formulations mean square* was calculated as follows:

$$s_T{}^2 = \frac{S_T}{f - 1} \tag{A.5}$$

Once the residues analysis was done to probe that the errors are independently and identically distributed in a normal distribution with mean zero and variance σ^2 (usually abbreviated as IIDN (0, σ^2)), the hypothesis of the analysis was probed. This hypothesis was that the formulations means were all equal and that there was no difference between formulations. The experimental F value was calculated by:

$$F_{exp} = \frac{s_T^{\,2}}{s_R^{\,2}} \tag{A.6}$$

which is the F value for v_T/v_R degrees of freedom, where $v_T = f\text{-}1$ and $v_R = N_t - f$. If the F_{exp} is within the F distribution for a given confidence level (i.e., 99%), the null hypothesis is true; on the other hand, if the F_{exp} is outside of the F distribution, the null hypothesis is discredit and some differences exist between formulations.

In this particular case, doing the above mentioned calculation for the data listed in Table A.1, the F_{exp} was 2.47 and the $F_{9,20}$ was 4.57 (at 99% confidence level). Therefore, from the statistical point of view, there was no difference between formulations.

Table A.1: Reaction rate constants for the different formulation utilized during the preliminary tests in Section 6.2.1

PT_1	PT_2	PT_3	PT_4	PT_5	PT_6	PT_7	PT_8	PT_9	PT_{10}
0.02154	0.02985	0.02506	0.02290	0.02204	0.02676	0.02967	0.02911	0.02413	0.02968
0.02290	0.02154	0.02389	0.01990	0.02440	0.02501	0.02814	0.02714	0.02569	0.02353
0.02415	0.02451	0.02489	0.02430	0.01990	0.02315	0.02468	0.02830	0.02147	0.02687

where:

PT_1: is referring to the formulation that used Nitric acid (HNO_3) instead of HCl

PT_2: is referring to the formulation that used 0.053 g H_2O mL^{-1} TTIP

PT_3: is referring to the formulation that used 0.13 mL HCl mL^{-1} TTIP

PT_4: is referring to the formulation that used 0.30 g P-25 mL^{-1} TTIP

PT_5: is referring to the formulation that used 0.50 g P-25 mL^{-1} TTIP

PT_6: is referring to the formulation that used a chitosan solution with a pH of 4.58

PT_7: is referring to the formulation that used a chitosan solution with a pH of 4.01

PT_8: is referring to the formulation that used a chitosan concentration of 15 g chitosan L^{-1}

PT_9: is referring to the formulation that had a drying process at 80°C for 20h

PT_{10}: is referring to the formulation that was calcined for 3 h at 600°C

- **Yates algorithm used for the experimental design**

Yates algorithm was used to calculate the effects and interactions among the different variables utilized during the experimental design described in Section 6.2.2 (Experimental design) for the catalyst improvement. In this experimental design, the activity and the catalyst attrition were the response variables.

As shown in Table A.2, five variables were analyzed in two different levels (different values of the variable). Using this information, the signs arrangement shown in Table A.3 was done, showing the different combination between variables. In this particular case, the levels of variable E were generated based on the signs of ABCD interaction (E = ABCD)

Table A.2: Variables included in the 2^{5-1} experimental design

Variable	Levels	
	-	+
Amount of Water, A (g mL^{-1} TTIP)	0.040	0.053
Amount of HCl, B (mL mL^{-1} TTIP)	0.133	0.200
Concentration of NH_4OH solution, C (%)	10	20
Drying conditions, D	RT-15 days	80°C – 20 h
Calcination time, E (h)	1	3

Table A.3: Signs arrangement for the 2^{5-1} factorial design

Run Number	Variables				
	A	**B**	**C**	**D**	**E**
5	-	-	-	-	+
6	+	-	-	-	-
7	-	+	-	-	-
4	+	+	-	-	+
3	-	-	+	-	-
8	+	-	+	-	+
2	-	+	+	-	+
1	+	+	+	-	-
12	-	-	-	+	-
16	+	-	-	+	+
9	-	+	-	+	+
15	+	+	-	+	-
14	-	-	+	+	+
11	+	-	+	+	-
13	-	+	+	+	-
10	+	+	+	+	+

Table A.4 shows the results obtained after applying Yates algorithm. One important consideration at this point was that all the effects of third and fourth order (represented by three-factor and four factor interactions) were ignored, assuming that detectable effects could be identify only with first and second order interactions.

Table A.4: Confounding pattern and estimates from 25-1 design of Table A.3

Confounding Pattern	Estimate
*l*A→A	-1.1939
*l*B→B	5.0939
*l*C→C	-2.2757
*l*D→D	0.1371
*l*E→E	0.0379
*l*AB→AB	-2.6568
*l*AC→AC	0.5455
*l*AD→AD	2.1939
*l*AE→AE	0.5106
*l*BC→BC	0.2789
*l*BD→BD	-1.3829
*l*BE→BE	-1.6264
*l*CD→CD	-0.5227
*l*CE→CE	0.3520
*l*DE→DE	3.6077
Average	*11.6841*

With the data listed in Table A.4, a normal plot (Figure A.1) can be done to determine the effects and interactions that are significant for the analysis. As can be seen, there are some points (close to zero) that can be adjusted to a linear regression which means that all those values can be explained by noise. The other values are considered significant for the analysis. Therefore, using just the significant effects, the estimate conversion for the process development data was given at the vertices of the design as is shown in Equation A.7.

$$\bar{y}_{est} = Average + \left(\frac{lAB}{2}\right)x_{AB} + \left(\frac{lC}{2}\right)x_C + \left(\frac{lBE}{2}\right)x_{BE} + \left(\frac{lBD}{2}\right)x_{BD} + \left(\frac{lAD}{2}\right)x_{AD} + \left(\frac{lDE}{2}\right)x_{DE} + \left(\frac{lB}{2}\right)x_B + \left(\frac{lA}{2}\right)x_A \quad \text{(A.7)}$$

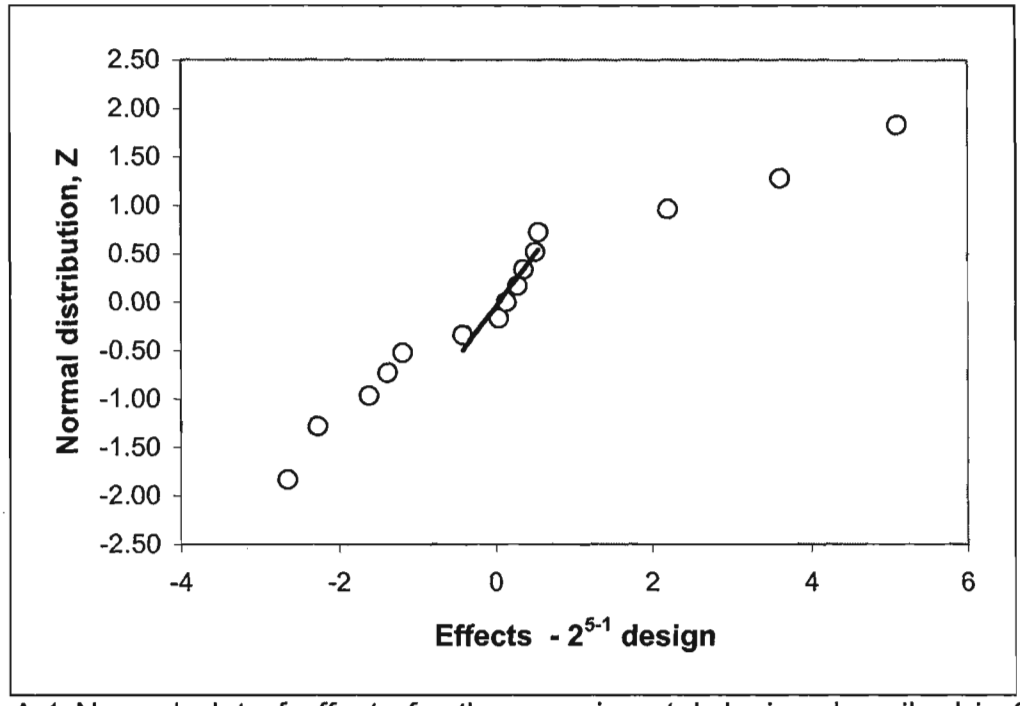

Figure A.1 Normal plot of effects for the experimental design described in Section 6.2.2

The difference between the estimated value (Equation A.7) and the values obtained experimentally (reaction rate constant and attrition values – Table 6.4) was defined as the residuals. Therefore, in order to check the model, a normal plot between of these residuals can be done (Figure A.2). In this case, all the points from this residual plot should lie close to the line, confirming the conjecture that effects other than AB, C, BE, BD, AD, DE, B and A are readily explained by random noise. As can be seen in Figure A.2, the points are fairly close to the line, which was enough to confirm the conjecture.

With these results, the values of the variables A,B,C,D and E (Table A.2) can be selected based on the combination that gives lower attrition and higher activity. The effect of the amount of water (A), the amount of HCl (B) and the concentration of NH_4OH solution (C) was selected directly from the results obtained based on the signs arrangements shown in Table A.3. But the effects of BE, BD, AD and DE cannot be interpreted separately because of the interaction between variables and is

better to consider the two-way table were the combine effect of the variables was analyzed.

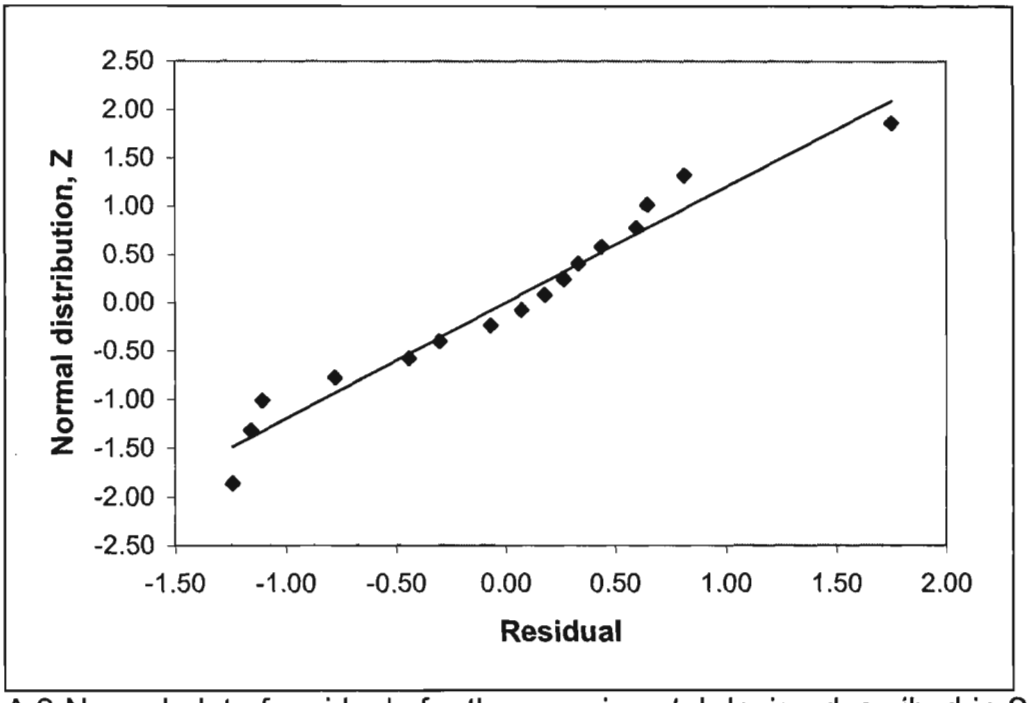

Figure A.2 Normal plot of residuals for the experimental design described in Section 6.2.2

- **Confidence interval calculations**

In order to calculate the error bars in all the graphs described in this document, the confidence interval was calculated following the approach described by Cumming *et al.* (2007). In this approach, the standard deviation (Equation A.8) was calculated to quantify the average difference between the data points and their mean. Then, the standard error was calculated (Equation A.9) to determine how variable the mean would be. Finally the confidence interval was calculated with Equation A.10.

$$SD = \sqrt{\frac{\sum (X - M_x)^2}{n_t - 1}} \tag{A.8}$$

$$SE = \frac{SD}{\sqrt{n_t}} \tag{A.9}$$

$$CI = M_x \pm t_{v(n_t-1)} SE \tag{A.10}$$

where X is each individual data, M is the mean, n is the number of independent samples, $t_{v(n-1)}$ is a critical value of t_v for n_t-1 degree of freedom at 95%. The confidence interval can be defined like the range of values where you can be 95% confident that contains the true mean.

- **Standard Error of the parameter**

The standard error of the parameter (rate constant degradation) was estimated using the standard error of the estimation and the covariance matrix (2x2) given for the exponential fit. These two parameters were obtained by the program CurveExpert 1.3. The standard error (Equation A.11) was calculated multiplying the standard error of the estimation (E_{est}) by the covariance element of the parameter (C_{elem})

$$S_{error} = (E_{est} \cdot C_{elem})^{0.5} \tag{A.11}$$

With this standard error and using the t distribution, the standard error of the parameter can be estimated as follows:

$$S_{param} = S_{error} \cdot t_{v(n_t-2)} \tag{A.11}$$

where t_v is the T distribution at $n_t - 2$ degrees of freedom (n_t is the number of points considered to do the exponential adjustment)

Appendix B

Particle Size Distribution of the TiO_2 Particles in Suspension

The particle size distribution analysis was done for the treated water after three hours of normal operation of the FBPR with spheres calcined at 600°C. The equipment used for the analysis (Mastersizer 2000 – Malvern Instruments) was located at UBC Environmental Group at the Department of Civil Engineering.

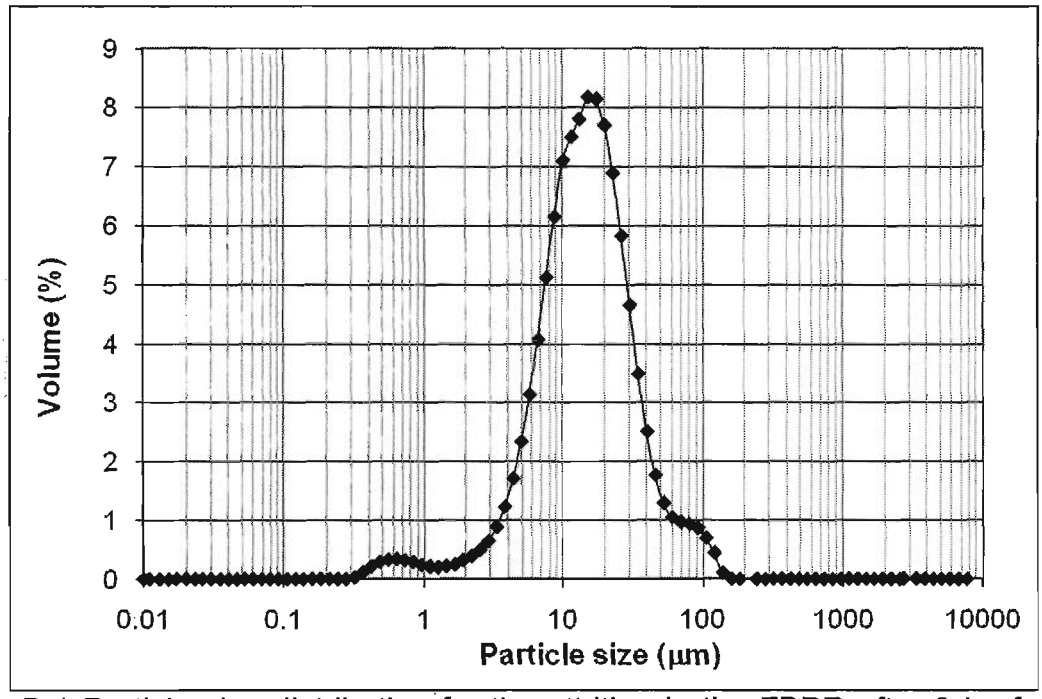

Figure B.1 Particle size distribution for the attrition in the FBPR after 3 h of normal operation using spheres calcined at 600°C

As can be seen in Figure B.1, a significant amount of particles had an average size around 15 μm.